Integrated characterization of CO_2 storage reservoirs on the Rock Springs Uplift combining geomechanics, geochemistry, and flow modeling

Final Scientific/Technical Report

Reporting Period Start Date: October 1, 2014
Reporting Period End Date: September 30, 2018

Principal Authors:
Drs. John Kaszuba (PI), Vladimir Alvarado, Erin Campbell, Dario Grana, Kam Ng, Erin Stoesz, Heng Wang, and Hua Yu

Issued: December 2018

DOE Award Number: DE-FE0023328

Submitting Organization: University of Wyoming, 1000 E. University Ave., Laramie, Wyoming 82071

DISCLAIMER

ABSTRACT

This project improves understanding of the effects CO_2 injection and storage on geomechanical, petrophysical, and other properties on two potential reservoirs, the Madison Limestone and Weber Sandstone, at the Rock Springs Uplift, southwest Wyoming. Rock physics studies, laboratory experiments, and computer simulations were employed. Two groups of rock samples were prepared, one aged with formation brine and the second aged with CO_2-saturated formation brine and subsequently used for geomechanical, geochemical, and petrophysical testing.

Rock physics studies provided a facies classification to discriminate among different lithologies and to investigate the feasibility of predicting petrophysical properties using seismic inversion. By applying a zone-wise regression relation established in this facies analysis, a 3D reservoir model was developed. It was determined that time-lapse seismic data are not feasible for monitoring CO_2 displacement at the Rock Springs Uplift or to mitigate leakage-risks situations because pressure and fluid saturation have small effects on elastic velocities and synthetic seismograms. The small variations that do occur are due to the low porosity of the sandstone and the high stiffness of the dolomite.

In the Madison Limestone, mineral dissolution due to reaction with CO_2-saturated brine was observed in highly permeable pathways while mineral precipitation happened in intergranular or micropores. Changes in pore size were quantified via Time-Domain Nuclear Magnetic Resonance transverse relaxation time (T_2) and diffusion coefficient distributions. As opposed to continuous injection of CO_2-saturated brine, a subtle increase in porosity after static 'soaking' with CO_2-saturated brine increases permeability due to the heterogeneity of changes in pore and pore throat sizes. Porosity-permeability relationships are fitted using a power-law function that can be adopted to model time-evolved porosity and permeability in a transport-limited CO_2 injection process.

The effect of CO_2-saturated brine on the linear elastic properties of Weber Sandstone and Madison Limestone cannot be generally concluded. Considering horizontal and vertical orientations and different confining pressures, no consistent relationship between stress (or strain) data and reaction with CO_2-saturated brine was observed in the nonlinear plastic and post-failure regime. The change of elastic constants due to reaction with CO_2-saturated brine is more significant in Madison Limestone than in Weber Sandstone; however, no consistent trend was observed. Reservoir simulations suggest that injectivity for Weber Sandstone is adversely impacted by low permeability. Changes in confining pressure do not impact injection rate and can be ignored while the effect of changes to pore pressure cannot. The effect of confining pressure and pore pressure on the size of the CO_2 plume in the Madison Limestone is negligible because of higher permeability. Geomechanical and petrophysical properties induced by CO_2-brine-rock reactions were time-dependent. Simulations considered these time-dependent properties and indicate that injectivity, porosity distribution, pressure distribution and CO_2 saturation were affected.

Table of Contents

EXECUTIVE SUMMARY

The goal of this project was to improve understanding of the effects CO_2 injection and storage on geomechanical, petrophysical, and other properties on two potential reservoirs, the Madison Limestone and Weber Sandstone, at the Rock Springs Uplift, southwest Wyoming. The approach developed in this project can be adapted to other sites to guide site characterization and design of surveillance and monitoring techniques to meet the goal of ensuring 99% storage permanence, contribute to Best Practice Manuals, and reduce time and cost of site characterization.

Cores, well logs, image logs, fluid samples and microfrac tests from a stratigraphic test well (RSU #1) that was previously drilled on the northeast flank of the Rock Springs Uplift were used to provide foundational information. Rock physics studies, laboratory experiments, and computer simulations were then employed. Two groups of limestone and sandstone samples were prepared, one aged with formation brine and the second aged with CO_2-saturated formation brine. Samples from both groups were used for geomechanical testing to determine standard rock mechanics properties and changes to these properties induced by reaction of the rocks with CO_2-saturated formation brine. Samples from both groups were also used for geochemical and petrophysical tests that evaluated the nature of mineral-fluid reactions as well as how these reactions affected the pore sizes and pore size distributions, all important parameters for understanding the geomechanical response of a reservoir to CO_2 injection and storage.

Rock physics studies of the Weber Sandstone and Madison Formation provided a facies classification in order to discriminate among different lithologies and to investigate the feasibility of predicting petrophysical properties (porosity and permeability) with the help of seismic inversion. By applying a zone-wise regression relation established in this facies analysis, a 3D reservoir model was developed. This model served as the basis for assessing the feasibility of monitoring CO_2 displacement during injection and to mitigate leakage-risks situations. It was determined that time-lapse seismic data are not feasible for monitoring CO_2 displacement during injection or to mitigate leakage-risks situations because pressure and fluid saturation have small effects on elastic velocities and synthetic seismograms. The small variations that do occur are due to the low porosity of the sandstone and the high stiffness of the dolomite. This information will be useful in developing technologies for future reservoir monitoring approaches.

In deep saline formations far from CO_2 injection wells or in post-injection scenarios, the spatial and temporal geochemical reactions are mostly constrained by mineral distribution heterogeneities, pore structure, and transport properties, leading to complicated changes in pore structure and petrophysical properties. These changes may impact CO_2 injectivity, migration and storage capacity. In the Madison Limestone, mineral dissolution due to reaction with CO_2-saturated brine was observed mainly in highly permeable pathways while mineral precipitation happens in intergranular or micro-pores. Changes in pore size were quantified via Time-Domain Nuclear Magnetic Resonance transverse relaxation time (T_2) and diffusion coefficient distributions. As opposed to continuous injection of CO_2-saturated brine, a subtle increase in porosity after static 'soaking' with CO_2-saturated brine leads to an apparent increase in permeability due to the heterogeneity of changes in pore and pore throat sizes. The porosity-permeability relationships are fitted using a power-law function, which can be adopted to model time-evolved porosity and permeability in a transport-limited CO_2 injection process. Logical

implications are that heterogeneous mineral dissolution and precipitation induce changes in pore structure, such as mineralogy, roughness of the pore surface, and pore throat size, that would also affect the dynamic properties associated to CO_2, such as wettability, relative permeability and capillary pressure. Changes in these crucial properties would affect pore-scale multi-phase flow, hysteresis of drainage and imbibition processes and capillary trapping, thus having a significant influence on the efficiency of capillary pressure trapping, CO_2 plume size and storage capacity, and even caprock sealing efficiency and integrity.

The effect of CO_2-saturated brine on the linear elastic properties of Weber Sandstone and Madison Limestone cannot be generally concluded. Considering horizontal and vertical orientations and different confining pressures, no consistent relationship between stress (or strain) data and reaction with CO_2-saturated brine was observed in the nonlinear plastic and post-failure regime. The change of elastic constants due to reaction with CO_2-saturated brine is more significant in Madison Limestone than in Weber Sandstone; however, no consistent trend was observed. These findings provide foundational data for designing future studies needed to decipher chemomechanical effects of CO_2-brine-rock reactions.

Reservoir simulations suggest that injectivity for Weber Sandstone is adversely impacted by low permeability. Changes in confining pressure do not impact injection rate and can be ignored while the effect of changes to pore pressure cannot. The effect of confining pressure and pore pressure on the size of the CO_2 plume in the Madison Limestone is negligible because of higher permeability. Geomechanical and petrophysical properties induced by CO_2-brine-rock reactions were time-dependent. Simulations considered these time-dependent properties and indicate that injectivity, porosity distribution, pressure distribution and CO_2 saturation were affected.

INTRODUCTION

One of the challenges to successfully implementing geologic carbon sequestration is the ability to reliably and economically predict the permanence of CO_2 in potential storage sites. The technology for injecting CO_2 into deep geologic formations already exists and has been applied for enhanced oil recovery and acid gas disposal. For geologic sequestration to become a viable option, however, potential storage sites must be assessed to determine if they can store much larger amounts of CO_2 over much greater periods of time. The challenge derives in part from the complex, heterogeneous nature of deep saline formations – important because of their large storage potential – that will serve as storage sites. Without an acceptable understanding of the ultimate fate and permanence of CO_2 in these storage sites, risk mitigation based on the integrity of a CO_2 reservoir cannot be achieved. Significant strides have been made towards achieving this goal, most notably in our understanding of the physics of flow of CO_2 in porous media and the geochemical and mineralogical changes imposed by CO_2 in a reservoir. Key missing pieces are our limited ability to understand, measure, and predict the petrophysical and geomechanical effects of CO_2 injection.

The goal of this project was to improve understanding of the effects CO_2 injection and storage on geomechanical, petrophysical, and other reservoir properties through a study of experimentation, analyses of existing data sets (Shafer, 2013; Surdam, 2013), and simulations representing conditions and processes at the Rock Springs Uplift (RSU), a potential geologic CO_2 storage site in southwest Wyoming. The project made use of the comprehensive dataset that was previously developed for the RSU by the Department of Energy (DOE Award Number: DE-FE0002142) and the State of Wyoming (Shafer, 2013; Surdam, 2013). The approach developed in this project can be adapted to other sites to guide site characterization and design of surveillance and monitoring techniques to meet the goal of ensuring 99% storage permanence, contribute to Best Practice Manuals, and reduce time and cost of site characterization.

This final report for the project is organized as follows. The Background Section provides geologic and historic context for the project. The Experimental Methods Section summarizes the methods used in the project and refers the reader to Appendices where these methods are described in detail. The Results and Discussion Section focuses on the most significant findings relevant to the project and refers the reader to Appendices where these results are discussed in greater detail. The Conclusions Section summarizes salient findings and presents logical implications of these findings with respect to technology development in the future; more detailed conclusions are presented in the relevant Appendices.

BACKGROUND

A stratigraphic test well (RSU #1) was drilled on the northeast flank of the RSU (Figure 1) for the purpose of obtaining rock cores, well logs, image logs, fluid samples and microfrac tests to identify possible target zones for CO_2 sequestration. Potential reservoirs for CO_2 sequestration at this location are the Madison Limestone and Weber Sandstone (Figure 2). The Madison Limestone and Weber Sandstone are deep saline aquifers and high quality reservoirs that could ensure commercial-scale carbon dioxide storage at the RSU (Surdam, 2013; Wang et al., 2018). RSU #1 core from these formations was previously analyzed for mechanical stratigraphy, fracture systems, and in-situ stress conditions (Shafer, 2013). Additional information regarding the RSU, RSU #1, and both formations is provided in Appendix I (Summary of Advanced Rock

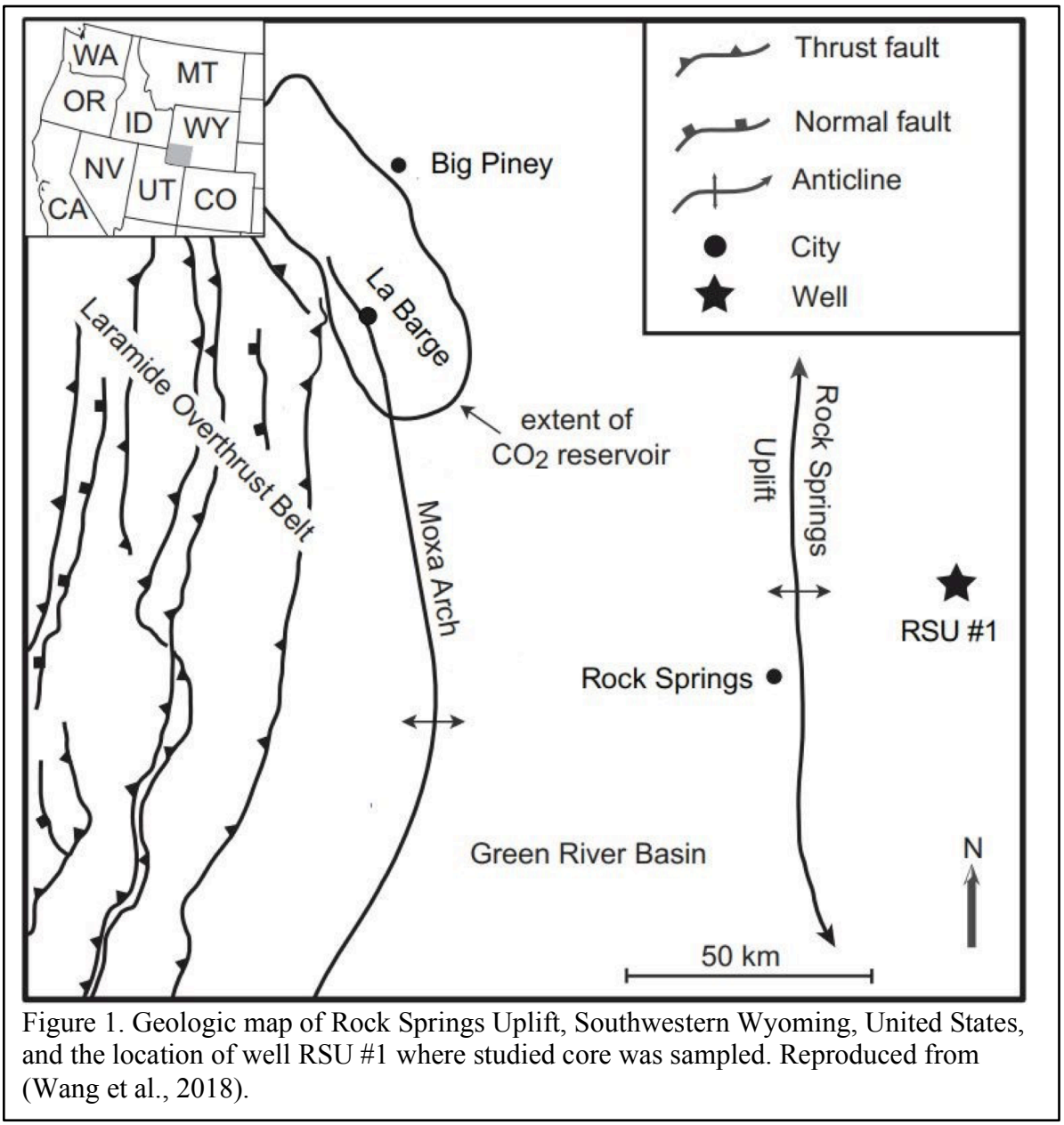

Figure 1. Geologic map of Rock Springs Uplift, Southwestern Wyoming, United States, and the location of well RSU #1 where studied core was sampled. Reproduced from (Wang et al., 2018).

Property Model); Grana et al. (2017), the rock physics and seismic reservoir characterization study developed for the project; and Wang et al. (2018), the nuclear magnetic resonance characterization of the RSU that was completed as part of this project.

METHODS

Reservoir Characterization

The facies classification study of the RSU included: 1) the log-facies classification based on rock properties derived from well log data, core sample description and geologic information; and 2) the facies classification of geophysical data (for example, elastic properties) both at the well log and geophysical (seismic) scales. The methodology was assessed using a statistical contingency analysis to compare the two classifications. The second step of the classification was obtained by

applying a cluster analysis technique to the set of mineral volumes and porosity computed logs and the validation of the facies discriminability in the elastic domain at the well log scale and at the seismic scale. Detailed descriptions of these methods are presented in Appendix I (Summary of Advanced Rock Property Model) and Appendix II (Rock Physics Model Development and Analysis).

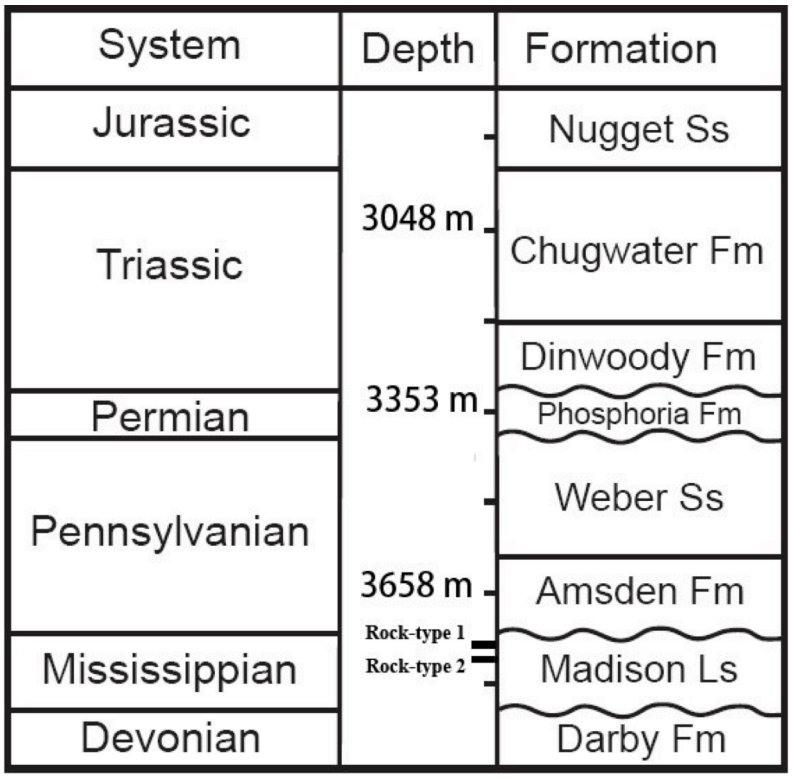

Figure 2. Stratigraphic column for well Rock Springs Uplift #1 including cored intervals; Ss = sandstone; Ls = limestone. Reproduced from (Wang et al., 2018).

Although the original RSU seismic data consisted of 245 inlines and 247 crosslines, low fold at the edges of the survey were not suitable for prestack waveform inversion. Therefore a 3D sub-volume of 176 inlines and 176 crosslines was extracted, over which the common midpoint fold was adequate for prestack waveform inversion. The prestack waveform inversion method takes the normal moveout uncorrected prestack seismic data as input and inverts for the isotropic elastic subsurface properties (P-wave velocity, V_P; S-wave velocity, V_S; and density, ρ). It uses a genetic algorithm as the search engine and the reflectivity method for forward synthetic computation. Detailed descriptions of these methods are presented in Appendix III (Seismic Reservoir Characterization).

Materials

Samples of Madison Limestone and Weber Sandstone used for this study are described in Appendix IV (List of Rock Samples Selected/Obtained for CO_2-Water-Rock Experiments). The Madison Limestone is a dolostone that is comprised predominantly of the mineral dolomite. In addition to dolomite, minor amounts of quartz, anhydrite, calcite, and pyrite are present. Two rock types of the Madison Limestone, vuggy and intergranular limestone, directly relate to pore types and reservoir behavior and are the main geologic CO_2 storage zones of the Madison Limestone. Vuggy Madison Limestone is the most heterogeneous, with less predictable flow pathways dictated by large-scale variability in pore size and distribution. Flow pathways within vuggy limestone prefer larger pore domains with minimal interaction in reduced pore size zones. Intergranular Madison Limestone behaves more heterogeneously in consideration of predictable flow pathways. Distribution of pores is more regular and flow pathways are more dispersed

across the entirety of the domain. The Weber Sandstone is an eolian quartz sandstone. It is predominantly comprised of quartz (~95%); the remainder of the rocks consists of feldspar, clay, pyrite, and carbonate cement.

Two groups of limestone and sandstone samples were prepared for the project, one aged with formation brine and the second aged with CO_2-saturated formation brine. Samples in Group 1 were aged (reacted) with formation brine for 800 hours at reservoir conditions (Table 1). Group 2 samples were aged with formation brine at reservoir conditions for 400 hours. Formation brine was subsequently displaced by CO_2-saturated brine (at reservoir conditions), and the samples were then aged for an additional 400 hours. Detailed descriptions of this process are presented in Appendix V (Analyses and Results Studied in the CO_2-Water-Rock Experiments) and Appendix VI (Results and Analyses of the Geomechanical Experiments).

Samples from both groups were used for geomechanical testing, while others were used for geochemical and petrophysical testing to evaluate the nature of mineral-fluid reactions as well as how these reactions affected the pore sizes and pore size distributions, all important parameters for understanding the geomechanical response of a reservoir to CO_2 injection and storage. A detailed description of this workflow is presented in Appendix VI.

Geochemical and Petrophysical Methods

Before and after reacting the samples with formation brine and with CO_2-saturated formation brine, gas (N_2) permeability, porosity and 1H-NMR transverse relaxation time (T_2) were measured. NMR T_2 distributions are sensitive to changes in overall pore-size distributions (surface-area/volume ratio). Scanning electron microscope SEM and thin section images were also collected. Detailed descriptions of all materials and equipment used as well as methods employed are presented in Appendix V. Detailed descriptions of the NMR T_2 methodology is presented in Wang and Alvarado (2018).

Geomechanical Methods

A servo-controlled triaxial equipment RTR-1500 manufactured by GCTS was used to conduct all geomechanical experiments. Laboratory testing parameters (e.g., confining pressure, pore pressure, and temperature) were determined based on in-situ reservoir conditions measured at the RSU #1 (Shafer, 2013). A total of eleven Weber Sandstone samples and six Madison Limestone samples were evaluated. Triaxial compression tests were conducted at three confining stress conditions and at in situ temperature and pore pressure. The effect of CO_2 on the mechanical behavior of reservoir rocks under three differential pressures (6.9, 34.5 and 55.2 MPa) and two orientations (vertical and horizontal) was compared and investigated based on quantified mechanical properties, including elastic constants at the linear stress-strain regime and strength properties at nonlinear plastic and post-failure regimes. The effect of CO_2 on coefficients of Mohr-Coulomb failure criterion of reservoir rocks was also investigated. A summary of the geomechanical conditions for these tests is presented in Table 1. Detailed descriptions of all materials and equipment used as well as methods employed are presented in Appendix VI, Appendix VII (Baseline Geomechanical Experiment Results), Ng et al. (2018), and Yu et al. (2018).

Table 1. Geomechanical test conditions

Geochemical Preparation	Sample ID	Depth (m)	P_c (MPa)	P_p (MPa)	T (°C)
Group1: Aged with brine	SV1b	3415.6-3417.5	43.4	35.4	90
	SH1b	3413.8-3415.6			
	SV2b	3413.8-3415.6	71.0		
	SH2b	3413.8-3415.6			
	SV3b	3413.8-3415.6	91.7		
	SH3b	3413.8-3415.6			
	DH1b	3765.1-3767.0	46.2	39.3	93
	DH2b	3784.4-3786.2	73.8		
	DH3b	3763.4-3765.9	94.5		
Group2: Aged with brine-CO2	SV1c	3413.8-3415.6	43.4	35.4	90
	SH1c	3413.8-3415.6			
	SV2c	3413.8-3415.6	71.0		
	SH2c	3526.4-3528.2			
	SH3c	3413.8-3415.6	91.7		
	DH1c	3765.1-3767.0	46.2	39.3	93
	DH2c	3765.1-3767.0	73.8		
	DH3c	3765.1-3767.0	94.5		

SV–Vertical sandstone; SH–Horizontal sandstone; DH–Horizontal dolomite; b–Aged with brine; c–Aged with brine-CO2; P_c–Confining pressure; P_p–Pore pressure; and T–Temperature. Reproduced from Appendix VI (Results and Analyses of the Geomechanical Experiments).

Fluid Flow Simulations

Fluid flow simulations were performed with CMG-GEM (Computer Modelling Group compositional simulator) version 2015.106. A history-matching procedure was applied to unsteady-state coreflooding experiments to obtain relative permeability curves. Relative permeability curves and time-dependent geomechanical and petrophysical properties were then incorporated into a 3D model to simulate larger-scale CO_2 injection and storage. Detailed descriptions of the simulation process are presented in Appendix VIII (Initial Simulations) and Appendix IX (Simulations).

RESULTS AND DISCUSSION

Seismic Reservoir Characterization

Rock physics studies of the Weber Sandstone and Madison Formation (Appendices I and II) provided a facies classification in order to discriminate between different lithology and to investigate the feasibility of predicting petrophysical properties (porosity and permeability) with the help of seismic inversion. Four main facies were identified: shale, limestone, sandstone, and dolomite (Figure 3).

By applying a zone-wise regression relation established in exploratory data analysis on well data on the inverted P-impedance, a 3D porosity volume was obtained (Appendix III). After obtaining the porosity volume (Figure 4, top), the regression relation between porosity and permeability established from RSU #1 core data was applied on the 3D porosity volume to obtain the 3D permeability volume (Figure 4, middle). To obtain the facies volume (Figure 4, bottom), the well log facies classification was extended with Bayesian analysis to 3D. The 'Seis Facies' (Figure 3) was used as the guiding parameter for classification. Several combinations of V_P, V_S and density were tested as input volumes. V_P/V_S and I_P (acoustic impedance, the product of V_P and density, sometimes referred to as Z_P) provided the best results, which is consistent with 'Seis Facies'.

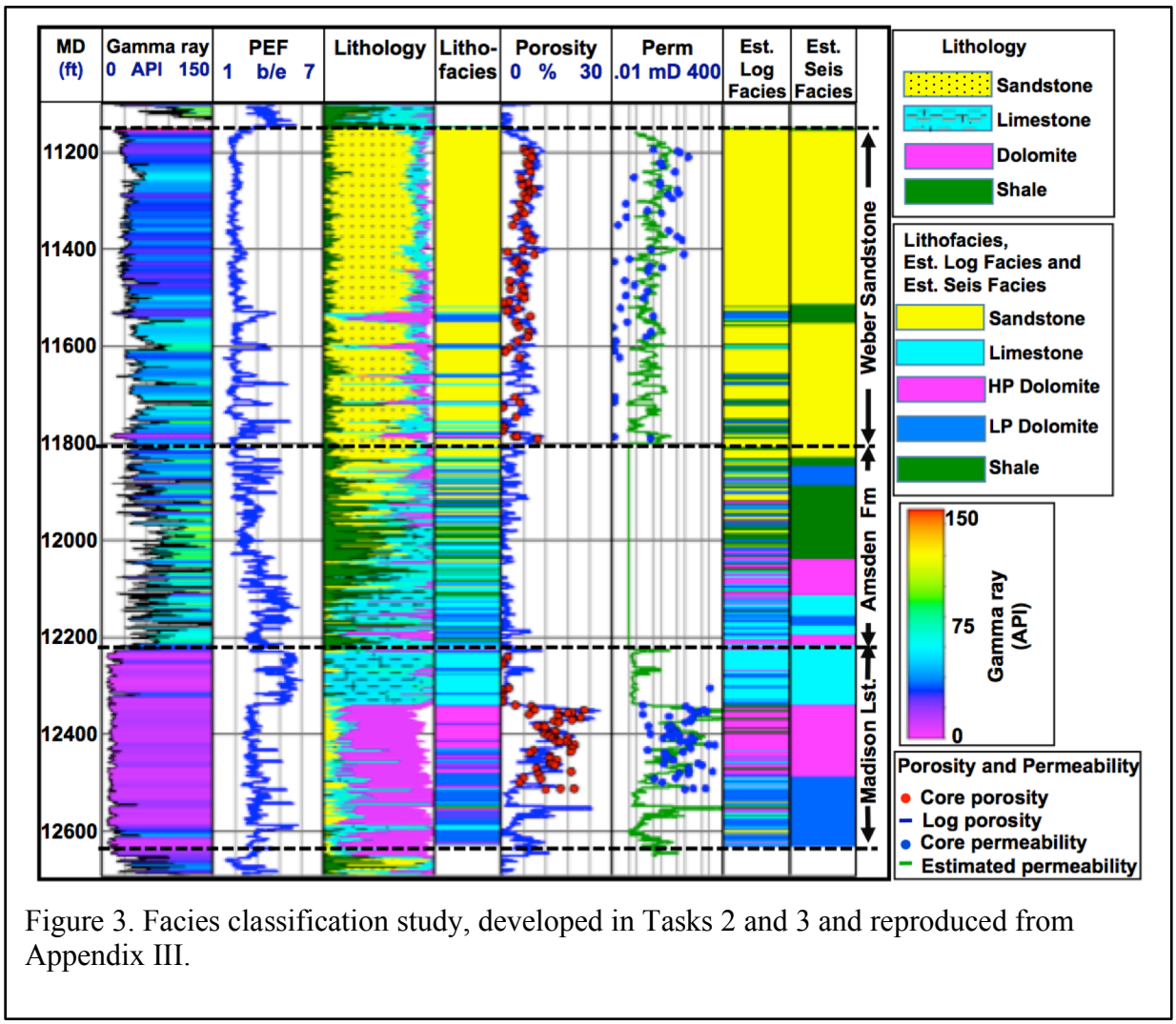

Figure 3. Facies classification study, developed in Tasks 2 and 3 and reproduced from Appendix III.

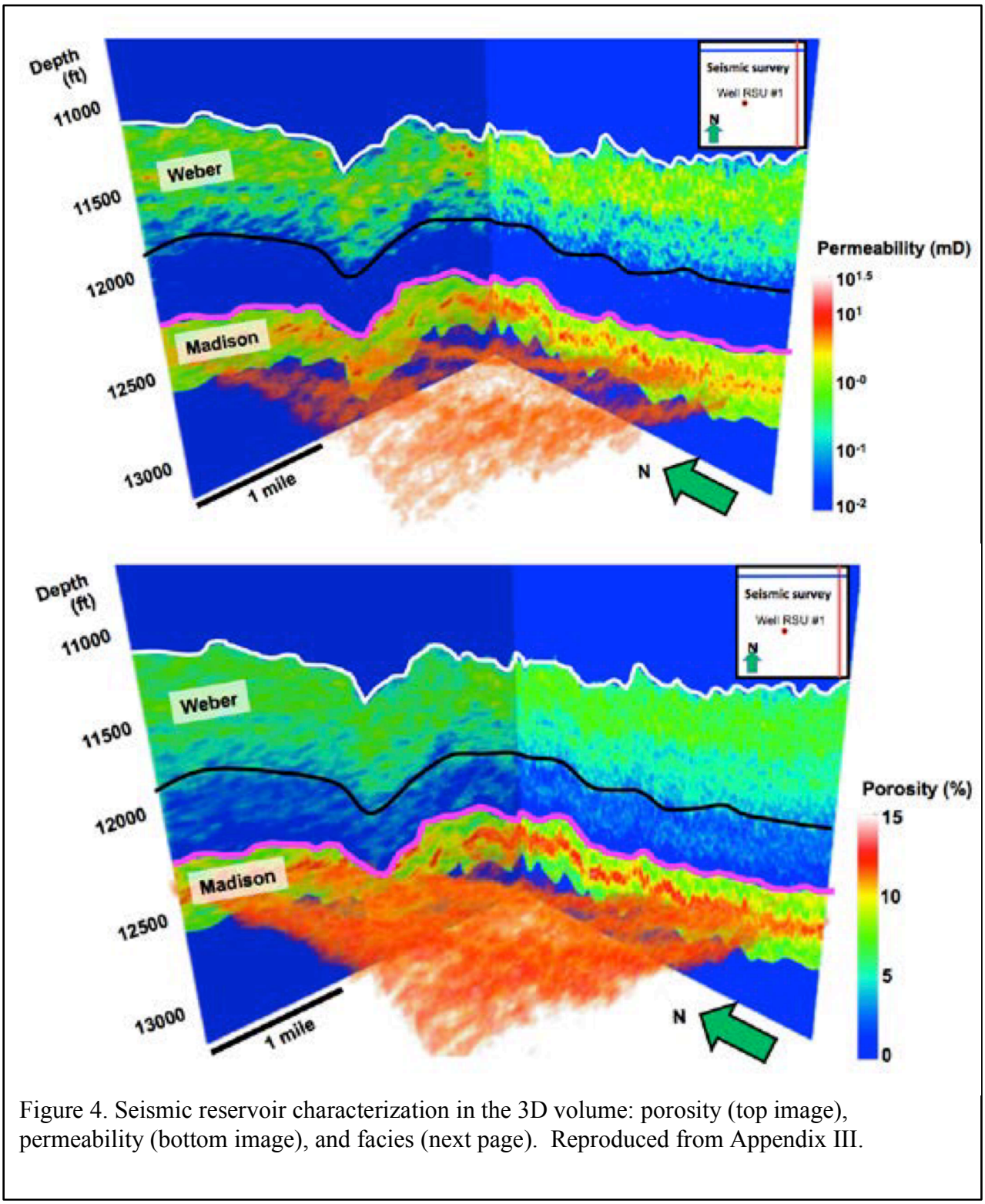

Figure 4. Seismic reservoir characterization in the 3D volume: porosity (top image), permeability (bottom image), and facies (next page). Reproduced from Appendix III.

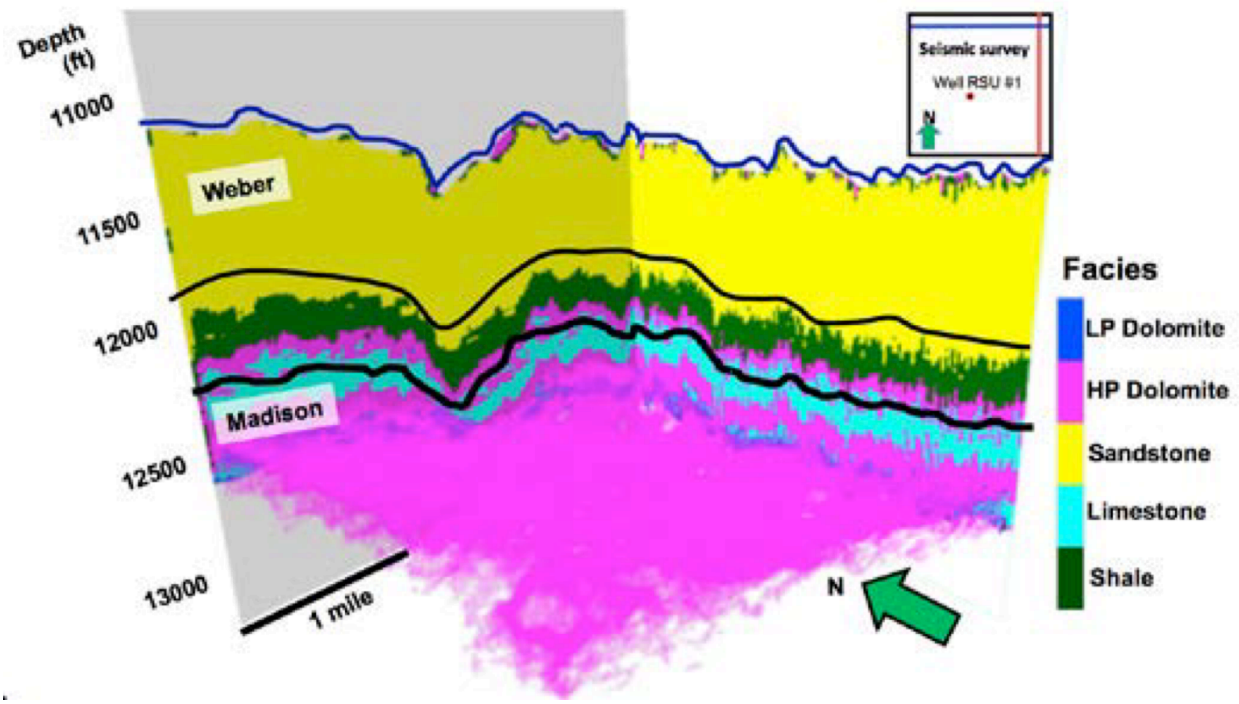

Figure 4. (continued). Seismic reservoir characterization in the 3D volume: facies. Reproduced from Appendix III.

Reservoir Monitoring Feasibility

To assess the feasibility of monitoring CO_2 displacement during injection and to mitigate leakage-risks situations, different pressure and saturation scenarios were simulated and their effects on elastic velocities and synthetic seismograms were modeled. Five pressure and fluid scenarios were applied and synthetic velocities and seismograms were modeled. When the effective pressure decreases with no change in fluid, the elastic moduli decrease and hence the P- and S-wave velocities decrease. In substituting CO_2 for fluid, the low bulk modulus of CO_2 causes V_P to decrease further, and this shows that both pressure and saturation effects produce a decreased V_P in CO_2-saturated rocks. The pressure effect dominates V_P over the saturation effect. Both pressure and saturation effects tend to decrease shear waves in brine-saturated rocks. Similarly, to compressional waves, the pressure effect also dominates shear waves over the saturation effect. For all modeled scenarios mentioned, the changes observed in velocities are rather small. On the other hand, and irrespective of the target formation, a change of density would be observed due to the difference in CO_2 saturation. An absolute change in density of about 1.2% was observed for a 20% CO_2 saturation, and about 5% change was observed for 80% CO_2 saturation. Additional information and details regarding the feasibility of reservoir monitoring is presented in Appendix X (Development and Analyses of the Initial Static Model).

Experimental Determination of Effects of CO_2-Brine-Rock Reactions on Pore Structure, Porosity and Permeability

CO_2 reservoirs can be reactive in the presence of injected CO_2, but impacts of geochemical reactions on pore structure and petrophysical properties are complicated and can relate to CO_2 migration. When CO_2 is injected into aquifers, a dry-out phenomenon occurs typically of the order of several meters near the wellbore (Mouzakis et al., 2016). For regions away from the wellbore or after injection is stopped, CO_2 migrates upward and/or laterally in a slow-flow regime (Peclet number (Pe) << 1) due to buoyancy, where mutual CO_2-H_2O solubility happens (Mouzakis et al., 2016). The pH of CO_2-enriched formation brine can decrease by 1-2 units (Kaszuba et al., 2005). The subsequent mineral reactions such as dissolution and precipitation change pore structures i.e. the pore shape, pore-size distribution, and mineral reactive surface area, thus impacting porosity, permeability and wettability (Luhmann et al., 2017) as well as geomechanical responses. In addition, the spatial heterogeneity of mineral reactions lead to complex changes in pore structure (Noiriel et al., 2016) due to heterogeneity of mineral distribution, reactive surface area as well as reaction rate (Luhmann et al., 2017), which are dependent on the Peclet (Pe) and Damkohler (Da) numbers (Tartakovsky et al., 2007).

The Péclet number (Pe) is a dimensionless number relating the rate of advection (transport by bulk flow in water) of a chemical component to the rate of diffusion (transport by a concentration gradient) of that component (Pe = advective transport rate / diffusive transport rate). Generally, Pe << 1 indicates a system that is dominated by chemical diffusion and Pe > 1 indicates a system dominated by mass flow or convection. The low-Péclet number regime better represents transport in the reservoir after injection has stopped or away from the carbon dioxide injection front. The Damköhler number (Da) is a dimensionless number relating the time scale of chemical reaction to the convection occurring in a system (Da = reaction rate / convective mass transport rate). Generally, Da < 0.1 indicates a system that is limited/controlled by chemical reaction and Da > 10 indicates a system limited/controlled by flow.

Geologic carbon sequestration research has focused on investigating continuous injection, which typically corresponds to high Pe and low Da values. In contrast, field injection practices vary. If CO_2 injection is interrupted, Pe << 1 as the flow rate in general is low and diffusion-dominant for molecules and ion transport in pore space. In addition, heterogeneity of mineral reactions are also time-dependent as Pe and Da numbers change in the pore network over time. Limited research on the spatial and temporal heterogeneity of mineral reactions and their impacts on porosity and permeability has been conducted.

The following three subsections present results of investigations into changes in pore structures and the impact of these changes on permeability and porosity due to mineral dissolution and precipitation induced by CO_2 injection into a brine-rock system. We reacted CO_2-saturated brine with core plugs at reservoir conditions (34.5 MPa and 93°C); the experiments were performed at static (batch) conditions to focus on diffusion-dominated effects in pore spaces. Scanning electron microscopy and optical analysis were conducted to visualize and characterize mineral dissolution, precipitation and pore structure changes resulting from heterogeneous mineral dissolution and precipitation. Additionally, proton Nuclear Magnetic Resonance (1H-NMR) transverse relaxation time (T2) was measured to determine changes in pore-size distribution (surface-area to pore volume ratio), providing quantitative evidence of pore size change after

CO_2-brine-rock reactions. The diffusion coefficient of hydrogen-containing molecules and/or ions provides a reference of dynamic equilibrium of transport properties during static CO_2-brine-rock reactions. We measured gas permeability and porosity in rock plugs before and after CO_2-brine-rock reactions. Integrated analysis of the data sets was performed to evaluate potential connections between reactivity large-scale effects on CO_2 storage.

These investigations were limited to Madison Limestone for two reasons: 1) Fewer reactive changes were expected for the Weber Sandstone and, given the scope of the project, this part of the study focused on Madison Limestone as the rock most susceptible to geochemical reaction; and 2) Madison Limestone possess a greater diversity of pore architecture than Weber Sandstone, providing greater spatial and temporal heterogeneity with which to evaluate diffusion-dominated effects and their impacts on porosity and permeability.

Mineral Dissolution and Precipitation

Porosity in the Madison Limestone is intergranular or vuggy dominated (Surdam, 2013). Zones of intergranular porosity are generally located near the top of the reservoir interval at the RSU #1, and are characterized by relatively uniform pore character and distribution. Examples of this porosity type are shown in Figure 5. Figure 5 (a) shows a vug in Rock-type 1 that is surrounded by smaller, uniform dolomite grains that typify the reservoir's intergranular porosity system. Though the intergranular pores are smaller, they are evenly distributed and provide the majority of the pore space in this facies of the Madison Limestone. For Rock-type 2, the dissolution has produced zones with massive pores and the highest overall porosity values, though they have a highly heterogeneous distribution. Vuggy, sometimes moldic, porosity forms by dissolution of the carbonate and/or anhydrite. Vuggy pores range in size and distribution, shown in Figure 5 (c), and are more heterogenous than intergranular pore systems. Authigenic quartz crystals (the white grains in the photomicrograph, shown in Figure 5 (d)), have nucleated in many of the larger pores. Authigenic dolomite grains are observed coating pore walls in the SEM image. In addition, small particles ranging from 0 to 10 μm were observed on the surface of dolomite crystals.

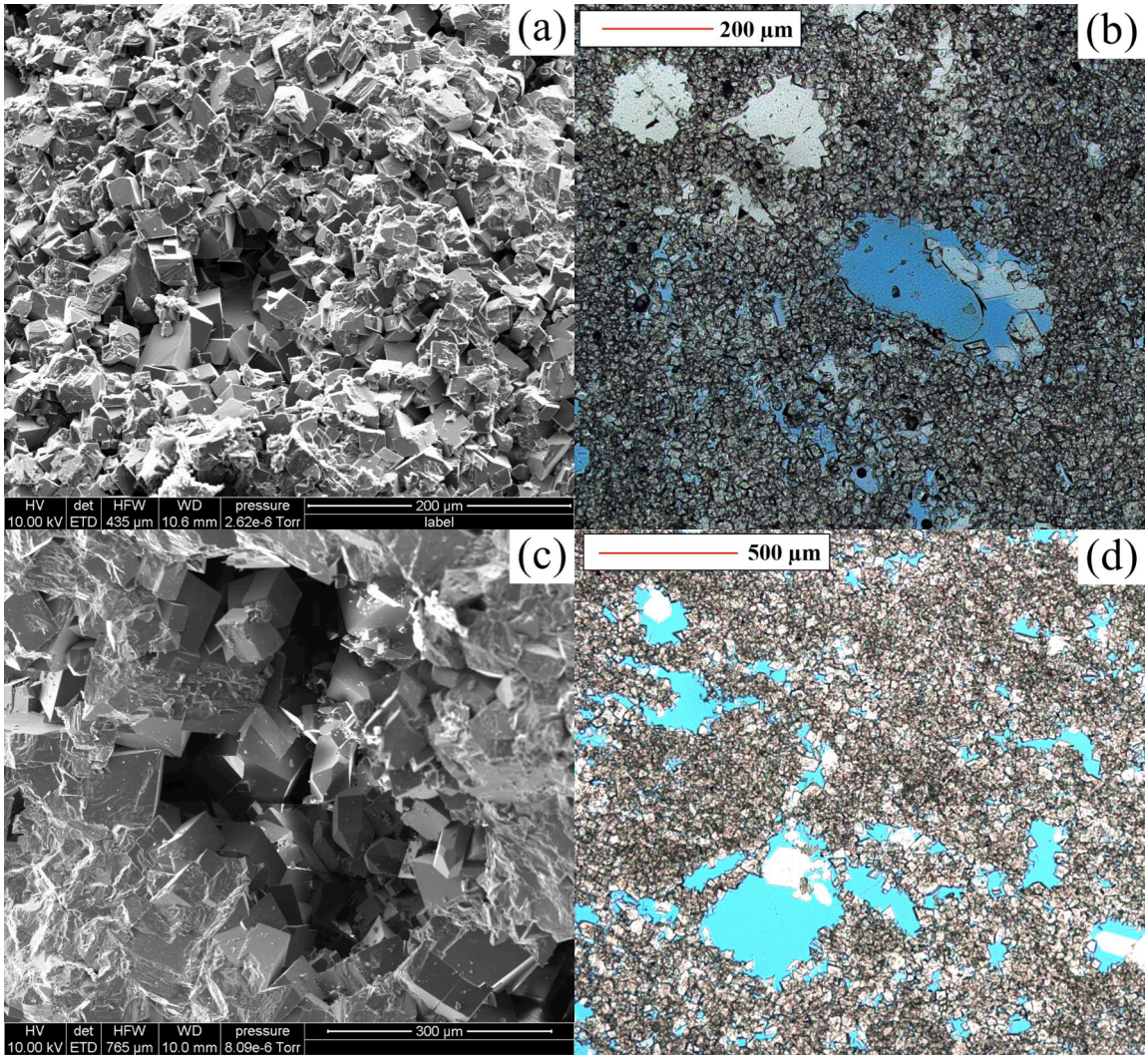

Figure 5. Scanning electron microscope (SEM) (left column) and thin sections images (right column) of Madison Limestone samples from the RSU#1 well. Thin sections are impregnated with blue epoxy to illustrate porosity. (a, b) Rock-type 1: a mixed intergranular and vuggy porosity system. Anhydrite cement fills two of the larger vugs in the top left quadrant of the thin section image. (c, d) Rock-type 2 a dominantly vuggy porosity system.

For sample MH1 (Table 2), porosity is composed mainly of homogeneous intergranular pores. These pores were filled by CO_2-enriched brine and dissolution happened uniformly in intergranular pores. Figure 6 shows SEM and thin section analysis of sample MH1 after static soaking. From the images (Figure 6 (a)), it is difficult to determine mineral dissolution from crystal corners or edges because of the volume limitation of the reactive fluids. However, pitting on the crystal surface and broken crystal faces become deeper, which is evidence for dolomite dissolution. The thin section image (Figure 6 (b)) shows 'bleached zones', wherein porosity has increased and dolomite crystals are lighter. The most prominent texture of additional dissolution within the integranular sample are nascent channel structures with walls of smaller (relative to matrix), partially digested dolomite crystals. Only larger dolomite crystals are retained in the

'bleached zones', suggesting increased porosity due to the dissolution of smaller dolomite grains within the matrix. Additionally, the number and size of small particles on crystal faces and within pores decrease. These observations also indicate that mineral surface area is a dominant control in the dissolution process.

Table 2: Summary of rock samples and properties before and after soaking with CO_2-saturated brine.

Sample ID	Rock Type	Dominant Porosity	Porosity, %		Permeability, mD	
			before	after	before	after
MH1	1	intergranular	16.22	16.39	14.06	15.27
MH2	2	vugs	18.16	22.29	65.09	150.10
MH3	1	intergranular	19.46	19.66	14.21	16.91
MH4	2	vugs	16.34	17.26	30.76	40.67

Notes: Routine core analyses (gas porosity and permeability) were carried out on all core plugs under a net confining stress of 1.5 MPa using a Coreval 700 permeameter and porosimeter (VINCI Technologies, France).

Pore systems in sample MH2 are vug-dominated, resulting in the displacement of reactant fluid along the most highly permeable pathways. Our results agree with previous studies in which reactions happen mainly in highly permeable pathways (vuggy pores), while in surrounding intergranular pores (matrix), the reactions are limited (Luquot et al., 2014). Figure 6 (c) shows an SEM image highlighting vuggy pores. Similar to MH1, pitting on the crystal surfaces became deeper after CO_2 soaking, while dissolution on the edge and corner of dolomite crystals cannot be validated based solely on the SEM images. The smallest particles on the surface of dolomite crystals are mostly dissolved (shown in Figure 6 (c)), which indicates the importance of surface area in dissolution process. In the thin-section image (shown in Figure 6 (d)), dolomite crystals that make up the walls of some of the pores are smaller than matrix dolomite grains. These textures are indicative of dissolution.

Mineral precipitation and dissolution happened simultaneously due to localized chemical equilibrium. Mineral precipitation is observed in both rock samples, shown in Figures 7 and 8. The newly precipitated minerals are located on dolomite crystals in small pores and have a distinctly irregular morphology. We collected the energy dispersive spectrum (EDS) of newly formed minerals from two CO_2-soaked samples and from pre-reacted dolomite crystals, shown in Figures 7 and 8. The EDS results show that the newly precipitated minerals are chemically similar to the original present. Another interesting observation is the precipitation of anhydrite, shown in Figure 8. The decrease in pH due to CO_2 dissolution increases the HCO_3^- concentration resulting in dissolution of dolomite, which ultimately leads to the increase in Ca^{2+} concentration within the reactive front saturations. Increased Ca^{2+} concentration prompts the precipitation of anhydrite.

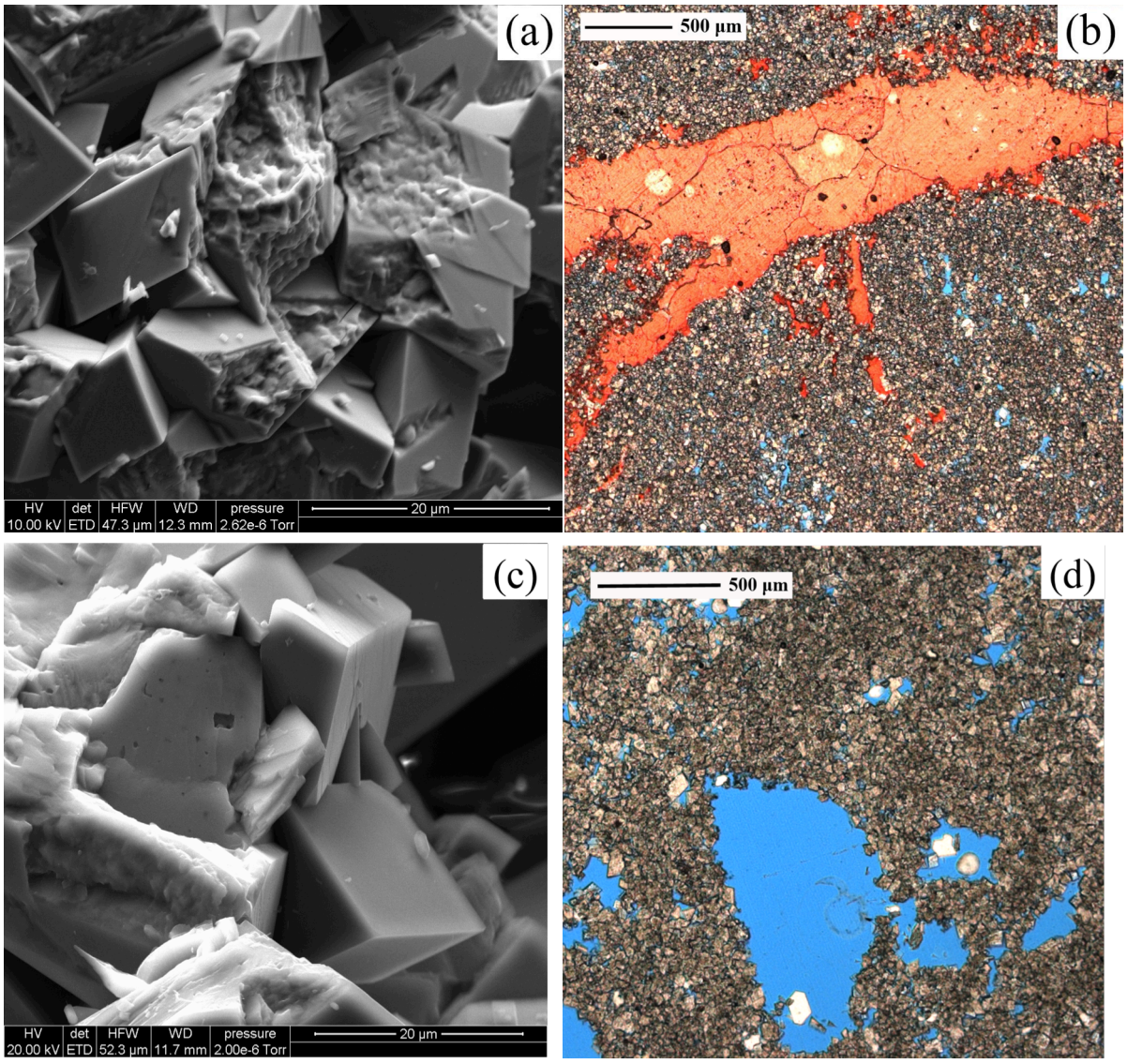

Figure 6. SEM and thin section images for MH1 and MH2 reacted with CO_2-saturated brine.

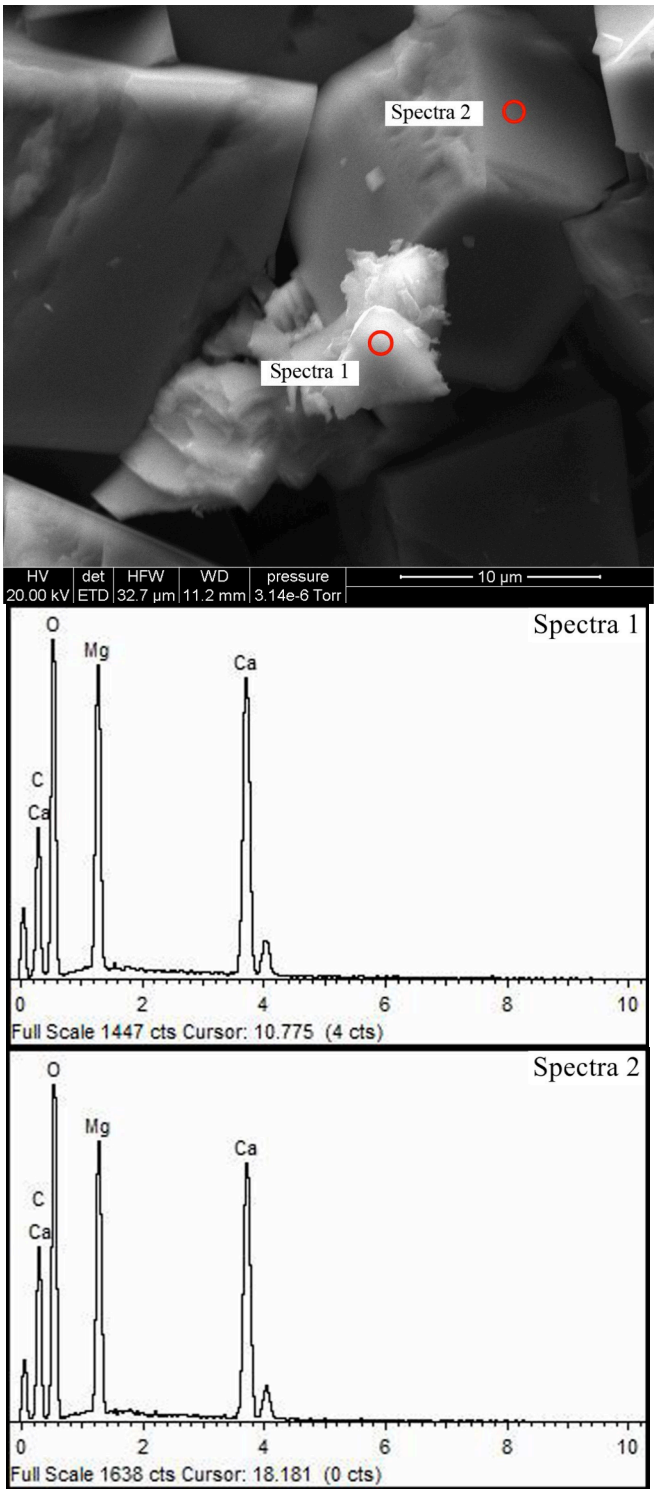

Figure 7. SEM image and EDS spectrum of newly precipitated minerals in sample MH1. Comparison of Spectra 1 (new mineral) to host dolomite (Spectra 2) show that dolomite is precipitated after digestion from CO_2.

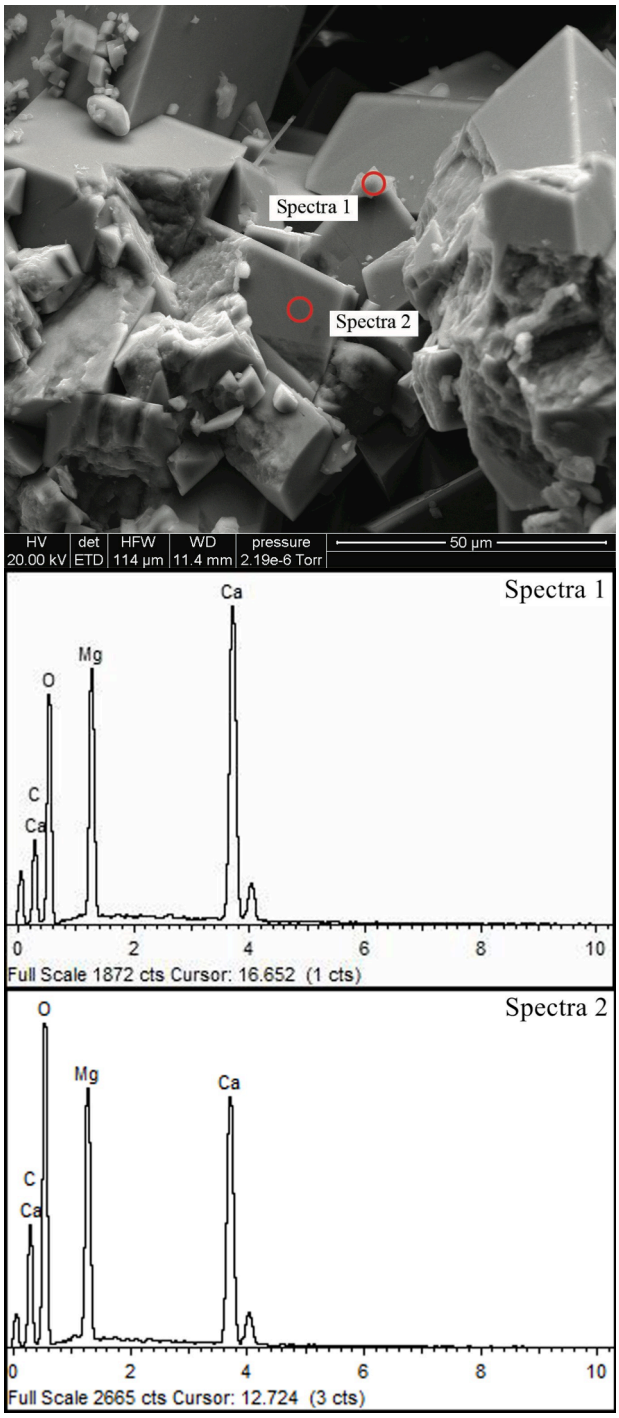

Figure 8. SEM image and EDS spectrum of newly precipitated minerals in sample MH2 show that dolomite is precipitated after digestion from CO_2.

Changes in Pore Size

Pore size changes due to mineral dissolution and precipitation can be determined from T_2 distributions, which is proportional to pore size distribution. Figure 9 shows T_2 distribution for samples MH3 and MH4. The dominant peaks for MH3, containing the intergranular pore structures, increase from 65.3 to 67.1 milliseconds (ms). The shifts for the dominant peaks agree with the SEM and thin section results showing mineral dissolution in intergranular pores. As for micropores, the decrease of T_2 values after soaking is observed, shown in Figure 9, meaning the decrease in micropores due to mineral dissolution. Shifts of the dominant peaks for plug MH4 are not recorded (Figure 9). However, the T_2 spectra of macro-pores (vugs) becomes wider after soaking because of both mineral dissolution and precipitation (as displayed in SEM micrographs of Figures 7 and 8). Moreover, smaller T_2 values representing intergranular pores after soaking is recorded in sample MH4.

Heterogeneous mineral dissolution and precipitation are responsible for pore size changes in different size pores. In this study, as no convective flow takes place during soaking, reactions are mainly related to the value of Da. As carbonic acid was introduced to highly permeable pathways (larger pores), dolomite dissolution happened quickly in the pore throats and intergranular pores for MH3 and in vuggy pores for MH4. With the decrease of carbonic acid activity, the concentration of Ca^{2+} increases and the size of pores where reactions happens increases as well. Driven by concentration gradients, Ca^{2+} migrates to smaller pores (micropores for MH3 and intergranular pores for MH4), which is controlled by static properties such as pore structure (e.g. pore and pore throat size) and dynamic properties such as the diffusion coefficient. The oversaturation of Ca^{2+} in smaller pores results in mineral precipitation, thus shrinking the volume of smaller pores.

Molecules and ions diffuse in restricted pore space representing a complex transport mechanism and affect CO_2 storage and transport, and heterogeneity of geochemical reactions. Diffusion coefficient of hydrogen-containing molecules (e.g. water) and ions (e.g. H^+) measured by the PFG-NMR method provides information on dynamic transport properties of molecules and ions in restricted pore space. Figure 10 shows diffusion coefficient decay as the applied gradient strength is increased. At the same gradient strength, the diffusion coefficient of both samples increased after soaking process. Since temperature, ionic strength and water chemistry are the same during all measurements, increased pore size due to mineral dissolution reduced the restriction effect by pore surface.[45] Furthermore, the increased diffusion coefficient also reveals that pore space increase is larger than that of decreasing portions because of mineral precipitation. Unlike T_2 distributions that are bimodal, the diffusion coefficient distribution before soaking for MH3 shows unimodal distributions (Figure 11). Because the pore volume of the mini plugs is small, the signal from micro pores where the pore volume is much smaller compared with pore volume of intergranular pores (shown in Figure 9) is too weak to be captured by the probe. However, a small peak emerged after soaking because of the increase of pore volume in pore throats or micropores due to mineral dissolution. Moreover, diffusion coefficient of the dominant peak increased because of the increase in the pore size of intergranular pores, which agrees with changes in the T_2 distribution.

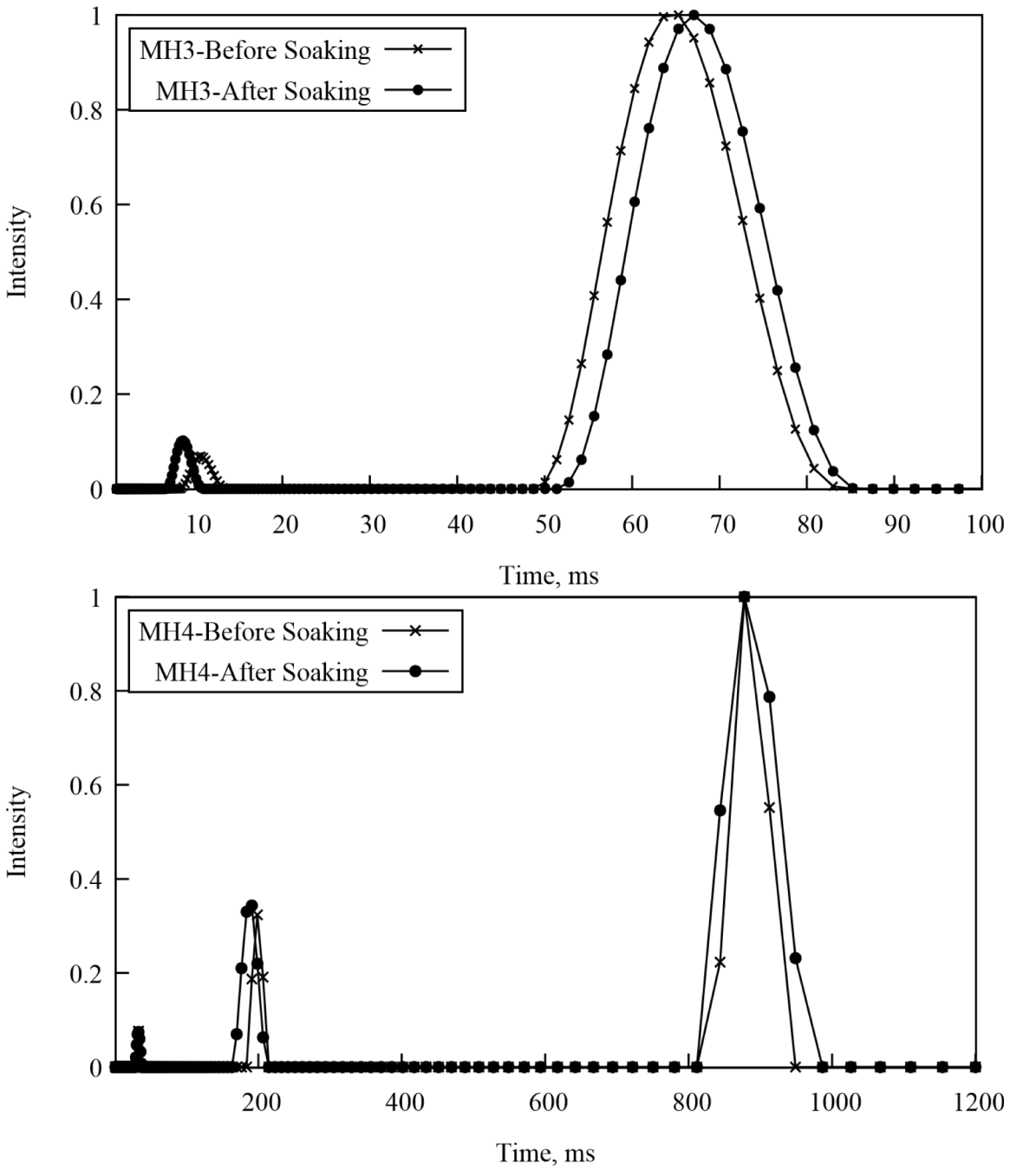

Figure 9. NMR T_2 distributions before and after soaking with CO_2-saturated brine.

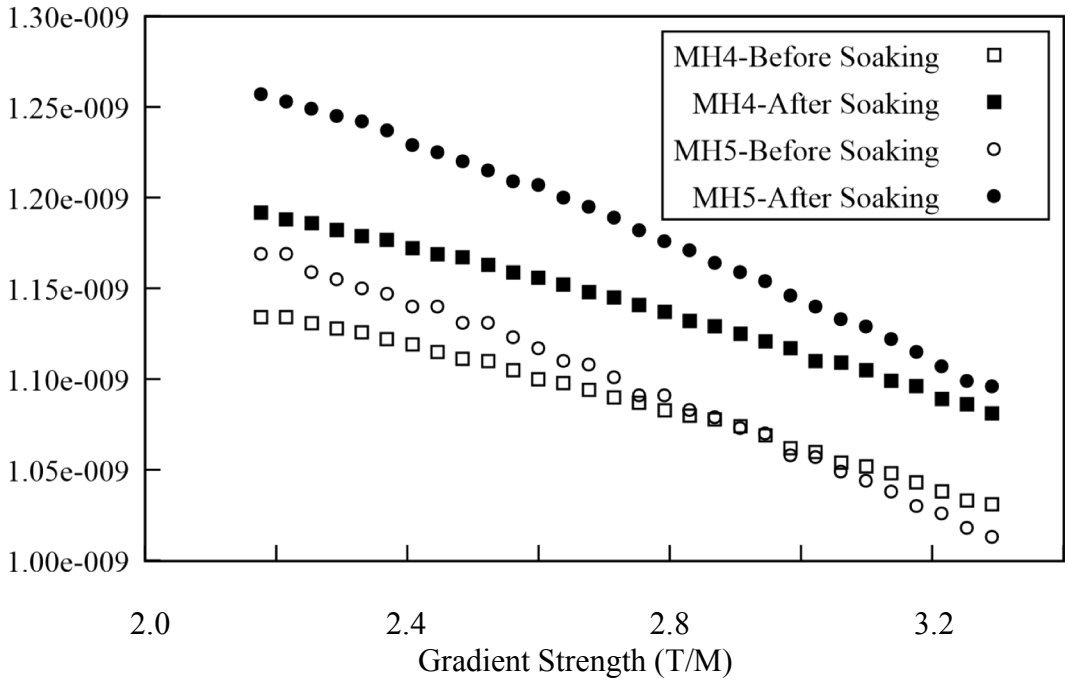

Figure 10. NMR diffusion coefficient decay before and after soaking with CO_2-saturated brine. The vertical axis is the Diffusion Coefficient (m^2/s).

Diffusion of hydrogen-containing ions or molecules in intergranular pores dominate transport properties for sample MH3. Similarly, higher concentration Ca^{2+} in macropores tends to transport to micropores driven by the concentration gradient as well as random translational motion. This directional diffusion accelerates mineral precipitation in smaller pores, which then decrease in size. However, because of relevant small pore volume in micropores, an equilibrium will be reached as the concentration gradient deceases, which will slow down the diffusion of Ca^{2+} in response to the corresponding mineral precipitation. After that, restricted diffusion (random translational motion) controls ions exchange between larger and micropores. If the surface area to pore volume ratio of micropores is larger than that of intergranular pores, restriction effect of the pore surface hinder the diffusion of molecules and ions from micropores to intergranular pores. In contrast, higher concentration ions such as Ca^{2+} prefer to transport from intergranular pores to micropores, leading to a much higher Ca^{2+} concentrations in micropore and mineral precipitation. Pore size of micropore therefore decreases.

Sample MH4 recorded two T_2 peaks, representing macro- and intergranular pores. The small peak shows that the pore volume of intergranular pores is small compared with macropore volumes. Furthermore, compared to MH3, the surface area-to pore volume ratio for MH4 is smaller due to the larger size of vuggy pores. That is why only a slight increase in the diffusion coefficient shows in Figure 11. Moreover, the Da number for sample MH4 is smaller than that of sample MH3. Diffusion of hydrogen-containing ions or molecules from vuggy pores to pore throats connecting with intergranular or micropores will accelerate dolomite dissolution in pore throats. The increase in the pore throat size will favor the fluid flow through porous media, i.e. it would increase rock permeability. Even though mineral precipitation happens in micropores,

permeability is constrained by pore throat size and the contribution of micropores can be ignored.

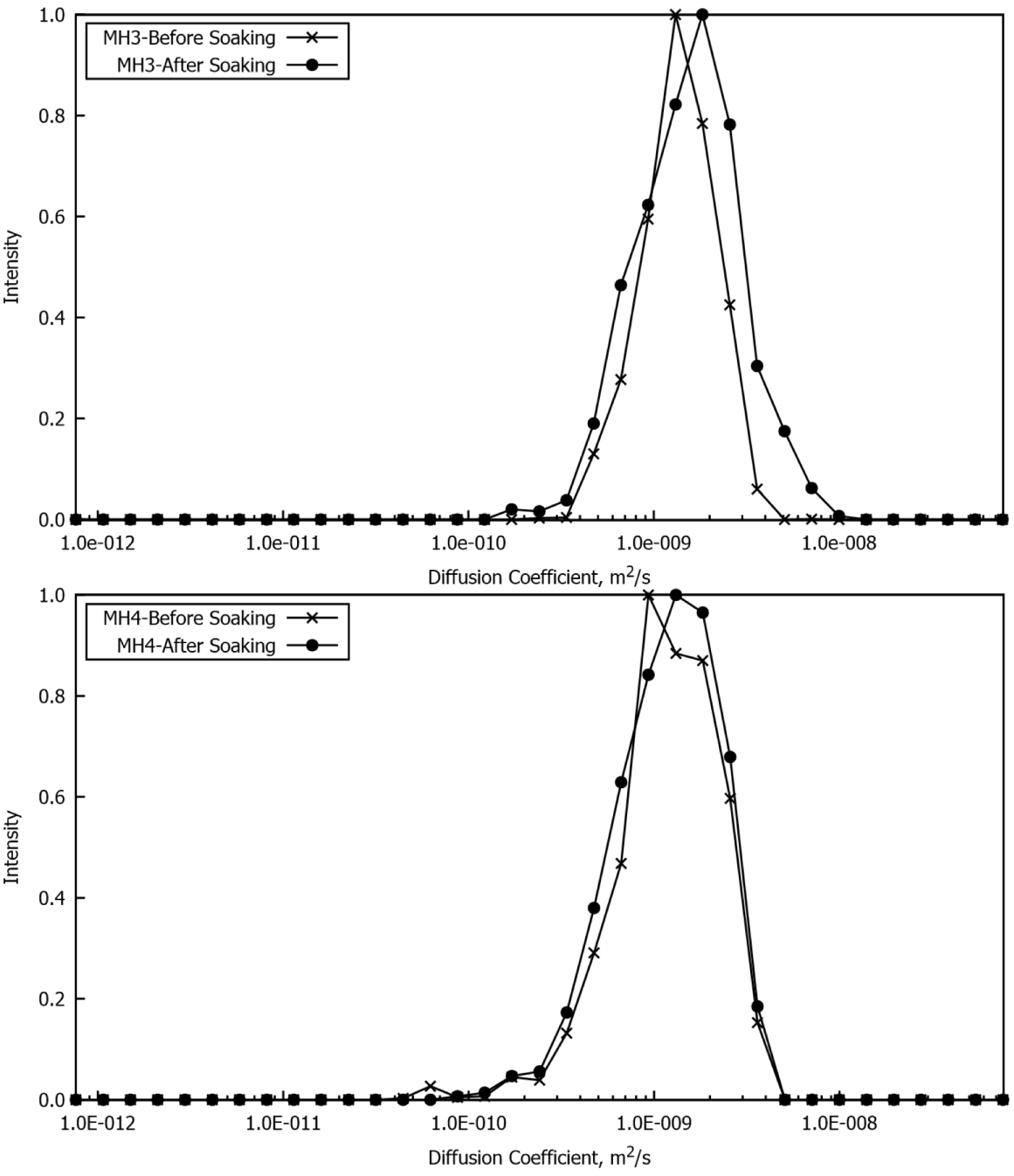

Figure 11. NMR diffusion coefficient distributions before and after soaking with CO_2-saturated brine.

Porosity and Permeability Relationship

Heterogeneities in the spatial distribution of mineral dissolution and precipitation have a strong influence on porosity and permeability. Mineral dissolution increases pore volume and precipitation decreases pore volume. The net change of porosity is determined by mineral dissolution and precipitation. Different from porosity, changes in permeability are determined by pore and by pore-throat sizes. Luhmann et al. (2017) analyzed critical paths that the heterogeneity of individual flow paths in a network of flow paths affects the overall permeability, which is dominated by smaller pore throats.[28] Therefore, changes in overall permeability of the pore network after soaking are strongly influenced by changes in pore throats sizes, especially for the smallest pore throat of the critical flow paths. Gas porosity and permeability before and after soaking are shown in Table 2. Porosity for all core plugs increases after reacting with CO2-saturated formation brine, which agrees with diffusion coefficient measurements, while the increment is relatively small (less than 1%) because of the finite amount of carbonic acid in the soaking process. Even though porosity of MH2 is smaller than that of MH1, permeability after soaking increased 1.32 times for MH2, while 1.19 time for MH1. The larger pore volume and smaller Da number in vugs accelerate mineral dissolution in pore throats, especially in smaller pore throats, resulting in a larger increment of permeability.

Power-laws are frequently used in characterizing porosity-permeability relationships for carbonate rocks (Luhmann et al., 2017; Luquot and Gouze, 2009). Luhmann et al. (2017) provides the relationship as:

$$\frac{k}{k_0} = \left(\frac{\varphi}{\varphi_0}\right)^n$$

where k and φ are porosity and permeability after reaction, k_0 and φ_0 are initial porosity and permeability, and the exponent, n, is a regression parameter and may not always be constant. In this study, the initial and final porosity and permeability were measured and we plotted $\log(k/k_0)$ as a function of $\log(\varphi/\varphi_0)$, shown in Figure 12. The slope n equals 3.6. However, the porosity-permeability relationship in this study is different from previous dynamic experiments, and it still agrees with the power law and gives the coefficient of determination (R^2) 0.9868.

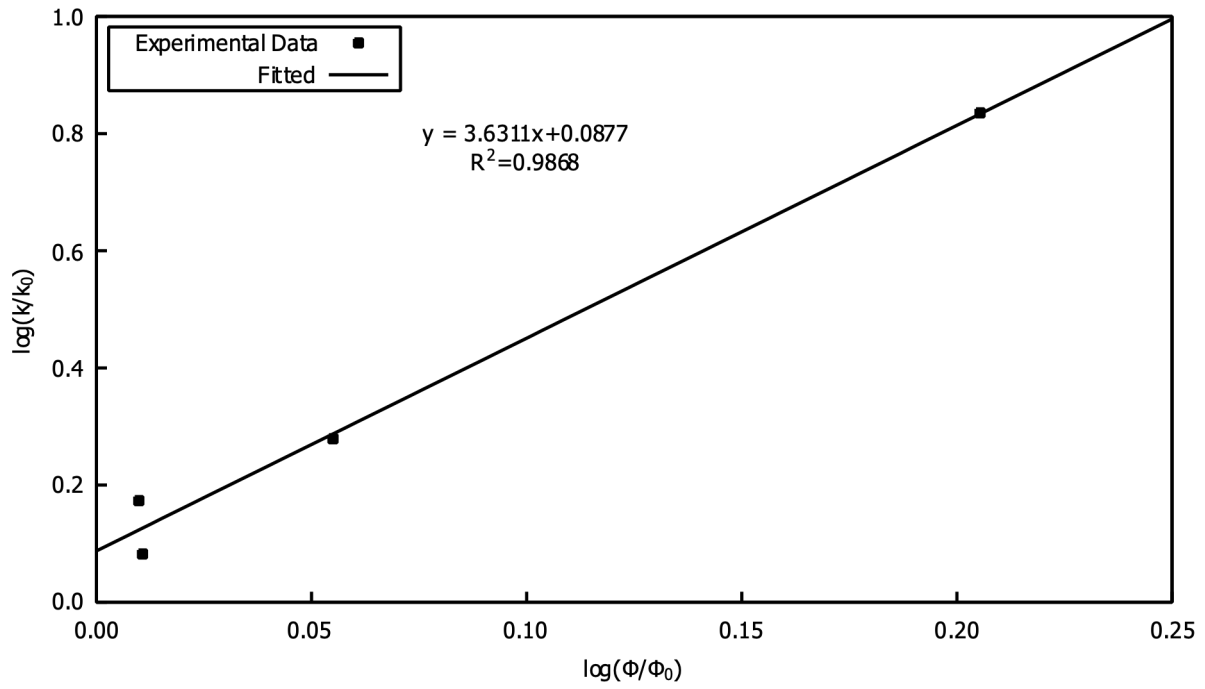

Figure 12. Permeability ratio (k/k_0) as a function of porosity ratio (φ/φ_0) for all experiments in log-log space.

Geomechanical

Table 3 summarizes the mechanical properties determined for the Madison Limestone and Weber Sandstone (Appendix VI). For rocks with same orientation and geochemical preparation, considering the effect of CO_2 on the geomechanical properties of Weber Sandstone samples except SV samples aged with brine (i.e., SV1b and SV2b), E increases and υ decreases with increasing Pc for rocks under the linear elastic regime. However, under the nonlinear plastic regime except for DH2b and SH3b that experienced abnormal P_c-ε_v responses, crack damage strength (σ_{cd}), crack damage strain (ε_{cd}), σ_{pk}, and ε_{pk} of these rocks increase with increasing P_c. For the post-failure behavior, the stable residual strength (σ_r) of SV2b and SH2c samples cannot be determined. For vertical sandstone samples aged with brine-CO_2 (i.e., SV1c and SV2c), σ_r significantly increases from 41.7 MPa to 195.7 MPa with increasing P_c. For horizontal sandstone samples aged with brine (i.e., SH1b and SH2b), σ_r also significantly increases from 46.1 MPa to 174.2 MPa with increasing P_c.

Considering the effect of CO_2 on the geomechanical properties of sandstone samples with the same orientation and stress conditions, except the SV1b and SV1c with a minimal difference in the E values, the estimated E values generally increase as the result of CO_2. On the other hand, the υ values generally decrease as the result of CO_2. In particular, significant differences in E and υ were observed in SV2b and SV2c with E increasing from 31.4 MPa to 48.5 MPa and υ decreasing from 0.29 to 0.14. Furthermore, E (31.4 GPa) of SV2b is lower than the E values of SV2c, SH2b, and SH2c under the same P_c of 71.0 MPa. Comparing the results of SV2b and

Table 3. Summary of triaxial test results of RSU samples aged with brine and brine-CO_2

Sample ID	E (GPa)	υ	σ_{cd} (MPa)	$\Delta\sigma_{cd}$ (%)	ε_{cd} (%)	$\Delta\varepsilon_{cd}$ (%)	σ_{pk} (MPa)	$\Delta\sigma_{pk}$ (%)	ε_{pk} (%)	$\Delta\varepsilon_{pk}$ (%)	σ_r (MPa)	$\Delta\sigma_r$ (%)
SV1b	42.1	0.24	208.4	-19.4	0.58	-15.5	282.7	-17.9	0.83	-7.2	77.1	-45.9
SV1c	40.1	0.29	168.0		0.49		232.2		0.77		41.7	
SH1b	33.9	0.30	146.3	8.0	0.53	-3.8	302.6	-22.5	1.13	-27.4	46.1	74.8
SH1c	36.1	0.29	158		0.51		234.5		0.82		80.6	
DH1b	27.8	0.42	71.9	114.6	0.29	41.4	134.7	60.7	0.62	1.6	59.5	43.5
DH1c	41.0	0.31	154.3		0.41		216.5		0.63		85.4	
SV2b	31.4	0.29	320.9	21.3	1.03	-14.6	440.3	9.6	1.50	-14.0	#	#
SV2c	48.5	0.14	389.1		0.88		482.7		1.29		195.7	
SH2b	41.5	0.19	335.4	4.8	0.85	-3.5	426.7	9.4	1.25	5.6	174.2	#
SH2c	47.4	0.22	351.5		0.82		466.7		1.32		#	
DH2b[$]	24.6	0.42	29.3	NA	0.12	NA	65.2	92.6	0.27	129.6	#	NA
DH2c	24.5	0.26	NA		NA		125.6		0.62		NA	
SH3b[$]	37.8	0.20	174.6	163.6	0.50	118.0	214.9	152.0	0.65	135.4	34.0	551
SH3c	47	0.16	460.3		1.09		541.5		1.53		221.4	
DH3b	34.2	0.22	102.7	NA	0.32	NA	150.0	-2.5	0.54	35.2	#	NA
DH3c	29.7	0.25	NA		NA		146.2		0.73		NA	

E–Young's modulus; υ–Poisson's ratio; σ_{cd}–Crack damage strength; ε_{cd}–Crack damage strain; σ_{pk}–peak strength; ε_{pk}–Axial strain corresponding to peak strength; σ_r–Residual strength; Δ–Percent difference in strength or strain; #–No stable daviatoric stress was measured; [$]–Sample experienced abnormal P_c-ε_v response; and NA–Not applicable due to a ductile behavior. Reproduced from Appendix VI.

SV2c, the change in elastic constants may not solely attributed to the effect of CO_2 but could be attributed to the unique physical property of SV2b. For DH samples, consistent trend of E and υ values cannot be observed. The E increases and υ decreases at a lower P_c state while at the higher P_c states, the E decreases and υ increases as the result of CO_2.

For rocks under the nonlinear plastic regime (until reaching the failure strength), σ_{cd}, σ_{pk} and corresponding axial strains (ε_{cd} and ε_{pk}) were used to investigate the effect of CO_2 on the geomechanical behavior of rocks. To quantify the effect of CO_2 on the stress and strain data of rocks in the plastic regime, the change in deviatoric stress (or axial strain) is determined by

$$\Delta\sigma\ (or\ \Delta\varepsilon) = \frac{\sigma\ (or\ \varepsilon)_c - \ \sigma\ (or\ \varepsilon)_b}{\sigma\ (or\ \varepsilon)_b} \times 100\%$$

where σ (or ε)$_c$ is measured deviatoric stress (or axial strain) data of rocks aged with brine-CO_2, and σ (or ε)$_b$ is measured deviatoric stress (or axial strain) data of rocks aged with brine. Therefore, the positive value of $\Delta\sigma$ (or $\Delta\varepsilon$) indicates that the stress (or strain) increases as the result of CO_2. Calculated $\Delta\sigma_{cd}$, $\Delta\varepsilon_{cd}$, $\Delta\sigma_{pk}$, and $\Delta\varepsilon_{pk}$ in percentage are summarized in Table 3.

Comparing the results of SV1b and SV1c, all $\Delta\sigma$ (or $\Delta\varepsilon$) values are negative. However, the all-negative trend was not observed on other samples. For example, the comparison of SH2b and SH2c shows that only $\Delta\varepsilon_{cd}$ is negative. Considering different orientations and P_c states, no consistent relationship between stress (or strain) data and CO_2 in the nonlinear plastic regime was observed. The differences in induced crack propagation governed by physical properties (e.g. initial crack density and crack geometry) of samples are believed the main factor causing the inconsistent result outcomes. In other words, the CO_2 is not the dominant factor that affects the plastic properties of rocks. The post-failure behavior of rocks is quantified and investigated based on the residual strength (σ_r). No consistent trend was again observed. For example, σ_r decreases from 77.1 MPa of SV1b to 41.7 MPa of SV1c while σ_r increases from 46.1 MPa of SH1b to 80.6 MPa of SH1c. For DH samples, the change in the mechanical properties in the plastic regime due to CO_2 is more significant than that of the sandstone samples (Table 3). However, no consistent trend was observed.

Table 4 summarizes the Mohr-Coulomb failure coefficients of RSU samples. Comparing the Mohr failure envelopes plotted for SV samples, the effect of CO_2 on mechanical properties includes the decrease in c from 47.0 MPa to 26.7 MPa and the increase in ϕ from 47.8° to 55.0°. Comparing the Mohr failure envelopes plotted, the effect of CO_2 decreases the c from 57.9 MPa to 28.8 MPa and increases the ϕ from 43.8° to 53.9°. Comparing the Mohr failure envelopes plotted in for DH samples, the effect of CO_2 decreases the c from 57.7 MPa to 30.6 MPa and increases the ϕ from 7.9° to 50.4°. The consistent trend of decreasing c and increasing ϕ was observed in all sandstone and dolomite samples.

Table 4. Summary of Mohr-Coulomb failure coefficients of RSU samples

Group	c (MPa)	ϕ (Deg.)
SV aged with brine	47	47.8
SV aged with brine and CO2	26.7	55
SH aged with brine	57.9	43.8
SH aged with brine and CO2	28.8	53.9
DH aged with brine	57.7	7.9
DH aged with brine and CO2	30.6	50.4

Note: Reproduced from Appendix VI.

Fluid Flow Simulations and Integrated Results

Simulations for CO_2 injection were performed assuming an injection rate of 500,000 ton/year (45,000 m^3/day), a maximum bottom hole pressure of 65 MPa for the injection well, and a constant bottom hole pressure of 30 MPa for the producing well (Appendix VIII). Simulations were conducted for 30 years. Four static models were developed: 1) a base case that assumes no properties change with CO_2 injection; 2) incorporate effects of pore pressure on porosity, permeability changes as a function of porosity; 3) permeability changes as a function of hydrostatic pressure; and 4) incorporate two-way coupling between geomechanics and fluid flow.

Based on these static models, two time-dependent models were developed (Appendix IX). Results from both models are presented in Figures 13 and 14. The first of the two models is a base-case model (labeled 'base_case' in Figures 13 and 14) that does not consider geochemical reactions or geomechanical properties. The second of the two models (labeled 'Geomechanical and Geochemical' in Figures 13 and 14) incorporates both geochemical reactions and geomechanical properties. Both models incorporate one injector well (RSU #1) and one producing well. As injecting CO_2 without producing water will increase reservoir pressure immediately and dramatically, water production was necessarily considered and thus one producing well was required. The designed CO_2 injection rate is 45,000 m^3/day and the bottom hole pressure of the producing well is 30 MPa.

The geomechanics module used in the 'Geomechanical and Geochemical' model solves for the force equilibrium of the formation and calculates the volumetric dilatation/compression as a result of both elastic and plastic straining. The pore volume changes may be caused by a combination of compression/tension or shear stresses. These changes in pore volume and the associated changes in transmissibilities are used in the reservoir model for calculating mass and energy balances in the reservoir and their impact on petrophysical property changes with time. Experimental results from geomechanics experiments performed in this study were used as input. As geomechanical properties were not measured as a function of time, input data consisted of geomechanical data (geomechanical experimental data before aging) (time 0) and geomechanical data derived from experiments after brine and CO_2 aging (time after 25 years).

The geochemistry module used in the 'Geomechanical and Geochemical' model uses standard geochemical reactions. These include reactions in aqueous phase, such as:

$$CO_2(aq) + H_2O = H^+ + HCO_3^- \quad (1).$$

These also include mineral reactions, such as the calcite dissolution reaction:

$$Calcite + H^+ = Ca^{2+} + HCO_3^- \quad (2).$$

For the Weber Sandstone, the designed CO_2 injection rate cannot be maintained in any of the cases due to low permeability (average permeability is 0.045 md). The designed CO_2 injection rate is achieved in the Madison Limestone because of the larger permeability (9.32 mD). The size of the CO_2 plume is consequently larger for the Madison Limestone than the Weber Sandstone. No CO_2 viscous fingering developed between the injection and producing well. As the permeability of the Madison Limestone formation is relative large, changes of pore pressure and confining pressure are relatively small because of water production.

Figure 13 shows CO_2 injection rate and water production rate for the base case and the case considering geomechanical and geochemical properties in the Madison Limestone. CO_2 injection rate is not affected because the injection pressure does not reach the maximum injection pressure. However, the bottom hole pressure at the initial stages of injection is larger for the case considering geomechanical and geochemical properties than the base case (Figure 14), suggesting that CO_2 injectivity is affected. After three years of injection, the bottom hole pressure for the injection well is smaller than that of the base case.

Water production decreased for the case considering geomechanical and geochemical properties in the Madison Limestone. As CO_2 was injected, pore pressure increased, leading to an increase of porosity around the injector, which slowed pressure migration. Therefore, the increase of reservoir pressure around the producing well is smaller, thereby reducing the pressure difference between reservoir pressure and the bottom hole pressure of the producing well.

After 30 years of CO_2 injection, the distributions of the CO_2 plume and pressure for the base case and the case considering geomechanical and geochemical properties in the Madison Limestone are approximately the same. However, the near-wellbore environment is affected by changes in geomechemical and geochemical properties over time, as demonstrated by porosity increases after CO_2 injection (Figure 15).

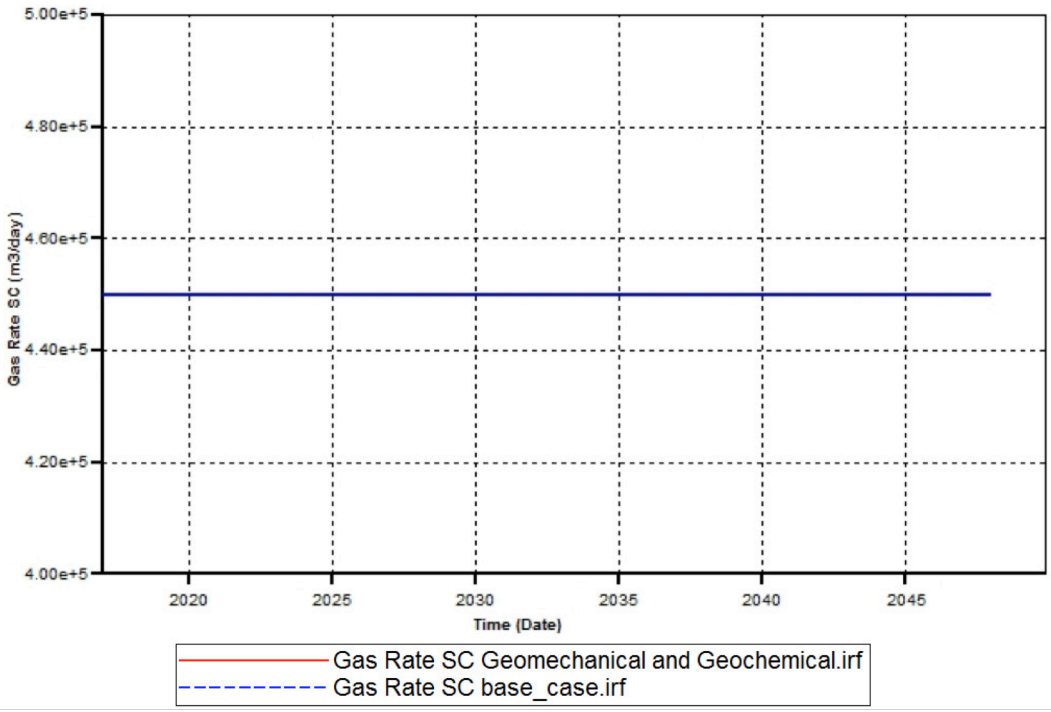

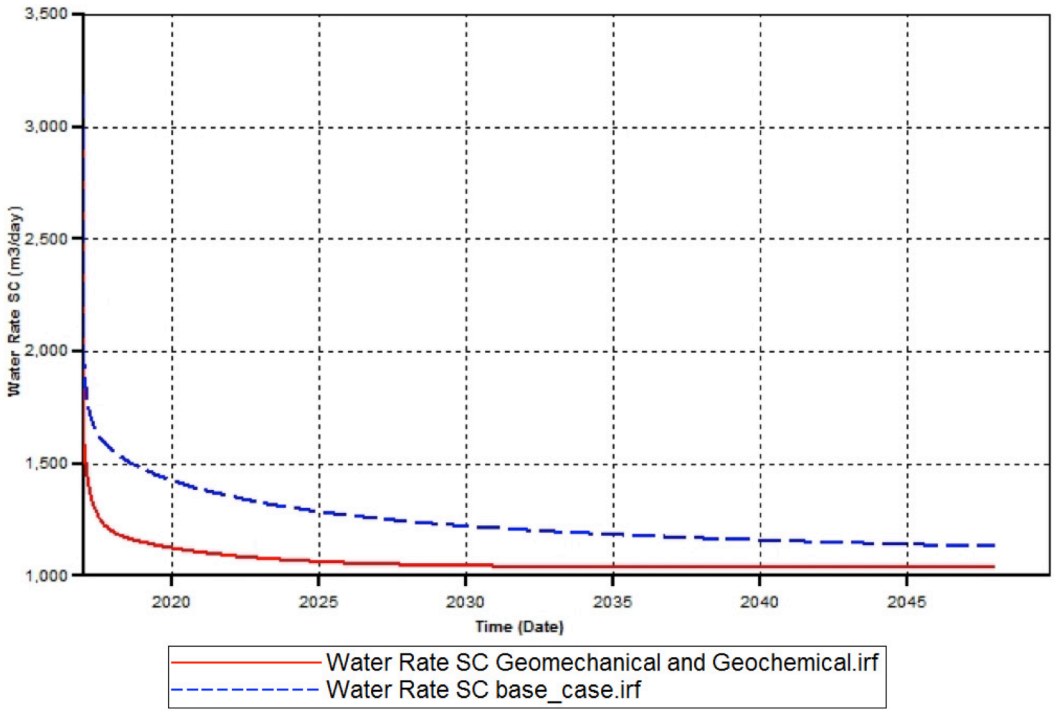

Figure 13. Comparison of CO_2 injection rate (top chart) and water production rate (bottom chart) for base case (blue dashed line) and case considering effects of CO_2–water rock interactions on geomechanical and geochemical properties (solid red line) of Madison Limestone. In the top chart, note that lines for the two cases overlie each other. Reproduced from Appendix IX.

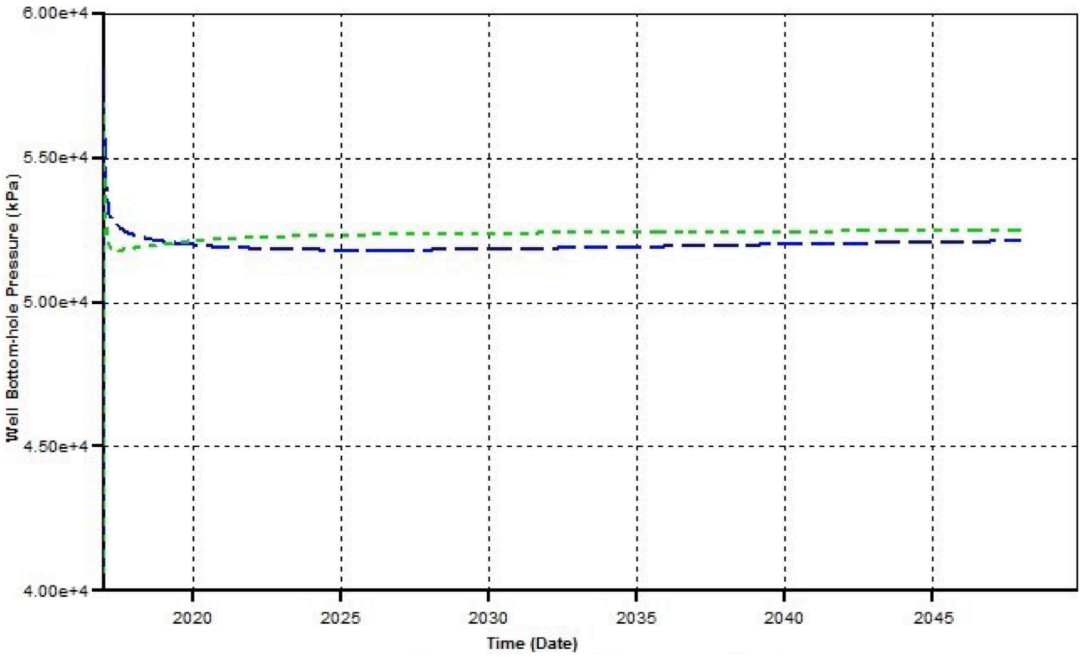

Figure 14. Comparison of bottom hole pressure in CO_2 injection well for base case (green dashed line) and case considering effects of CO_2–water rock interactions on geomechanical and geochemical properties (blue dashed line) of Madison Limestone. Reproduced from Appendix IX.

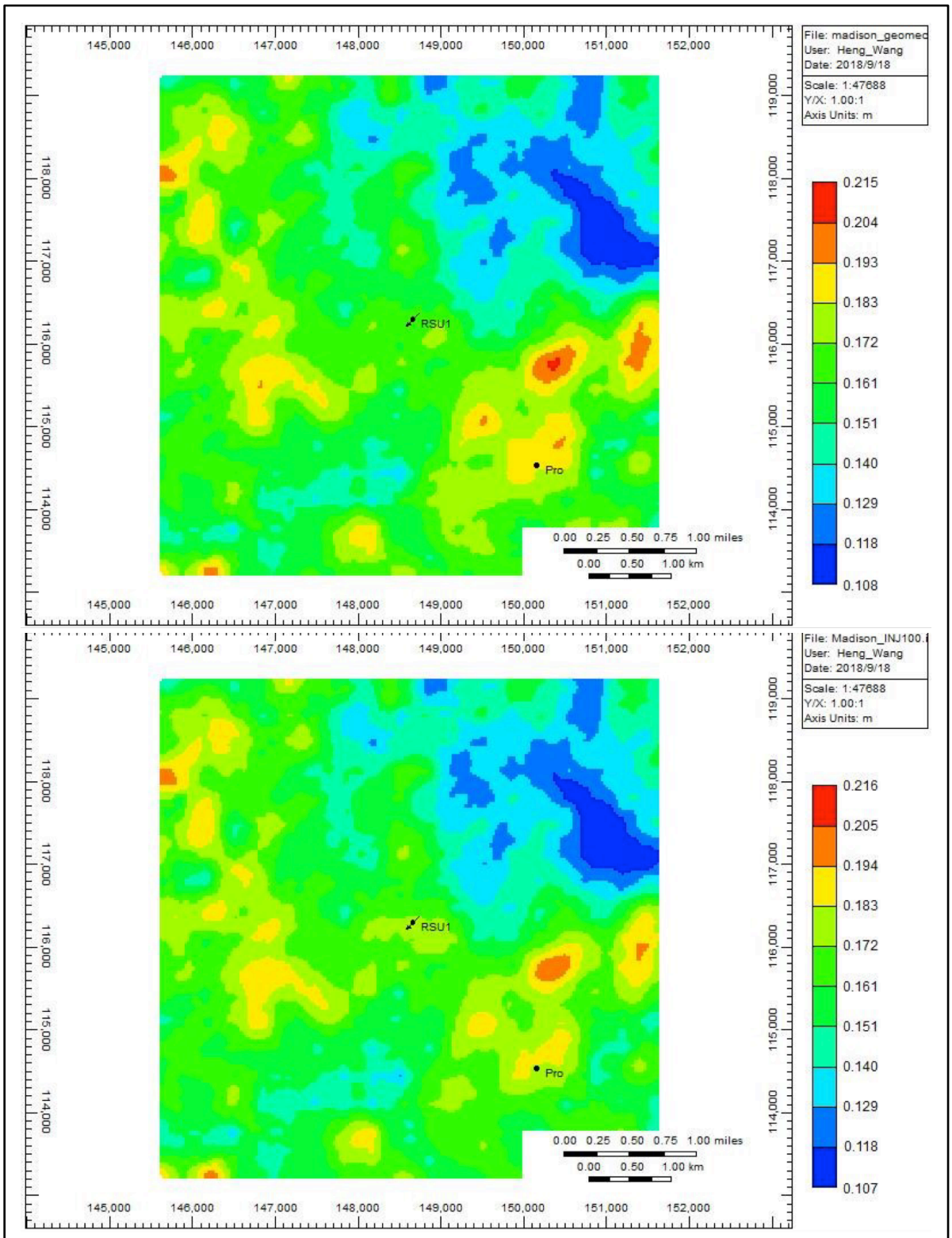

Figure 15. Comparison of porosity distribution for base case (top) and case considering effects of CO_2–water rock interactions on geomechanical and geochemical properties (bottom) of the Madison Limestone. Reproduced from Appendix IX.

Workflow

A workflow was developed to provide a sequence of steps to evaluate CO_2 storage in the Madison Limestone and Weber Sandstone on the RSU. The workflow also provides a way to estimate CO_2 storage using multicomponent/multiphase flow simulations in compositional mode. The workflow should be applicable to other target sites, provided analogous conditions are similar to formations and storage considerations to those at the RSU. The workflow is based on (1) elements of geology, geochemistry, petrophysics, reservoir simulation, and geomechanics using current data from the RSU; and (2) experimental results from petrophysical, geochemical, geomechanical, and multiphase flow experiments on rock and fluids characteristics of the RSU. While simulation models possible on the Computer Modelling Group compositional simulator, GEM, allow for complex couplings among geochemical, geomechanical and multiphase flow, the workflow intends to simplify the analysis whenever possible, due in part on computational demands and input data for complex simulations. The workflow, depicted in Figure 16, was constructed through the following steps:

1) Rock and fluid characterization. This step focuses on sampling of rock and fluids representative of the target formations and their characterization. The ultimate goal of the this step is to determine time scales associated to reactivity, baseline geomechanics, calibration of petrophysical properties (core - well logs correlations), and determination of relative permeability and capillary pressure curves prior to exposing samples of rock to carbonic acid over long time frames.
2) Subsurface characterization. This step aims at collecting the necessary datasets to build the static model for reservoir simulations. The main sources of data are available seismic surveys, well logs and core-well log petrophysical correlations. Interpretation of the reservoir should include identification of facies and possibly rock types as well.
3) Construction of a static model. This model represents one of the data deck components (portion of the simulation input file) containing constraints of the structure (tops of formations), petrophysical properties distributions, pressure-volume-temperature (PVT) formulation (thermodynamic formulation) as well as gridding details in the model. Geostatistical model choices should consider availability of data sources and type, geological settings and needs for a adequate description for simulation purposes.
4) Analysis of geochemical effects. This step feeds off the contrast between baseline analysis of geomechanical, porosity and permeability, and relative permeability and capillary pressure. The results of this geochemical coupling with other property types, i.e. geomechanical, petrophysical and multiphase flow functions, guide the choices of experimental conditions and duration of assays. Rock-plug simulation models are used to history-match production and pressure drop data from coreflooding experiments to produce relative permeability and capillary pressure curves, usually with the inclusion of hysteresis. While many researchers have considered the accuracy of steady-state experiments to obtain multiphase flow functions, the reactive conditions with carbonic acid inhibits the use of steady-state experiments, given the coupling between geochemistry and other properties such as permeability and relative permeability, among others. This should also be true for geomechanical properties. In this sense, we rely on unsteady fluid flow experiments, given the short duration of the coreflood experiments in contrast with steady-state experiments. The same conditions used to age samples for multiphase flow are maintained for samples used in geomechanical experiments.

5) Construction of dynamic model. The type of model will depend on results from reactive experiments. If geochemical coupling with any of the other property types (Geomechanical and Multiphase Flow) is found to have a limited impact, then a conditional model construction is conducted. In the case of the RSU, the Weber Sandstone was less susceptible to alteration through exposure to carbonic acid. Geomechanical properties as well as petrophysical and multiphase flow properties were more invariant with respect to the baseline characterization and therefore, a more traditional simulation approach without restart steps is sufficient. On the other hand, the Madison Limestone was a more reactive lithology and in order of importance, relative permeability, permeability and geomechanical properties must be updated in time-dependent simulations, and therefore restart steps must be followed in the simulations.

The explanation in the preceding text for Steps 1 through 5 and the depiction of these steps in Figure 16 track well with each other. Steps 6 and 7 possess several decision points and loops; the following explanation for these two steps is therefore more complicated.

6) This step requires two different actions:
   a) Inclusion of multiphase flow properties. This generally boils down to addition of relative permeability and capillary pressure tables along with some ancillary data.
   b) Definition of the so-called schedule in the simulation model. The intent of this is to declare well architecture, e.g. horizontal well, and locations in the model as well as operating constraints (rates and bottomhole pressures). This sub-step defines the scenario to be evaluated.
   c) If restart steps become necessary, i.e. reservoir properties change in a significant way over time, updates of these properties in the model are conducted and the simulation is restarted. In the current workflow, only one restart step is carried out, because our evaluation included only the baseline (before reactive conditions) and one point in time after 400 hours of exposure to carbonic acid. If changing conditions are monitored over time or a predictive model (data-driven or first-principles model) is available, then several restart steps can be taken in the simulation process. The precise time of the updates has to account for changes in saturation and formation of carbonic acid fronts. In the current formulation, dry-out regions near the wellbore are neglected as this study did not track rock alteration because of exposure to water-saturated CO_2. This effect is likely of second order, but further evaluation in future projects will yield a data-supported answer to this question.
7) Evaluation of injection scenarios. This step focuses on a sensitivity analysis of well locations, injection rates and time periods, pressure constraints, rates of brine withdrawal and potential reinjection of broken-through CO_2 streams, etc. This step is the culmination of the workflow objective.

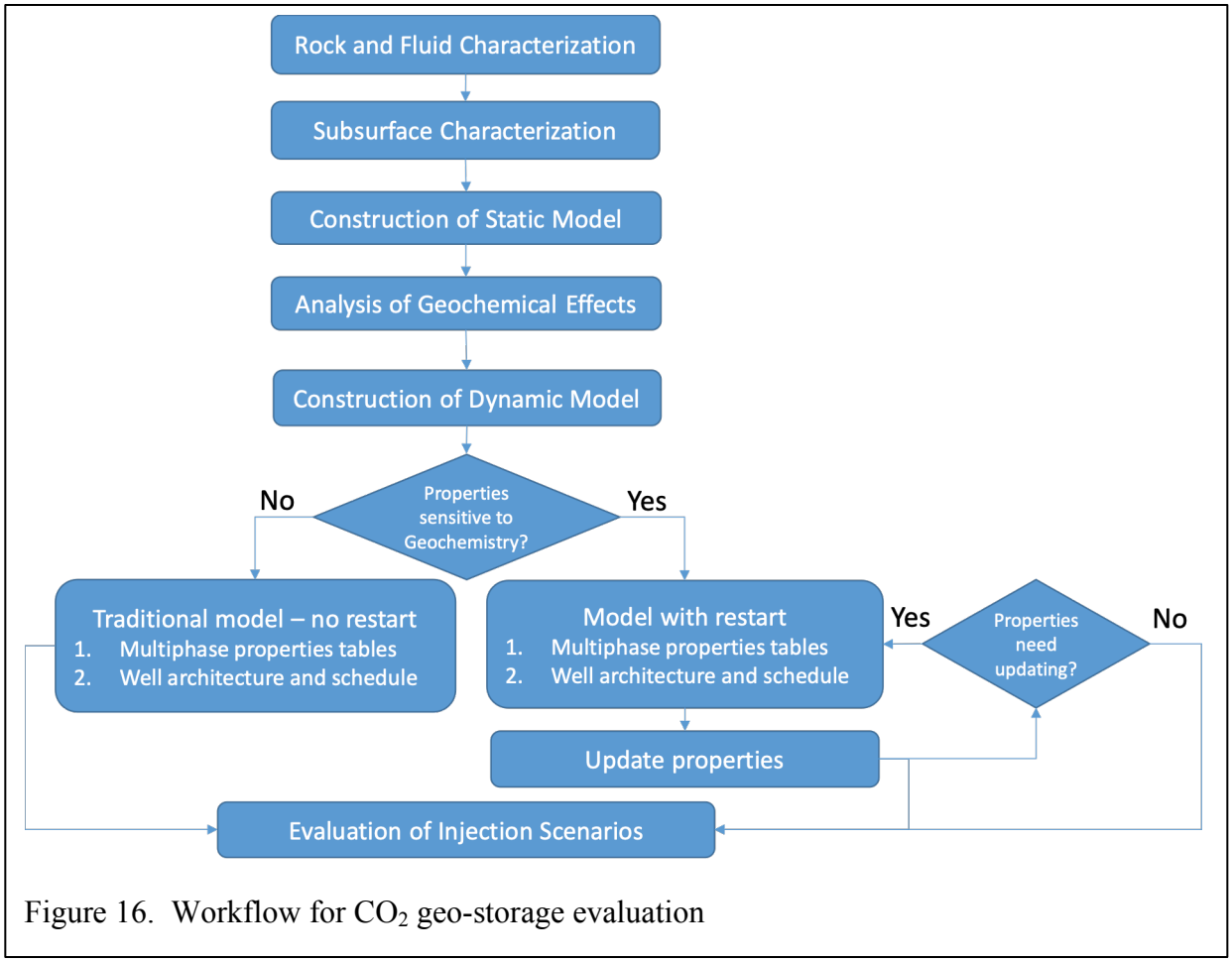

Figure 16. Workflow for CO_2 geo-storage evaluation

CONCLUSIONS

Reservoir Characterization

Porosity as well as permeability in the Weber Sandstone is high in the upper part of the formation and decreases uniformly into the lower part of the formation. The facies volume analysis indicates that the Weber Sandstone is primarily comprised of the sandstone facies, and the V_P/V_S ratio can also be used as a lithology indicator. In the Madison Limestone, porosity and permeability vary smoothly in 3D. The predicted facies volume indicates that the high porosity dolomite layer exists in the entire 3D volume and has minimal variation in thickness. Limestone and low porosity dolomite facies overlap on the V_P vs. V_S crossplot, which indicates that these two facies have similar characteristics and cannot be distinguished based on elastic properties.

Reservoir Monitoring Feasibility

At the RSU, time-lapse seismic data are not feasible for monitoring CO_2 displacement during injection or to mitigate leakage-risks situations. Pressure and fluid saturation have small effects on elastic velocities and synthetic seismograms. The small variations that do occur are due to the low porosity of the sandstone and the high stiffness of the dolomite. These small changes on elastic velocities and density might be challenging to capture because of the presence of noise in recorded data. This negative finding is an important result and will be useful in developing technology for future reservoir monitoring approaches.

Geochemical and Petrophysical

Temporal and spatial heterogeneity of mineral dissolution and precipitation due to reaction with CO_2-saturated brine have a great effect on pore structure, especially on pore throat size; net porosity does not change significantly, but redistribution of porosity affects permeability and connectivity, with implications for CO_2 injectivity, plume propagation and storage capacity. For example, the increased permeability favors fluid flow in porous media, thus increases CO_2 mobilities, while on the other hand, it will also reduce CO_2 sweep efficiency, especially for heterogeneous formations as pore throats increase in size in high permeable pathways and decrease in low permeable pathways. In addition, it is important to emphasize that in our experiments, static CO_2-enriched brine soaking is representative of most field scenarios in which flow rates are expected to be much lower or diffusion-dominated in geologic formations during the injection process or after injection comes to a halt; this approach contrasts with most published studies wherein dynamic core flood experiments using unnaturally-high injection rates are employed. Thus, experimental results in this study provide basic knowledge to understand geochemical reactions and subsequent rock physical properties changes for the majority of the life span of a storage reservoir. Technology development in the future must account for geochemical reactivity and petrophysical changes in these more representative regimes.

Extending this study, heterogeneous mineral dissolution and precipitation induce changes in pore structure, such as mineralogy, roughness of the pore surface, and pore throat size, that would also affect the dynamic properties associated to CO_2, such as wettability, relative permeability and capillary pressure. Changes in these crucial properties would affect pore-scale multi-phase flow, hysteresis of drainage and imbibition processes, and capillary trapping, thus having a significant influence on the efficiency of capillary pressure trapping, CO_2 plume size and storage capacity, and even caprock sealing efficiency and integrity.

Geomechanical

The effect of CO_2-saturated brine on the linear elastic properties of Weber Sandstone and Madison Limestone cannot be generally concluded from this study. The E values of Weber Sandstone reacted with CO_2-saturated brine generally increase and the υ values generally decrease under the linear elastic regime. Under the nonlinear plastic regime, σ_{cd}, ε_{cd}, σ_{pk}, and ε_{pk} increase with increasing P_c. However, no consistent trend was observed in the post-failure behavior of rocks in terms of σ_r as a result of increasing P_c. Considering horizontal and vertical orientations and different P_c, no consistent relationship between stress (or strain) data and reaction with CO_2-saturated brine was observed in the nonlinear plastic and post-failure regime. The change of elastic constants due to reaction with CO_2-saturated brine is more significant in Madison Limestone than in Weber Sandstone; however, no consistent trend was observed. These findings provide foundational data for designing future studies needed to decipher chemomechanical effects of CO_2-brine-rock reactions. Future experimental designs needed to feed modeling approaches will need to consider the laboratory time scales of this study. Potential experimental strategies include increased laboratory reaction times (1000s of hours, instead of the 100s of hours used in this study, with concomitant decrease in the number of geomechanical experiments) and augmenting laboratory studies with geomechanical measurements on samples retrieved from natural analogues.

Fluid Flow Simulations and Integrated Results

Reservoir simulations suggest that injectivity for Weber Sandstone is adversely impacted by low permeability. Changes in confining pressure do not impact injection rate and can be ignored while the effect of changes to pore pressure cannot. The effect of confining pressure and pore pressure on the size of the CO_2 plume in the Madison Limestone is negligible because of higher permeability. Geomechanical and petrophysical properties induced by CO_2-brine-rock reactions were time-dependent. Simulations considered these time-dependent properties and indicate that injectivity, porosity distribution, pressure distribution and CO_2 saturation were affected.

Workflow

The project culminated in a workflow to provide a sequence of steps to evaluate CO_2 storage in the Madison Limestone and Weber Sandstone on the RSU. The workflow also provides a way to estimate CO_2 storage using multicomponent/multiphase flow simulations. The workflow should be applicable to other target sites, provided analogous conditions are similar to formations and storage considerations of this project. The workflow is based on 1) elements of geology, geochemistry, petrophysics, reservoir simulation, and geomechanics using current data from the RSU; and 2) experimental results from petrophysical, geochemical, geomechanical, and multiphase flow experiments on rock and fluids characteristics of the RSU. The workflow consists of seven steps: Rock and fluid characterization, Subsurface characterization, Construction of a static model, Analysis of geochemical effects, Construction of dynamic model, a step that provides decision loops for restarting models, and Evaluation of injection scenarios.

GRAPHICAL MATERIALS LIST

List of Figures

List of Tables

List of Appendices

Appendix VII - Baseline Geomechanical Experiment Results
Appendix VIII - Initial Fluid Flow Simulations
Appendix IX – Final Fluid Flow Simulations
Appendix X - Development and Analyses of the Initial Static Model

REFERENCES

Grana, D., Verma, S., Pafeng, J., Lang, X.Z., Sharmab, H., Wu, W.T., McLaughlin, F., Campbell, E., Ng, K., Alvarado, V., Mallick, S. and Kaszuba, J. (2017) A rock physics and seismic reservoir characterization study of the Rock Springs Uplift, a carbon dioxide sequestration site in Southwestern Wyoming. *Int. J. Greenhouse Gas Control* **63**, 296-309.

Kaszuba, J.P., Janecky, D.R. and Snow, M.G. (2005) Experimental evaluation of mixed fluid reactions between supercritical carbon dioxide and NaCl brine: Relevance to the integrity of a geologic carbon repository. *Chem. Geol.* **217**, 277-293.

Luhmann, A.J., Tutolo, B.M., Bagley, B.C., Mildner, D.F.R., Seyfried, W.E. and Saar, M.O. (2017) Permeability, porosity, and mineral surface area changes in basalt cores induced by reactive transport of CO_2-rich brine. *Water Resour. Res.* **53**, 1908-1927.

Luquot, L. and Gouze, P. (2009) Experimental determination of porosity and permeability changes induced by injection of CO_2 into carbonate rocks. *Chem. Geol.* **265**, 148-159.

Luquot, L., Rodriguez, O. and Gouze, P. (2014) Experimental characterization of porosity structure and transport property changes in limestone undergoing different dissolution regimes. *Transp. Porous Media* **101**, 507-532.

Mouzakis, K.M., Navarre-Sitchler, A.K., Rother, G., Banuelos, J.L., Wang, X.Y., Kaszuba, J.P., Heath, J.E., Miller, Q.R.S., Alvarado, V. and McCray, J.E. (2016) Experimental study of porosity changes in shale caprocks exposed to CO_2-saturated brines I: Evolution of mineralogy, pore connectivity, pore size distribution, and surface area. *Environ. Eng. Sci.* **33**, 725-735.

Ng, K., Yu, H., Wang, H., Kaszuba, J., Alvarado, V., Grana, D. and Campbell, E. (2018) The effect of CO_2 on the mechanical properties of the reservoir sandstone under a low differential pressure, 52nd U.S. Rock Mechanics/Geomechanics Symposium. American Rock Mechanics Association, Seattle, Washington.

Noiriel, C., Steefel, C.I., Yang, L. and Bernard, D. (2016) Effects of pore-scale precipitation on permeability and flow. *Advances in Water Resources* **95**, 125-137.

Shafer, L.R. (2013) Assessing injection zone fracture permeability through the identification of critically stressed fractures at the Rock Springs Uplift CO_2 sequestration site, SW Wyoming, Geology and Geophysics. University of Wyoming, Laramie, Wyoming.

Surdam, R.C. (2013) Geological CO_2 storage characterization: The key to deploying clean fossil energy technology. Springer Science & Business Media.

Tartakovsky, A.M., Meakin, P., Scheibe, T.D. and West, R.M.E. (2007) Simulations of reactive transport and precipitation with smoothed particle hydrodynamics. *J. Comput. Phys.* **222**, 654-672.

Wang, H. and Alvarado, V. (2018) Ionic strength-dependent pre-asymptoic diffusion coefficient distribution in porous media - Determination through the pulsed field gradient technique. *J. Nat. Gas Sci. Eng.* **49**, 250-259.

Wang, H., Alvarado, V., McLaughlin, J.F., Bagdonas, D.A., Kaszuba, J.P., Campbell, E. and Grana, D. (2018) Low-field nuclear magnetic resonance characterization of carbonate and sandstone reservoirs from Rock Spring Uplift of Wyoming. *J. Geophys. Res.-Solid Earth* **123**, 7444-7460.

Yu, H., Ng, K.W., Grana, D., Kaszuba, J., Alvarado, V. and Campbell, E. (2018) Experimental investigation of the effect of compliant pores on reservoir rocks under hydrostatic and triaxial compression stress states. *Canadian Geotechnical Journal*.

BIBLIOGRAPHY – Publications from Project

Refereed Journal Articles

Grana, D., Verma, S., Pafeng, J., Lang, X.Z., Sharmab, H., Wu, W.T., McLaughlin, F., Campbell, E., Ng, K., Alvarado, V., Mallick, S. and Kaszuba, J. (2017) A rock physics and seismic reservoir characterization study of the Rock Springs Uplift, a carbon dioxide sequestration site in Southwestern Wyoming. *Int. J. Greenhouse Gas Control* **63**, 296-309.

Wang, H. and Alvarado, V. (2018) Ionic strength-dependent pre-asymptoic diffusion coefficient distribution in porous media - Determination through the pulsed field gradient technique. *J. Nat. Gas Sci. Eng.* **49**, 250-259.

Wang, H., Alvarado, V., McLaughlin, J.F., Bagdonas, D.A., Kaszuba, J.P., Campbell, E. and Grana, D. (2018) Low-field nuclear magnetic resonance characterization of carbonate and sandstone reservoirs from Rock Spring Uplift of Wyoming. *J. Geophys. Res.-Solid Earth* **123**, 7444-7460.

Yu, H., Ng, K.W., Grana, D., Kaszuba, J., Alvarado, V. and Campbell, E. (2018) Experimental investigation of the effect of compliant pores on reservoir rocks under hydrostatic and triaxial compression stress states. *Canadian Geotechnical Journal*.

PhD Dissertations

Wang, H. (2018) Nuclear magnetic resonance studies of rock characterization in CO_2 storage and sequestration, Department of Petroleum Engineering. University of Wyoming, Laramie, Wyoming, p. 157.

Yu, H. (2018) Geomechanical Characterization of CO_2 Storage Reservoirs on the Rock Springs Uplift, WY, Department of Civil and Architectural Engineering. University of Wyoming, Laramie, Wyoming, p. 157.

Conference Papers

Grana, D., Campbell-Stone, E., MacLaughlin, F., Ng, K., Alvarado, V., Mallick, S. and Kaszuba, J. (2017) Rock physics characterization and monitoring feasibility study of a CO_2 storage reservoir in the Rock Springs Uplift, Wyoming, EAGE/SEG Research Workshop 2017: Geophysical Monitoring of CO_2 Injection – CCS and CO_2-EOR, Trondheim, Norway.

Ng, K., Yu, H., Wang, H., Kaszuba, J., Alvarado, V., Grana, D. and Campbell, E. (2018) The effect of CO_2 on the mechanical properties of the reservoir sandstone under a low differential pressure, 52nd U.S. Rock Mechanics/Geomechanics Symposium. American Rock Mechanics Association, Seattle, Washington.

Manuscripts in Preparation for Refereed Journal Articles

Wang, H., Alvarado, V., Bagdonas, D.A., McLaughlin, J.F., Kaszuba, J.P., Grana, D., Campbell, E. and Ng, K. (2019) Experimental determination of CO_2-brine-rock reactions effects on pore structure, porosity and permeability changes in dolomite. *Environ. Sci. Technol.* **in preparation**.

Yu, H., Ng, K., Grana, D., Alvarado, V., Kaszuba, J. and Campbell, E. (2019a) A generalized power-law failure criterion for rocks. *in preparation*.

Yu, H., Ng, K., Kaszuba, J., Grana, D., Alvarado, V. and Campbell, E. (2019b) A new methodology for estimating elastic constants and crack propagation thresholds in brittle rocks. *in preparation*.

LIST OF ACRONYMS AND ABBREVIATIONS

c	Inherent shear strength
Ca^{2+}	Calcium ion
CO_2	Carbon dioxide
D	Dry dolomite sample
Da	Damkohler number
DH	Horizontal dolomite sample
ε	Axial strain
ε_i	Axial strain data point
ε_f	Failure axial strain
ε_v	Total volumetric strain
ε_{cc}	Crack closure axial strain
ε_{cd}	Crack damage axial strain
ε_{ci}	Crack initiation axial strain
ε_{pk}	Axial strain coresponding to the peak deviatoric stress
ε_{vc}	Crack volumetric strain
ε_{ve}	Elastic volumetric strain
E	Young's modulus
EDS	Energy Dispersive X-Ray Spectroscopy
E_{est}	Estimated Young's modulus
ESR	Effective stress ratio
G	Shear modulus
I_P	Acoustic impedance, the product of V_P and density. Sometimes referred to as Z_P.
k	Permeability after reaction
k_0	Initial permeability
K_{dry}	Effective bulk modulus of a dry rock
K_{sat}	Bulk modulus of a saturated rock
LVDT	Linear variable differential transformers
MPa	megapascals
ms	milliseconds
m^2/s	Meter squared per second, units of measure for diffusion coefficient
n	User defined interval
NMR	Nuclear magnetic resonance
P_c	Confining pressure
Pe	Peclet number
φ	Porosity after reaction
φ_0	Initial porosity
P_p	Pore pressure
PVT	pressure-volume-temperature
R^2	Coefficient of determination
RSU	Rock Springs Uplift
S	Dry sandstone sample
SEM	Scanning electron microscope
S_{Hmax}	Maximum horizontal stress

S_{Hmin}	Minimum horizontal stress
SH	Horizontal sandstone sample
SV	Vertical sandstone sample
T_2	NMR transverse relaxation time in milliseconds
T/m	Tesla/meter, units of measure for NMR gradient strength
UCS	Unconfined compressive strength
V_P	P-wave velocity
V_S	S-wave velocity
Z_P	Acoustic impedance, the product of V_P and density. Usually referred to as I_P.
σ	Axial stress
σ_1	Major principal stress
σ_3	Minor principal stress
σ_{cd}	Crack damage stress
σ_{de}	Estimated deviatoric stress
σ_{dm}	Measured deviatoric stress
σ_{diff}	Difference in deviatoric stress
σ_{pk}	Peak deviatoric stress
σ_r	Residual strength
ϕ	Internal friction angle
μm	micrometer
υ	Poisson's ratio
ρ	Density

Appendix I

Summary of
Advanced Rock Property Model

Summary

The reservoir characterization study consists of a quantitative analysis of well log data and of the relations between rock-fluid properties and elastic properties in the different formations of the target zones at the well location. This study is divided into 4 main activities: 1) formation evaluation analysis; 2) facies classification; 3) rock physics modeling; 4) geomechanical modeling.

We first computed a standard formation evaluation analysis with the goal of obtaining the volume of the different rock types: shale, sand, dolomite and limestone; effective and total porosity, and the fluid saturation. The formation evaluation analysis was obtained using Baker Hughes software. Then we derived a statistical facies classification to define the main litho-facies classes in the intervals of interests and computed a facies profile consistent with well log data, mud-reports, core analysis and sedimentological/depositional models. This classification accounts for petrophysical, elastic and geomechanical properties to better identify rock and fluid properties especially in injection intervals. In each facies, we then defined a rock physics model to link rock and fluid properties and elastic attributes at the well-log scale and subsequently at the seismic resolution and we determined relations between elastic and geomechanical properties. We compared different mathematical methods to determine the most accurate facies classification and assess the uncertainty associated to it. We also performed a sensitivity analysis to reveal the most relevant parameters in the fluid flow characterization study. The classifications obtained at the well locations using petrophysical, elastic and geomechanical properties are consistent with the conceptual geological model; however, the preliminary feasibility study of the seismic reservoir shows that an accurate facies classification at the seismic scale can be achieved only from a seismic dataset with adequate signal-to-noise ratio and resolution.

Methodology and results

The Rock Springs Uplift (RSU), located in Wyoming Greater Green River Basin, is a north-south asymmetric anticline formed during the late Cretaceous to early Tertiary (Figure 1). The geologic structure and lithology of RSU meet the screening criteria for CO_2 sequestration (Bachu, 2002, and Bachu 2008). A test well (RSU #1) was drilled on the northeast flank of the RSU for the purpose of obtaining core samples and petrophysical data to identify possible target zones for CO_2 sequestration. The Weber Sandstone and Madison Limestone are potential reservoir zones for long-term CO_2 injection and sequestration (Figure 2). For a detailed description of the geology of the site, we refer the reader to Surdam and Jiao, 2007 and Shafer, 2013. The available dataset (Figure 3) contains:

- A complete set of petrophysical and sonic logs;
- A 3D multicomponent seismic survey;
- A 3D electromagnetic survey.

This Appendix shows results at the well location based on well log data. This report also shows the results of the formation evaluation analysis, the facies classification, the calibrated rock physics models and the geomechanical analysis.

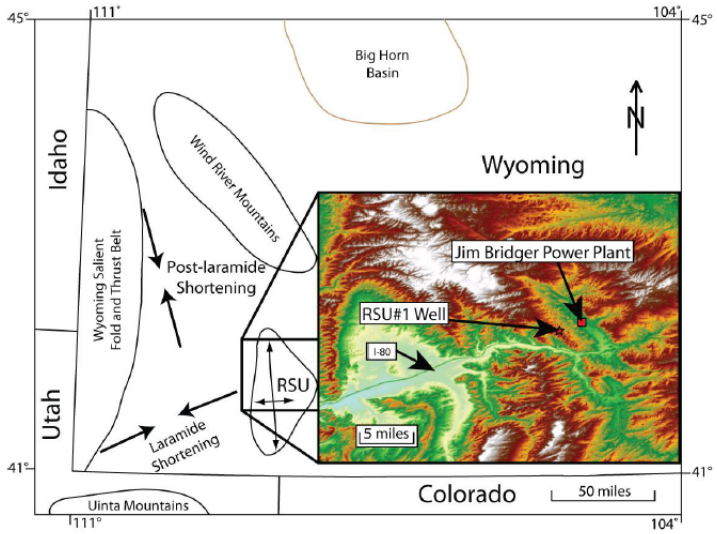

Figure 1: Location map showing position of the RSU, Jim Bridger Power Plant, RSU #1 well, and paleo-stress directions. Color on inset map represents topography; Whites are high elevations and greens are low elevations.

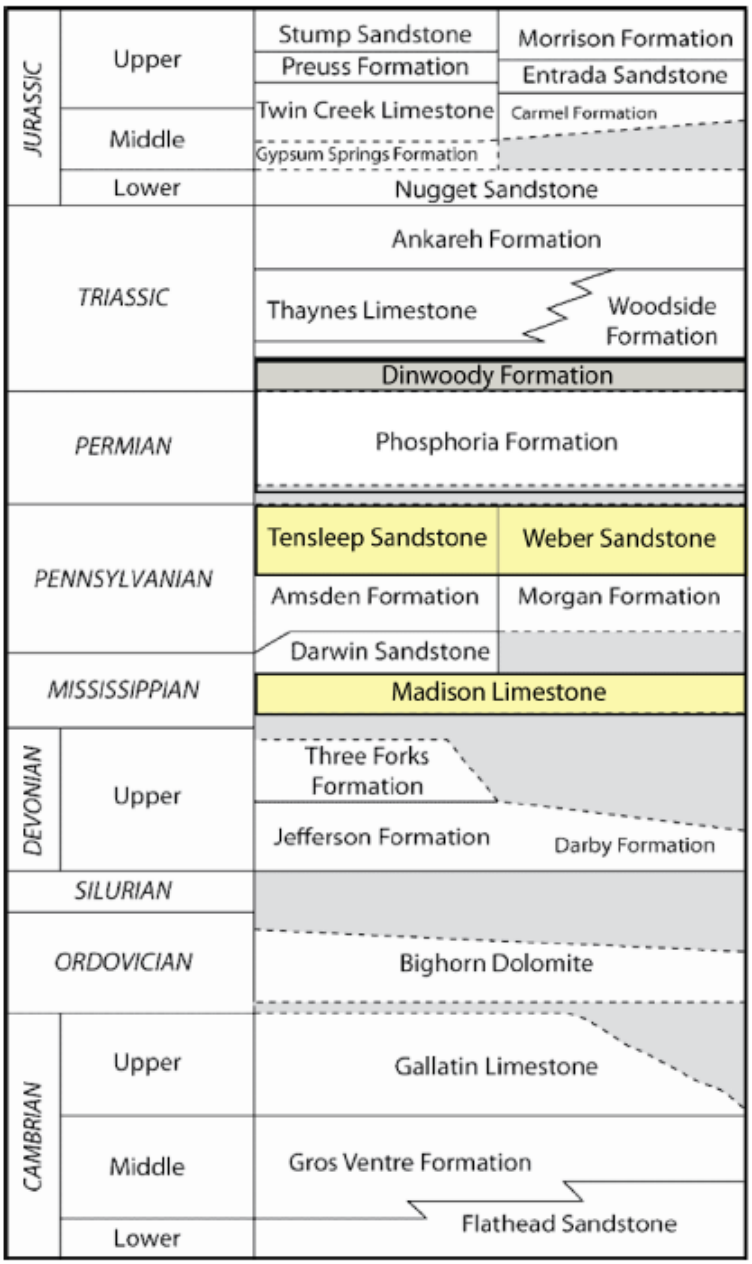

Figure 2: Stratigraphic column showing Paleozoic stratigraphy in the Rock Springs Uplift area. Confining formation is highlighted in brown and injection formations in yellow. (Shafer, 2013, and Love et al., 1993).

Formation evaluation analysis

The available information from RSU #1 includes a complete set of well logs such as neutron porosity, gamma ray, density, resistivity as well as sonic and petrophysical measurements (Figure 3).

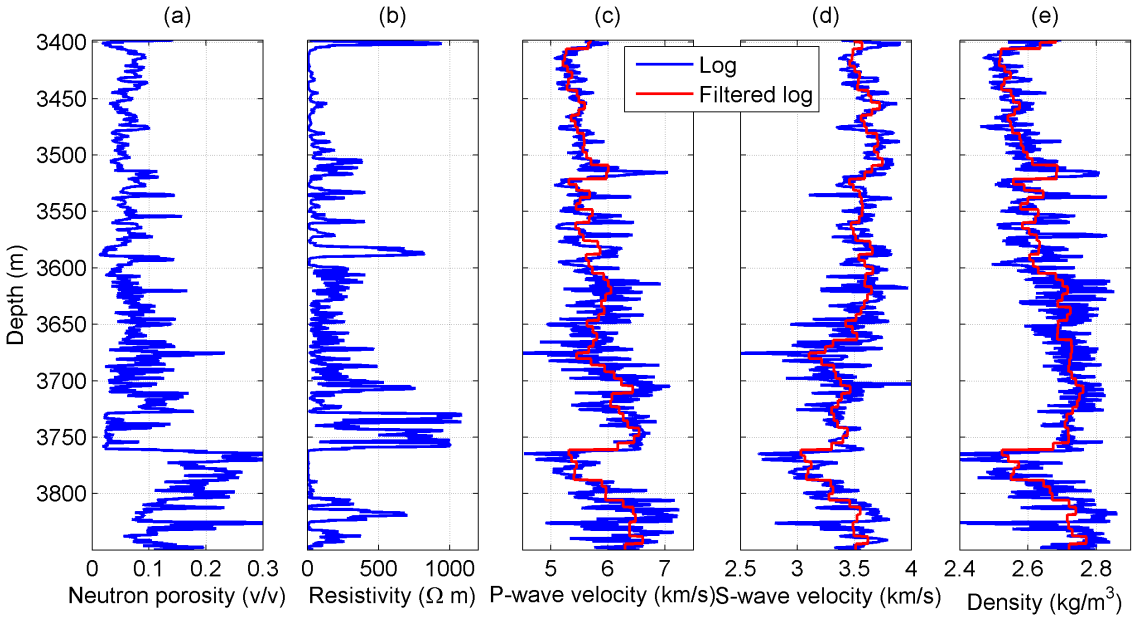

Figure 3 Measured well logs: (a) neutron porosity, (b) resistivity, (c) P-wave velocity (red represents inverted P-wave velocity), (d) S-wave velocity (red represents inverted S-wave velocity), (e) density (red represents inverted density from seismic). The interval 3400-3550m corresponds to Weber Sandstone; the interval 3750-3850m corresponds to Madison Limestone.

Inverted P-wave, S-wave velocities and densities from seismic at the well location were also acquired. For this study, standard formation evaluation analysis has been performed to derive volumetric fractions of lithological components and porosity from log measurements (Figure 4).

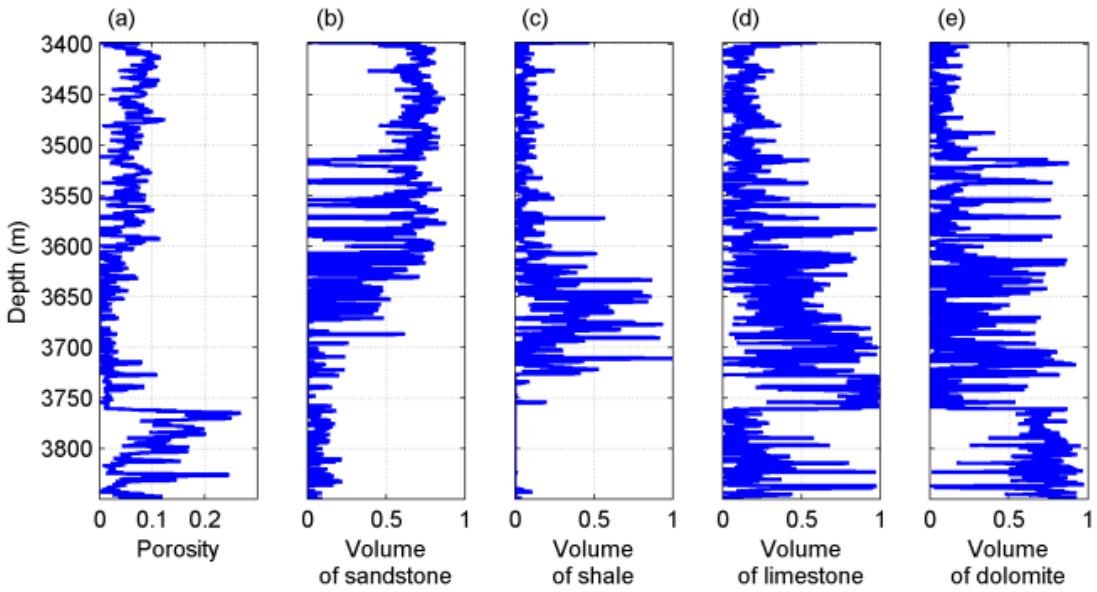

Figure 4: Petrophysical curves computed from measured well logs in formation evaluation analysis: (a) porosity, (b) volume of sandstone, (c) volume of shale, (d) volume of limestone, (e) volume of dolomite. The interval 3400-3550m corresponds to Weber Sandstone; the interval 3750-3850m corresponds to Madison Limestone.

Permeability was also measured on a set of core samples at the RSU well site (Figure 5) as shown in Surdam and Jiao (2007). The measured permeability of Weber Sandstone ranges from 0.001 mD to 13.8 mD and averages at 1.4 mD, with the highest permeability in the upper, eolian unit. The most permeable zones in Madison Limestone are in dolostone lithofacies. The permeability in the vuggy dolostones ranges from 0.001 mD to 176 mD and has an average of 22.7 mD. The confining unit of Amsden Formation and upper Madison Limestone has an average permeability around 0.01 mD. The measured permeability can be extended to the whole well by applying Kozeny-Carman relation (Mavko et al., 2009).

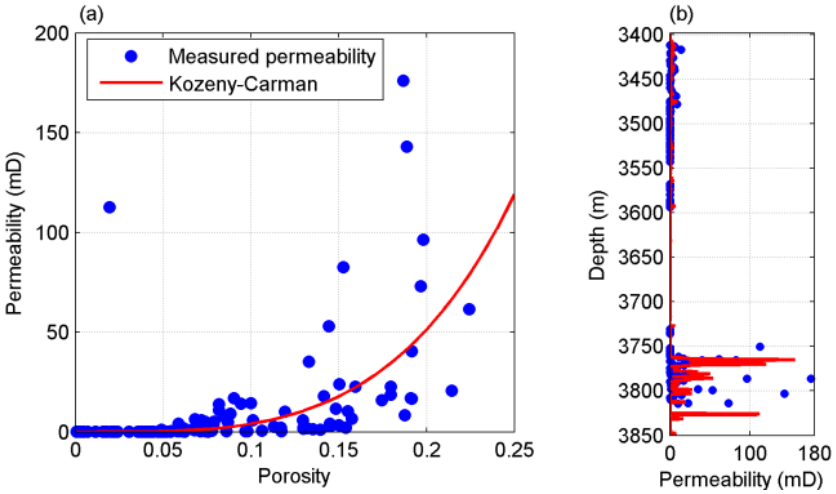

Figure 5: Measured permeability at RSU well location: (a) porosity versus measured permeability (blue represents measured permeability (Surdam and Jiao, 2007); red represents fitted permeability by Kozeny-Carman), (b) permeability versus depth at well location (blue represents measured permeability; red represents fitted permeability by Kozeny-Carman). The interval 3400-3550m corresponds to Weber Sandstone; the interval 3750-3850m corresponds to Madison Limestone.

Facies definition and classification

Four types of facies are defined at the well-log scale: shale, limestone, sandstone and dolomite. The Weber Sandstone (between 3399 m and 3599 m) is comprised of an upper, eolian unit with mainly quartz sandstone and a basal, marine unit with interbedded shale, dolomite and limestone. The entire Weber Sandstone is characterized by low porosity values. The Madison Limestone (between 3726 m and 3856 m) can be divided into two main lithologic facies: an upper limestone unit and a lower basal dolostone unit. Limestone facies generally has low porosity and dolostone has a wider range of porosities between 0.3% and 26.8%. Amsden Formation lying between the Weber Sandstone and Madison Limestone serves as the seal for injected CO_2 within underlying reservoirs. The lithological composition of Amsden Formation is complex with alternating layers of shale, limestone, sandstone, and dolomite. For this work, we are mainly interested in facies classification of the Weber Sandstone and Madison Limestone.

In hydrocarbon exploration and production, it is important to predict lithologic facies in the reservoir, as this prediction is the building block for all reservoir characterization. In this paper, we applied statistical rock physics workflow to classify facies at RSU #1. For the classification, we compared four statistical methods: Expectation Maximization, Bayesian classification, Gaussian mixture classification, and k-means clustering (Hastie et al., 2009). These methods provided similar results. Bayesian classification was performed to obtain the most probable facies at the well location. The predicted log-facies was validated by wireline logs. The workflow can be extended to the entire reservoir model to predict the rock types of the reservoir away from the well location. It is important to classify different facies at RSU location, because the amount and rate at which, CO_2 can be injected into the subsurface is dependent on the lithologic characteristics of the formations.

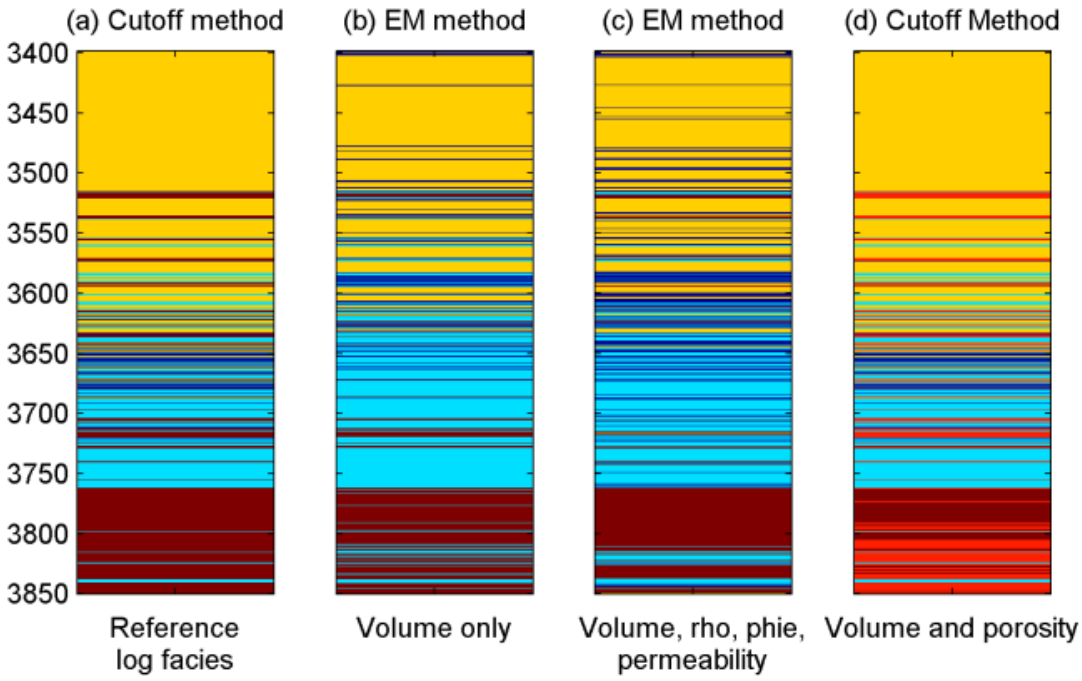

Figure 6: Facies classification based on the cutoff and EM methods for Weber through Madison Formations: (a) classification with cutoff method based on volume of shale, sandstone, limestone, and dolomite, (b) classification with EM method based on volume of sandstone, limestone, and dolomite, (c) classification with EM method based on volume of sandstone, limestone, and dolomite, density, porosity and permeability, (d) classification with cutoff method based on volume of shale, sandstone, limestone, dolomite, and porosity. Yellow represents sandstone, cyan represents limestone, blue represents shale, brown represents dolomite for (a), (b) and (c), brown represents dolomite with porosity greater than 10%, red represents dolomite with porosity less than 10% for (d). The interval 3400-3550m corresponds to Weber Sandstone; the interval 3750-3850m corresponds to Madison Limestone.

Based on the volume of shale, limestone, sandstone and dolomite at RSU well, a facies indicator is assigned to each depth of the well by a simple cutoff method to obtain the reference log facies (Figure 6a). Expectation Maximization (EM) algorithm was also applied to classify facies at the well location. EM method is an iterative algorithm requiring a data set of combined well logs

and an initial guess for the parameters of the Gaussian components that correspond to a lithological facies. Six petrophysical parameters were chose as the input data: volume of limestone, sandstone and dolomite, density, porosity, and permeability. EM classification method was able to identify formation boundaries and distinguish dolomite and limestone at the lower Madison formation. However, it generates too much noise at the Weber formation (Figure 6b and 6c). As a forth method, dolomite was split into two categories based on porosity values. Five facies can be obtained by dividing dolomite into dolomite with porosity greater than 0.10 and dolomite with porosity less than 0.10 (Figure 6d).

To relate petrofacies to seismic data, cross plots of different elastic parameters were used. In Figure 7, we present the cross plots in the petroelastic domains color coded based on the facies classified using the cut-off method (in Figure 6a). In V_p-V_s domain, the sandstone cluster can be well discriminated from other facies. Dolomite cluster in general is less easy to be separated from shale and limestone. On the other hand, dolomite with porosities above 10% can be better discriminated from limestone and lower porosity dolomite can be better resolved from shale (Figure 7b).

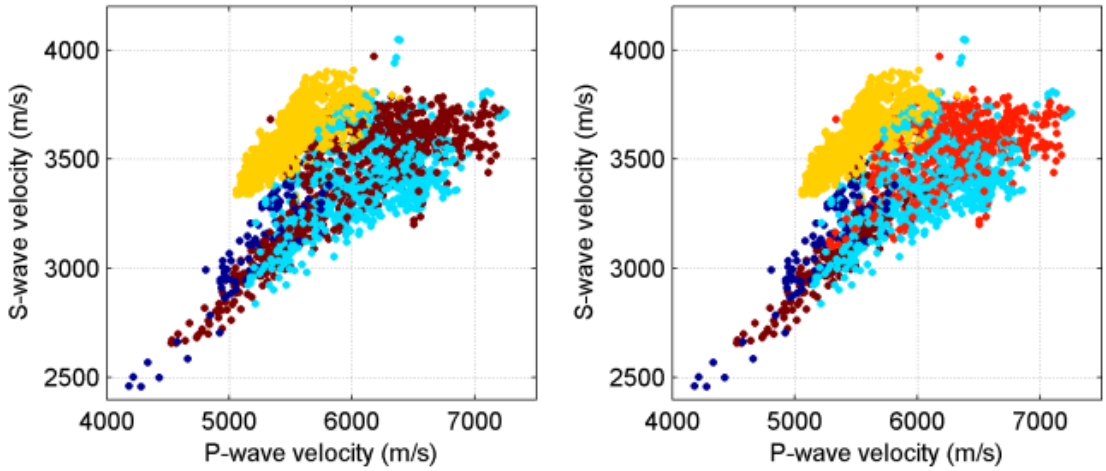

Figure 7: Rock-physics analysis: (a) P-wave velocity versus S-wave velocity (four facies), (b) P-wave velocity versus S-wave velocity (five facies). Yellow represents sandstone, blue represents shale, cyan represents limestone, brown represents dolomite for (a), brown represents dolomite with porosity greater than 10%, red represents dolomite with porosity less than 10% for (b). The plots include data in the interval 3400-3850m.

Given the reference classification, we can then estimate the likelihoods of each sample in the well log of belonging to each facies, assuming the coupling of elastic parameters follows a bivariate Guassian distribution. Based on the probability density functions (pdfs) of V_p-V_s in this case, the probabilities for each facies were calculated by a Bayesian approach. The probability of a given facies conditioned by V_p - V_s properties can be calculated by $\mathrm{P}(\mathrm{Facies}|V_p,V_s) \propto \mathrm{P}(V_p,V_s|\mathrm{Facies})\mathrm{P}(\mathrm{Facies})$, where we assume each facies is equally probable. Bayesian classification was conducted at each depth of the well and the most probable facies

were constructed at the well location based on V_p-V_s and inverted P-wave and S-wave velocities (Figure 8). For the case of four facies, the predicted elastic facies are in good agreement with reference log facies at the Weber Sandstone. At the Madison Limestone, dolomite is misclassified as shale for predicted elastic facies (Figure 8a). The inverted seismic velocities have lower resolutions which reflect on the predicted seismic facies. The predicted seismic facies is able to follow the major variations of the facies, however dolomite was misclassified as limestone at the lower Madison Limestone (Figure 8b). The mismatch in facies predictions can be due to: overlap of dolomite and limestone clusters in the elastic domain or lack of resolution of the inverted data compared to well log. By dividing dolomite into two groups, the predicted elastic facies matches with reference log facies quite well both in the Weber Sandstone and Madison Limestone (Figure 8c). For the case of predicted seismic facies (five facies), limestone is able to be distinguished from dolomite with higher and lower porosities (Figure 8d).

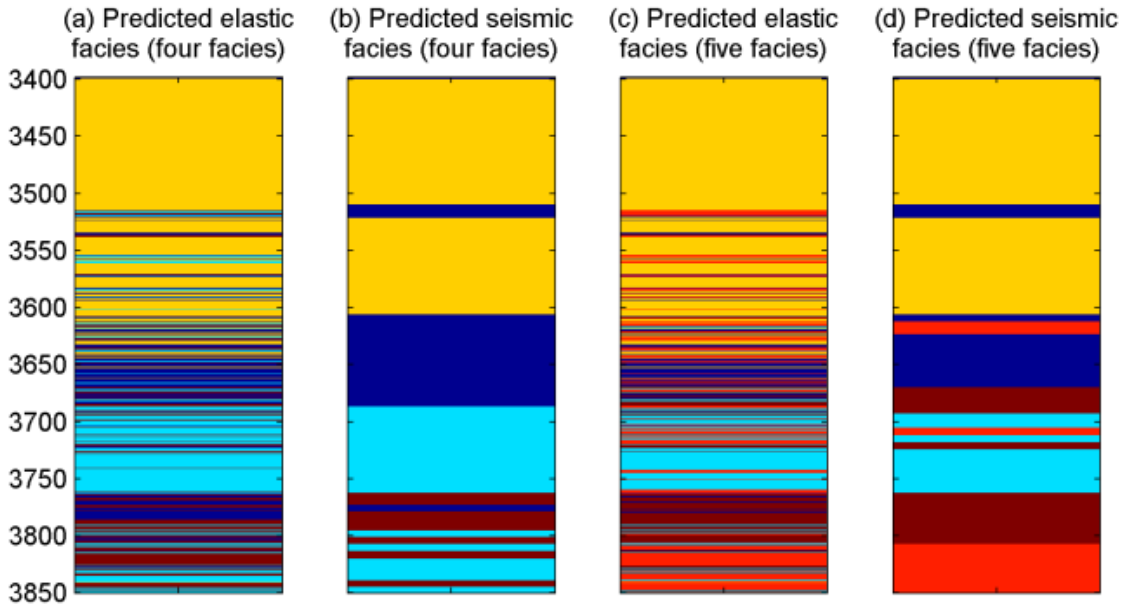

Figure 8: Bayesian classification of facies: (a) classification of four facies with P-wave and S-wave velocities, (b) classification of four facies with inverted P-wave and S-wave velocities, (c) classification of five facies with P-wave and S-wave velocities, (d) classification of five facies with inverted P-wave and S-wave velocities. Yellow represents sandstone, blue represents shale, cyan represents limestone, brown represents dolomite for (a) and (b), brown represents dolomite with porosity greater than 10%, red represents dolomite with porosity less than 10% for (c) and (d). The interval 3400-3550m corresponds to Weber Sandstone; the interval 3750-3850m corresponds to Madison Limestone.

The predicted elastic facies were compared with reference log facies to test our prediction process by the application of a confusion matrix (Table 1 and Table 2). The diagonal elements of the matrix show the success rate of the prediction for each petrofacies. The off-diagonal elements quantify which facies has been confused with which. In general, a confusion matrix with large diagonal numbers and small off-diagonal numbers suggests a good quality prediction. For the case of four elastic facies, shale and sandstone were well resolved (Table 1). Dolomite

tends to be confused with limestone (31.3% of the time) and shale (23.1% of the time). For five elastic facies, dolomite with porosity greater than 10% can be well resolved from limestone (Table 2). However, dolomite with porosities lower than 0.10 still has 17% of chance to be misclassified as limestone. This can be interpreted from the crossplot in the elastic domain: the cluster of dolomite with higher porosities is better separated from limestone compared to dolomite with relatively lower porosities (Figure 7).

		Classified Elastic Facies			
Petrofacies		Shale	Limestone	Sandstone	Dolomite
	Shale	0.900	0.017	0.017	0.067
	Limestone	0.178	0.621	0.035	0.166
	Sandstone	0.047	0.008	0.943	0.002
	Dolomite	0.231	0.313	0.024	0.431

Table 1: Confusion matrix of elastic log facies of four facies.

		Classified Elastic Facies				
Petrofacies		Shale	Limestone	Sandstone	Dolomite (φ>0.1)	Dolomite (φ>0.1)
	Shale	0.733	0.008	0.017	0.0167	0.225
	Limestone	0.117	0.438	0.034	0.271	0.139
	Sand	0.038	0	0.942	0.019	0
	Dolomite (φ<0.1)	0.068	0.170	0.028	0.663	0.070
	Dolomite (φ>0.1)	0.110	0.034	0.017	0.003	0.835

Table 2: Confusion matrix of elastic log facies of five facies.

Rock physics and geomechanical relations

In each facies, we defined a rock physics model and estimated elastic, electric and geomechanical parameters (in the following named geophysical attributes). The model that links rock and fluid properties with geophysical attributes is non-linear and depends on several rock and fluid parameters; however in each lithology these relations can be approximated by linear models. For the rock physics model we tested several relations available in literature: in sandstone we tested empirical relations, stiff and cemented sand models (Dvorkin et al., 2014). Dvorkin's stiff sand model based on Hertz-Mindlin contact theory (Mavko et al., 2009) and modified Hashin Shtrikmann bounds (Mavko et al., 2009) provides a good fit. Similar results have been obtained using the semi-empirical Raymer equation. In Figure 9, we show that the relation is approximately linear in the range of porosity of the Weber Sandstone. In limestone and dolomite the relation is linear as well; however, most of the empirical models do not fit the data; inclusion models, such as Kuster-Toksoz and Xu-White relations (Mavko et al., 2009) provide a good fit. Inclusion models require empirical measurements of several parameters, such as critical porosity and aspect ratio of the rock; therefore, for simplicity we decided to use a

linear regression (Figure 9). The relation between rock and fluid properties and resistivity is difficult to calibrate because of the lack of direct measurements of porosity and water saturation; therefore, we adopted the Archie's model used in formation evaluation analysis (Figure 9, right plot). Finally, we computed a set of geomechanical properties including Poisson ratio, Young's modulus and brittleness index (Figure 10). Poisson ratio and Young's modulus provide a good indicator of the ability of the rock to resist to deformation. Brittle failure is associated with materials that undergo little to no permanent deformation before failure. Brittle rocks have a strong tendency to fracture. This is appealing to development geophysicists because elastic moduli are readily available from well logs and accessible from seismic data via seismic inversion.

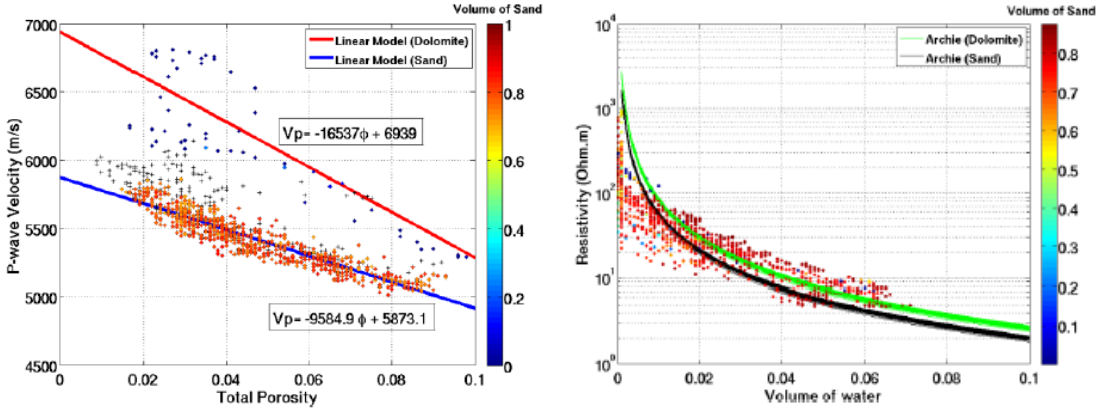

Figure 9: (Left) Rock physics model calibrated at the well location in wet conditions. A linear regression model has been applied in the Weber Sandstone with different coefficients in sandstone (blue line) and dolomite (red line). Color code is volume of sandstone. (Right) Archie model applied in the Weber Sandstone. Green lines represent Archie's model for dolomite; black lines represent Archie's model for sandstone. Different lines represent different porosity values (ranging from 0 to 0.1). Color code is volume of sandstone.

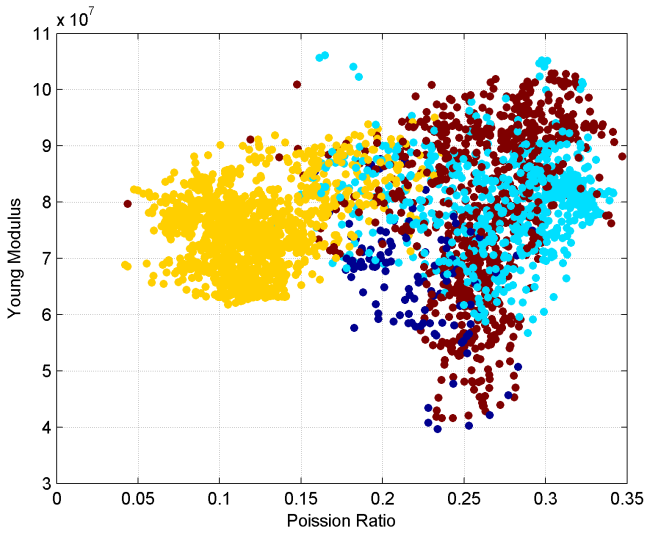

Figure 10: Crossplot of Poisson ratio vs Young's modulus color coded by facies. The brittleness index can be computed using Young's modulus E and Poisson's ratio v to estimate brittleness.

Feasibility study at seismic scale

Most of the results and conclusions derived in previous work rely on the high accuracy and resolution of well log data; however, the ability to extend the previous model to the 3D static model of the reservoir depends on the quality of the available seismic data. In this preliminary analysis we mimicked the resolution of the available geophysical data (seismic and electromagnetic) by filtering the well logs to a lower resolution and inverting these properties to estimate porosity and saturation at the seismic scale. The results of the inversion test, i.e. the inversion of filtered velocities and resistivities for porosity and saturation, are shown in Figure 11. Overall, the results are satisfactory since the posterior distributions in Figure 11 correctly predict porosity and water volume and capture the uncertainty associated to the inversion. The inverted results in Figure 11 show that the method can be applied to seismic and electrical inverted data; however, results from seismic and EM inversion could be affected by noise in the data. A sensitivity analysis on the signal to noise ratio will be performed in order to assess the effect of the noise in the data on the result.

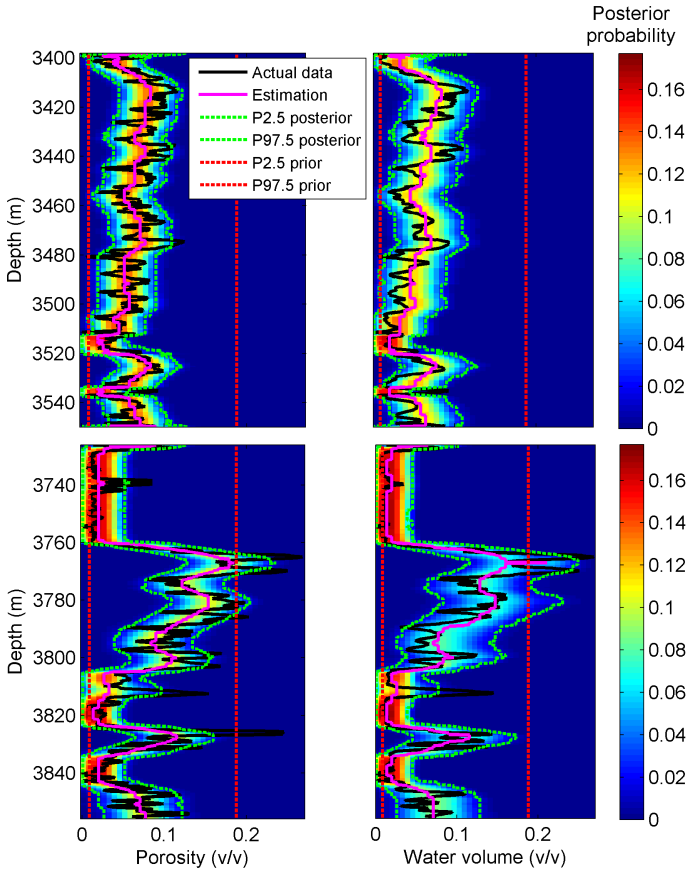

Figure 11: Posterior probability estimation at well location: porosity and water volume conditioned by filtered log data (P- and S-wave velocity and resistivity) shown in Figure 9. The background color is the estimated posterior probability. Black lines are the actual porosity and water volume curves. Red lines represent the 95% confidence interval of the prior distribution, green lines represent the 95% confidence interval of the posterior distribution. The magenta line is the maximum a posteriori of the posterior distribution. Top plots show the Weber Sandstone, bottom plots show the Madison Limestone.

Conclusions

We completed the formation evaluation analysis, rock physics modeling including elastic and geomechanical properties, facies classification, and uncertainty study. We identified two main formations and four main rock types: sand, shale, limestone and dolomite. For each rock type in each formation, we determined a rock physics model to link rock and fluid properties, such as porosity, lithology and fluid saturations, with elastic and geomechanical properties. The facies-dependent rock physics model that links porosity to elastic properties is approximately linear. The fluid content does not affect elastic properties too much due to the low porosity in most of the formations and the small difference in wave velocity in oil and water. Several classifications have been tested. All the methods are based on probabilistic approaches to quantify the uncertainty in the classification. We chose the Bayesian classification, which is also the most popular in the oil industry. The uncertainty studied showed that we can clearly distinguish sandstone from other lithologies using elastic properties, whereas there is a large overlap in the

classification of limestone and dolomite. The uncertainty increases if the classification is performed at the seismic resolution rather than the well log scale. Additional properties such as estimated permeability and geomechanical properties (Young's modulus and Poisson ratio computed from P- and S-wave velocity) were included in the classification; however, because these properties are computed from the original well logs, the extended classification does not provide significant insight in the uncertainty study. A better understanding of the importance of these properties in the rock physics model could be achieved combining well log data and geomechanical measurements.

References

Bachu, S., 2002, Sequestration of CO_2 in geological media in response to climate change: road map for site selection using the transform of the geological space into CO_2 space: Energy Conversion Management, 43, 87-102.

Bachu, S., 2008, CO_2 storage in geological media: role, means, status and barriers to deployment: Progress in Energy and Combustion Sciences, 34, 254-273.

Dvorkin J., Gutierrez, M., and Grana, D., 2014, Seismic reflections of rock properties: Cambridge University Press.

Hastie, T., Tibshirani, R., and Friedman, J., 2009, The elements of statistical learning: Springer.

Lang, X. and Grana, D., 2015, Bayesian rock physics inversion of acoustic and electrical properties for rock-fluid property estimation, SEG Annual Meeting, New Orleans.

Love, J.D., Christiansen, A.C., and Ver Ploeg, A.J., 1993, Stratigraphic chart showing Phanerozoic nomenclature for the State of Wyoming. Geological Survey of Wyoming Map Series, report 41; 1993

Mavko, G., Mukerji, T., and Dvorkin, J., 2009, The rock physics handbook: Cambridge University Press.

Shafer, L., 2013, Assessing injection zone fracture permeability through the identification of critically stressed fractures at the Rock Springs Uplift CO_2 sequestration site, SW Wyoming: master thesis, University of Wyoming.

Smith, L. B., Eberli, G. P., and Sonnenfeld, M., 2004, Sequence-stratigraphic and paleogeographic distribution of reservoir-quality dolomite, Madison Formation, Wyoming and Montana: American Association of Petroleum Geologists, 80, 67-92.

Surdam, R.C., and Jiao, J., 2007, The Rock Springs Uplift-An outstanding geological CO_2 sequestration site in southwest Wyoming: Wyoming State Geological Survey Challenges in Geologic Resource Development, 2, 31.

Wu, W., Grana, D., Campbell-Stone, E., and McLaughlin, F., 2015, Bayesian facies classification in a CO_2 sequestration study using statistical rock physics modeling of elastic and electrical properties, SEG Annual Meeting, New Orleans.

Appendix II

Rock Physics Model Development and Analysis

Introduction:

We perform a quantitative analysis of well log and core sample data and calibrate a set of physical relations to validate the feasibility of obtaining reservoir properties, such as porosity and permeability, from seismic inversion results. The complete set of petrophysical well logs (Figure 1) was processed to obtain a set of petrophysical parameters: including volume of sand, volume of shale, volume of dolomite, volume of limestone, and porosity. The mineral volumes were computed using mass balance equations based on gamma ray, density and photoelectric effect; and porosity was derived from density according to the estimated solid density and brine density. The porosity computed curve was validated using a set of more than 100 samples (Figure 1). The properties derived from the sonic logs, P-impedance and S-impedance, are shown in Figure 2. Because poro-elastic relations are facies-dependent, we first derive a facies classification profile at the well location. In each facies, we then calibrate a rock physics model. This section is organized in two parts: facies classification and rock physics modeling.

Results

The facies classification study of the Rock Spring Uplift reservoir includes the identification of a set of litho-facies based on the mineral volumes estimated at the well location and the validation of the consistency of the so-derived classification in the elastic domain at both well log and seismic resolution. The second step of the classification is crucial for the seismic reservoir characterization study. The definition of litho-facies relies on the petrophysical properties (mineral volumes and porosity) of the reservoir rocks in the borehole; however, far away from the well, the only available properties are seismically-derived elastic attributes. It is fundamental to prove that the litho-facies can be discriminated in the elastic domain and at the seismic scale.

We first define the main rock types in the reservoir, according to the geological information and the available core data. We identified five main litho-facies (Appendix I): shale, limestone,

sandstone, high-porosity dolomite and low-porosity dolomite (Figure 1). The litho-facies classification at the well location (Figure 1, last plot) is obtained by applying a cluster analysis technique to the set of mineral volumes and porosity computed logs (Grana et al., 2012). The Weber sandstone formation (from 3401m to 3609m) comprises an upper eolian unit with mainly quartz-sandstone and a basal marine unit with interbedded shale, dolomite and limestone (Surdam, 2013). The sandstone shows porosity values lower than 12%. The Madison limestone formation (from 3727m to 3847m) comprises an upper limestone unit and a basal dolomite unit. The limestone shows porosity close to 0%, whereas the dolomite shows a wide range of porosities between 3% and 27%. Because of the wide range of porosity values, we split the dolomite facies into two litho-facies, namely high-porosity dolomite and low-porosity dolomite. The Amsden formation, lying between the Weber and Madison formations, serves as the seal for CO_2 injection in the Madison and it is mostly made by shale and limestone. The litho-facies classification in the Amsden shows several thinlayers; however, we believe that these artifacts are mostly due to the noise in the mineral volume logs.

The second step in the facies classification is the validation of the facies discriminability in the elastic domain at the well log scale and at the seismic scale. The well logs of P- and S-impedance and density are compared in Figure 2 with the elastic attributes inverted from the seismic trace collocated at the well location to compare the resolution of the two datasets. Because the estimation of density from seismic data is generally uncertain, in the facies discriminability analysis we only use P-wave and S-wave velocity. In the V_P-V_S domain (Figure 3, right plot), the sandstone facies can be well discriminated from other facies due to the lower V_P/V_S ratio. The dolomite facies shows a large overlap the limestone facies; however, high-porosity dolomite can be discriminated from limestone. We then compute a facies profile (elastic facies) based on elastic properties only. This profile is obtained by applying a Bayesian classification approach to estimate the posterior probability of elastic facies conditioned by P-wave and S-wave velocity. The prior distribution is assumed to be uniform to avoid introducing a bias in the elastic facies estimation by using the actual litho-facies proportions. The likelihood function in

the Bayesian classification, i.e., the probability of P-wave and S-wave velocity given the facies, is assumed to be Gaussian in each facies and is estimated using the reference litho-facies profile. Wu et al. (2015) performed a sensitivity analysis on the set of conditioning elastic properties including P-wave and S-wave velocity, Poisson ratio, V_p/V_s ratio, P- and S-impedance, elastic impedance, density, and AVO attributes and showed consistent result for the different sets of combinations. We then compute the posterior probability $P(F \mid V_p, V_s)$ of the elastic facies conditioned by P-wave and S-wave velocity in a Bayesian classification setting and compute the most likely value at each depth along the well log interval. The elastic facies classification is shown in Figure 2, and it shows a good match with the actual litho-fluid classification.

As a feasibility study, we repeat the same procedure using inverted seismic attributes instead of the actual elastic logs. The objective of the feasibility study is to verify the facies discriminability at the seismic scale. We first compute a synthetic seismic profile at the well location from filtered well log data and invert the so-obtained trace to estimate the seismically-inverted velocities. No noise is added to the synthetic seismic. We then repeat the facies classification with the same prior and likelihood but we use the seismically-inverted velocities to condition the posterior distribution. In the second test, we adopt the same procedure using real seismic data extracted from the acquired seismic survey at the well location. The seismic facies profiles estimated from synthetic and real seismic data show a good agreement with the litho-facies and seismic-facies profiles, despite the lower resolution. We notice that the seismic facies shows a mismatch in the lower Madison formation, where limestone and low-porosity dolomite are misclassified. The misclassification might be due to the noise in the real data combined with the overlap between these two facies in the elastic domain (Figure 3, right plot). The average success rates of the so-obtained classifications compared to the actual litho-fluid classifications (i.e., the percentage of samples correctly classified in the corresponding litho-facies) is 76% for the elastic facies classification, 67% for the synthetic seismic facies classification and 54% for the real seismic facies classification.

In Figure 3 (left plot), we also notice that different litho-facies show different poro-elastic

trends between porosity and P-wave velocity. Consequently, we proposed to derive two different rock physics models for the Weber and Madison formations. Rock physics models provide a set of relations to link elastic properties to petrophysical variables. Different models are available in the literature (Mavko et al., 2009; Dvorkin et al., 2014). As shown in Figure 3, in the presence of multiple rock-types, it is necessary to calibrate a facies-dependent model. Two main groups of models can be identified in the rock physics literature: granular media models based on Hertz-Mindlin contact theory (Mavko et al., 2009) and inclusion models (Mavko et al., 2009). Granular media models are suitable for sandstone and shaley sandstone; whereas inclusion models can be applied to carbonate rocks where the pore structure mainly consists of cracks and fractures. In our work, we propose to use the stiff sand model for the Weber sandstone and the Berryman's inclusion model for the Madison limestone and dolomite. For the density we use a linear average of the solid density and the brine density, weighted by the rock porosity.

The stiff sand model combines Hertz-Mindlin equations to compute the elastic moduli at the critical porosity, the elastic average equations to compute the elastic moduli at 0 porosity, and the modified Hashin-Shtrikmann upper bound for porosities between 0 and the critical porosity (Dvorkin and Nur, 1996). The predicted moduli, and consequently the predicted velocity, depend on the elastic property of the solid phase (sandstone in our example), the fluid saturation (brine), and the porosity of the rock. The stiff sand model also requires other rock parameters: the coordination number is assumed to be 12 and the critical porosity is assumed to be 0.36. The brine effect is obtained by applying Gassmann's equations (Mavko et al., 2009) to the stiff sand model prediction. Because the sandstone in the Weber contains variable percentages of other minerals, we account for some uncertainty in the elastic moduli of the sandstone and compute the stiff sand model for different values of the sandstone elastic moduli. The calibrated model is shown in Figure 4 and matches the measured velocities in the Weber.

Berryman's inclusion model (Berryman, 1980) allows the prediction of the elastic moduli of the rock from the porosity and the elastic moduli of the solid. Inclusion models can describe different pore shapes through a geometrical factor, namely the aspect ratio of the inclusion. From

the core samples, we assume ellipsoidal inclusions; however, because of the complexity of the estimation of the aspect ratio from core samples, we accounted for some uncertainty in the parameter and we calibrated it by fitting the model equations to the data. As a result of this optimization we obtained an average aspect ratio of 0.22, which is consistent with the core sample observations. We also accounted for some uncertainty in the volume of limestone and dolomite. The calibrated inclusion model is shown in Figure 5 and matches the measured velocities in the Madison. The rock physics model predicted logs of P-wave and S-wave velocity and density are shown in Figure 6, and they show a good overall match when compared to the measured logs.

Finally we established a rock physics model to link porosity and permeability. This model was established using core data only due to the lack of a measured permeability log. Approximately 110 core samples with permeability and porosity measurements are available at the RSU #1 well. The measured permeability in the Weber sandstone ranges from 0.001 mD to 13.8 mD, with an average of 1.4 mD and the highest permeability is in the upper eolian unit (McLaughlin et al., 2013). The most permeable zones in the Madison are in the dolomite facies. The permeability in the vuggy dolomite ranges from 0.001 mD to 176 mD and has an average of 22.7 mD. The limestone facies in the upper part of Madison Limestone has low permeability. We calibrate the porosity-permeability relation at the well location by applying the Kozeny-Carman relation (Mavko et al., 2009) for different geometrical factors. The geometrical factor is the product of a parameter describing the pore diameter and a parameter describing the pore tortuosity. These parameters cannot be directly measured from core samples; therefore, we tested a large range of parameters and fitted the model to the measured data. The fitted relations for different geometrical factors are shown in Figure 7. The core samples in the Madison show a large variability in both permeability and porosity, probably due to different limestone and dolomite percentages and different rock textures. In the Weber, we observe two clusters of data and two different trends: data in the lower Weber (triangles) shows lower porosity and lower permeability than data in the upper Weber (circles), probably due to the higher percentage of

clay and limestone.

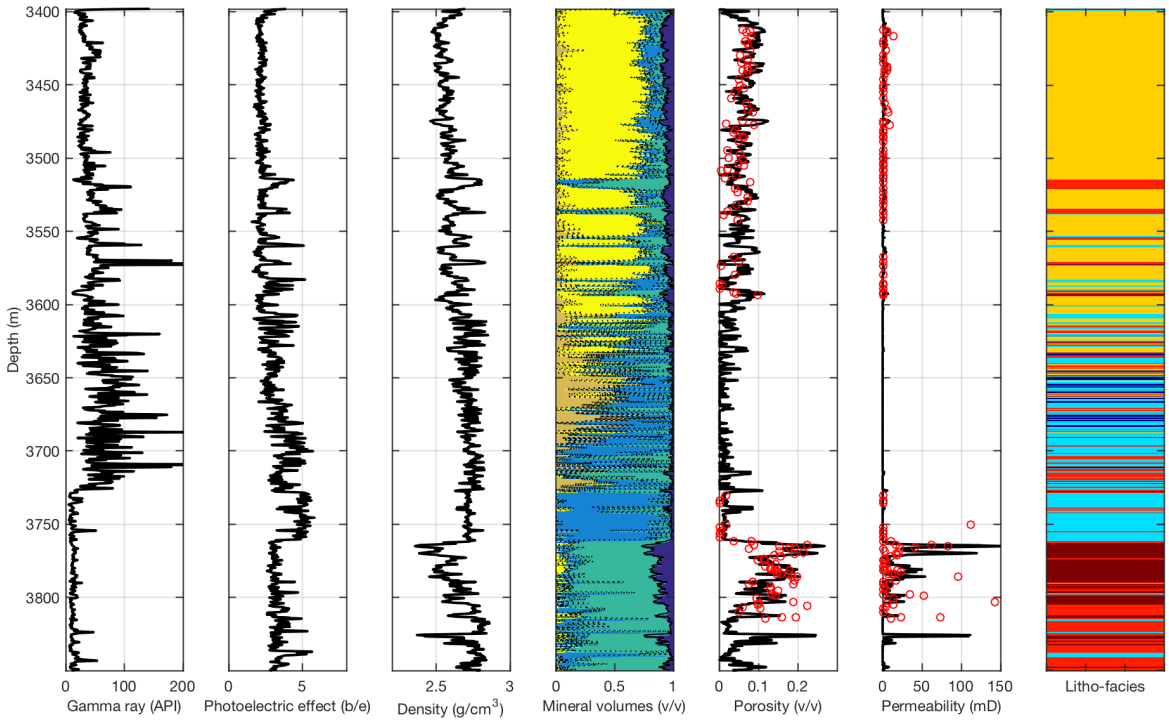

Figure 1 – Well log data

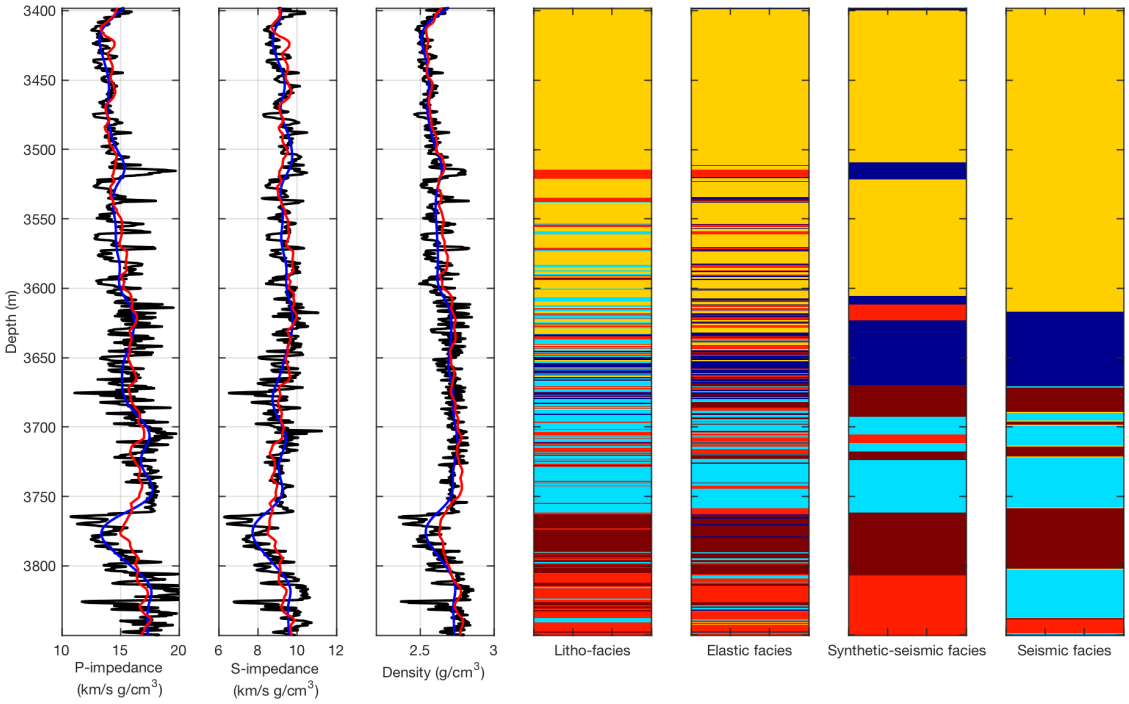

Figure 2 – Multiscale facies classification.

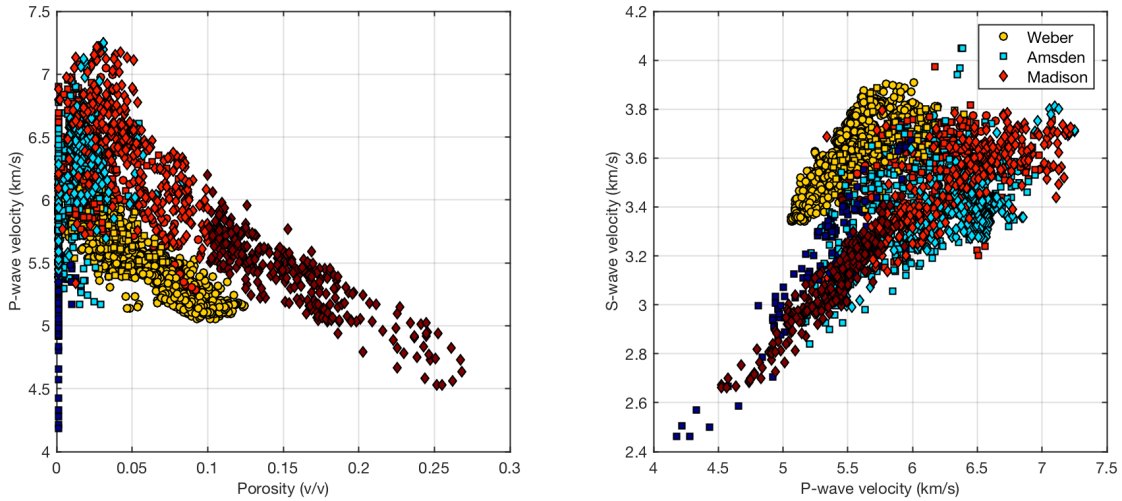

Figure 3 – Logscale facies discriminability in poroelastic domains.

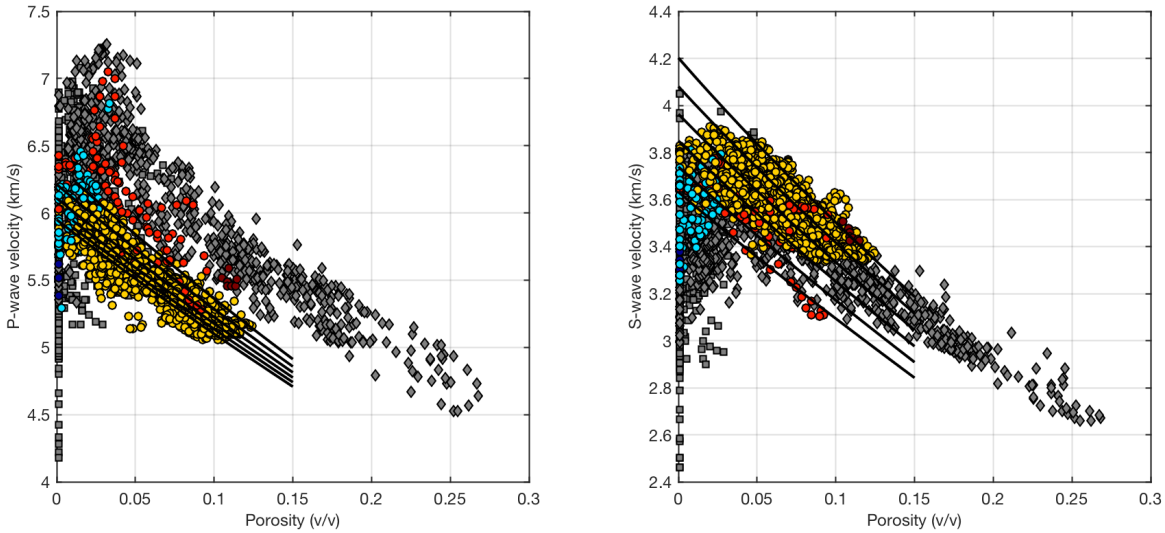

Figure 4 – Rock physics model (stiff sand model) in the poro-elastic domain for the Weber formation.

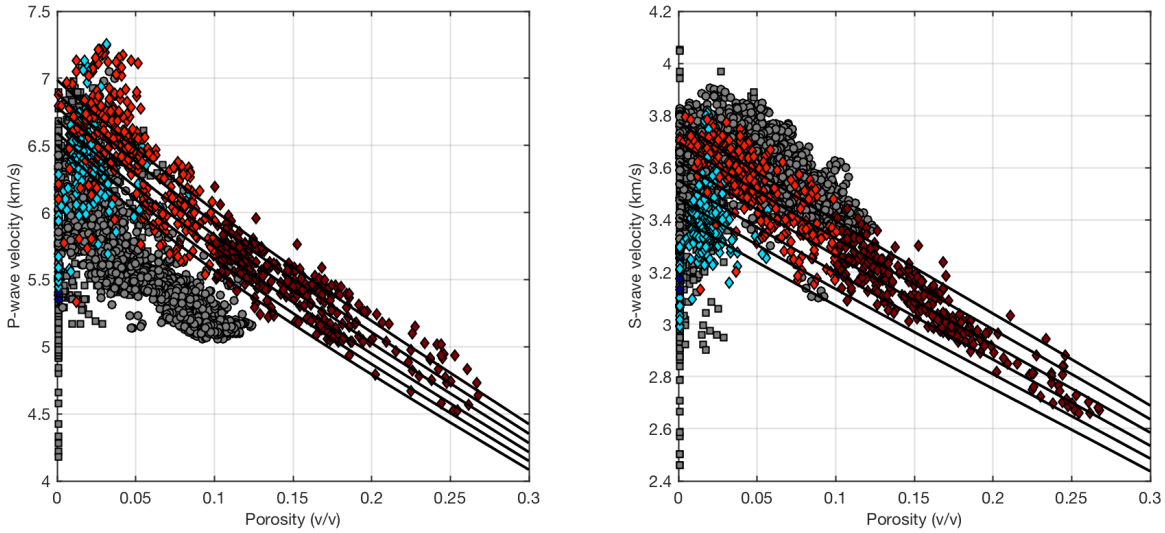

Figure 5 - Rock physics model (Berryman's model) in the poro-elastic domain for the Madison formation.

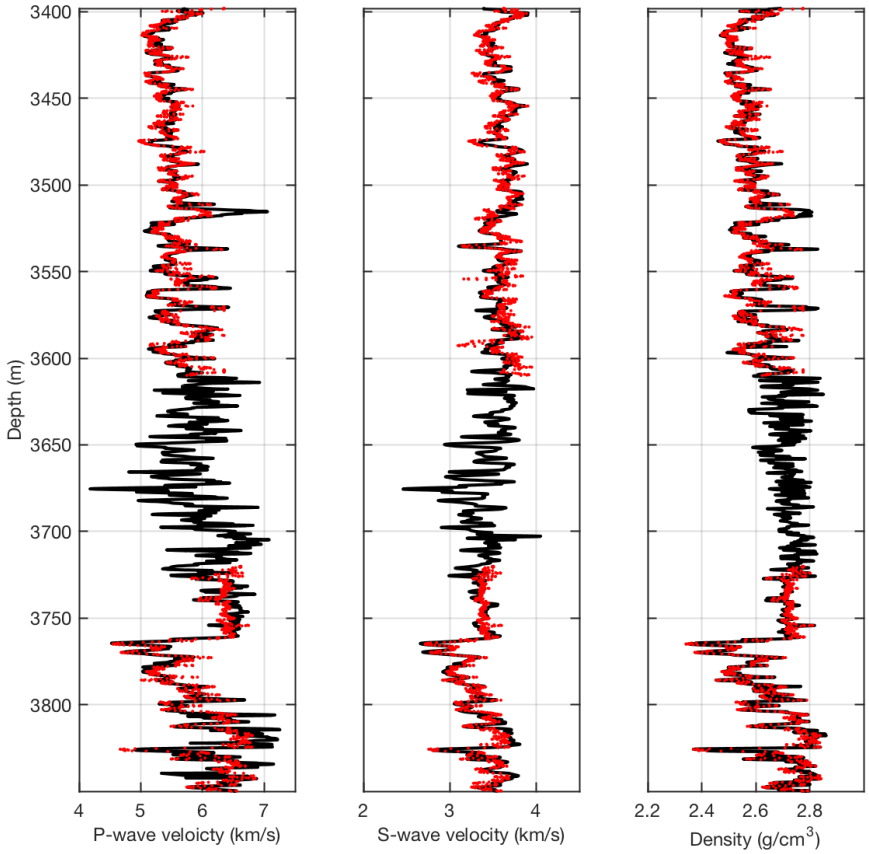

Figure 6 - Rock physics model predictions at the well location.

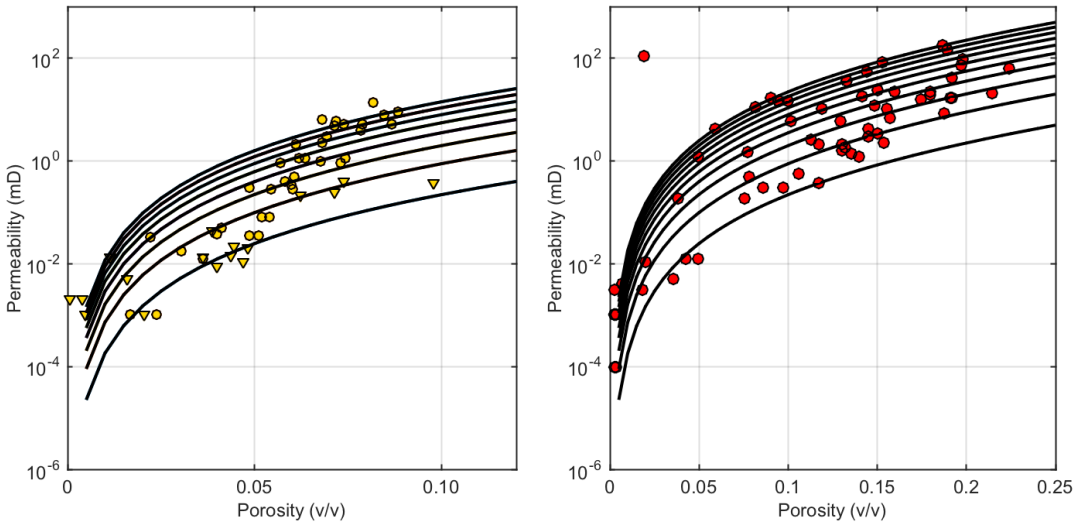

Figure 7 - Porosity-permeability model calibrated using core samples.

REFERENCES

Avseth, P., T. Mukerji, and G. Mavko, 2005, Quantitative seismic interpretation: Cambridge University Press.

Berryman, J. G., 1980, Long-wavelength propagation in composite elastic media II. Ellipsoidal inclusions: The Journal of the Acoustical Society of America, 68, 6, 1820-1831.

Campbell-Stone, E., R. Lynds, C. Frost, T. P. Becker, and B. Diem, 2010, The Wyoming carbon underground storage project: geologic characterization of the Moxa Arch and Rock Springs Uplift: Energy Procedia, 4, 4656–4663.

Dvorkin, J., M. Gutierrez, and D. Grana, 2014, Seismic reflections of rock properties: Cambridge University Press.

Dvorkin, J., and A. Nur, 1996, Elasticity of high-porosity sandstones: Theory for two North Sea data sets: Geophysics, 61, 5, 1363-1370.

Grana, D., and E. Della Rossa, 2010, Probabilistic petrophysical-properties estimation integrating statistical rock physics with seismic inversion: Geophysics, 75, 3, O21-O37.

Grana, D., M. Pirrone, and T. Mukerji, 2012, Quantitative log interpretation and uncertainty propagation of petrophysical properties and facies classification from rock-physics modeling and formation evaluation analysis: Geophysics, 77, 3, WA45-WA63.

Grana, D., 2014, Probabilistic approach to rock physics modeling: Geophysics 79, 2, D123-D143.

Grude, S., M. Landrø, and B. Osdal, 2013, Time-lapse pressure–saturation discrimination for CO_2 storage at the Snøhvit field: International Journal of Greenhouse Gas Control, 19, 369-378.

Grude, S., M. Landrø, and J. Dvorkin, 2015, Permeability variation with porosity, pore space geometry, and cement type: A case history form the Snøhvit field, the Barents Sea: Geophysics, 80, 1, D43-D49.

Lang, X., and D. Grana, 2015, Bayesian rock physics inversion of acoustic and electrical properties for rock-fluid property estimation: 85th Annual International Meeting, SEG, Expanded Abstracts, 2931-2935.

Li, T., and S. Mallick, 2015, Multicomponent, multi-azimuth pre-stack seismic waveform inversion for azimuthally anisotropic media using a parallel and computationally efficient non-dominated sorting genetic algorithm: Geophysical Journal International, 200, 2, 1134-1152.

Mavko, G., T. Mukerji, and J. Dvorkin, 2003, The Rock Physics Handbook: Cambridge University Press.

McLaughlin, J. F., and M. Garcia-Gonzalez, 2013, Detailed geologic characterization of core and well data from the Weber and Madison Formations and associated seals at a potential CO_2 sequestration site in southwest Wyoming: Defining the lithologic, geochemical, diagenetic, and burial histories relative to successful CO_2 storage, in R. C. Surdam, ed., Geological CO_2 storage characterization: Springer, Environmental Science and Engineering, 55–96.

Phan, S. and M. K. Sen, 2010, Porosity estimation from seismic data at Dickman Field, Kansas for carbon sequestration, 80th Annual International Meeting, SEG, Expanded Abstracts, 2299-2303.

Prasad, M., 1999, Correlating permeability with velocity using flow zone indicators: 69th Annual International Meeting, SEG, Expanded Abstracts, 184-187.

Shafer, L., 2013, Assessing injection zone fracture permeability through the identification of critically stressed fractures at the Rock Springs Uplift CO_2 sequestration site, SW Wyoming: MS Thesis, University of Wyoming.

Simm, R., and M. Bacon, 2014, Seismic Amplitude: An Interpreter's Handbook: Cambridge University Press.

Surdam, R. C., 2013, Geological CO_2 storage characterization: The key to deploying clean fossil energy technology: Springer.

Westphal, H., G. P. Eberli, L. B. Smith, G. M. Grammer, and J. Kislak, 2004, Reservoir characterization of the Mississippian Madison Formation, Wind River Basin, Wyoming: AAPG Bulletin, 88, 4, 405–432.

Wu, W., D. Grana, E. Campbell-Stone, and F. McLaughlin, 2015, Bayesian facies classification in a CO_2 sequestration study using statistical rock physics modeling of elastic and electrical properties: 85th Annual International Meeting, SEG, Expanded Abstracts, 2748-2753.

Appendix III

Seismic Reservoir Characterization

This facies classification study of the Rock Spring Uplift reservoir (Appendix I and Figure 1) includes: 1) the log-facies classification based on rock properties derived from well log data, core sample description and geologic information; and 2) the facies classification of geophysical data (for example, elastic properties) both at the well log and geophysical (seismic) scales. The methodology was assessed using a statistical contingency analysis to compare the two classifications. The rock physics study (Appendix II) allowed us to derive a facies classification in order to discriminate between different lithology and to investigate the feasibility of predicting petro-physical properties (porosity and permeability) with the help of seismic inversion.

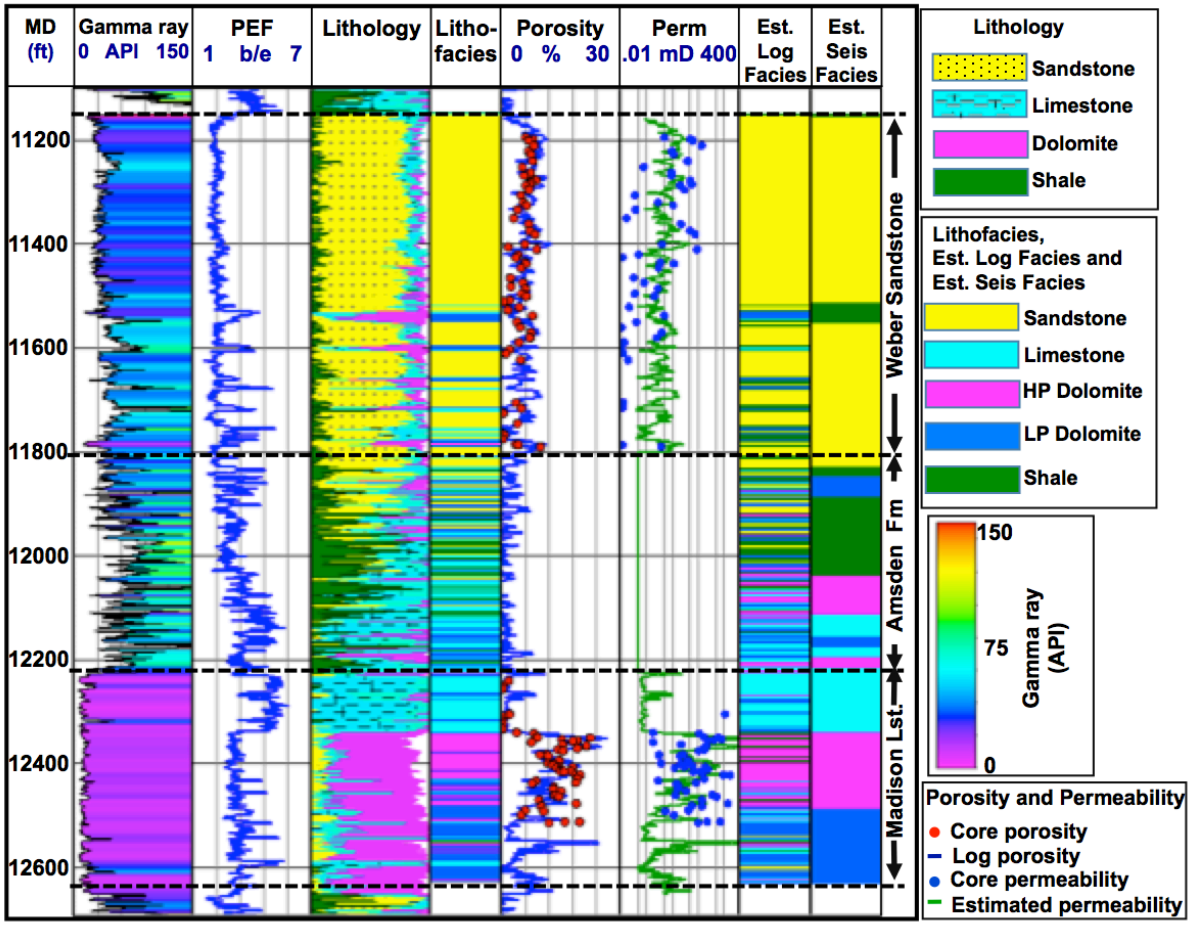

Figure 1 – Facies classification study.

In this study, we focus on the facies classification in the Weber and Madison formations only. We then analyzed the facies discriminability in the elastic domain. This study was performed at both the well log scale and at a lower resolution scale (using inverted geophysical properties). In the V_P-V_S domain, the sandstone cluster can be well discriminated from other facies, whereas the dolomite cluster is less distinguishable from shale and limestone (Figure 2). On the other hand, high porosity (HP) dolomite can be better discriminated from limestone and low porosity (LP) dolomite (porosity<10%) can be better resolved from shale (see Figure 2). Based on the classification described by Wu et al. (2015), we used a Bayesian approach to estimate the facies probability conditioned by geophysical properties. We also performed a sensitivity analysis on the choice of the set of properties by testing elastic properties only, and elastic and electrical properties jointly. For the elastic case, we also tested several combinations of elastic attributes, chosen from among P- and S-wave velocity, Poisson ratio, P-impedance, density, and AVO attributes. We show here the results obtained using P- and S-wave velocities. In Figure 1 (indicated as 'Est. Log Facies' and 'Est. Seis Facies'), we present two facies profiles estimated using the posterior probability $P(F \mid V_P, V_S)$ obtained using Bayes' rule. In Figure 1, 'Est. Log Facies' corresponds to the facies classification results on the well log resolution, whereas 'Est. Seis Facies' corresponds to the facies classification at seismic resolution. At the well log scale, the mismatch in facies predictions is generally due to the large facies overlap (Figure 2), whereas the misclassifications at the seismic scale are generally due to the low resolution of seismic data. By dividing dolomite into two sub-facies, the predicted elastic facies consistently match with the reference log facies in both formations.

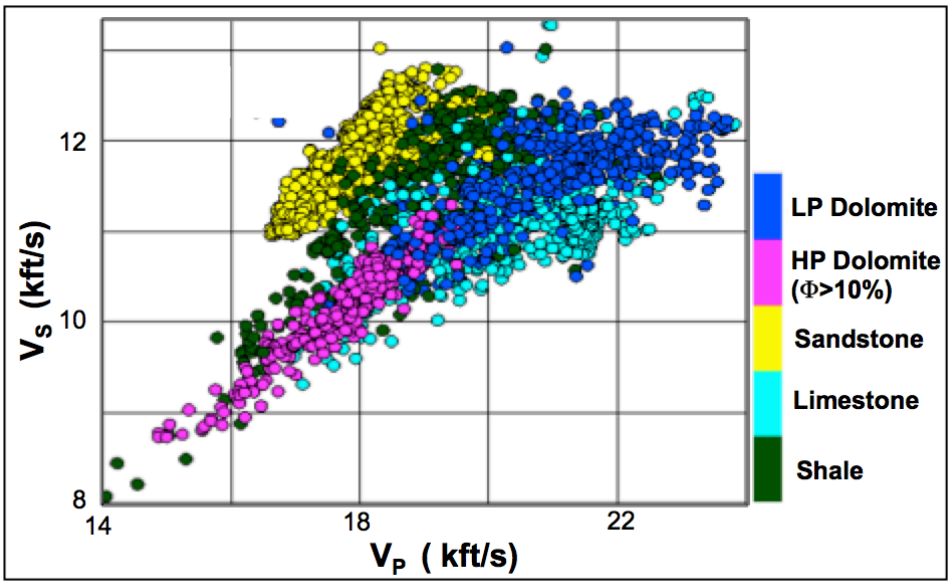

Figure 2 – Facies discrimination in the elastic domain.

SEISMIC INVERSION

Although the original RSU seismic data consisted of 245 inlines and 247 crosslines, low fold at the edges of the survey were not suitable for prestack waveform inversion (PWI). We therefore extracted a 3D sub-volume of 176 inlines and 176 crosslines over which the common midpoint (CMP) fold was adequate for PWI. This sub-volume covered an approximate area of 13 square miles.

The PWI method takes the normal moveout (NMO) uncorrected prestack seismic data as input and inverts for the isotropic elastic subsurface properties (V_p, V_s, and ρ). It uses a genetic algorithm (GA) as the search engine and the reflectivity method (Fuchs and Müller, 1971; Kennett, 1983) as implemented by Mallick and Frazer (1987, 1988, 1990, and 1991) for forward synthetic computation. Because RSU geology is structurally simple, the 1D assumption inherent to the reflectivity method was adequate once the 3D data were prestack time-migrated. Prior to running GA, prestack seismic data were processed through prestack time migration using a relative amplitude preservation (RAP) workflow, details of which can be found in Resnick

(1993) and Mallick (1999). Also note that for an inversion window as large as 2 seconds, such as ours, AVO-based inversion methods must account for wavelet variations over the window. AVO inverts for primary reflection only. Complex wave effects such as the short-period interbed multiples and mode-conversions etc., tend to have a filtering effect on data, especially at large angles, known as the stratigraphic filtering or the O'Doherty-Anstey effect (Banik et al., 1985a, b). Because AVO methods do not model this effect in the algorithm, they must account for the wavelet variations. The reflectivity method used in PWI on the other hand, models the O'Doherty-Anstey effect in the algorithm itself, and therefore does not require implementing any wavelet variation.

A genetic algorithm (GA) is a nonlinear global optimization method that uses the prior information on model parameters and the physics of the forward problem to compute synthetic data and match with the observed data to obtain the maximum likelihood function in the model space. The best set of models that satisfies the observation to a user-defined accuracy is then estimated from the likelihood function. At the start, GA generates a random population of initial models within a user-defined search window. For this reason, we first interpolated the P- and S-wave sonic and density log from the RSU #1 well over the geological horizons interpreted from the stacked seismic data and applied a 10 Hz high-cut filter to this interpolated model. We then defined a search window around this filtered model and generated our initial set of random models. Following generation of the random models, the next step of GA is computing synthetic seismograms and comparing them with observation to give each random model a measure of its fitness or objective. Following synthetic computation and matching, GA modifies the models using its main steps- reproduction (tournament selection), crossover, mutation, and update (elitism). Once the new set of models is generated, GA computes synthetic data, matches observed data, and modifies them again using its main steps. This entire process is repeated until a subset of models that best matches the observed data are obtained. Note that the GA runs sequentially over all CMP locations for the entire 3D data volume.

Figure 3 shows a comparison of the real well log of RSU#1 and PWI inversion results.

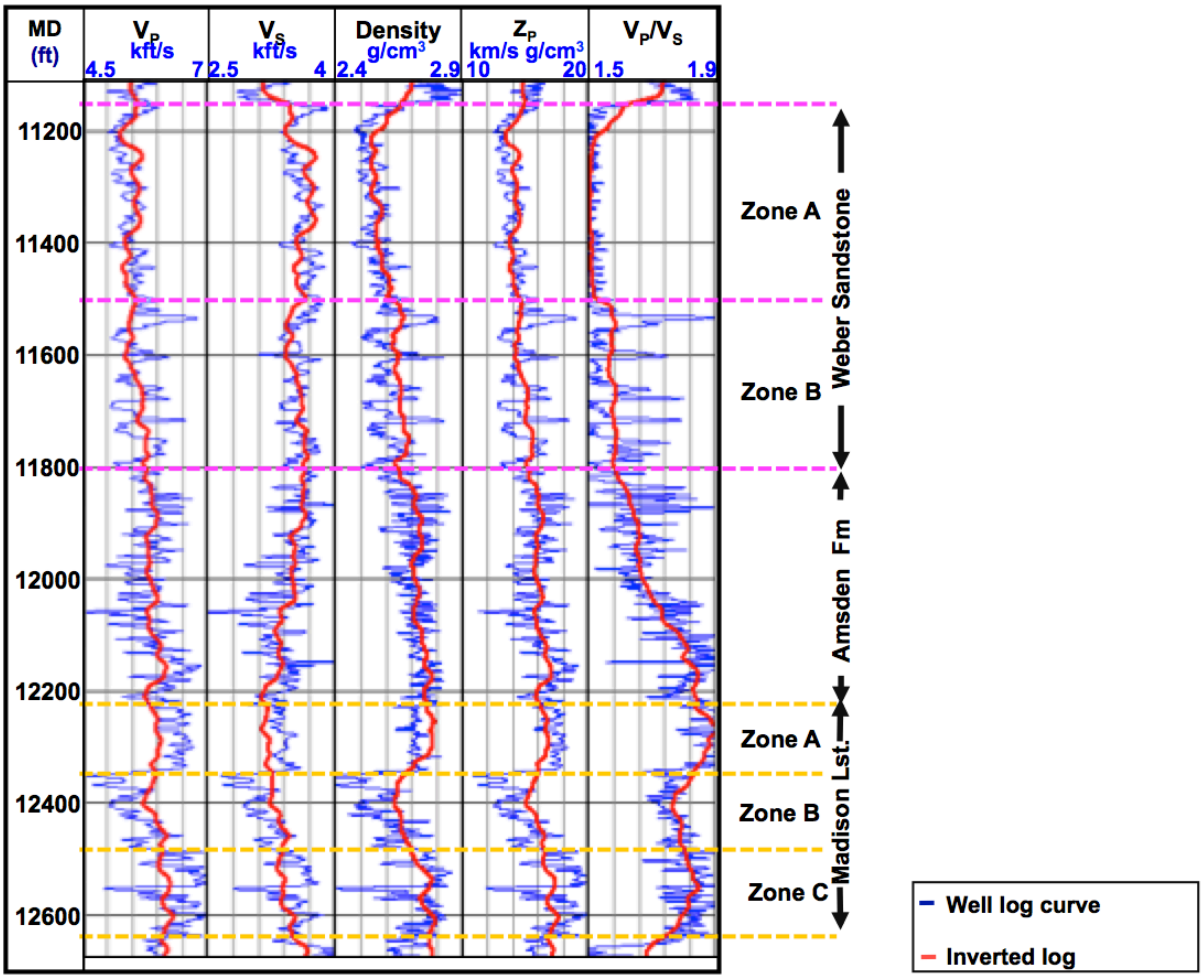

Figure 3 – Seismic inversion at the well location.

Figure 4 shows the inverted P- and S-wave velocity and density for one inline at the RSU #1 well location. Notice that our inversion captured different layer boundaries to a satisfactory resolution up to a depth of about 13,000 feet. Detailed stratigraphic features for the RSU area are easily distinguishable from the inverted models shown in Figure 4.

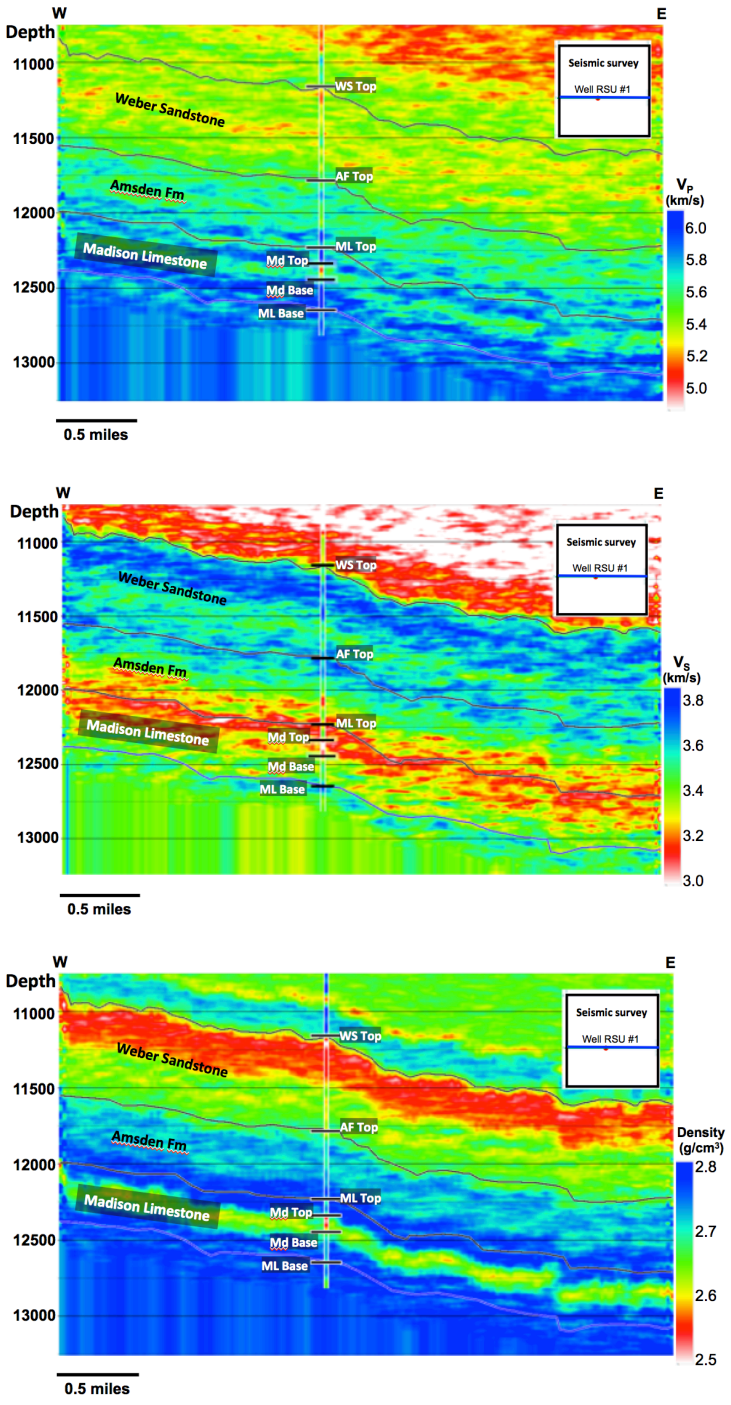

Figure 4 – Seismic inversion along a 2D section

SEISMIC RESERVOIR CHARACTERIZATION

In order to characterize the two potential CO_2 reservoirs, Weber Sandstone formation and Madison Limestone formation, we obtained a 3D porosity volume by applying the zone wise regression relation established in exploratory data analysis on well data on the inverted P-impedance. We utilized seismic horizons and applied two different regression relations in Weber Sandstone formation and Madison Limestone formation on the 3D volume, After obtaining the porosity volume (Figure 5, top), we applied the regression relation between porosity and permeability established from RSU #1 well core data on 3D porosity volume to obtain the 3D permeability volume (Figure 5, middle). In order to obtain facies volume (Figure 5, bottom), we extended our well log facies classification with Bayesian analysis to 3D. We used the 'Seis Facies' (Figure 1) as the guiding parameter for classification. We tried several combinations of V_P, V_S and density as input volumes. We found that V_P/V_S and Z_P provides the best results, which is consistent with 'Seis Facies'.

Figure 5 (top and middle) shows that the porosity as well as permeability in the Weber Sandstone is high in the top part and decreases in the bottom part. The variation of porosity and permeability in Weber Sandstone formation is smooth. The facies volume indicates that the Weber Sandstone is primarily comprised of sandstone facies. V_P/V_S ratio can also be used as a lithology indicator. Figure 5 indicates that Zone A (Figure 3), which is predominately eolian sandstone, has low V_P/V_S. On the other hand, Zone B (Figure 3) has relatively higher values of V_P/V_S than Zone A. In the Madison Limestone formation, Zone B (Figure 5, top and middle) has the highest porosity and permeability. Porosity and permeability vary smoothly in 3D. The predicted facies volume (Figure 5, bottom) indicates that the high porosity dolomite layer exists in the entire 3D volume and has minimal variation in thickness. In Zone C, the well log analysis

indicates the presence of low porosity dolomite (Figure 1), whereas the predicted facies volume at the well location shows it as a combination of limestone and low-porosity dolomite facies. Limestone and low porosity dolomite facies overlap on the V_P vs. V_S crossplot, which indicates that these two facies have similar characteristics and cannot be distinguished based on elastic properties.

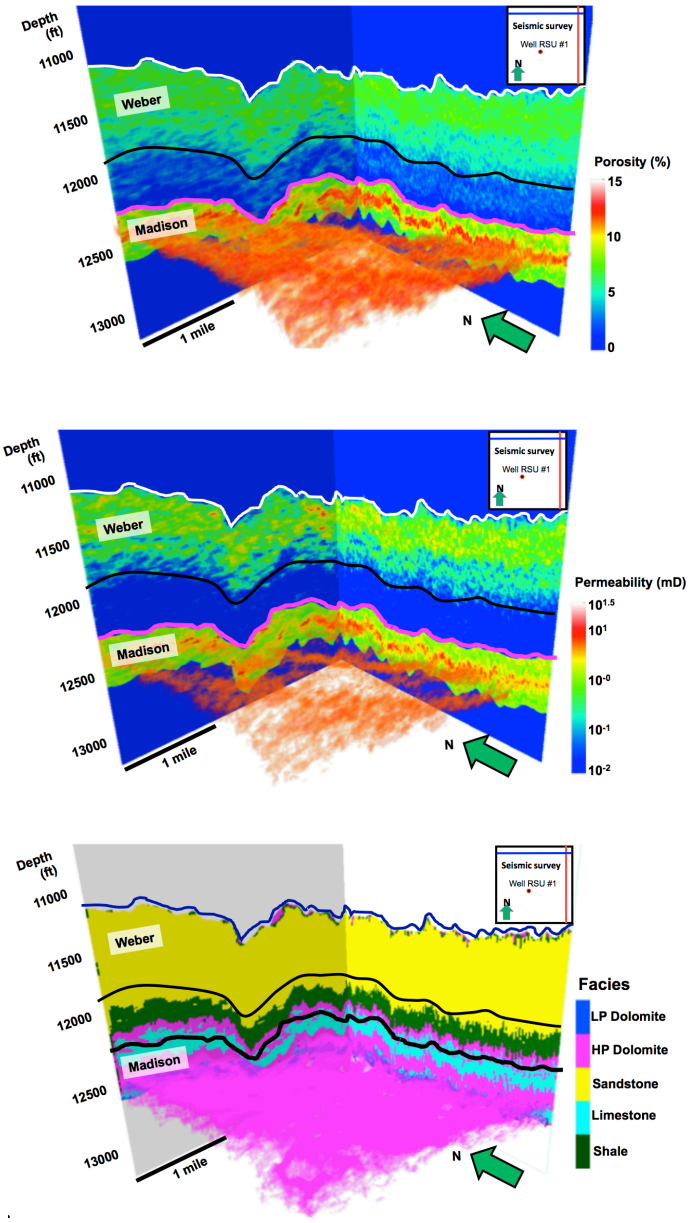

Figure 5 – Seismic reservoir characterization in the 3D volume: porosity, permeability, and facies.

REFERENCES

Campbell-Stone, E., R. Lynds, C. Frost, T. P. Becker, and B. Diem, 2010, The Wyoming carbon underground storage project: geologic characterization of the Moxa Arch and Rock Springs Uplift: Energy Procedia, **4**, 4656–4663.

Dickinson, W. R., M. A. Klute, M. J. Hayes, S. U. Janecke, E. R. Lundin, M. A. McKittrick, and M. D. Olivares, 1988, Paleogeographic and paleotectonic setting of Laramide sedimentary basins in the central Rocky Mountain region: Geological Society of America Bulletin, **100**, 1023- 1039.

Downton, J. E., and B. Roure, 2015, Interpreting azimuthal Fourier coefficients for anisotropic and fracture parameters: Interpretation, **3**, no. 3, ST9-ST27.

Frost, C. D., and A. C. Jakle, 2010, Geologic carbon sequestration in Wyoming: prospects and progress: Rocky Mountain Geology, **45**, no. 2, 83-91.

Gray, D., P. Anderson, J. Logel, F. Delbecq, D. Schmidt, and R. Schmid, 2012, Estimation of stress and geomechanical properties using 3D seismic data: First Break, **30**, 59-68.

Grechka, V., and I. Tsvankin, 1998, 3-D description of normal moveout in anisotropic inhomogeneous media: Geophysics, **63**, no. 3, 1079-1092.

Grude, S., M. Landrø, and J. Dvorkin, 2013, Rock physics estimation of cement type and impact on the permeability for the Snøhvit field, the Barents Sea: 83rd Annual International Meeting, SEG, Expanded Abstracts, 2670-2674.

Hampson, D. P., B. H. Russell, and B. Bankhead, 2005, Simultaneous inversion of pre-stack seismic data: 75th Annual International Meeting, SEG, Expanded Abstracts, 1633-1637.

Jenner, E., 2002, Azimuthal AVO: Methodology and data examples: The Leading Edge, **21**, no. 8, 782-786.

Jiao, Z., and R.C. Surdam, 2013, Advances in estimating the geologic CO_2 storage capacity of the Madison Limestone and Weber Sandstone on the Rock Springs Uplift by utilizing detailed 3-D reservoir characterization and geologic uncertainty reduction, *in* R. C. Surdam, ed., Geological CO_2 storage characterization: Springer, Environmental Science and Engineering, 191- 231.

Johnson, E. A., 2005, Geologic assessment of undiscovered oil and gas resources in the Phosphoria total petroleum system, southwestern Wyoming province, Wyoming, Colorado, Utah, *in* USGS Southwestern Wyoming Province Assessment Team, ed., Petroleum Systems and Geologic Assessment of Oil and Gas in the Southwestern Province, Wyoming, Colorado, and Utah: U. S. Geological Survey.

Johnson, P. L., and D. W. Anderson, 2009, Concurrent growth of uplifts with dissimilar orientations in the southern Green River Basin, Wyoming: Implications for Paleocene–Eocene patterns of foreland shortening: Rocky Mountain Geology, **44**, no. 1, 1–16.

Lang, X., and D. Grana, 2015, Bayesian rock physics inversion of acoustic and electrical properties for rock-fluid property estimation: 85th Annual International Meeting, SEG, Expanded Abstracts, 2931-2935.

Li, T., and S. Mallick, 2015, Multicomponent, multi-azimuth pre-stack seismic waveform inversion for azimuthally anisotropic media using a parallel and computationally efficient non-dominated sorting genetic algorithm: Geophysical Journal International, **200**, no. 2, 1134-1152.

Mallick, S., 1999, Some practical aspects prestack waveform inversion using a genetic algorithm: an example from the east Texas Woodbine gas sand: Geophysics, **64**, no. 2, 326-336.

Mallick, S., and S. Adhikari, 2015, Amplitude-variation-with-offset and prestack-waveform inversion: A direct comparison using a real data example from the Rock-Springs Uplift, Wyoming, USA: Geophysics, **80**, no. 2, B45-B59.

Mallick, S., D. Mukherjee, L. Shafer, and E. Campbell-Stone, 2016, Azimuthal anisotropy analysis of P-wave seismic data and estimation of the orientation of the in situ stress fields – an example from the Rock-Springs uplift, Wyoming, USA: under review in Geophysics.

McLaughlin, J. F., and M. Garcia-Gonzalez, 2013, Detailed geologic characterization of core and well data from the Weber and Madison Formations and associated seals at a potential CO_2 sequestration site in southwest Wyoming: Defining the lithologic, geochemical, diagenetic, and burial histories relative to successful CO_2 storage, *in* R. C. Surdam, ed., Geological CO_2 storage characterization: Springer, Environmental Science and Engineering, 55–96.

Mukherjee, D., S. Mallick, L. Shafer, and E. Campbell-Stone, 2012, Estimation of in-situ stress fields from P-wave seismic data: 82nd Annual International Meeting, SEG, Expanded Abstracts, 1-5.

Padhi, A., and S. Mallick, 2014, Multicomponent pre-stack seismic waveform inversion in transversely isotropic media using a non-dominated sorting genetic algorithm: Geophysical Journal International, **196**, no. 3, 1600-1618.

Pafeng, J., S. Mallick, and H. Sharma, 2015, 3-D prestack waveform inversion-a real data example: 85th Annual International Meeting, SEG, Expanded Abstracts, 3413-3419.

Phan, S. and M. K. Sen, 2010, Porosity estimation from seismic data at Dickman Field, Kansas for carbon sequestration, 80th Annual International Meeting, SEG, Expanded Abstracts, 2299-2303.

Rüger, A., 1998, Variation of P-wave reflectivity with offset and azimuth in anisotropic media: Geophysics, **63**, no. 3, 935-947.

Shafer, L., 2013, Assessing injection zone fracture permeability through the identification of critically stressed fractures at the Rock Springs Uplift CO_2 sequestration site, SW Wyoming: MS Thesis, University of Wyoming.

Surdam, R. C., 2013, Geological CO_2 storage characterization: The key to deploying clean fossil energy technology: Springer.

Wu, W., D. Grana, E. Campbell-Stone, and F. McLaughlin, 2015, Bayesian facies classification in a CO2 sequestration study using statistical rock physics modeling of elastic and electrical properties: 85th Annual International Meeting, SEG, Expanded Abstracts, 2748-2753.

Appendix IV

List of Rock Samples Selected/Obtained for CO_2-Water-Rock Experiments

Zone 1
Weber Sandstone
Facies: Aeolian sandstone
Lithology: quartz arenite, higher porosity than most Weber, thin section shows dolomite in crossbeds
Depth: 11,200–11,240

Zone 2a
Weber Sandstone
Facies: Aeolian sandstone
Lithology: quartz arenite, lightly crossbedded, moderate porosity
Depth: 11,570–11,590

Zone 2b (alternate option)
Weber Sandstone
Facies: Aeolian sandstone
Lithology: quartz arenite, lightly crossbedded, moderate porosity
Depth: 11,400–11,420

Zone 3
Madison Limestone
Facies: Limestone/Dolomite
Lithology: intragranular porosity, must avoid stylolites and fractures
Depth: 12,350–12,405

Zone 4a
Madison Limestone
Facies: Limestone/Dolomite
Lithology: moldic/vuggy porosity; must avoid chert, stylolites and fractures
Depth: 12,420–12,430

Zone 4b
Madison Limestone
Facies: Limestone/Dolomite
Lithology: moldic/vuggy porosity; visible porosity, must avoid fractures
Depth: 12,470–12,480

Appendix V

Analyses and Results Studied in the CO_2-Water-Rock Experiments

Part I. Geochemical-Mineralogic Experiments

1 Introduction

A total of four experiments were performed to evaluate CO_2-water-rock reaction, two for the Madison Limestone and two for the Weber Sandstone. For both formations, one baseline experiment (rock + formation water) and one injection experiment (rock + formation water + injected supercritical CO_2) were conducted. Table 1 summarizes design parameters and other pertinent information for each of these experiments.

2 Methods and Materials

2.1 Approach

The selection of pressure and temperature (Table 1) were based on data for core from the RSU #1 presented in Surdam (2013) and Shafer (2013). The determination of reaction times and water-rock ratios were based on experience with previous CO_2-water-rock experiments as described in Kaszuba et al. (2003, 2005), Chopping and Kaszuba (2012), Marcon (2013), and unpublished data. Reaction times were selected to allow experiments to approach a steady state to the extent possible.

2.2 Experimental Apparatus and Procedure

The experiments were conducted in a rocking autoclave, also known as a rocker bomb, using established methods for hydrothermal experiments (Seyfried et al., 1987). This equipment allows external control and monitoring of temperature and pressure. Estimated maximum temperature and pressure uncertainty is ± 1°C and ± 0.6 MPa, respectively. Our apparatus is equipped with a Dickson-type reaction cell consisting of a flexible 240 cm^3 gold cell, titanium head, and titanium capillary tube ported with a metered sampling valve.

Water samples were periodically withdrawn from the reaction cell without perturbing the ongoing experiment. Water samples were rapidly cooled and depressurized to ambient conditions in a few seconds and subsequently analyzed. Retrograde reactions with minerals that may occur during a prolonged quench process were consequently avoided and solution composition was analyzed along a reaction pathway. The minerals and quenched water were also analyzed after the experiments were terminated.

Table 1: Experimental Parameters

Experiment	Madison Ls + Fm Water	Madison Ls + Fm Water + $scCO_2$	Weber Ss + Fm Water	Weber Ss + Fm Water + $scCO_2$
Temperature (°C)	94	94	90	90
Pressure (MPa), pre-$scCO_2$ Injection	37	37	33	33
Pressure (MPa), post-$scCO_2$ Injection	NA	45	NA	42.5
Rock Mass[a] (g)	15.6	11.1	14.0	12.3
Mass of Fm Water[b] (g)	326.8	223.2	277.4	249.5
Initial Fm Water/Rock Ratio[c]	21.0/1	20.0/1	19.8/1	20.3/1
Fm Water-Rock Reaction Time (hours)[d]	604.8	1008.8	1312.3	1436.2
Mass $scCO_2$ injected (g)	NA	12.7	NA	18.5
Millimole $scCO_2$ injected	NA	289	NA	420
Mass of Remaining Fm Water[e] (g)	NA	159.7	NA	188.4
Fm Water/$scCO_2$/Rock Ratio[f]	NA	14.4/1.1/1	NA	15.3/1.5/1
Water-Rock-$scCO_2$ Reaction Time (hours)[g]	NA	359.6	NA	1008.5
Total Reaction Time (hours)[h]	604.8	1368.4	1312.3	2444.7

Notes:
[a]Rock mass and [b]mass of formation water in reaction cell at beginning of experiment.
[c]Ratio of mass of brine to the mass of minerals at the beginning of the experiment.
[d]Reaction time between formation water and rock before injecting supercritical CO_2.
[e]Mass of formation water remaining in the experiment before injecting supercritical CO_2.
[f]Ratio of mass of formation water to supercritical CO_2 to rock immediately after injecting the supercritical CO_2. The mass of CO_2 removed during subsequent sampling of formation water (as dissolved CO_2) is negligible compared with the mass of CO_2 injected.
[g]Reaction time after injecting supercritical CO_2.
[h]Total reaction time of experiment.
Ls = Limestone
Ss = Sandstone
$scCO_2$ = supercritical CO_2
Fm = formation
NA = not applicable

Carbon dioxide was introduced into the reaction cell for two of the experiments using a Teledyne-ISCO 260D syringe pump. At experimental pressures and temperatures, carbon dioxide is a supercritical fluid that freely reacts. Excess carbon dioxide was injected to ensure that two immiscible fluid phases (Duan et al., 2006; Shyu et al., 1997; Takenouchi and Kennedy, 1964), a constant carbon dioxide fugacity, and carbon dioxide saturation of water existed for the duration of each experiment. Injection of carbon dioxide increased pressure in direct proportion to the mass of supercritical carbon dioxide added to the experiment. In these closed-system experiments, pressure subsequently decreased due to dissolution of supercritical carbon dioxide into brine. The described procedure is consistent with previous investigations that evaluate supercritical carbon dioxide-water-rock reactions using rocking autoclaves (Kaszuba et al., 2003; Kaszuba et al., 2005; Palandri and Kharaka, 2005; Rosenbauer et al., 2005).

2.3 Materials

Materials are described in Appendix IV (List of Rock Samples Selected/Obtained for CO_2-Water-Rock Experiments). For our experiments, we used Madison Limestone from Zone 4a (basal dolostone, depth interval of 12,420–12,430 feet) and Weber Sandstone from Zone 1 (aeolian sandstone, depth interval of 11, 200–11,206 feet). The Madison Limestone used in these experiments is a dolostone that is comprised predominantly of the mineral dolomite. In addition to dolomite, minor amounts of quartz, anhydrite, calcite, and pyrite are present. The Weber Sandstone used in these experiments is an eolian quartz sandstone. It is predominantly comprised of quartz (~95%); the remainder of the rocks consists of feldspar, clay, pyrite, and carbonate cement.

Fragments and powders (25 wt% fragments and 75 wt% powders) were used in each experiment. Use of fragments promoted recovery of material of sufficient size that reaction textures could be evaluated. Use of powders enhances reactivity and maximizes reaction rates. Fragments were 0.5 to 3.0 mm in size. Powders were prepared by grinding in a ceramic mortar and pestle and sieving with a 45 μm sieve.

Formation water was prepared using laboratory-grade salts. Nanopure water (18 Ω) was sparged with argon gas prior to synthesis in order to remove dissolved gasses, particularly dissolved

oxygen. The bulk composition and ionic strength of the water were based on analyses of formation waters presented for the RSU #1 in Surdam (2013). To minimize mineral reaction with the brine before injection of carbon dioxide, the major element composition of brine in equilibrium with each rock type at experimental conditions was calculated. Quantities of iron and aluminum required to bring the water into equilibrium with the rock are exceedingly small and difficult to measure accurately. Therefore, the brine was synthesized without iron or aluminum. Despite these efforts, the water was not perfectly pre-equilibrated with the minerals in each experiment. Lack of equilibrium was due to solid solution in the minerals and weighing errors incurred during water synthesis.

2.4 Analytical Methods

A titanium filter is installed in the head of the reaction cell to filter the water samples. To prevent mineral precipitation, the samples for cation analysis were acidified to pH 2 using trace metal grade nitric acid. Dissolved major cations (Na, K, Ca, Mg, Fe, Mn, and SiO_2) were determined by inductively coupled plasma optical emission spectroscopy (ICP-OES), dissolved minor cations (e.g., Cu and Sr) by inductively coupled plasma mass spectroscopy (ICP-MS), and dissolved anions (Cl and SO_4) by ion chromatography. The pH was measured using an Orion pH meter and Ross microelectrode on water samples cooled to 25°C and depressurized to 0.1 MPa. Total dissolved inorganic carbon (as carbon dioxide) was determined for in-situ conditions by analyzing a sample of water plus exsolved gas collected in a glass gas-tight syringe. The analysis was performed using coulometric titration (Huffmann, 1977). Total dissolved inorganic carbon (as carbon dioxide) was also determined on degassed brine samples cooled to 25°C and depressurized to 0.1 MPa. Minerals were analyzed using optical microscopy, high resolution field emission scanning electron microscopy (FE-SEM), energy dispersive spectra (EDS), X-ray diffraction (XRD), and ICP-OES and ICP-MS after acid digestion.

2.5 Geochemical Calculations

Geochemical calculations were performed using The Geochemist's Workbench® version 10 (Bethke and Yeakel, 2009), the b-dot ion association model, and the resident thermodynamic database thermo.com.V8.R6+.dat. Thermo.com.V8.R6+.dat was chosen because it contains the most comprehensive data compilation for relevant minerals, aqueous complexes and gasses.

Geochemical calculations were used to evaluate the geochemistry of individual samples collected from each experiment. These calculations determined in-situ pH, saturation state, and activities of aqueous species and minerals in reacted brine. In-situ pH for samples of brine that did not react with supercritical carbon dioxide were determined by speciating the fluid. In-situ pH for samples of brine that reacted with supercritical carbon dioxide were determined using the method of Newell et al. (2008). This method used "benchtop" pH and dissolved inorganic carbon, the chemical analysis, and in-situ dissolved inorganic carbon to calculate in-situ pH.

3 Results and Discussion

Aqueous geochemical data for the experiments, including charge balance and analytical uncertainties, are reported in Tables 2 and 3. Charge balance errors are within acceptable limits (≤12%). In one exception, the charge balance for the sample collected from the Madison Limestone-formation water-supercritical carbon dioxide experiment at 1129.1 hours is 23.3% because dissolved carbon dioxide for this sample was not analyzed due to equipment problems. Select aqueous data are plotted as a function of time (Figures 1-6) and discussed in the following section.

Table 2: Aqueous major and minor element geochemistry for Madison Limestone experiments

Madison Limestone + Formation Water (mmol/kg)

Comment	Sample	Time (hours)	pH (ex situ)	pH (in situ)	SiO_2 (aq)	Na	K	Ca	Sr	Mg	Fe	Al	Cl	SO_4	$\sum CO_2$ (ex situ)	$\sum CO_2$ (in situ)	Charge Balance
Initial Water	0	0	6.3	--	0.03	1278	94.4	5.81	6.06E-04	0.94	6.22E-04	0.004	1600	15.5	5.1	NA	-7.7
	1	25.4	6.6	6.6	0.12	1317	96.2	7.75	2.51E-02	1.47	1.68E-03	0.007	1544	18.6	5.1	5.5	-4.3
	2	45.6	6.7		0.12	1349	96.3	7.97	2.85E-02	1.54	7.09E-04	0.005	1486	18.0	6.5	5.7	-1.4
	3	124.2	6.7	6.5	0.15	1139	86.8	7.40	2.78E-02	1.51	1.18E-03	0.005	1531	19.0	5.3	6.0	-10.9
	4	190.9	6.6	6.5	0.16	1213	93.7	7.75	2.91E-02	1.62	1.52E-03	0.005	1602	19.8	5.5	6.2	-10.1
	5	384.3	6.6	6.5	0.18	1241	94.8	7.86	2.92E-02	1.70	2.14E-03	0.007	1706	21.1	5.2	5.9	-11.9
	6	604.8	6.6	6.4	0.19	1194	91.6	7.86	2.93E-02	1.73	2.32E-03	0.007	1516	18.5	5.1	5.9	-7.9
	7	650.9	6.1	4.4	0.25	1210	94.9	15.26	3.25E-02	6.35	2.84E-02	0.008	1468	18.2	36.8	NA	-4.6
Quench	Q		7.4	7.4	0.22	1224	96.9	13.96	3.15E-02	6.21	1.21E-02	0.005	1415	17.1	33.7	NA	-2.6
Uncertainty	--		±0.1	±0.1	±0.002	±54	±2.68	±0.096	±1.1E-05	±0.021	1.1E-04	±4.7E-05	±7	±0.34	±10%	±10%	--

Madison Limestone + Formation Water + Supercritical CO_2 (mmol/kg)

Comment	Sample	Time (hours)	pH (ex situ)	pH (in situ)	SiO_2 (aq)	Na	K	Ca	Sr	Mg	Fe	Al	Cl	SO_4	$\sum CO_2$ (ex situ)	$\sum CO_2$ (in situ)	Charge Balance
Initial Water	0	0	6.2	--	0.02	1300	95.2	5.78	6.12E-04	0.94	3.27E-04	0.004	1518	15.1	NA	NA	-4.3
	1	72.3	6.5	6.3	0.04	1233	96.0	8.44	2.76E-02	1.56	2.72E-02	0.006	1684	20.5	6.7	8.7	-11.6
	2	96.1	6.6	6.5	0.04	1386	96.5	8.56	2.89E-02	1.59	3.67E-03	0.007	1510	18.5	7.1	7.8	-0.8
	3	169.8	6.5	6.5	0.05	1457	98.6	8.70	3.04E-02	1.71	7.95E-03	0.005	1742	21.0	6.7	7.5	-5.7
	4	266.4	6.5	NA	0.06	1211	96.2	8.48	3.03E-02	1.73	4.73E-03	0.006	1506	18.7	8.3	6.9	-6.8
	5	432.0	6.5	6.5	0.07	1158	89.6	8.04	2.92E-02	1.68	5.60E-02	0.007	1523	19.3	7.0	7.6	-9.5
	6	846.0	6.5	6.4	0.09	1249	98.0	8.69	3.21E-02	1.89	5.27E-03	0.006	1689	21.2	6.7	7.4	-11.1
	7	1008.8	6.6	6.5	0.10	1231	96.1	8.56	3.12E-02	1.85	5.50E-03	0.006	1627	20.4	7.0	7.9	-9.9
inject CO2																	
	8	1033.2	6.3	4.5	0.11	1208	92.2	15.72	3.30E-02	6.76	1.95E-02	0.007	1528	19.0	44.5	589	-6.8
	9	1056.2	6.1	4.9	0.12	1233	94.7	16.36	3.34E-02	7.52	2.72E-02	0.007	1560	19.2	50.0	577	-6.8
	10	1129.1	6.2	5.0	0.14	1413	104.3	12.40	3.27E-02	8.79	1.23E-03	0.003	2491	16.4	56.6	NA	-23.3
	11	1226.4	6.3	4.6	0.14	1297	94.0	16.96	3.33E-02	8.44	7.15E-02	0.007	1640	20.4	50.7	555	-6.9
	12	1392.8	6.3	5.0	0.16	1252	97.6	17.75	3.41E-02	8.98	4.12E-02	0.006	1524	19.0	56.5	568	-4.7
Quench	Q		6.3	6.3	0.16	1331	100.2	17.61	3.43E-02	8.97	2.72E-02	0.005	1498	20.5	56.1	NA	-1.4
Uncertainty	--		±0.1	±0.1	±0.002	±54	±0.34	±0.096	±1.1E-05	±0.021	1.1E-04	±4.7E-05	±7	±0.34	±10%	±10%	--

Table 3: Aqueous major and minor element geochemistry for Weber Sandstone experiments

Weber Sandstone + Formation Water (mmol/kg)

Comment	Sample	Time (hours)	pH (ex situ)	pH (in situ)	SiO_2 (aq)	Na	K	Ca	Sr	Mg	Fe	Al	Cl	SO_4	$\sum CO_2$ (ex situ)	$\sum CO_2$ (in situ)	Charge Balance
Initial Water	0	0	8.0	6.9	0.13	1642	44.0	5.13	9.39E-04	0.69	1.32E-03	0.007	1341	42.5	NA	NA	9%
	1	14.2	7.7	7.2	0.10	1487	40.7	3.50	6.70E-04	0.54	1.20E-03	0.006	1194	40.7	1.1	NA	9%
	2	87.6	7.7	7.1	0.10	1735	46.4	4.17	6.38E-04	0.63	6.84E-04	0.004	1594	52.9	1.2	NA	2%
	3	470	7.2	7.1	0.10	1788	47.3	4.15	8.57E-04	0.65	1.71E-03	0.006	1343	43.8	1.1	1.5	12%
	4	763.8	6.7	6.9	0.10	2091	49.0	4.50	9.25E-04	0.68	1.18E-03	0.005	1836	62.0	1.6	2.2	4%
	5	1309.9	6.8	6.8	0.10	1693	41.5	4.23	1.00E-03	0.60	1.01E-03	0.005	1330	46.0	2.8	4.6	10%
Quench	Q		7.0		0.06	1814	39.9	4.03	8.29E-04	0.60	1.90E-03	0.005	2060	73.2	2.5	3.9	-9%

Weber Sandstone + Formation Water + Supercritical CO_2 (mmol/kg)

Comment	Sample	Time (hours)	pH (ex situ)	pH (in situ)	SiO_2 (aq)	Na	K	Ca	Sr	Mg	Fe	Al	Cl	SO_4	$\sum CO_2$ (ex situ)	$\sum CO_2$ (in situ)	Charge Balance
Initial Water	0	0	8.0	6.9	0.13	1642	44.0	5.13	9.39E-04	0.69	1.32E-03	0.007	1341	42.5	NA	NA	9%
	1	2.1	7.0	7.2	0.02	1884	9.7	0.89	6.00E-04	0.22	8.97E-03	0.007	1549	49.3	NA	NA	7%
	2	20.7	6.8	7.0	0.04	1706	23.3	2.29	5.77E-04	0.39	6.56E-03	0.005	1591	53.7	NA	NA	1%
	3	186.2	7.6	7.1	0.10	1590	43.7	4.06	7.07E-04	0.59	1.83E-02	0.005	1805	59.0	1.3	1.7	-8%
	4	354.8	7.9	7.1	0.07	1279	32.2	3.06	4.70E-04	0.45	3.07E-03	0.003	1235	39.3	2.0	1.9	0%
	5	715	7.7	7.1	0.10	1756	44.8	4.60	7.11E-04	0.67	5.02E-03	0.004	1307	44.2	1.4	0.0	13%
	6	1385.8	6.9	6.9	0.08	1480	38.4	3.54	7.01E-04	0.55	1.15E-02	0.005	1531	52.9	2.7	2.5	-4%
Inject CO2		1436.2															
	7	1440	5.8	4.0	0.08	1426	37.5	5.11	1.29E-03	1.36	7.58E-02	0.008	1497	48.6	4.8	396.7	-4%
	8	1462.4	5.9	5.0	0.08	1531	40.0	6.75	1.16E-03	2.65	2.89E-02	0.007	1218	38.5	7.9	62.1	10%
	9	1866	6.4	4.5	0.11	1740	45.5	10.98	1.80E-03	5.27	1.09E-01	0.017	1434	48.5	7.5	262.8	8%
	10	2442.4	6.1	4.5	0.10	1755	46.3	11.68	1.37E-03	5.95	5.90E-02	0.008	1745	57.9	8.8	274.5	-1%
Quench	Q		6.3		0.12	1798	48.7	12.18	1.67E-03	6.26	4.70E-02	0.010	1712	56.6	8.8	10.9	1%

3.1 Formation Water Chemistry and Integrity of Experiments

Sodium and chloride concentrations in the formation waters remained constant throughout the duration of all four experiments (Tables 2 and 3). Constant concentration of the conservative anion chloride in closed-system experiments such as ours indicates that the gold reaction cells maintained their integrity for the duration of each experiment.

3.2 pH of Formation Water

The pH of unreacted formation water in the two Madison Limestone experiments and the two Weber Sandstone experiments is ~6.2 and 8.0, respectively (measured at 25°C, see Tables 2 and 3 as well as Figures 1 and 2). Calculated in-situ pH stabilizes within 20 to 72 hours in the baseline experiments and prior to injection of carbon dioxide in the injection experiments, to a value of approximately 6.5 in the Madison Limestone experiments and 7.1 in the Weber Sandstone experiments.

Injection of supercritical carbon dioxide into the experiments abruptly decreases pH (Figures 1 and 2). This pH decrease is consistent with dissolution of supercritical carbon dioxide into brine and subsequent formation and dissociation of carbonic acid. In-situ pH decreased by 2 pH units (from pH 6.5 to pH 4.5) in the Madison Limestone injection experiment and by 2.9 pH units (from pH 6.9 to pH 4) in the Weber Sandstone injection experiments. In-situ pH remained within ~0.5 pH units of these values for the remainder of both experiments. These steady state in-situ pH values are similar to values calculated in published laboratory studies of supercritical carbon dioxide-water-rock interactions (Chopping and Kaszuba, 2012; Kaszuba et al., 2003, 2005; Rosenbauer et al., 2005).

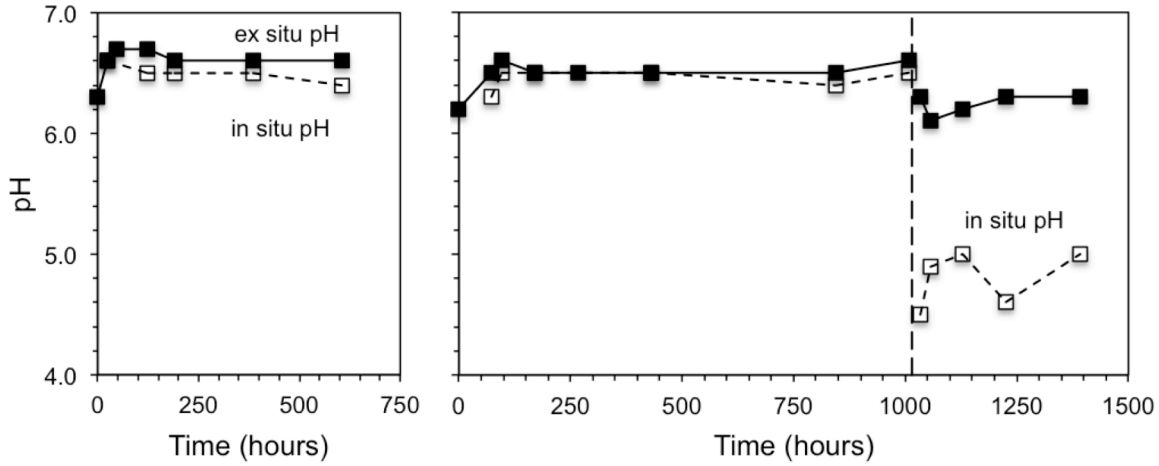

Figure 1. Evolution of pH of formation water as a function of time for the Madison Limestone-formation water experiment (chart on left) and the Madison Limestone-formation water-supercritical carbon dioxide ($scCO_2$) experiment (chart on right). The vertical dashed line in the chart on the right denotes the time at which $scCO_2$ was injected into the experiment. For both experiments, pH of cooled, degassed brine (ex situ pH, filled square) and calculated in-situ pH (square) are shown.

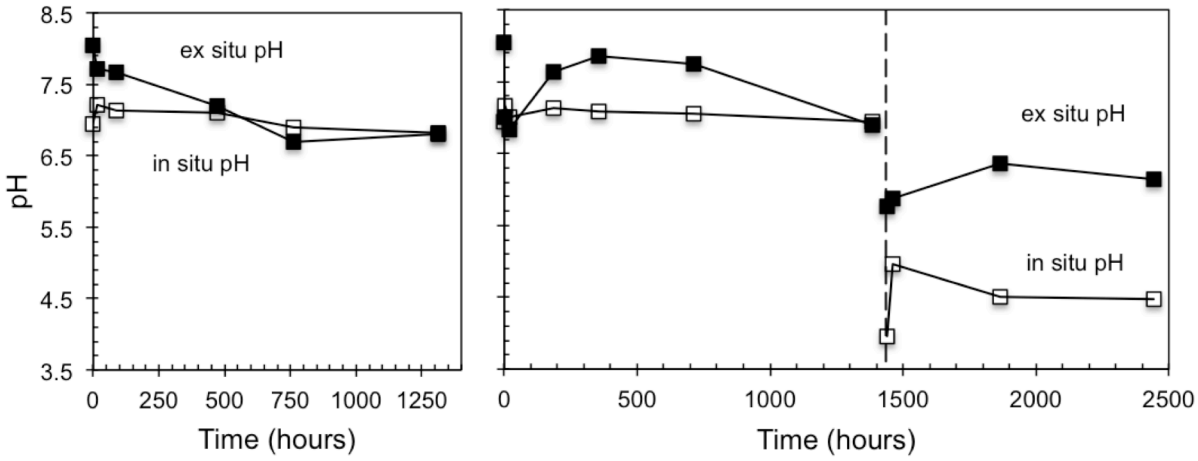

Figure 2. Evolution of pH of formation water as a function of time for the Weber Sandstone-formation water experiment (chart on left) and the Weber Sandstone-formation water-supercritical carbon dioxide ($scCO_2$) experiment (chart on right). The vertical dashed line in the chart on the right denotes the time at which $scCO_2$ was injected into the experiment. For both experiments, pH of cooled, degassed brine (ex situ pH, filled square) and calculated in-situ pH (square) are shown.

3.3 Formation Water Chemistry and Carbonate Minerals

The evolution of calcium, magnesium, and strontium in the experiments are important indicators of reaction of carbonate minerals. Carbonate mineral reactivity is important for the Madison Limestone because this formation is predominantly composed of dolomite. Although the Weber Sandstone is predominantly composed of quartz, the mineral calcite is an important cement that contributes to the mechanical integrity of this formation.

Calcium, magnesium, and strontium concentrations stabilize within the first ~100 hours of the Madison Limestone and Weber Sandstone baseline experiments and prior to injection of carbon dioxide into both injection experiments (Figures 3 and 4). The stabilization of calcium, magnesium, and strontium concentrations as well as in-situ pH suggests that the formation water achieved an approximate steady state within 100 hours, as controlled by the limestone and sandstone mineral assemblages (Chopping and Kaszuba, 2012; Chopping and Kaszuba, 2017; Kaszuba et al., 2003, 2005).

The evolution of iron can be an indicator of reaction of carbonate minerals; however, iron never achieved steady state concentrations in any of the four experiments (Figures 3 and 4). The multiple sources of iron in these rocks, especially pyrite, and the low concentrations of aqueous iron evolved during the experiments suggest that iron is not a reliable indicator for carbonate mineral reactivity in these rocks.

Injection of carbon dioxide produced significant changes in formation water chemistry in all four experiments. Calcium and magnesium concentrations increase in the first sample collected after carbon dioxide was injected into the Madison Limestone and Weber Sandstone injection experiments (Figures 3 and 4); calcium and magnesium concentrations stabilize within ~400 hours after injection. Iron concentrations also increased in response to injection of supercritical carbon dioxide, but iron never achieved steady state concentrations. Finally, strontium concentrations also increased in response to injection into the Weber Sandstone experiment but not the Madison Limestone experiment. The lack of response of strontium to injection of supercritical carbon dioxide into experiments containing carbonate rocks has been observed in other studies (e.g., Chopping and Kaszuba, 2012; Chopping and Kaszuba, 2017). The increase

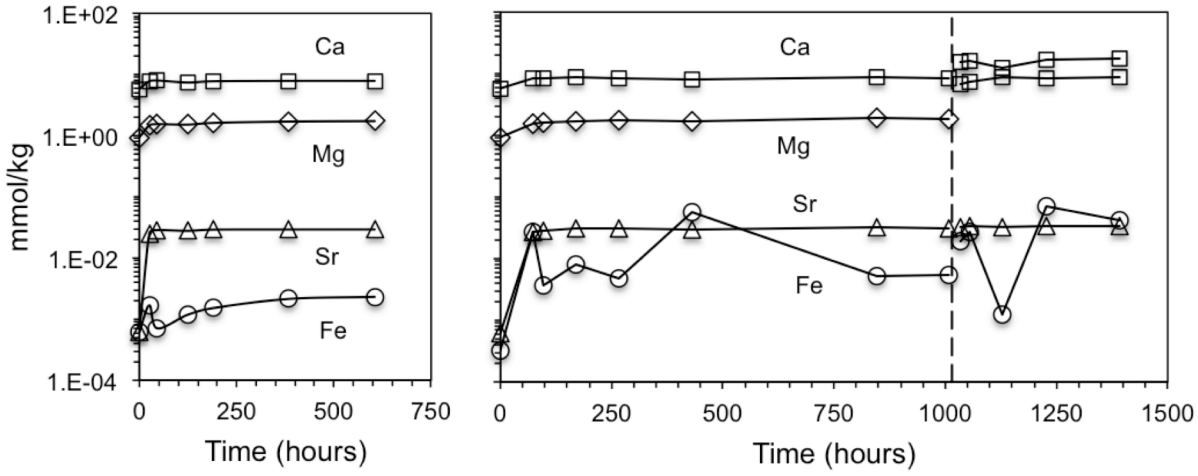

Figure 3. Geochemical evolution of formation water as a function of time for the Madison Limestone-formation water experiment (chart on left) and the Madison Limestone-formation water-supercritical carbon dioxide ($scCO_2$) experiment (chart on right). The vertical dashed line in the chart on the right denotes the time at which $scCO_2$ was injected into the experiment. Log concentration of calcium (square), magnesium (diamond), strontium (triangle), and iron (circle) are depicted.

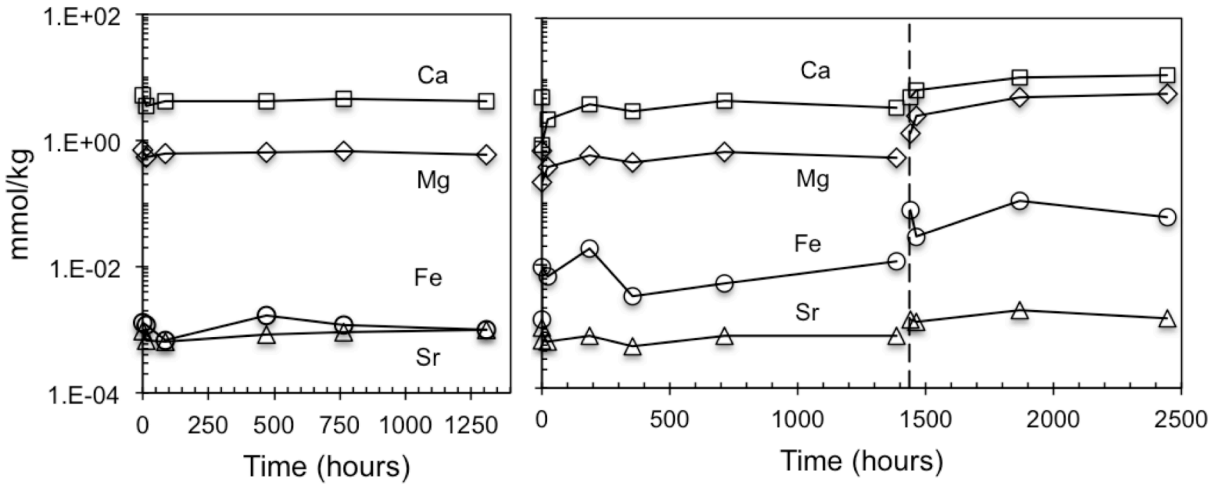

Figure 4. Geochemical evolution of formation water as a function of time for the Weber Sandstone-formation water experiment (chart on left) and the Weber Sandstone-formation water-supercritical carbon dioxide ($scCO_2$) experiment (chart on right). The vertical dashed line in the chart on the right denotes the time at which $scCO_2$ was injected into the experiment. Log concentration of calcium (square), magnesium (diamond), strontium (triangle), and iron (circle) are depicted.

in calcium and magnesium concentrations suggests that carbonate minerals dissolved by reaction with formation water, behavior consistent with the decrease of in-situ pH (Figures 1 and 2) that accompanied injection of supercritical carbon dioxide and concomitant dissolution of carbon dioxide into the brine.

3.4 Formation Water Chemistry and Silicate Minerals

The evolution of silica and aluminum in the experiments are important indicators of reaction of silicate minerals. Although the Madison Limestone is predominantly composed of dolomite, the accessory quartz (and thus the evolution of aqueous silica) may provide important clues as to the reactivity of the rock. Silicate mineral reactivity is potentially important for the Weber Sandstone because of the accessory silicate minerals feldspar and clay that are present in addition to the abundant quartz. Aqueous aluminum can provide important clues as to the reaction of feldspar and clays.

Silica concentrations increase continuously and do not stabilize within the Madison Limestone baseline experiment or prior to injection of carbon dioxide into the Madison Limestone injection experiment (Figure 5). Aqueous silica continues to increase, and at a greater rate, after injection of carbon dioxide into the Madison Limestone injection experiment.

In contrast, silica concentrations stabilize within ~24 hours in the Weber Sandstone baseline experiment (Figure 6). Prior to injection of carbon dioxide into the Weber Sandstone injection experiment, the concentrations of silica vary around the same steady state value (0.1 mmol/kg) as observed in the Weber Sandstone baseline experiment. This phenomenon is likely an experimental artifact as opposed to a geochemical process (Kaszuba et al., 2003, 2005), and we interpret silica concentrations in the Weber Sandstone injection experiment as being at steady state prior to injection of carbon dioxide. Silica concentrations rebound after injection of carbon dioxide into the Weber Sandstone injection experiment (Figure 6) but do not display the continuous increase observed in the Madison Limestone injection experiment (Figure 5).

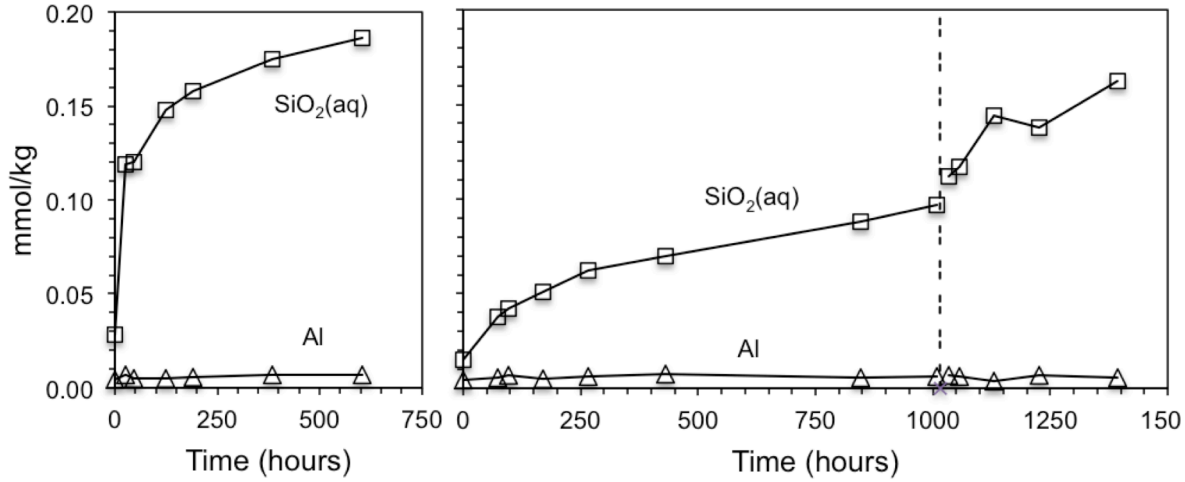

Figure 5. Geochemical evolution of formation water as a function of time for the Madison Limestone-formation water experiment (chart on left) and the Madison Limestone-formation water-supercritical carbon dioxide ($scCO_2$) experiment (chart on right). The vertical dashed line in the chart on the right denotes the time at which $scCO_2$ was injected into the experiment. Concentration of silica (square) and aluminum (triangle) are depicted.

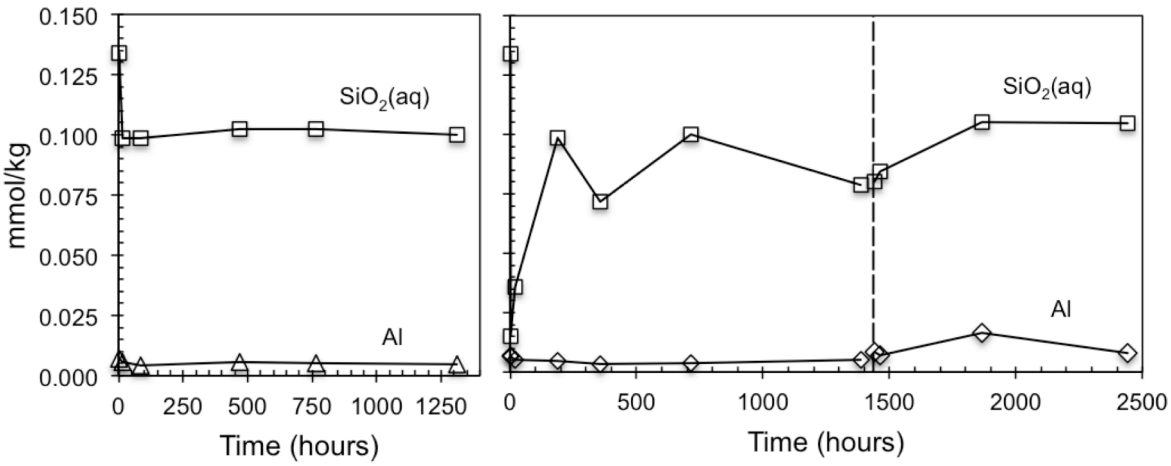

Figure 6. Geochemical evolution of formation water as a function of time for the Weber Sandstone-formation water experiment (chart on left) and the Weber Sandstone-formation water-supercritical carbon dioxide ($scCO_2$) experiment (chart on right). The vertical dashed line in the chart on the right denotes the time at which $scCO_2$ was injected into the experiment. Concentration of silica (square) and aluminum (triangle) are depicted.

Aluminum concentrations stabilize within the first ~24 hours in both the Madison Limestone and Weber Sandstone baseline experiments (Figures 5 and 6). Injection of carbon dioxide has no effect on the concentration of aluminum in the Madison Limestone injection experiment. Aluminum concentrations are not stable after injection of carbon dioxide into the Weber Sandstone injection experiment. This phenomenon is likely an experimental artifact due to the difficult of obtaining aqueous aluminum data (Kaszuba et al., 2003, 2005), and we interpret aluminum concentrations in the Weber Sandstone injection experiment as being at steady state after injection of carbon dioxide.

4 Summary and Conclusions

This experimental investigation evaluates carbon dioxide-water-rock reactions and processes in two reservoir rocks of the Rock Springs Uplift: the Madison Limestone and the Weber Sandstone. This information provides foundational understanding for potential impacts of carbon dioxide-water-rock reactions on geomechanical and petrophysical properties of these reservoir rocks. The following are concluded from this investigation:

1) In-situ pH stabilizes within 20 to 72 hours in baseline experiments and prior to injection of carbon dioxide into injection experiments, to a value of approximately 6.5 in the Madison Limestone experiments and 7.1 in the Weber Sandstone experiments.
2) In-situ pH decreases by ~2 to ~3 pH units in the formation waters of the Madison Limestone and the Weber Sandstone, respectively, due to injection of supercritical carbon dioxide. pH remains at these lower values for the duration of the experiments (100s of hours).
3) Calcium and magnesium concentrations stabilize within the first ~100 hours of the Madison Limestone and Weber Sandstone baseline experiments and prior to injection of carbon dioxide into both injection experiments. Calcium and magnesium concentrations increase in the first sample collected after carbon dioxide was injected into both injection experiments and stabilize within ~400 hours after injection. Carbonate mineral reactivity is greatest within these time intervals and diminishes afterwards.
4) Silica and aluminum concentrations in these experiments are not reliable indicators of silicate mineral reactivity.

References

Bethke, C.M., Yeakel, S., 2009. The Geochemist's Workbench Release 8.0: Reaction Modeling Guide. University of Illinois, Champaign, Illinois, 84 pp.

Chopping, C. and Kaszuba, J.P. (2012) Supercritical carbon dioxide-brine-rock reactions in the Madison Limestone of Southwest Wyoming: An experimental investigation of a sulfur-rich natural carbon dioxide reservoir. *Chem. Geol.* **322**, 223-236.

Chopping, C. and Kaszuba, J.P. (2017) Reactivity of supercritical sulfur dioxide and carbon dioxide in a carbonate reservoir: An experimental investigation of supercritical fluid-brine-rock interactions relevant to the Madison Limestone of Southwest Wyoming. *Interpretation* **5**, SS43–SS58.

Duan, Z.H., Sun, R., Zhu, C., Chou, I.M., 2006. An improved model for the calculation of CO_2 solubility in aqueous solutions containing Na^+, K^+, Ca^{2+}, Mg^{2+}, Cl^-, and SO_4^{2-}. Mar. Chem. 98(2-4), 131-139.

Huffmann, E., 1977. Performance of a new automatic carbon dioxide coulometer. Microchem J. 22(4), 567-573.

Kaszuba, J.P., Janecky, D.R. and Snow, M.G. (2003) Carbon dioxide reaction processes in a model brine aquifer at 200^{o}C and 200 bars: Implications for geologic sequestration of carbon. *Appl. Geochem.* **18**, 1065-1080.

Kaszuba, J.P., Janecky, D.R. and Snow, M.G. (2005) Experimental evaluation of mixed fluid reactions between supercritical carbon dioxide and NaCl brine: Relevance to the integrity of a geologic carbon repository. *Chem. Geol.* **217**, 277-293.

Marcon, V. (2013) Carbon dioxide-water-rock interaction in a carbonate reservoir capped by clay: An experimental investigation on the evolution of trace metals. M.Sc., University of Wyoming.

Newell, D.L., Kaszuba, J.P., Viswanathan, H.S., Pawar, R.J., Carpenter, T., 2008. Significance of carbonate buffers in natural waters reacting with supercritical CO_2: Implications for monitoring, measuring and verification (MMV) of geologic carbon sequestration. Geophys. Res. Lett. 35(23), 5.

Rosenbauer, R.J., Koksalan, T. and Palandri, J.L. (2005) Experimental investigation of CO_2–brine–rock interactions at elevated temperature and pressure: Implications for CO_2 sequestration in deep-saline aquifers. *Fuel Process. Technol.* **86**, 1581-1597.

Seyfried, W.E., Jr., Janecky, D.R., Berndt, M.E., 1987. Rocking autoclaves for hydrothermal experiments, II. The flexible reaction-cell system. In: Ulmer, G.C., Barnes, H.L. (Eds.), Hydrothermal Experimental Techniques. John Wiley & Sons, New York, pp. 216-239.

Shafer, L.R., 2013, Assessing injection zone fracture permeability through identification of critically stressed fractures at the Rock Springs Uplift CO_2 sequestration site, SW Wyoming, M.S. Thesis, University of Wyoming, 118 p.

Surdam, R.C., ed., 2013, Geological CO_2 Storage Characterization: The Key to Deploying Clean Fossil Energy Technology: New York, Springer-Verlag, 310 p.

Takenouchi, S., Kennedy, G.C., 1964. The binary system H_2O-CO_2 at high temperatures and pressures. Am. J. Sci. 262, 1055-1074.

Part II. In Situ Observation of Permeability, Porosity, and Pore Structure Changes Induced by Supercritical CO_2-Rock-Brine Reaction

Abstract

Reaction-induced changes in pore structure, porosity and permeability were measured in batch-style CO_2-brine-Madison Limestone experiments. Batch experiments were conducted at reservoir conditions (90°C and 34.5 MPa); baseline experiments reacted Madison Limestone with formation brine whereas the effects of CO_2 were evaluated in experiments that reacted Madison Limestone with CO_2-saturated formation brine. Madison Limestone with two different porosity types (small, dispersed intergranular pores and larger vuggy pores with a matrix of small, dispersed intergranular pores) were evaluated. Nuclear Magnetic Resonance transverse relaxation time (NMR T2), scanning electron microscopy (SEM) and thin section analysis were used to characterize pore size and pore structure changes resulting from dissolution and secondary mineralization. SEM images show that small dolomite grains and K-feldspar dissolution were observed along vuggy pores, as induced by reaction with CO_2-saturated brine. New dolomite with irregular morphology precipitated in intergranular pores in rocks with both styles of pores. Furthermore, thin section images show the formation of crack-like vuggy pores for both vug-dominated and intergranular-dominated Madison Limestone; 'bleached zones' associated with intergranular pores could represent dissolution. In contrast, no dissolution or precipitation was found in Madison Limestone reacted with brine without CO_2. T2 distributions remained the same for samples reacted with brine. In addition, changes after reaction were also measured and results show that porosity and permeability increased for rocks reacted with CO_2-saturated formation brine. Aqueous Ca, Mg and K concentrations increased due to mineral dissolution.

1 Introduction

Substantial reductions of carbon dioxide (CO_2) emissions could be achieved by available technology; capture and storage of CO_2 will aid in the transition to an energy economy in which other forms of energy, including nuclear, wind and solar energy, will play a more substantial role [1]. CO_2 capture and storage in the subsurface has been the focus of many studies; strategies that have been studied include enhanced oil recovery (EOR) using CO_2 [2, 3, 4, 5], injection into depleted oil and gas reservoirs [6, 7, 8, 9, 10]), injection into unminable coal beds [11, 12, 13, 14, 15], and injection into deep saline aquifers [16, 17, 18,19, 20].

Deep saline aquifers are ideal candidates for geological carbon storage due to their broad distributions, large storage potential, greater depths, substantial well connectivity, and storage security (presence of overlying low-permeability seals, e.g. shales and evaporites) [21, 22, 23]. In general, pressure and temperature of deep saline aquifers are greater than the critical pressure (7.38 MPa) and temperature (31.0 C) of CO_2, thus allowing CO_2 to react in the subsurface. The density and viscosity of supercritical CO_2 are smaller than that of formation water. Therefore, the CO_2 plume migrates upward due to buoyancy until stopped by low permeability layers. Four dominant trapping mechanisms contribute to the long-term storage of CO_2, including structural/stratigraphic, capillary residual, solubility and mineral trapping. Capillary trapping is considered the most promising option for carbon sequestration [24]; After injection, the buoyant CO_2 plume migrates upward and laterally, and water displaces CO_2 at the trailing edge of the CO_2 plume

in an imbibition process, leading to trapping of disconnected CO_2 ganglia within the pore space.

When CO_2 is injected, brine is enriched in CO_2 at the trailing edge of the plume due to CO_2 diffusion and in some circumstances convection. The pH of formation brine decreases by 1-2 units [25] and induces a state of geochemical disequilibrium locally in the pore space. Subsequent mineral dissolution and precipitation can induce changes in the pore networks (i.e. the pore shape, pore-size distribution, and internal surface area), thus changing porosity, permeability and wettability. These changes can significantly influence fluid saturation distribution and/or CO_2 injectivity. Therefore, understanding how geochemical reactions can alter pore networks advances our ability to evaluate both short and long-term CO_2 storage and sequestration. A significant amount of geochemical research has been conducted in recent years to understand CO_2-water-rock interactions in deep saline systems, and many of these are laboratory studies that have focused on changes in the composition of formation brine [26, 27, 28, 29, 30, 31, 32], mineral dissolution and precipitation [18, 25, 33, 34, 35, 36, 37], and modification of porosity/permeability [38, 39, 40, 41, 42, 43, 44, 45, 46, 47, 48, 49].

To date, studies of changes to petrophysical properties induced by interactions among CO_2, formation water, and reservoir rock have relied on dynamic coreflood studies wherein fluids are continuously injected into samples of reservoir rock [38, 41, 50, 48]. No published studies have investigated changes of pore structure and petrophysical properties resulting from mineral dissolution and precipitation in carbonate reservoirs after

CO_2 injection is stopped. When CO_2 is injected into aquifer formations, the non-wetting CO_2 displaces the water-wetting brine in a drainage-like process. In a region near the borehole, water is expelled by CO_2 and only residual water is left. A thin film of brine left near the pore surface or in micro-pores is saturated with CO_2; geochemical reactions happen due to the disturbed equilibrium. If dry CO_2 is injected, residual CO_2-saturated brine would be continuously decreased due to water evaporation, therefore new minerals would precipitate, leading to a decreasing porosity and permeability. In the two-phase region, CO_2 and water flow simultaneously. Transport reactions happen in CO_2 saturated brine. The reacted brine that also is CO_2-saturated will be expelled toward to the edge of CO_2 plume. At the trailing edge of the plume, the increase of cation concentra- tion produced by carbonate dissolution can eventually supersaturate fluids with respect to carbonate minerals. In this case, precipitation processes are expected to lead to the decrease of porosity and permeability at this front. After CO_2 injection is stopped, the buoyant CO_2 plume migrates upward and laterally, and water displaces CO_2 at the trailing edge of the CO_2 plume in an imbibition process, leading to trapping of disconnected CO_2 ganglia within the pore space. At the same time, the original brine will expel reacted brine and will be saturated with CO_2. The dilute effect due to fresh water imbibition will continuously lead to mineral dissolution, which will increase porosity and permeability in the imbibition region. The subsequent reactions will accelerate the imbibition process due to mineral dissolution, therefore it will affect CO_2 plume stability and shape in long-term storage.

The objective of this study is to investigate permeability and porosity

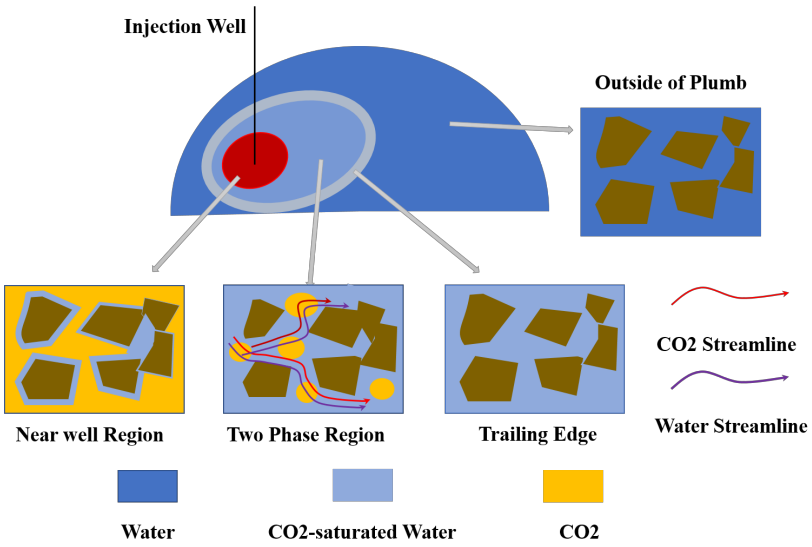

Figure 1: Schematic of the injection process

changes associated with mineral dissolution and precipitation due to CO_2-water-rock reactions in the region of imbibition. Because the imbibition process is quite slow compared to drainage, batch (static) experiments were conducted for this study. A parallel (baseline) experiment was performed without CO_2 to provide a basis of understanding for the interaction of synthetic brine with the rock. Scanning electron microscopy (SEM) and thin section analysis were performed to visualize and characterize mineral dissolution, precipitation and pore structure changes. We also measured gas permeability and porosity before and after experiments. In addition, ^{1}H-NMR transverse relaxation time (T_2) was also measured as its distribution is sensitive to changes in overall pore-size distribution (surface-area/volume ratio). Additionally, as macroscopic changes in pores and mineralogy

are critically dependent on reactions, brine samples before and after aging were analyzed to track the water composition change. Our studies provide an reference not only to numerical simulation, but also to monitor the change of CO_2 plume in long term.

2 Materials and Methods

2.1 Experimental Design and Setup

Before aging rock samples, gas (N_2) permeability, porosity and NMR T_2 distribution were collected. SEM and thin section images were also collected at location close to the rock plugs used in this study. Single-aqueous phase brine saturated with CO_2 was injected at 90 $^{\circ}$C and 34.5 MPa using a high pressure/high temperature coreflooding system, shown in Figure 2. The rock samples wrapped with heat shrinkage tube and sleeve were installed inside the coreholder, and then saturated with brine. After that, the target pressure and temperature were added. High precision syringe pumps (Teledyne ISCO 260D, Lincoln, NE, USA) were used to maintain pore, confining and back pressures, and to inject fluids. Two rock plugs represent two different rock types were aged for 400 hrs with brine first. Afterward, the reactant fluid (CO_2-saturated brine), which was generated through equilibrium between the brine and CO_2 phases for 24 hrs in a Vinci floating piston accumulator, was injected through the sample. The injection was stopped until a constant CO_2 production rate that was monitored by a Ritter gas meter (Germany) was reached. In general, less than five pore volume were injected to reach the constant CO_2 production. Finally, the rock plug was aged for another

400 hrs with the reactant fluid. In addition, one rock plug was aged with brine exclusively for 800 hrs as the base case.

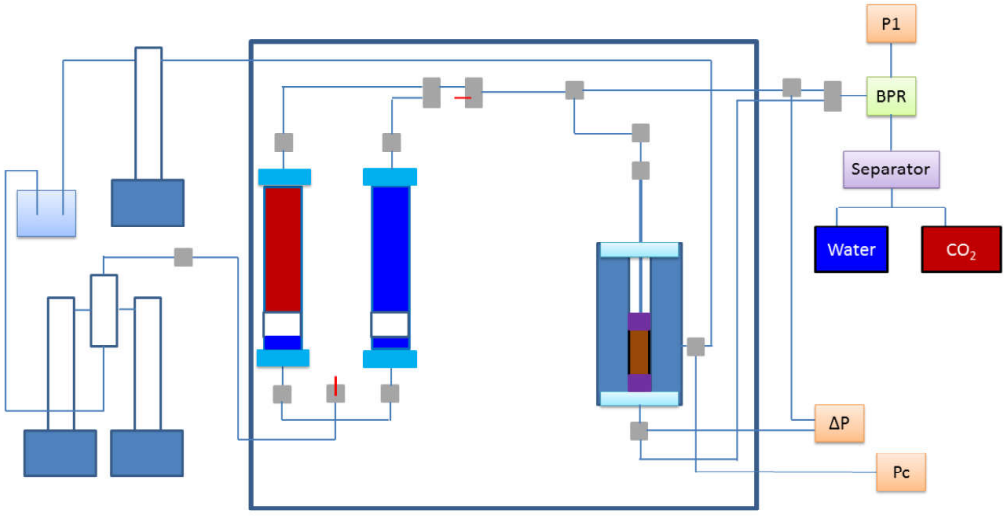

Figure 2: Schematic of coreflooding system used in this study

After aging, we collected and analyzed filtered (0.45 μm) aqueous samples for analyzing major cations and major anions by inductively-coupled plasma optical emission spectroscopy (ICPOES), ion chromatography (IC), and inductively-coupled plasma mass spectrometry (ICP-MS), respectively. The samples for cation analysis were diluted 10× or 100× and acidified with trace-metal-grade nitric acid. The aged core plugs were cleaned, and gas (N_2)

permeability, porosity, NMR T_2 distribution, SEM and thin section images were collected for comparison.

2.2 Materials

We selected three Madison Limestone rock plugs from the RSU #1. Rock plugs were cut horizontally with respect to bedding into dimensions of 25.4 mm × 50.8 mm (D × L). Rock samples for SEM and thin section measurements were also collected next to core plug in core boxes. Then, all rock samples were cleaned in soxhlet extractors using toluene and methanol until the plugs are clean for at least 2 weeks. After that, plugs were oven-dried at 100°C for at least 24 hrs. Routine core analyses (porosity and permeability) were performed on all samples under the net confining stress (NCS) of 1000 psi (6.9 MPa) using a Coreval 700 permeameter and porosimeter (VINCI Technologies, France). Initial properties of each sample are summarized in Table 2. Based on major oxide data and normalized mineralogy calculations, the core sample consists of the following composition: 85.0 wt% dolomite, 6.5 wt% calcite, 6.5 wt% anhydrite, 1.5 wt% quartz, 0.5 wt% pyrite.

The formation brine was analyzed based on natural conditions found within Madison Limestone; the ionic strength and the pH were 3.46 molal and 5.7 at 90 °C, respectively. To synthesize the brine, research-grade salts and standards were mixed with deionized water. The initial brine composition was calculated to be in equilibrium, or as close as possible, with the rock minerals used in the experiments at reservoir conditions in order to minimize reaction between the minerals and brine. However, unexpected precipitation of gypsum (≈ 1.5 g in 2 L solution) occurred while stirring the

solutions for 12 hrs. Then, final solution were filtered using a 0.45 μm filter to eliminate the precipitated particles and analyzed to measure the total concentrations by inductively coupled plasma-atomic emission spectrometry (ICP-AES). Before conducting injection, brine was degased for 30 minutes under vacuum.

2.3 T_2 distribution

NMR measures the ability of the hydrogen protons in a porous media to relax after being subjected to a magnetic field sequence. For brine saturated in rock samples, the hydrogen protons relax in three independent relaxation mechanisms: bulk fluid (T_{2bulk}), surface ($T_{2surface}$) and diffusion ($T_{2diffusion}$) when a magnetic field gradient exists. For a single pore and fast diffusion, the T_2 relaxation can be described as:

$$\frac{1}{T_2} = \frac{1}{T_{2bulk}} + \frac{1}{T_{2surface}} + \frac{1}{T_{2diffusion}} = \frac{1}{T_{2bulk}} + \rho(\frac{S}{V_p}) + \frac{D(\gamma g \tau)^2}{12} \qquad (1)$$

where

- ρ=surface relaxivity
- S/V_p=surface area to pore volume ratio
- D=diffusion coefficient
- γ=proton gyromagnetic ratio
- g=magnetic filed gradient intensity
- τ=inter-echo spacing in CPMG sequence

For brine-saturated rock samples, because diffusion relaxation is minimized and bulk relaxation rate is sufficiently small ([51, 52]), T_2 is dominated by $T_{2surface}$. So T_2 can be simplified as:

$$\frac{1}{T_2} \approx \rho \frac{S}{V_p} \tag{2}$$

Because the ratio V_p/S is proportional to the size of pores, the T_2 distribution can be related directly to the pore-size distribution. For example, V_p/S for cylindrical pores and spherical pores equal $1/2$ and $1/3$ of the pore radius, respectively. In the fast diffusion limit, the NMR relaxation process results in a magnetization decay as a function of the relaxation time of the individual pores. The magnetization decay ($M(t)$) resulting from spin-spin relaxation can be expressed as a sum of exponential decays:

$$M(t) = \sum_{i=1} A_i e^{-\frac{t}{T_{2i}}} \tag{3}$$

When a rock sample is fully saturated with brine, the NMR decay can be inverted into a T_2 distribution, which is analogous to the pore-size distribution of the rock sample. In this study, NMR T_2 measurements for all rock samples were performed using Bruker LF110 at 25°C and atmospheric pressure. NMR spectroscopic measurements of T_2 relaxation were performed using a standard Carr-Purcell-Meiboom-Grill (CPMG) pulse sequence. Later, conversion of relaxation signal into a continuous distribution of relaxation components (T_2), was performed using CONTIN application provided by the equipment vendor.

2.4 Thin Section and SEM Imaging

To characterize mineralogy, primary and authigenic minerals, and morphology of the grains, samples from same depth intervals that evaluated with NMR measurements were collected for thin section and SEM imaging.

Selected end trims and plugs were sent to Wagner Petrographic, Lindon, Utah, for thin section preparation. Most of the thin sections were stained for calcite and feroan carbonates and impregnated with epoxy for porosity evaluation. Petrographic analysis of the thin sections was done on a Carl Zeiss Stereo Discovery V8 micorscope with an AxioCam MRc camera attachment and Axiovision imaging software. As for SEM imaging, carbon-coated rock fragments were affixed to glass slides and loaded two at a time into the SEM. Both back-scattered electrons (BSE) and Everhart-Thornley detector (ETD) were used. Photographs of samples were taken using the SEM run program on-board software and the chemical composition of the fresh rock fragments was determined using an electron microprobe, at an accelerating voltage of 10/20 kV and a beam current of 5 nA.

Porosity systems in the Madison Limestone are intergranular and/or vug dominated [53, 54]. The intergranular porosity is generally located near the top of the reservoir interval, and has a relatively uniform pore character and distribution. A vug with larger secondary dolostone crystals is observed near the center of the SEM image, shown in Figure 3 (a). The vug is surrounded by smaller, uniform dolomite grains that comprise the intergranular porosity system. Though the intergranular pores are smaller, they are evenly distributed and provide the majority of pore space in this facies of the Madison Limestone. Anhydrite cement fills two of the larger vugs in the top left quad-

rant of the thin section image (Figure 3 (b)). The dissolution has produced zones with massive pores and the highest overall porosity values, though they have a highly heterogenic distribution. Vuggy, sometimes moldic, porosity formed by dissolution of the carbonate. Pores range in size and distribution, shown in Figure 3 (c). Authigenic quartz crystals, the white grains in the thin section image (Figure 3 (d)), have nucleated in many of the larger pores. Authigenic dolomite grains are observed coating pore walls in the SEM image. It is worth to notice that lots of small particles were found on the surface of dolomite crystals.The size of the particles ranges from 0 to 10 μm.

3 Results and Discussion

3.1 Mineral dissolution and participation

Compared the SEM images of MH1 with brine-aged rock sample in Figure 3, no evidence of mineral dissolution or mineral growth was observed, shown in Figure 4. The morphology of dolomite crystals is regular. From the thin section image, note that the authigenic minerals in large vugs, and the dolomite crystals that surround the pore space, have sharp, fully annealed edges and terminated points; dolomite crystals surrounding pore spaces are observed to be similar in size to matrix dolostone. Furthermore, different with continuous or cycling injection, which will cause the transport of small particles inside the porous media, static experiments in this study was performed. In our experiment, within 5 PV was injected before reaction, and the transport of small particles can be ignored. [5] observed that dolomite particles (powder) have larger relative surface area compared with dolomite crystals, and prefer

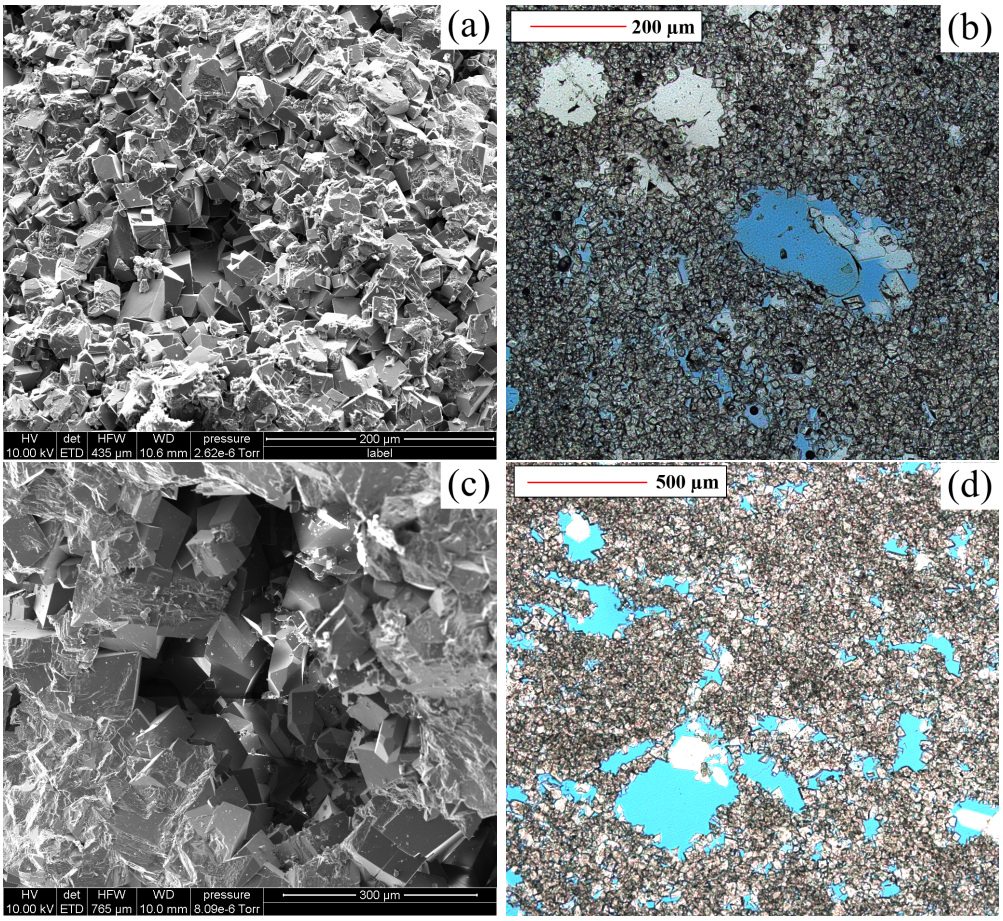

Figure 3: Scanning electron microscope (SEM) (left column) and thin sections images (right column) of two Madison Limestone (c, d) samples from the RSU#1 well. The depth for (a, b) and (c, d) are 3766 and 3785 m, respectively. Thin sections are impregnated with blue epoxy to illustrate porosity. (a, b) Madison Limestone sample with a mixed intergranular and vuggy porosity system. (c, d) Madison Limestone sample with a vuggy porosity system.

to dissolute if reaction exists. Therefore, the number and size of particle size can be used to determine mineral dissolution in this study. From Figure 4, it is hard to identify the change of the number and size of particles on the dolomite crystal surface, and it also supports no mineral dissolution.

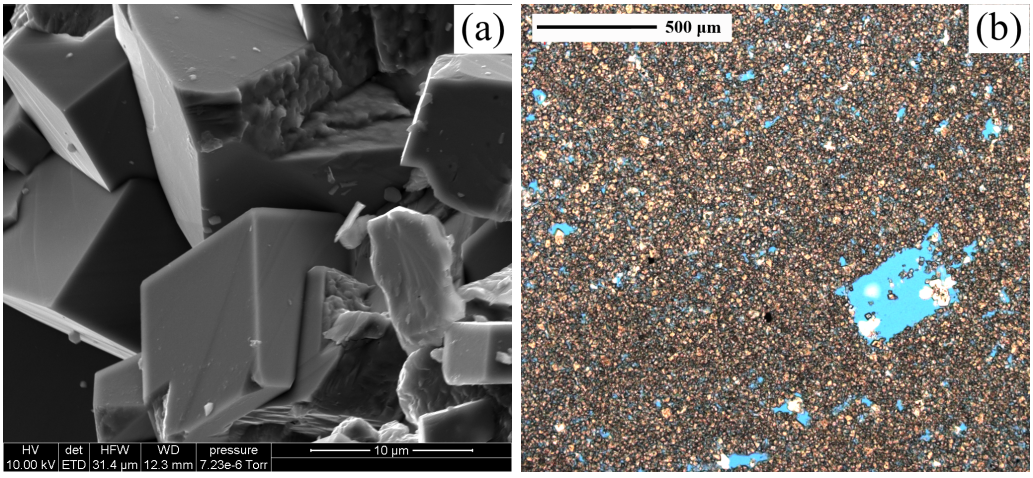

Figure 4: SEM and thin section images aged with brine.

Figure 5 shows SEM and EDS analysis of CO_2 aged rock samples. For sample MH2, the porosity is mainly from intergranualr pores. The displacement of CO_2-saturated brine can be regarded as piston-like. Therefore, reactions happen most pores of the rock plug. Similar as rock sample reacted with brine, it is hard to determine mineral dissolution from crystal edges because of the limited reaction time. However, the dents on the crystal surface and also broken crystals become deeper after reaction. Thin section image collected from MH2 after being aged with CO_2 show evidence of additional dissolution. Samples with intergranular porosity have 'bleached zones', wherein porosity has increased and dolomite crystals are lighter, shown in Figure 5. The most prominent texture of additional dissolution are nascent channel structures

with walls of smaller (relative to matrix), partially digested dolomite crystals. Only larger dolomite crystals are retained in the 'bleached zones', suggesting increased porosity due to the dissolution of smaller dolomite grains within the matrix.Additionally, the number and size of small particles decrease. This observation is consistent with analyzed aqueous sample results that the molality of Ca and Mg increased. Even though the collected aqueous samples are not absolutely same as brine inside the rock plugs due to the unreacted brine in tubes, the increased molalities of Ca and Mg still support the dolomite mineral dissolution,shown in Table 1.

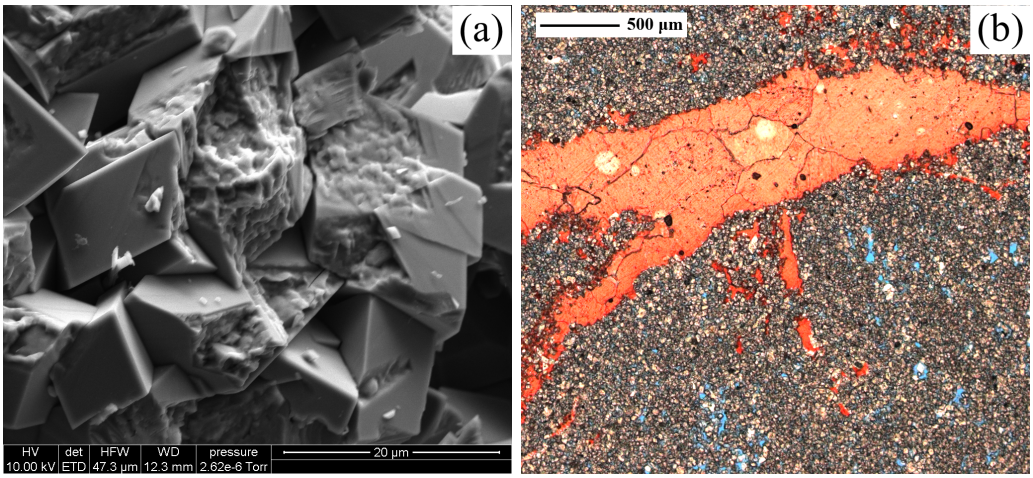

Figure 5: SEM and thin section images for MH2 aged with CO_2 for MH2

Pore systems of MH3 are vug dominated. The displacement of reactant fluid prefers to flow in high permeable pathways. Our results agree with previous studies that reactions happen mainly in high permeable pathways (vuggy pores), while in intergranular pores (matrix), reactions can be ignored [55]. Figure 6 (a) shows SEM image from vuggy pore. Same as MH2, the dents on the crystal surface and also broken crystals become deeper after

Table 1: Chemical Concentrations of synthesized Weber and Madison Formation Brine

Major Species/Complexes	Initial brine, mol/kg	Finial brine, mol/kg
SO4	0.1052	0.1060
Cl	1.6190	1.4864
Na	1.4760	1.3384
K	0.0596	0.1006
Mg	0.0030	0.0020
Ca	0.0040	0.0104
Fe	N/A	3.0E-5

reaction, while the dissolution on the edge and surface of dolomite crystals cannot be identified based on the SEM image. Furthermore, small particles on the surface of dolomite crystals almost disappear due to reaction in vuggy pore (shown in Figure 6 (a)), while in intergrnular pore, small particles still exist, shown in Figure 6 (b). In thin section image (shown in Figure 6 (c)), dolomite crystals that make up the walls of some of the pores are smaller than matrix dolomite, and are not fully annealed. These textures could also represent dissolution.

Mineral participation and dissolution happened simultaneously in different pore spaces due to difference of local chemical equilibrium. Mineral participations are also observed in both rock samples, shown in Figure 7 and Figure 8. The newly formed minerals were located near the corner of dolomite crystals. Different with original mineral morphology, the morphology of newly formed mineral is irregular. We collected the EDS spectrum

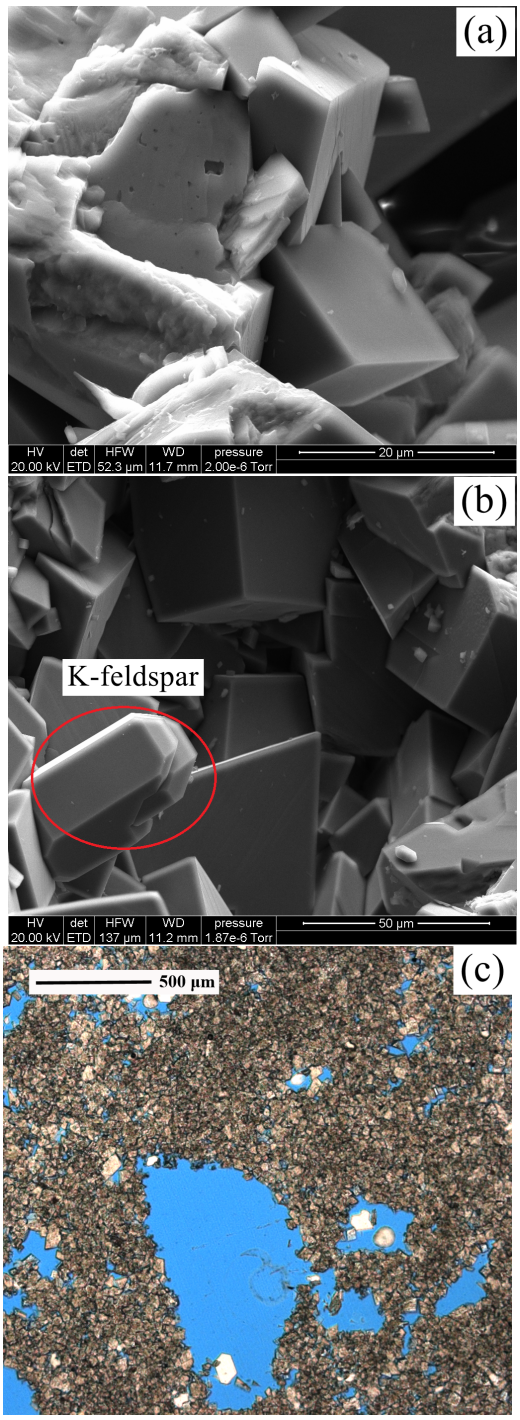

Figure 6: SEM image, EDS spectra and thin section data after reactions for MH3

of newly formed mineral for two CO_2 aged samples and original dolomite crystals, shown in Figure 7 and Figure 8, and the results show the newly formed minerals are similar as spectrum of original dolomite crystals.

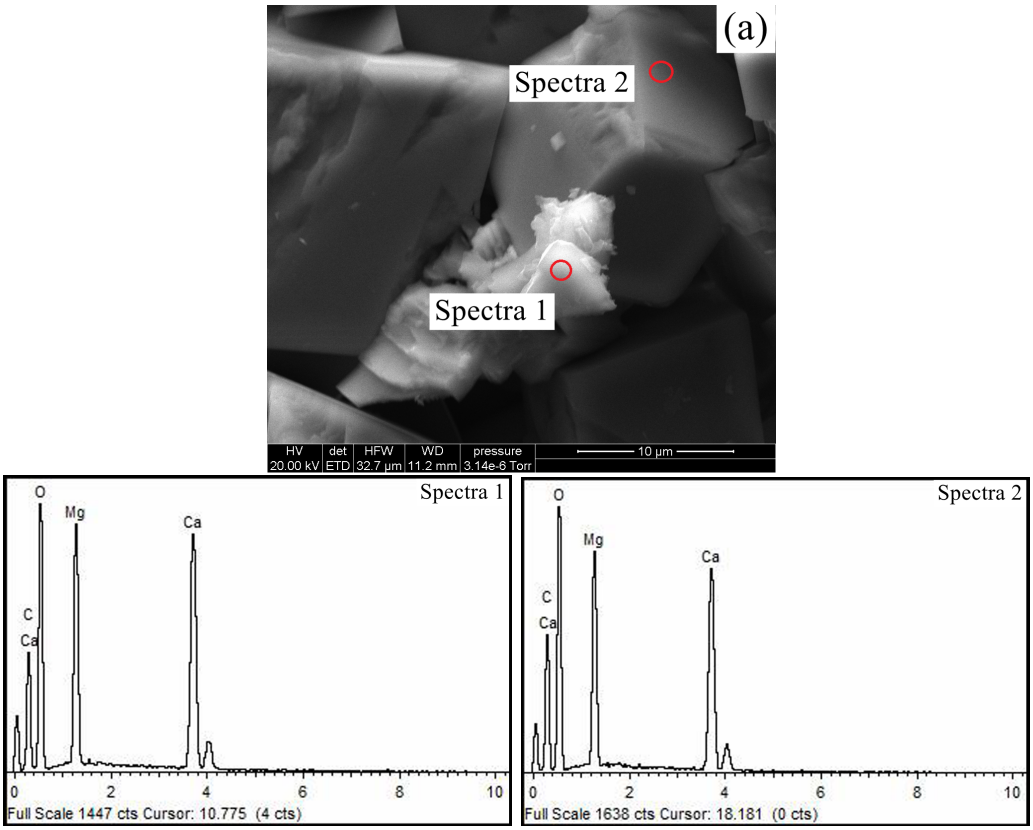

Figure 7: SEM image and EDS spectrum of newly formed minerals in sample MH2

Another interesting finding is the dissolution of K-feldspar, shown in Figure 9. The EDS spectrum of crystal surface shows the existence of K, Si, Al and O, which proves the K-feldspar. Different with regular morphology of K-feldspar before reaction, the reaction k-feldspar crystals are irregular, and the mineral dissolution happened at two end of the crystals and gradually went

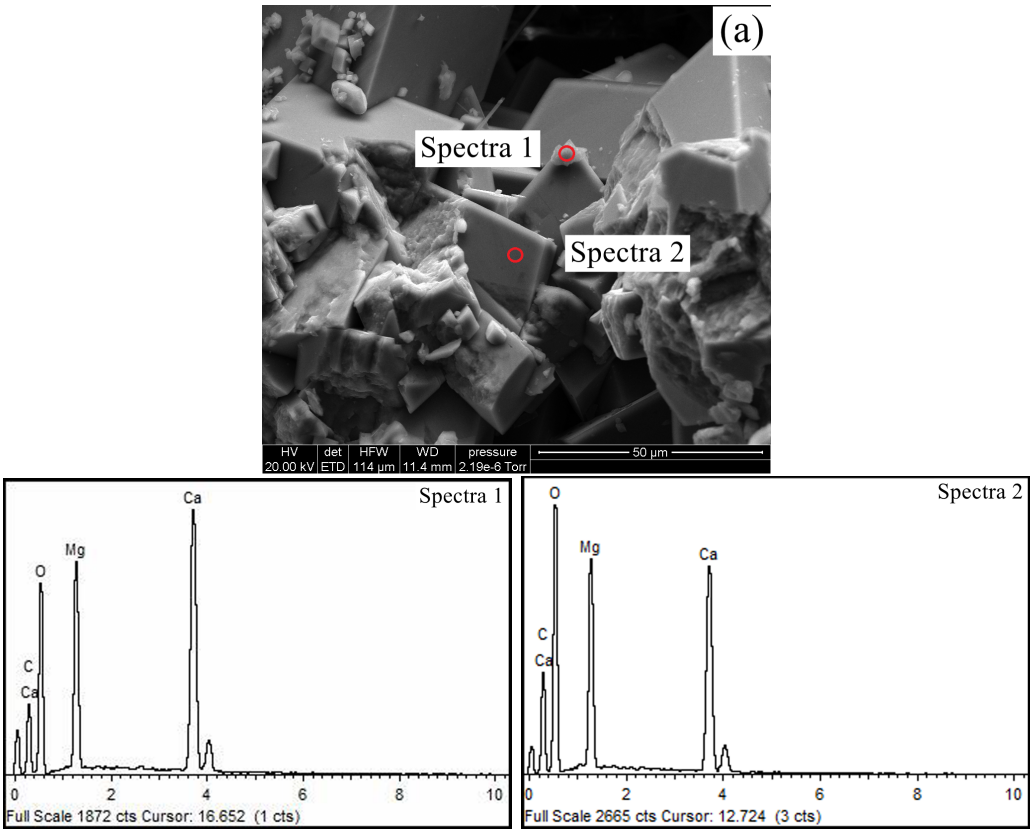

Figure 8: SEM image and EDS spectrum of newly formed minerals in sample MH3

inside. Additionally several K-feldspar crystals were analyzed, but no change in composition could be detected from EDS spectra. It is interesting to note that the dissolution of K-feldspar only happened in vuggy pores, while in intergranular pores, the K-feldspar crystal did not change, shown in Figure 6 (b). This also supports that dolomite dissolution mainly in vuggy pores. Furthermore, the possible reactions between CO_2 and K-feldspar are shown below, and the release of K leads to the increase of the molality of K after reaction. Aqueous analysis results show the increase of K, seen in Table 1. The increased molality of K can come from clays and dissolved K-feldspar. However, K from clays are limited due to small volume of clay content in studied rock samples. Therefore, the increased molality of K agrees with K-feldspar dissolution seen from SEM image. Another feature observed after reaction was that in the vugy pore with K-feldspar existed, the dissolution of small particles was inhibited due to the dissolution of K-feldspar.

$$2\,KAlSi_3O_8 + 2\,CO_2(aq) + 2\,H_2O \longleftrightarrow \text{muscovite (illite)} + 6\,SiO_2 + K^+\,2\,HCO_3^- \tag{4}$$

$$2\,KAlSi_3O_8 + Na^+ + CO_2(aq) + 2\,H_2O \longleftrightarrow NaAlCO_3(OH)_2 + 3\,SiO_2 + K^+ \tag{5}$$

3.2 Porosity and Permeability Changes

During mineral dissolution and participation, the porosity, permeability and surface area were changed. For example, when mineral dissolution occurs, pore volume increases. The specific surface area for individual grains increases due to mineral dissolution, while the overall specific surface area may

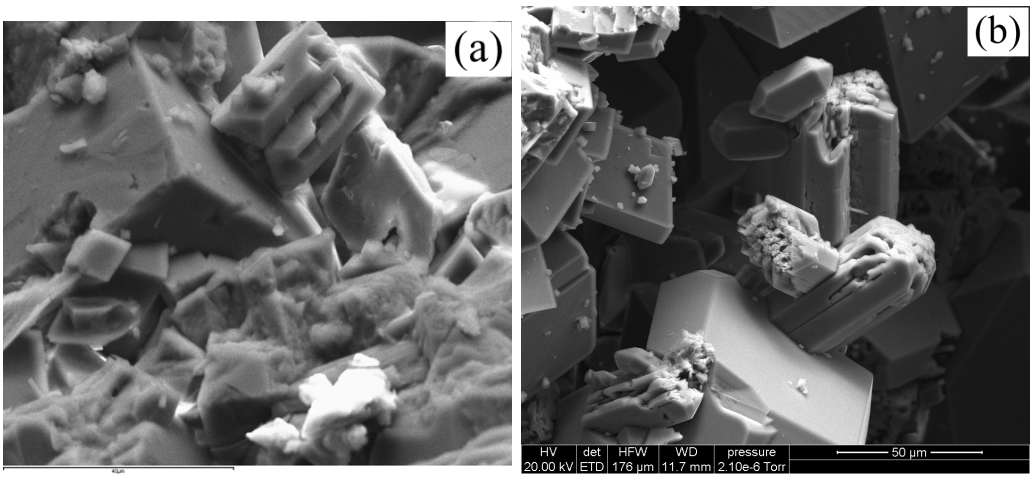

Figure 9: SEM images of K-feldspar crystals: (a) before aging, (b) after aging.

change differently because small particles that have a large specific surface area dissolve firstly. Permeability change due to mineral participation and dissolution is complex. It depends on place and degree of mineral participation, which are quite dependent on rock mineralogy and pore types. For example, if mineral participates on pore throats, permeability will decrease, and vice versa. But if mineral participation and dissolution both occur on pore throats and/or bodies, permeability change cannot be determined just based on reaction results. In this study, from SEM images, the dolomite dissolution and participation, and K-feldspar dissolution were observed in intergranular pores for MH2 and mainly in vuggy pores for MH3. Therefore, it is hard to determine porosity and permeability change.

Gas porosity and permeability were measured before and after reaction. The change of surface area is not studied in this work. Table 2 shows the porosity and permeability change for all experiments. Porosity and perme-

ability for MH1 decrease slightly. The migration of small particles that would block the pore throats, might account for the decreases even though a small number of pore volumes of brine were injected. On the contrary, porosity and permeability of CO_2 aged samples are increased. This result was consistent with observations from SEM and thin section imaging results. Minerals participation are in charge of the porosity and permeability decreasing, and dissolution in high permeable pathways increased porosity and permeability. It is worth to notice that increasing ratio of porosity and permeability for MH2 (1.01/1.19) are smaller than that of MH3 (1.06/1.32). One reason that explains the increasing ratio is that pore volume of MH3 is larger than that of MH2, therefore the volume of saturated reactant fluid is larger for MH3. On the hand, the pore connectivity of MH3 is better than MH2, resulting a larger diffusivity of reactant fluid, thus increased the reaction rate.

Table 2: Summary of rock sample properties before and after reaction

Sample ID	Depth, m	Porosity, %		Permeability, mD		T_{2LM}, ms	
		before	After	before	After	before	After
MH1	3415.0	23.47	22.97	29.68	25.30	342	216
MH2	3415.0	19.46	19.66	14.21	16.91	287	176
MH3	3415.1	16.34	17.26	30.76	40.67	450	360

Note: Permeability showed in Table 2 are Klinkenberg-corrected values

Power-laws are frequently used in porosity-permeability relationships for percolation theory when perform porosity-permeability relationship analysis for carbonate [38, 56, 55, 57]. [57] gived the relationship as:

$$\frac{k}{k_0} = (\frac{\phi}{\phi_0})^n \tag{6}$$

where k and ϕ are porosity and permeability after reaction, k_0 and ϕ_0 are initial porosity and permeability. The exponent, n, is a regression parameter and may not always be constant. In this study, the initial and finial porosity and permeability were measured and we plotted $\log(k/k_0)$ as a function of $\log(\phi/\phi_0)$, shown in Figure 10. n given by the slope of the data equals 3.6311, which agrees with previous results. Even through, the porosity-permeability relationship in this study is different with previous dynamic experiments, it still agrees with the power law and gives the coefficient of determination 0.9868.

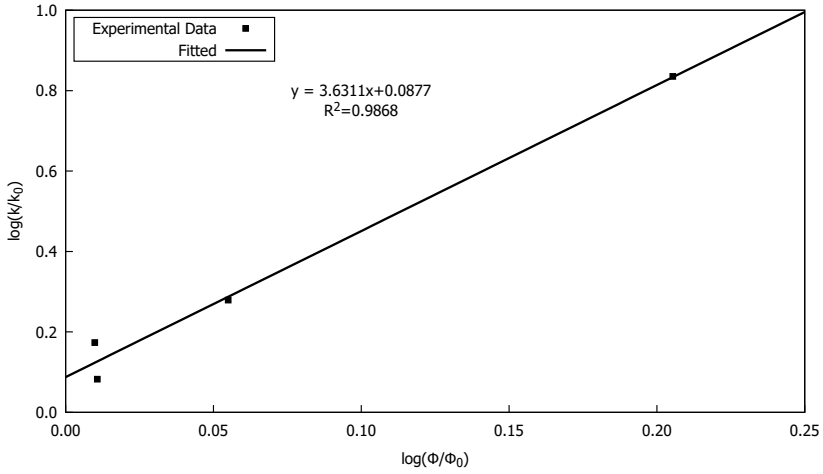

Figure 10: Permeability ratio (k/k_0) as a function of porosity ratio (ϕ/ϕ_0) for all experiments in log-log space.

3.3 T_2 distribution

Even though SEM and thin section can provide the place of mineral dissolution and participation, quantitative change of pore-size distribution due to dissolution and participation cannot be given just based on the images. NMR T_2 distributions are always used to represent pore-size distribution and the area under the peak represents pore volume in different size pores. Therefore, pore size change due to mineral dissolution and participation can be observed via T_2 distribution. Figure 11 shows the T_2 distributions for pre- and postreaction samples. The T_2 distributions are almost same for sample MH1 compared pre- and postreaction with brine, which agrees with the SEM and thin section results. For sample MH2 and MH3, the distributions show a shift to shorter T_2 times and an amplitude decrease, which are not consistent with the observed porosity and permeability increases. As shown in Table 1, Fe appeared after aging due to the corrosion of transfer vessel, which increases the relaxation rate.

4 Conclusions

We investigated the geophysical response to microstructural and petrophysical properties changes of rock plugs induced by the CO_2-saturated brine under reservoir conditions. We used a suite of SEM and thin section images, NMR as well as porosity and permeability measurements to build a comprehensive interpretation of the effects of imbibition process when CO_2 injection is stopped. Mineral dissolution and participation were observed in two investigated rock plugs. Different with previous observations, the disso-

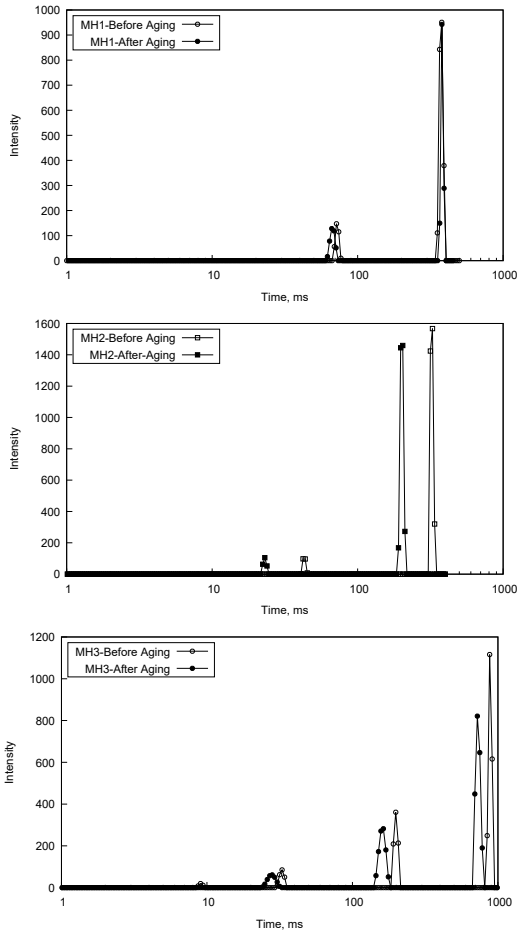

Figure 11: NMR T_2 distributions before and after aging

lution affects number and size of small particles, while it is hard to identify the change on surface and corner of dolomite crystals. Furthermore, thin section images show the formation of cracklike vuggy pores for MH3. SEM images indicate dissolution occurs primarily in the vuggy pores, while in intergranular pore, dissolution cannot be identified. In addition, K-feldspar dissolution was observed, leading to an increased K observed in aqueous sample analysis results. For MH2, 'bleached zones' in intergranular pores were found and could represent dissolution. New irregular morphology dolomite was observed in two rock types from SEM images. Porosity and permeability enhancements are minimal in investigated carbonate types and much smaller than previously reported continuous injection experiments, which a larger fluid volume was injected. Additionally, T_2 measurements indicate no significant pore-geometry alterations are induced during injection. T_2 relaxation time is similar compared with pre- and postreaction for brine aged sample, while for CO_2 aged samples, T_2 relaxation times decrease due to the appearance of Fe.

References

[1] M. I. Hoffert, K. Caldeira, G. Benford, D. R. Criswell, C. Green, H. Herzog, A. K. Jain, H. S. Kheshgi, K. S. Lackner, J. S. Lewis *et al.*, "Advanced technology paths to global climate stability: Energy for a greenhouse planet," *Science*, vol. 298, no. 5595, pp. 981–987, 2002.

[2] J. Shaw, S. Bachu *et al.*, "Screening, evaluation, and ranking of oil reservoirs suitable for CO_2-flood EOR and CO_2 sequestration,"

Journal of Canadian Petroleum Technology, vol. 41, no. 09, 2002.

[3] Z. Dai, R. Middleton, H. Viswanathan, J. Fessenden-Rahn, J. Bauman, R. Pawar, S.-Y. Lee, and B. McPherson, "An integrated framework for optimizing CO_2 sequestration and enhanced oil recovery," *Environmental Science & Technology Letters*, vol. 1, no. 1, pp. 49–54, 2013.

[4] Z. Tao and A. Clarens, "Estimating the carbon sequestration capacity of shale formations using methane production rates," *Environmental Science & Technology*, vol. 47, no. 19, pp. 11 318–11 325, 2013.

[5] H. Wang, X. Liao, X. Dou, B. Shang, H. Ye, D. Zhao, C. Liao, and X. Chen, "Potential evaluation of CO_2 sequestration and enhanced oil recovery of low permeability reservoir in the Junggar Basin, China," *Energy & Fuels*, vol. 28, no. 5, pp. 3281–3291, 2014.

[6] Y. Le Gallo, P. Couillens, T. Manai *et al.*, "CO_2 sequestration in depleted oil or gas reservoirs," in *SPE International Conference on Health, Safety and Environment in Oil and Gas Exploration and Production*. Society of Petroleum Engineers, 2002.

[7] A. Kovscek and Y. Wang, "Geologic storage of carbon dioxide and enhanced oil recovery. I. Uncertainty quantification employing a streamline based proxy for reservoir flow simulation," *Energy Conversion and Management*, vol. 46, no. 11, pp. 1920–1940, 2005.

[8] A. Kovscek and M. Cakici, "Geologic storage of carbon dioxide and enhanced oil recovery. II. Co-optimization of storage and recovery," *Energy Conversion and Management*, vol. 46, no. 11, pp. 1941–56, 2005.

[9] W. Ampomah, R. S. Balch, R. B. Grigg, Z. Dai, F. Pan *et al.*, "Compositional simulation of CO_2 storage capacity in depleted oil reservoirs," in *Carbon Management Technology Conference*. Carbon Management Technology Conference, 2015.

[10] D. Sun, J. Ripmeester, and P. Englezos, "Phase equilibria for the $CO_2/CH_4/N_2/H_2O$ system in the hydrate region under conditions relevant to storage of CO_2 in depleted natural gas reservoirs," *Journal of Chemical & Engineering Data*, vol. 61, no. 12, pp. 4061–4067, 2016.

[11] J. Gale and P. Freund, "Coal-bed methane enhancement with CO_2 sequestration worldwide potential," *Environmental Geosciences*, vol. 8, no. 3, pp. 210–217, 2001.

[12] S. Harpalani, B. K. Prusty, and P. Dutta, "Methane/CO_2 sorption modeling for coalbed methane production and CO_2 sequestration," *Energy & Fuels*, vol. 20, no. 4, pp. 1591–1599, 2006.

[13] E. Ozdemir, "Modeling of coal bed methane (CBM) production and CO_2 sequestration in coal seams," *International Journal of Coal Geology*, vol. 77, no. 1, pp. 145–152, 2009.

[14] C. M. White, D. H. Smith, K. L. Jones, A. L. Goodman, S. A. Jikich, R. B. LaCount, S. B. DuBose, E. Ozdemir, B. I. Morsi, and K. T. Schroeder, "Sequestration of carbon dioxide in coal with enhanced coalbed methane recovery: A review," *Energy & Fuels*, vol. 19, no. 3, pp. 659–724, 2005.

[15] S. Bachu, "Sequestration of CO_2 in geological media: Criteria and approach for site selection in response to climate change," *Energy Conversion and Management*, vol. 41, no. 9, pp. 953–970, 2000.

[16] ——, "Screening and ranking of sedimentary basins for sequestration of CO_2 in geological media in response to climate change," *Environmental Geology*, vol. 44, no. 3, pp. 277–289, 2003.

[17] S. Bachu and J. Adams, "Sequestration of CO_2 in geological media in response to climate change: Capacity of deep saline aquifers to sequester CO_2 in solution," *Energy Conversion and Management*, vol. 44, no. 20, pp. 3151–3175, 2003.

[18] J. P. Kaszuba, D. R. Janecky, and M. G. Snow, "Carbon dioxide reaction processes in a model brine aquifer at 200 C and 200 bars: Implications for geologic sequestration of carbon," *Applied Geochemistry*, vol. 18, no. 7, pp. 1065–1080, 2003.

[19] N. I. Gershenzon, R. W. Ritzi, D. F. Dominic, M. Soltanian, E. Mehnert, and R. T. Okwen, "Influence of small-scale fluvial architecture on CO_2 trapping processes in deep brine reservoirs," *Water Resources Research*, vol. 51, no. 10, pp. 8240–8256, 2015.

[20] L. Trevisan, R. Pini, A. Cihan, J. T. Birkholzer, Q. Zhou, A. González-Nicolás, and T. H. Illangasekare, "Imaging and quantification of spreading and trapping of carbon dioxide in saline aquifers using meter-scale laboratory experiments," *Water Resources Research*, vol. 53, no. 1, pp. 485–502, 2017.

[21] R. Bruant, A. Guswa, M. Celia, and C. Peters, "Safe storage of CO_2 in deep saline aquifers," *Environmental Science and Technology*, vol. 36, no. 11, pp. 240A–245A, 2002.

[22] S. J. Friedmann, "Geological carbon dioxide sequestration," *Elements*, vol. 3, no. 3, pp. 179–184, 2007.

[23] S. M. Benson and D. R. Cole, "CO_2 sequestration in deep sedimentary formations," *Elements*, vol. 4, no. 5, pp. 325–331, 2008.

[24] S. Krevor, M. J. Blunt, S. M. Benson, C. H. Pentland, C. Reynolds, A. Al-Menhali, and B. Niu, "Capillary trapping for geologic carbon dioxide storage–from pore scale physics to field scale implications," *International Journal of Greenhouse Gas Control*, vol. 40, pp. 221–237, 2015.

[25] J. P. Kaszuba, D. R. Janecky, and M. G. Snow, "Experimental evaluation of mixed fluid reactions between supercritical carbon dioxide and nacl brine: Relevance to the integrity of a geologic carbon repository," *Chemical Geology*, vol. 217, no. 3, pp. 277–293, 2005.

[26] C. Chopping and J. P. Kaszuba, "Supercritical carbon dioxide–brine–rock reactions in the madison limestone of southwest Wyoming: An experimental investigation of a sulfur-rich natural carbon dioxide reservoir," *Chemical Geology*, vol. 322, pp. 223–236, 2012.

[27] M. Xu, K. Sullivan, G. VanNess, K. G. Knauss, and S. R. Higgins, "Dissolution kinetics and mechanisms at dolomite–water interfaces: effects of

electrolyte specific ionic strength," *Environmental Science & Technology*, vol. 47, no. 1, pp. 110–118, 2012.

[28] Y. Hu, J. R. Ray, and Y.-S. Jun, "Na^+, Ca^{2+}, and Mg^{2+} in brines affect supercritical CO_2–brine–biotite interactions: Ion exchange, biotite dissolution, and illite precipitation," *Environmental Science & Technology*, vol. 47, no. 1, pp. 191–197, 2012.

[29] C. L. Ré, J. P. Kaszuba, J. N. Moore, and B. J. McPherson, "Fluid–rock interactions in CO_2-saturated, granite-hosted geothermal systems: Implications for natural and engineered systems from geochemical experiments and models," *Geochimica et Cosmochimica Acta*, vol. 141, pp. 160–178, 2014.

[30] V. Marcon and J. P. Kaszuba, "Carbon dioxide–brine–rock interactions in a carbonate reservoir capped by shale: Experimental insights regarding the evolution of trace metals," *Geochimica et Cosmochimica Acta*, vol. 168, pp. 22–42, 2015.

[31] L. Zhang, Y. Kim, H. Jung, J. Wan, and Y.-S. Jun, "Effects of salinity-induced chemical reactions on biotite wettability changes under geologic CO_2 sequestration conditions," *Environmental Science & Technology Letters*, vol. 3, no. 3, pp. 92–97, 2016.

[32] J. Lu, R. Darvari, J.-P. Nicot, P. Mickler, and S. A. Hosseini, "Geochemical impact of injection of Eagle Ford brine on Hosston Sandstone formation—Observations of autoclave water–rock interaction experiments," *Applied Geochemistry*, vol. 84, pp. 26-40, 2017.

[33] M. Wigand, J. Carey, H. Schütt, E. Spangenberg, and J. Erzinger, "Geochemical effects of CO_2 sequestration in sandstones under simulated in situ conditions of deep saline aquifers," *Applied Geochemistry*, vol. 23, no. 9, pp. 2735–2745, 2008.

[34] S. J. Hangx and C. J. Spiers, "Reaction of plagioclase feldspars with CO_2 under hydrothermal conditions," *Chemical Geology*, vol. 265, no. 1, pp. 88–98, 2009.

[35] J. Kaszuba, B. Yardley, and M. Andreani, "Experimental perspectives of mineral dissolution and precipitation due to carbon dioxide-water-rock interactions," *Reviews in Mineralogy and Geochemistry*, vol. 77, no. 1, pp. 153–188, 2013.

[36] A. G. Ilgen and R. T. Cygan, "Mineral dissolution and precipitation during CO_2 injection at the Frio-I brine pilot: Geochemical modeling and uncertainty analysis," *International Journal of Greenhouse Gas Control*, vol. 44, pp. 166–174, 2016.

[37] R. Xu, R. Li, J. Ma, D. He, and P. Jiang, "Effect of mineral dissolution/precipitation and CO_2 exsolution on CO_2 transport in geological carbon storage," *Accounts of Chemical Research*, vol. 50, no. 9, pp. 2056–2066, 2017.

[38] L. Luquot and P. Gouze, "Experimental determination of porosity and permeability changes induced by injection of CO_2 into carbonate rocks," *Chemical Geology*, vol. 265, no. 1, pp. 148–159, 2009.

[39] S. Sadhukhan, P. Gouze, and T. Dutta, "Porosity and permeability changes in sedimentary rocks induced by injection of reactive fluid: A simulation model," *Journal of Hydrology*, vol. 450, pp. 134–139, 2012.

[40] H. Abdoulghafour, L. Luquot, and P. Gouze, "Characterization of the mechanisms controlling the permeability changes of fractured cements flowed through by CO_2-rich brine," *Environmental Science & Technology*, vol. 47, no. 18, pp. 10 332–10 338, 2013.

[41] P. O. Mangane, P. Gouze, and L. Luquot, "Permeability impairment of a limestone reservoir triggered by heterogeneous dissolution and particles migration during CO_2-rich injection," *Geophysical Research Letters*, vol. 40, no. 17, pp. 4614–4619, 2013.

[42] J. P. Nogues, J. P. Fitts, M. A. Celia, and C. A. Peters, "Permeability evolution due to dissolution and precipitation of carbonates using reactive transport modeling in pore networks," *Water Resources Research*, vol. 49, no. 9, pp. 6006–6021, 2013.

[43] M. M. Smith, Y. Sholokhova, Y. Hao, and S. A. Carroll, "CO_2-induced dissolution of low permeability carbonates. Part I: Characterization and experiments," *Advances in Water Resources*, vol. 62, pp. 370–387, 2013.

[44] L. Chen, Q. Kang, H. S. Viswanathan, and W.-Q. Tao, "Pore-scale study of dissolution-induced changes in hydrologic properties of rocks with binary minerals," *Water Resources Research*, vol. 50, no. 12, pp. 9343–9365, 2014.

[45] Q. Kang, L. Chen, A. J. Valocchi, and H. S. Viswanathan, "Pore-scale study of dissolution-induced changes in permeability and porosity of porous media," *Journal of Hydrology*, vol. 517, pp. 1049–1055, 2014.

[46] B. Lamy-Chappuis, D. Angus, Q. Fisher, C. Grattoni, and B. W. Yardley, "Rapid porosity and permeability changes of calcareous sandstone due to CO_2-enriched brine injection," *Geophysical Research Letters*, vol. 41, no. 2, pp. 399–406, 2014.

[47] K. M. Mouzakis, A. K. Navarre-Sitchler, G. Rother, J. L. Bañuelos, X. Wang, J. P. Kaszuba, J. E. Heath, Q. R. Miller, V. Alvarado, and J. E. McCray, "Experimental study of porosity changes in shale caprocks exposed to CO_2-saturated brines I: Evolution of mineralogy, pore connectivity, pore size distribution, and surface area," *Environmental Engineering Science*, vol. 33, no. 10, pp. 725–735, 2016.

[48] A. J. Luhmann, B. M. Tutolo, B. C. Bagley, D. F. Mildner, W. E. Seyfried, and M. O. Saar, "Permeability, porosity, and mineral surface area changes in basalt cores induced by reactive transport of CO_2-rich brine," *Water Resources Research*, vol. 53, no. 3, pp. 1908–1927, 2017.

[49] Y. Soong, D. Crandall, B. H. Howard, I. Haljasmaa, L. E. Dalton, L. Zhang, R. Lin, R. M. Dilmore, W. Zhang, F. Shi *et al.*, "Permeability and mineral composition evolution of primary seal and reservoir rocks in geologic carbon storage conditions," *Environmental Engineering Science*, vol. 35, pp. 391-400, 2018.

[50] L. Luquot, P. Gouze, A. Niemi, J. Bensabat, and J. Carrera, "CO_2-rich brine percolation experiments through Heletz Reservoir rock samples (Israel): Role of the flow rate and brine composition," *International Journal of Greenhouse Gas Control*, vol. 48, pp. 44–58, 2016.

[51] R. L. Kleinberg and M. A. Horsfield, "Transverse relaxation processes in porous sedimentary rock," *Journal of Magnetic Resonance (1969)*, vol. 88, no. 1, pp. 9–19, 1990.

[52] J. Lai, G. Wang, Z. Fan, J. Chen, S. Wang, Z. Zhou, and X. Fan, "Insight into the pore structure of tight sandstones using NMR and HPMI measurements," *Energy & Fuels*, vol. 30, pp. 10200–10214, 2016.

[53] J. F. McLaughlin, S. Quillinan, and R. Surdam, "Characterizing diagenesis and its opposing impacts on porosity in the Weber and Madison Formations in southwest Wyoming: Applying geochemical, petrographic, and isotopic analysis to describe reservoir heterogeneity in potential CO_2 storage sites," *GSA Annual Meeting in Charlotte*, 2012.

[54] J. F. McLaughlin, R. D. Bentley, and S. A. Quillinan, "Regional geologic history, CO_2 source inventory, and groundwater risk assessment of a potential CO_2 sequestration site on the Rock Springs Uplift in southwest Wyoming," in *Geological CO_2 Storage Characterization*. Springer, 2013, pp. 33–54.

[55] L. Luquot, O. Rodriguez, and P. Gouze, "Experimental characterization of porosity structure and transport property changes in limestone un-

dergoing different dissolution regimes," *Transport in Porous Media*, vol. 101, no. 3, pp. 507–532, 2014.

[56] P. Gouze and L. Luquot, "X-ray microtomography characterization of porosity, permeability and reactive surface changes during dissolution," *Journal of Contaminant Hydrology*, vol. 120, pp. 45–55, 2011.

[57] A. J. Luhmann, X.-Z. Kong, B. M. Tutolo, N. Garapati, B. C. Bagley, M. O. Saar, and W. E. Seyfried, "Experimental dissolution of dolomite by CO_2-charged brine at 100 C and 150 bar: Evolution of porosity, permeability, and reactive surface area," *Chemical Geology*, vol. 380, pp. 145–160, 2014.

Appendix VI

Results and Analyses of the Geomechanical Experiments

List of Acronyms

c	Inherent shear strength
DH	Horizontal dolomite sample of Madison Limestone
ε_a	Axial strain
ε_v	Total volumetric strain
ε_{cd}	Crack damage axial strain
E_{pk}	Axial strain at the peak strength
ε_{pk}	Axial strain coressponding to the peak deviatoric stress
E	Young's modulus
K_b	Bulk modulus
LVDT	Linear variable differential transformer
P_c	Confining pressure
P_p	Pore pressure
SH	Horizontal sandstone sample
SV	Vertical sandstone sample
UCS	Uniaxial compressive strength
σ_{cd}	Crack damage strength
σ_{pk}	Peak strength
σ_r	Residual strength
ϕ	Internal friction angle
υ	Poisson's ratio

Executive Summary

Carbon dioxide (CO_2) injection into reservoirs may lead to mechanical, chemical, and hydrological effects on the host and seal formations, both in the short- and long-term. Numerous studies have shown that no significant effect of CO_2 on the mechanical properties (including elastic constants and uniaxial compressive strength, UCS) of reservoir rocks is observed. However, the research on investigating the effect of CO_2 on nonlinear plastic regime, post-failure behavior, and coefficients in Mohr-Coulomb failure criterion of reservoir rocks is inconclusive. To comprehensively investigate the effect of CO_2 on mechanical properties of two reservoirs, the Weber Sandstone and Madison Limestone from the Rock Springs Uplift, Wyoming, a potential site for carbon sequestration, were selected in this study. The purpose of this project (DE-FE0023328) is to determine the effect of CO_2 on the geomechanical characteristics of these two formations. In this Appendix, we present results of geomechanical experiments of Weber Sandstone and Madison Limestone and data analyses to determine the effect of CO_2 on their geomechanical behaviors.

Eleven Weber Sandstone plugs were prepared at both horizontal and vertical orientations to the rock cores while six dolomite plugs from Madison Limestone were prepared only at the horizontal orientation. Plugs of each formation were divided into two groups that were aged with brine for 800 hours and brine saturated with CO_2 for 800 hours. Triaxial compression tests were conducted at three confining stress conditions and at in situ temperature and pore pressure. Each triaxial test was conducted at three loading stages to enable us to determine poroelastic and elastic properties as well as strength parameters.

The experimental results conclude that the effect of CO_2 generally increases the Young's modulus and decrease the Poisson's ratio of sandstone samples in the elastic regime. However, similar trends were not observed in dolomite samples. The effect of CO_2 on the geomechanical properties of reservoir rocks at both nonlinear plastic and post-failure regimes cannot be generally concluded. However, the effect of CO_2 on the geomechanical properties of dolomite samples is more significant than that of the sandstone samples. The trend of decreasing cohesion and increasing friction angle due to CO_2 was observed on both sandstone and dolomite samples.

1. Introduction

Greenhouse Gases (GHGs) emissions, as the inevitable results of burning fossil fuels, which currently play an essential role on providing energy in the United States, raise public concern because it could lead to some environmental issues, such as climate change. According to the United States Environmental Protection Agency, carbon dioxide (CO_2) accounted for 82 percent of U.S. GHGs emissions in 2012. Therefore, reducing CO_2 emission level has become an urgent issue especially for balancing between future energy security and environmental impacts due to increasing concentrations of GHGs in the atmosphere. Carbon capture and sequestration (CCS), as an option of reducing CO_2 emissions, has been investigated in recent years. CO_2 injection into clastic hydrocarbon reservoirs may lead to mechanical, chemical, and hydrological effects on the host and seal formations, both in the short- and long-term (Johnson et al., 2004).

Numerous studies (Busch et al., 2014; Erickson et al., 2015; Hangx et al., 2010, 2013, 2014, 2015; Marbler et al., 2013; Mikhaltsevitch et al., 2014) have shown inconclusive effect of CO_2 on the mechanical properties (including elastic constants and uniaxial compressive strength, UCS) of reservoir sandstones. For example, Hangx et al (2013) compared laboratory measured elastic constants, including Young's modulus (E), Poisson's ratio (υ), and bulk modulus (K_b), of Captain Sandstone samples after flowing-through with brine and CO_2-saturated brine. The mechanical parameters did not consistently reduce as the result of CO_2, and their changes were insignificantly small ($E = 18.4 \pm 3.1$ GPa; $\upsilon = 0.22 \pm 0.03$; $K_b = 11.2 \pm 3.1$ GPa). Cerasi et al. (2016) indicated that no dramatic reduction in the uniaxial compressive strength (UCS) of Berea Sandstone was observed due to an aggressive CO_2-flood procedure. The UCS values of the Berea Sandstone saturated with brine and CO_2-saturated brine are 56.7 MPa and 55.7 MPa, respectively. However, limited investigations are conducted to understand the effect of CO_2 on nonlinear plastic regime, post-failure behavior, and coefficients in Mohr-Coulomb failure criterion of reservoir rocks.

For limestone, the permeability and porosity increase (Luquot et al., 2013; Luquot and Gouze, 2009) and elastic properties decrease (Vialle et al., 2014) due to the presence of CO_2 (Luquot et al., 2013; Luquot and Gouze, 2009). Similarly, Vialle and Vanorio (2011) indicated that, for carbonate rocks, rock porosity and permeability increase and rock strength decreases due to CO_2 injection.

For the study described in this Appendix, 11 Weber Sandstone samples and six dolomite samples of Madison Limestone from the Rock Springs Uplift, Wyoming, were prepared. Rock plugs of each formation were divided into two groups that were aged with brine for 800 hours and brine saturated with CO_2 for 800 hours. Triaxial compression tests were conducted at three confining stress conditions and at in situ temperature and pore pressure. The effect of CO_2 on the mechanical behavior of reservoir rocks under three differential pressures (6.9, 34.5 and 55.2 MPa) and two orientations (vertical and horizontal) was compared and investigated based on quantified mechanical properties, including elastic constants at the linear stress-strain regime and strength properties at nonlinear plastic and post-failure regimes. The effect of CO_2 on coefficients of Mohr-Coulomb failure criterion of reservoir rocks was also investigated.

2. Geological Background and Laboratory Experiments

2.1 Geological background

The Rock Springs Uplift (RSU), located in Wyoming Greater Green River Basin shown in Figure 1, is a north-south plunging, asymmetric anticline formed during the late Cretaceous to early Tertiary from the uplift of a basement-core thrust fault. The geologic structure and lithology of RSU meet the screening criteria for CO_2 sequestration (Bachu, 2002, 2008). A stratigraphic test well (RSU #1) was drilled on the northeast flank of the RSU for the purpose of obtaining rock cores, well logs, image logs, fluid samples and microfrac tests to identify possible target zones for CO_2 sequestration. The potential reservoirs for the long-term CO_2 injection and sequestration are the Weber Sandstone and Madison Limestone. These formations had been analyzed for mechanical stratigraphy, fracture systems, and in-situ stress conditions at the RSU #1 well location. The detailed description of the geology of the RSU site can be found in Shafer (2013) and Grana et al. (2017). The studies of stratigraphic and sedimentologic characteristics of the Weber Sandstone can be found in Zahm and Hennings (2009).

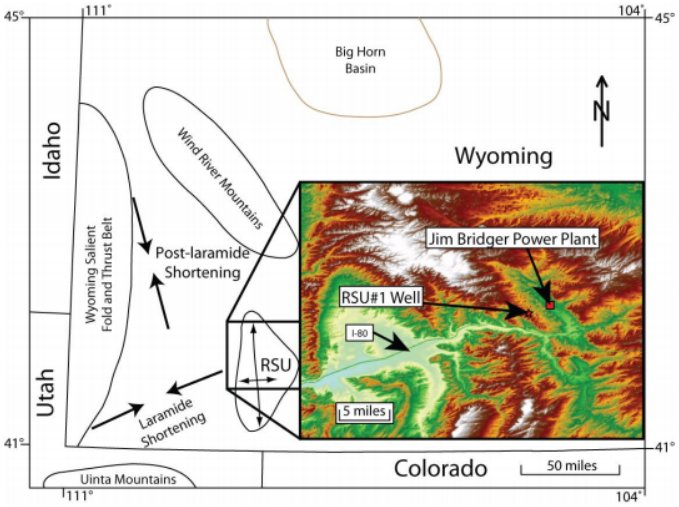

Figure 1. Wyoming map showing the RSU, paleo-stress direction and RSU #1 well (after Shafer, 2013).

2.2 Rock samples and laboratory experiments

Rock cores obtained from the Weber Sandstone and Madison Limestone from the RSU were used in this study. Rock plug samples were prepared using a rock core drill machine to 25.4 mm diameter and 50.8 mm in length (ASTM D4543-08). All rock samples were cleaned in soxhlet extractors using toluene and methanol until the plugs are clean for at least two weeks. After that, plugs were oven-dried at 100°C for at least 24 hrs. As shown in Table 1, rock samples were divided into two groups: Group 1 aged with brine and Group 2 aged with brine and CO_2. Aging process was conducted in a high pressure and high temperature core flooding system at the University of Wyoming as shown in Figure 2. Each rock plug wrapped with heat shrinkage tube and Teflon sleeve was loaded inside the coreholder. After applying 3.5 MPa confining pressure, rock plugs were vacuum-saturated to 100% saturation with synthetic brine. Then pore and confining pressure were increased in small steps, typically 0.69 to 1.38 MPa at a time using high precision syringe pumps (Teledyne ISCO 260D, Lincoln, NE, USA) until the test conditions were met without fluid flow. At the same time, temperatures were increased to in-situ

temperature of 90°C. Samples in Group 1 were left in the coreholder for 800 hours with brine under test conditions. For Group 2 samples, they were aged with brine for 400 hours first. Afterward, the reactant fluid (compressed CO_2-saturated brine), which was generated through equilibrium between the brine and CO_2 phases for 24 hours in a Vinci floating piston accumulator, was injected through the sample. The injection was stopped until a constant CO_2 production rate was reached. Finally, the samples in Group 2 were aged for another 400 hours with the reactant fluid.

After the geochemical preparation, triaxial compression tests were conducted in the laboratory at the University of Wyoming. Geomechanical experiments were conducted to investigate stress-strain behaviors under different stress conditions and quantify the relevant mechanical properties of rock samples. The temperature of the confining fluid was raised at a rate of 1.5°C per minutes until it attained the target in-situ temperature. The temperature of the system was then allowed to reach thermal equilibrium. The sample was judged to be at thermal equilibrium when readings of two axial linear variable differential transformers (LVDTs) and one radial LVDT were within 1% of each other; this procedure took approximately four hours. Each complete geomechanical experiment was conducted in three continuous stages. In Stage 1, confining pressure (P_c) was increased at a rate of 5 MPa per minute as recommended by Fabre and Gustkiewicz (1997) until it reached the target value while the pore pressure (P_p) was kept constant at 0.34 MPa. In Stage 2, the P_p was increased at a rate of 5 MPa per minute until it reached the target value while the P_c was kept constant. In Stage 3, a triaxial compression test under drained condition was performed with the axial strain (ε_a) control at a rate of 0.2% per minute. Table 1 summarizes the RSU rock samples and geomechanical test conditions.

Figure 2. The core flooding system at the University of Wyoming.

Table 1. Rock samples and geomechanical test conditions of RSU rock samples.

Geochemical Preparation	Sample ID	Depth (m)	P_c (MPa)	P_p (MPa)	T (°C)
Group1: Aged with brine	SV1b	3415.6-3417.5	43.4	35.4	90
	SH1b	3413.8-3415.6			
	SV2b	3413.8-3415.6	71.0		
	SH2b	3413.8-3415.6			
	SV3b	3413.8-3415.6	91.7		
	SH3b	3413.8-3415.6			
	DH1b	3765.1-3767.0	46.2	39.3	93
	DH2b	3784.4-3786.2	73.8		
	DH3b	3763.4-3765.9	94.5		
Group2: Aged with brine-CO_2	SV1c	3413.8-3415.6	43.4	35.4	90
	SH1c	3413.8-3415.6			
	SV2c	3413.8-3415.6	71.0		
	SH2c	3526.4-3528.2			
	SH3c	3413.8-3415.6	91.7		
	DH1c	3765.1-3767.0	46.2	39.3	93
	DH2c	3765.1-3767.0	73.8		
	DH3c	3765.1-3767.0	94.5		

SV–Vertical sandstone; SH–Horizontal sandstone; DH–Horizontal dolomite; b–Aged with brine; c–Aged with brine-CO_2; P_c–Confining pressure; P_p–Pore pressure; and T–Temperature.

3. Test Results and Discussion

3.1 Poroelastic stress-strain behaviors

The stress-strain behaviors of RSU rock samples aged with brine and brine-CO_2 in Stage 1 and Stage 2 are shown in Figure 3 for vertical sandstone (SV) samples, Figure 4 for horizontal sandstone (SH) samples, and Figure 5 for horizontal dolomite (DH) samples. The poroelastic behaviors of SV samples aged with brine under three hydrostatic compression test conditions are shown in Figure 3(a) and Figure 3(b) for Stage 1 and Stage 2 loading conditions, respectively. Figure 3(a) shows that the P_c increases with the increase in the volumetric strain (ε_v), indicating rock compression or decrease in rock volume. The convex P_c-ε_v curves indicate that the gradient increases initially and reaches a constant value toward the end of Stage 1 loading. The P_c-ε_v curves of SV1b and SV2b are almost identical, indicating a similar microstructure of these two samples at a relatively low confining pressure or volumetric strain. Figure 3(b) shows the increase in P_p with respect to the decrease in the volumetric strain (i.e., rock expansion or increase in rock volume). For each SV sample, the P_c increased to its maximum target value in Stage 1 followed by increasing the P_p to its target value in Stage 2. The fluctuation observed in SV2b at the end of the P_c-εv curve continues in the P_p-ε_v curve. The fluctuation could be attributed to the effect of pore collapse as a result of increasing P_c and ε_v. The ε_v decreases with increasing P_p. However, a smaller decrease in the ε_v is observed at a higher P_c. This phenomenon could be attributed to the effect of applying a higher P_c on the initial microcracks, which are difficult to reopen by the subsequent increase in the P_p. At a high P_c, the minerals in the porous granular rock are also harder to be rearranged by the increasing P_p (i.e., the rock frame becomes stiffer under the high P_c). The nonlinearity of the P_p-ε_v curves decreases with the increase in the

P_c value. In other words, the nonlinear P_p-ε_v relationship at a lower P_c condition changes to an almost linear relationship at a higher P_c condition.

Similar P_c-ε_v and P_p-ε_v relationships are observed on SV samples aged with brine-CO_2. Fluctuation of measurements was not observed. Rock compression was experienced in Stage 1 loading and rock expansion was observed in Stage 2 loading. The convex and almost identical P_c-ε_v relationships were observed for both SV1c and SV2c, again indicating the similar microstructure of these two samples. P_p-ε_v curves change from a nonlinear relationship at a lower P_c to an almost linear relationship at a higher P_c.

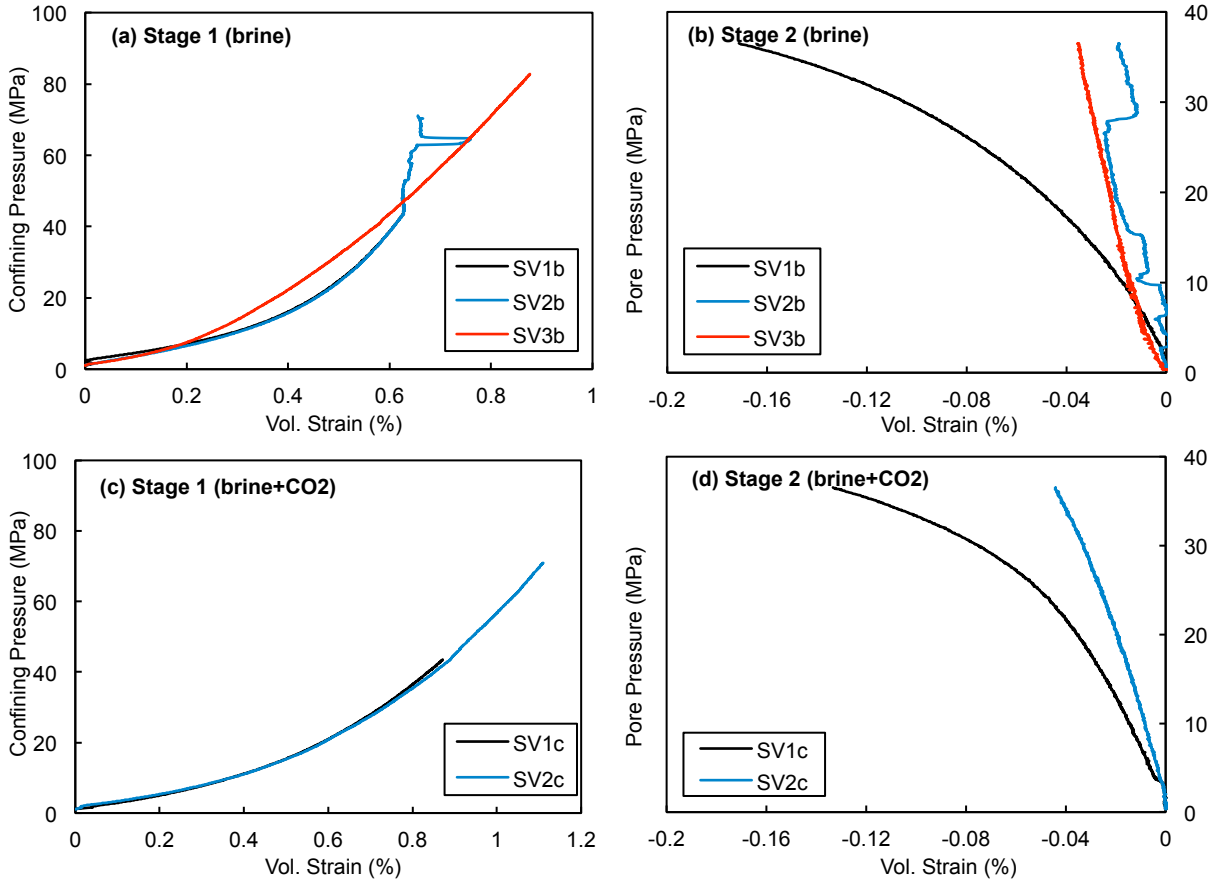

Figure 3. Stress-strain curves of (a) SV Samples aged with brine in Stage 1, (b) SV Samples aged with brine in Stage 2, (c) SV Samples aged with brine-CO_2 in Stage 1, and (d) SV Samples aged with brine-CO_2 in Stage 2.

The poroelastic behaviors of SH samples are presented in Figure 4. Similar P_c-ε_v and P_p-ε_v relationships were observed in all SH samples except SH3b subjecting to the highest P_c value of 91.7 MPa (Figure 4a). The sudden decrease in the ε_v or rock expansion during the mid of Stage 1 loading on SH3b could be attributed to the rapid buildup of excess pore fluid pressure inside pore spaces that are either isolated or lack connected networks for fluid drainage and dissipation of excess pore fluid pressure. The excess pore fluid pressure induced by the increase in P_c causes the decrease in the ε_v or expands the rock matrix.

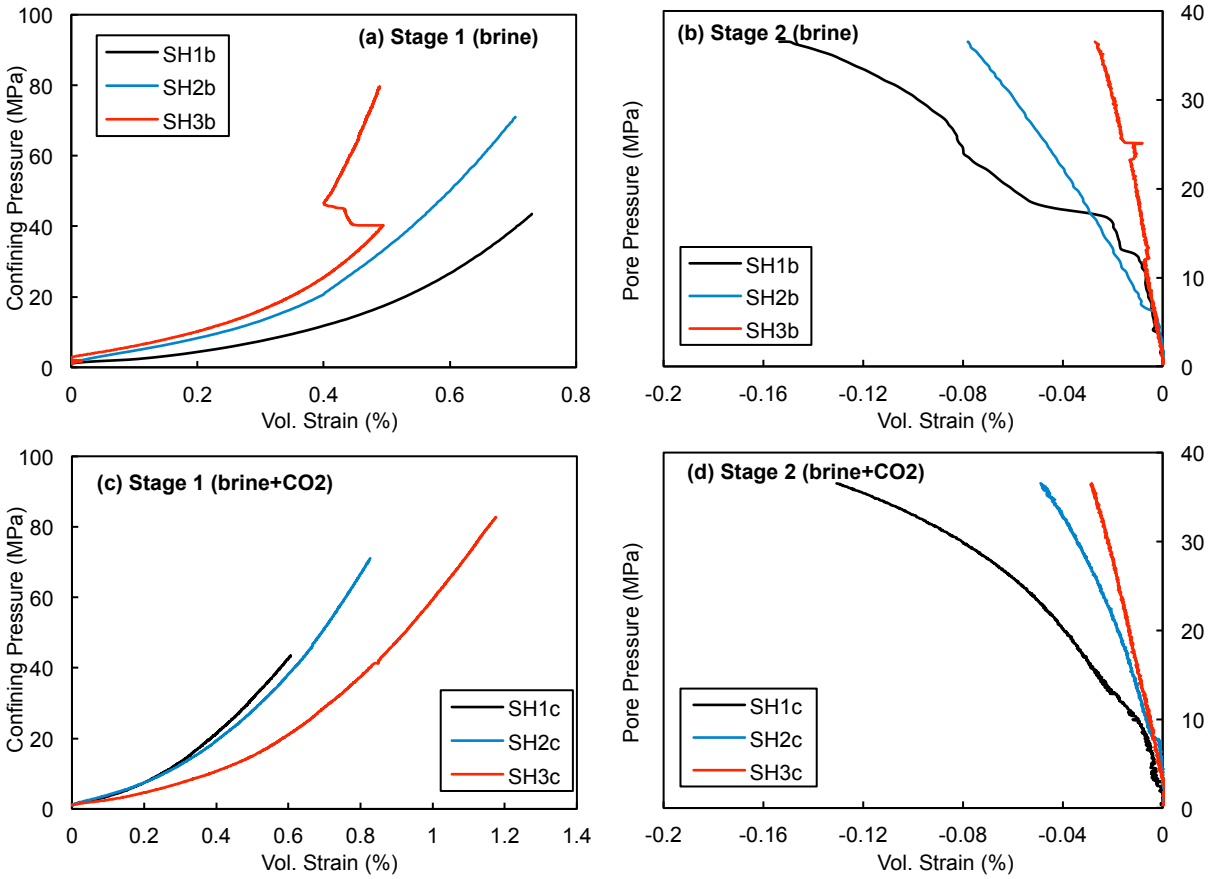

Figure 4. Stress-strain curves of (a) SH Samples aged with brine in Stage 1, (b) SH Samples aged with brine in Stage 2, (c) SH Samples aged with brine-CO_2 in Stage 1, and (d) SH Samples aged with brine-CO_2 in Stage 2.

The poroelastic behaviors of DH samples are presented in Figure 5. The convex P_c-ε_v relationships obtained from Stage 1 loading were observed in all DH samples except DH2b subjecting to a moderately high P_c of 71 MPa (Figure 5a). The hypothesis of building up excess pore fluid pressure in pore spaces leading to the sudden decrease in the ε_v observed in SH3b explains the similar phenomenon observed in DH2b. The P_p-ε_v relationships of DH samples aged with brine shown in Figure 5(b) do not follow the consistent trend of shifting from a nonlinear to linear relationship with the increase in P_c. Particularly, a relatively high decrease in the volumetric strain or rock expansion is observed in DH3b during the initial increase in P_p to about 5 MPa (Figure 5b). This phenomenon could be attributed to a higher compliant porosity than its stiff porosity. The increase in P_p initiates the propagation of cracks from the existing compliant pores in DH3b sample and expands the rock matrix which leads to the decrease in the ε_v. In the case of DH samples aged with brine-CO_2, the P_p-ε_v relationships follow the typical trend.

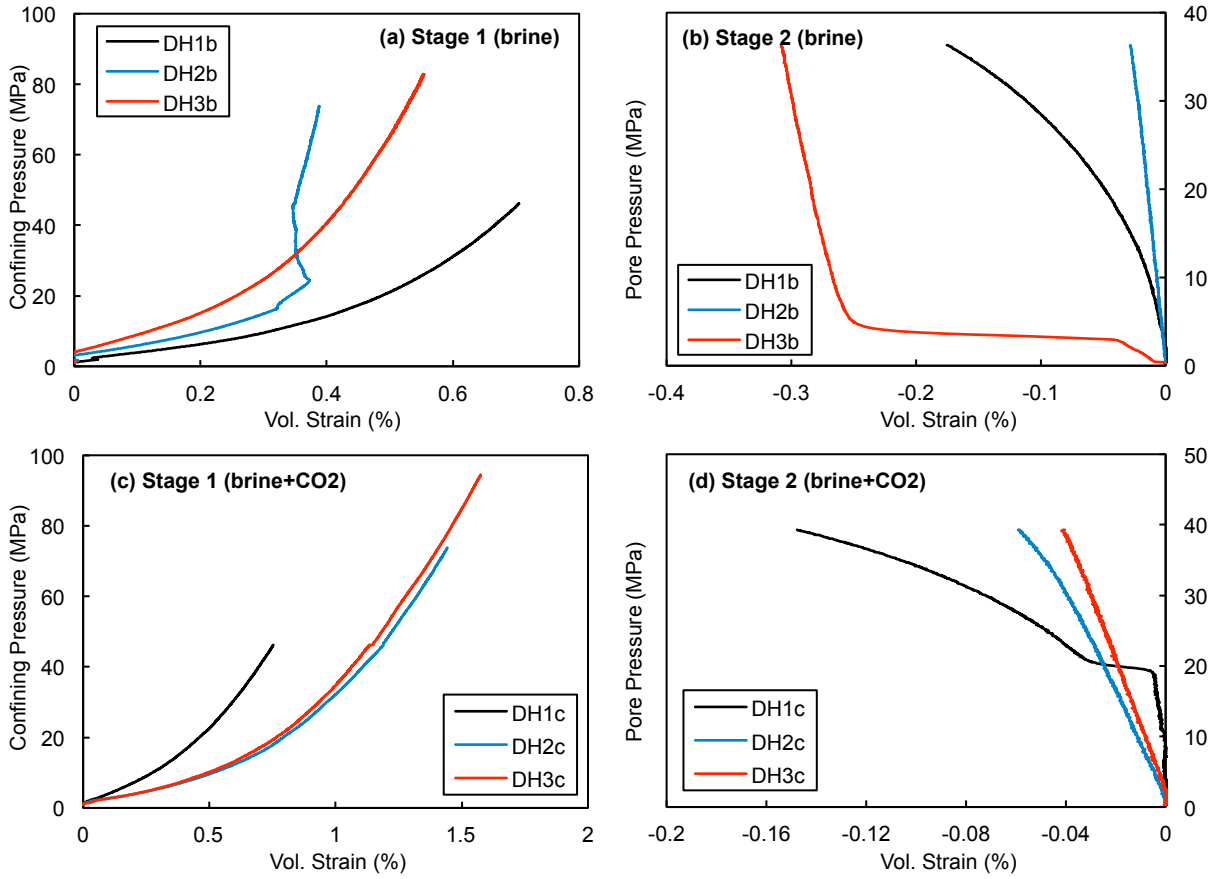

Figure 5. Stress-strain curves of (a) DH Samples aged with brine in Stage 1, (b) DH Samples aged with brine in Stage 2, (c) DH Samples aged with brine-CO_2 in Stage 1, and (d) DH Samples aged with brine-CO_2 in Stage 2.

3.2 Deviatoric stress-strain behaviors

The deviatoric stress-strain behaviors of SV samples aged with brine and brine-CO_2 under different confining stress states are shown in Figure 6. The positive axial strain indicates axial compression while the negative radial strain indicates radial expansion. The strains began with an initial non-linear behavior due to the closure of microcracks. The strains continued to increase along a linear relationship with the deviatoric stress before reaching the well-defined peak deviator stresses. Comparing the results between Figure 6(a) and Figure 6(c) for SV samples aged with brine and between Figure 6(b) and Figure 6(d) for SV samples aged with brine-CO_2, the peak strength (σ_{pk}) and the axial strain at the peak strength (ε_{pk}) increase with the increase in the P_c. At the lowest P_c of 43.4 MPa, the σ_{pk} values decrease from 282.7 MPa of SV1b (Figure 6(a)) to 232.2 MPa of SV1c (Figure 6(b)). However, the trend of σ_{pk} values reverses at a higher P_c of 71 MPa (Figure 6(c) and Figure 6(d)); the σ_{pk} values increase from 440.3 MPa of SV2b (Figure 6(c)) to 482.7 MPa of SV2c (Figure 6(d)). Since the post failure behavior is not important for the application in the CCS, post failure results are excluded in the plots. Nevertheless, brittle failures are observed in all SV samples.

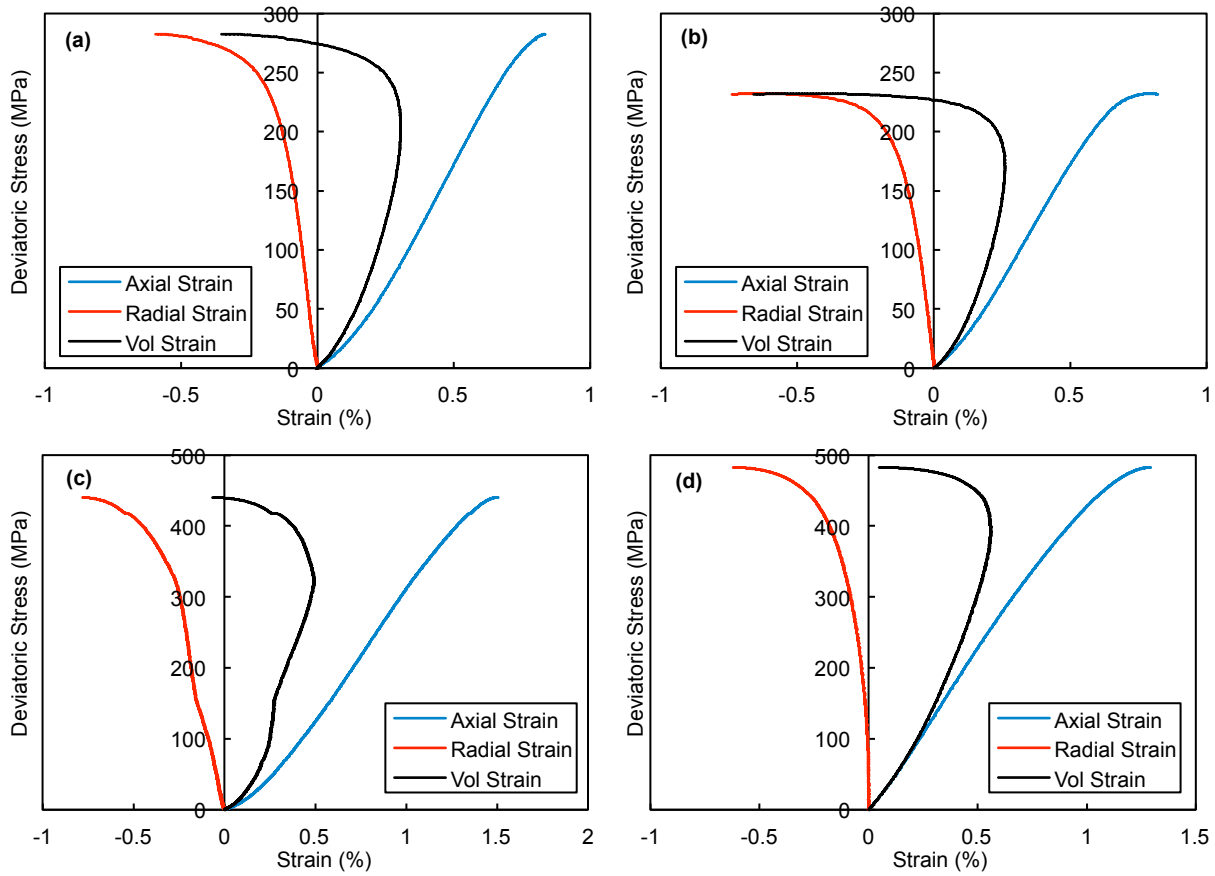

Figure 6. Deviatoric stress-strain results from triaxial compression tests (Stage 3) of (a) SV1b, (b) SV1c, (c) SV2b, and (d) SV2c.

The deviatoric stress-strain behaviors of SH samples aged with brine and brine-CO_2 under different confining stress states are shown in Figure 7. Typical deviatoric stress-strain relationships are observed in all SH samples. Regardless of the two different aging conditions, Figure 7 shows that σ_{pk} and ε_{pk} increase with the increase in the P_c except in the case of SH3b. The exception is attributed to the abnormal geomechanical response of SH3b observed in Stage 1 loading (Figure 4(a)). The propagation and joining of isolated microcracks due to excess pore fluid pressure buildup and subsequent pore fluid filling in SH3b are believed to cause the sudden decrease in the volumetric strain and subsequent reduction in the σ_{pk} and ε_{pk}. The effects of CO_2 and P_c on SH samples are similar to that of SV samples. At the lowest P_c of 43.4 MPa, the σ_{pk} values decrease from 302.6 MPa of SH1b (Figure 7(a)) to 234.5 MPa of SH1c (Figure 7(b)). At the higher P_c values of 71 MPa and 91.7 MPa, the σ_{pk} values increase as a result of aging with brine-CO_2.

The observed deviatoric stress-axial strain behaviors are broadly similar for all sandstone rock samples under different P_c values. After the initial non-linear behavior due to the closure of cracks, rock samples show linearly elastic loading behavior to axial strains, followed by the departure from linearity and subsequent failure, marked by well-defined peak shear strengths. The unstable stress drop (i.e., brittle failure) was observed in all sandstone samples. For rocks under the same geochemical condition, σ_{pk} increases with increasing P_c. For the deviatoric stress-

volumetric strain behaviors shown in Figure 6, Figure 7 and Figure 8, the ε_v increases in the beginning of applying the deviatoric stress and decreases after reaching the crack damage strength. The detailed discussion of the effect of CO_2 on the geomechanical properties of SH and SV samples is provided in Section 3.3.

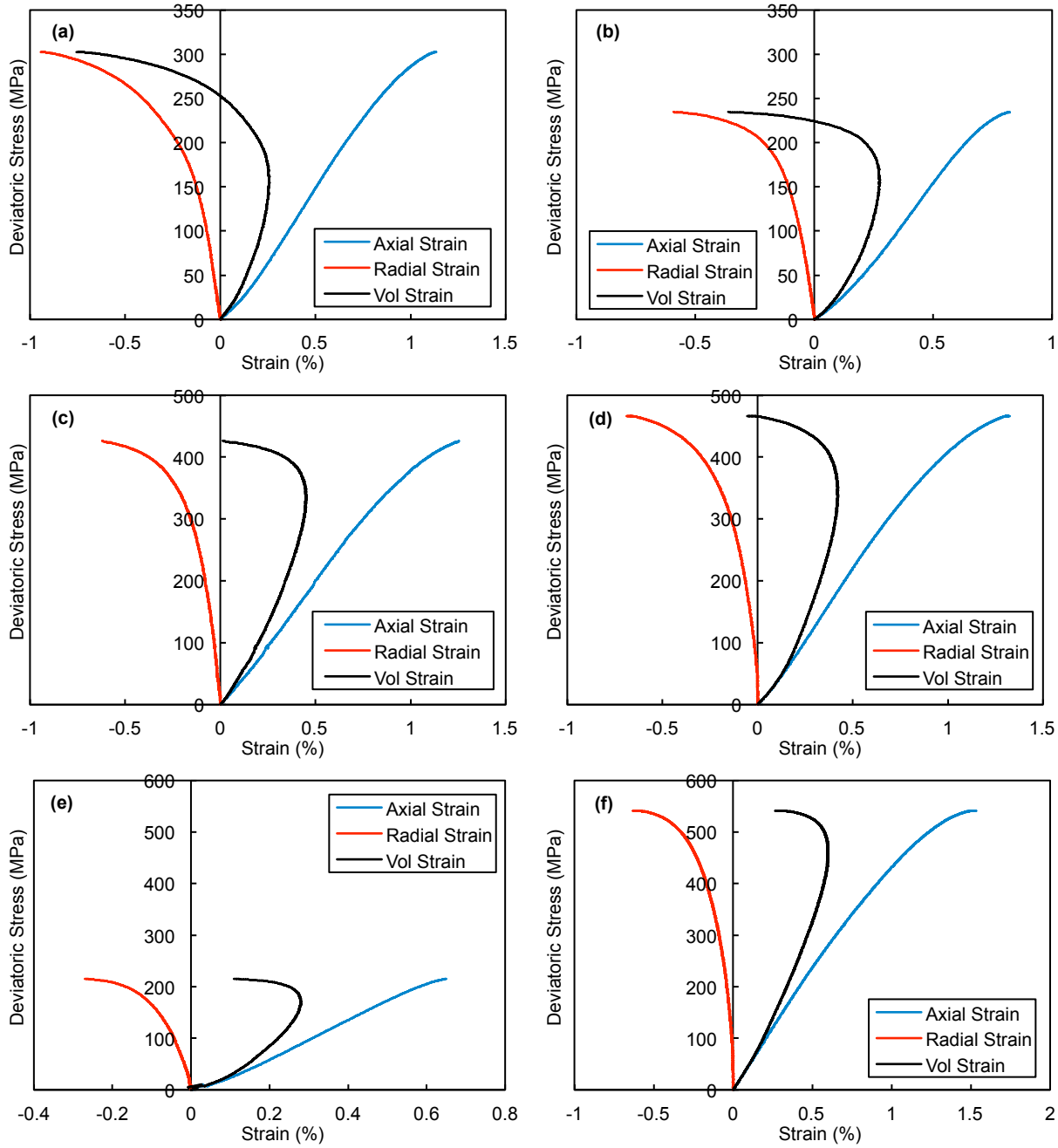

Figure 7. Deviatoric stress-strain results from triaxial compression tests (Stage 3) of (a) SH1b, (b) SH1c, (c) SH2b, (d) SH2c, (e) SH3b, and (f) SH3c.

The deviatoric stress-strain behaviors of DH samples are presented in Figure 8. For the DH samples aged with brine, brittle failures are observed. The σ_{pk} values increase with increasing P_c (Figure 8(a) and Figure 8(e)) except in the case of DH2b which experiences an abnormal P_c-ε_v response during Stage 1 loading (Figure 5(a)). Similar to that of SH3b, the sudden decrease in ε_v as a result of propagation and joining of isolated microcracks, induced by the excess pore fluid pressure buildup, leads to the reduction in shear strength. On the other hand, the deviatoric stress-strain behaviors of DH1c, DH2c and DH3c samples aged with brine-CO_2, shown in Figure 8(b), Figure 8(d) and Figure 8(f) respectively, deviate from the typical deviatoric stress-strain trend of a brittle failure. A brittle-ductile transition was observed from a "brittle" failure in DH1c to a ductile failure in DH3c as illustrated by the reduction in the differences between σ_{pk} and σ_r or the diminishing of the σ_{pk} with increasing P_c. Furthermore, the σ_{pk} of DH samples aged with brine-CO_2 decreases with increasing P_c while the difference in the σ_{pk} values of DH2c and DH3c is minimal. The detailed discussion of the effect of CO_2 on the geomechanical properties of DH samples is provided in Section 3.3.

3.3 Elastic constants and strength properties

Table 2 summarizes the mechanical properties of the RSU rock samples. For rocks with same orientation and geochemical preparation, considering the effect of P_c on the geomechanical properties of Weber Sandstone samples except SV samples aged with brine (i.e., SV1b and SV2b), E increases and υ decreases with increasing Pc for rocks under the linear elastic regime. However, under the nonlinear plastic regime except for DH2b and SH3b that experienced abnormal P_c-ε_v responses described in Section 3.2, crack damage strength (σ_{cd}), crack damage strain (ε_{cd}), σ_{pk}, and ε_{pk} of these rocks increase with increasing P_c. For the post-failure behavior, the stable residual strength (σ_r) of SV2b and SH2c samples cannot be determined. For vertical sandstone samples aged with brine-CO_2 (i.e., SV1c and SV2c), σ_r significantly increases from 41.7 MPa to 195.7 MPa with increasing P_c. For horizontal sandstone samples aged with brine (i.e., SH1b and SH2b), σ_r also significantly increases from 46.1 MPa to 174.2 MPa with increasing P_c.

Considering the effect of CO_2 on the geomechanical properties of sandstone samples with the same orientation and stress conditions, except the SV1b and SV1c with a minimal difference in the E values, the estimated E values generally increase as the result of CO_2. On the other hand, the υ values generally decrease as the result of CO_2. In particular, significant differences in E and υ were observed in SV2b and SV2c with E increases from 31.4 MPa to 48.5 MPa and υ decreases from 0.29 to 0.14. Furthermore, E (31.4 GPa) of SV2b is lower than the E values of SV2c, SH2b, and SH2c under the same P_c of 71.0 MPa. Comparing the results of SV2b and SV2c, the change in elastic constants may not solely attributed to the effect of CO_2 but could be attributed to the unique physical property of SV2b. For DH samples, consistent trend of E and υ values cannot be observed. The E increases and υ decreases at a lower P_c state while at the higher P_c states, the E decreases and υ increases as the result of CO_2.

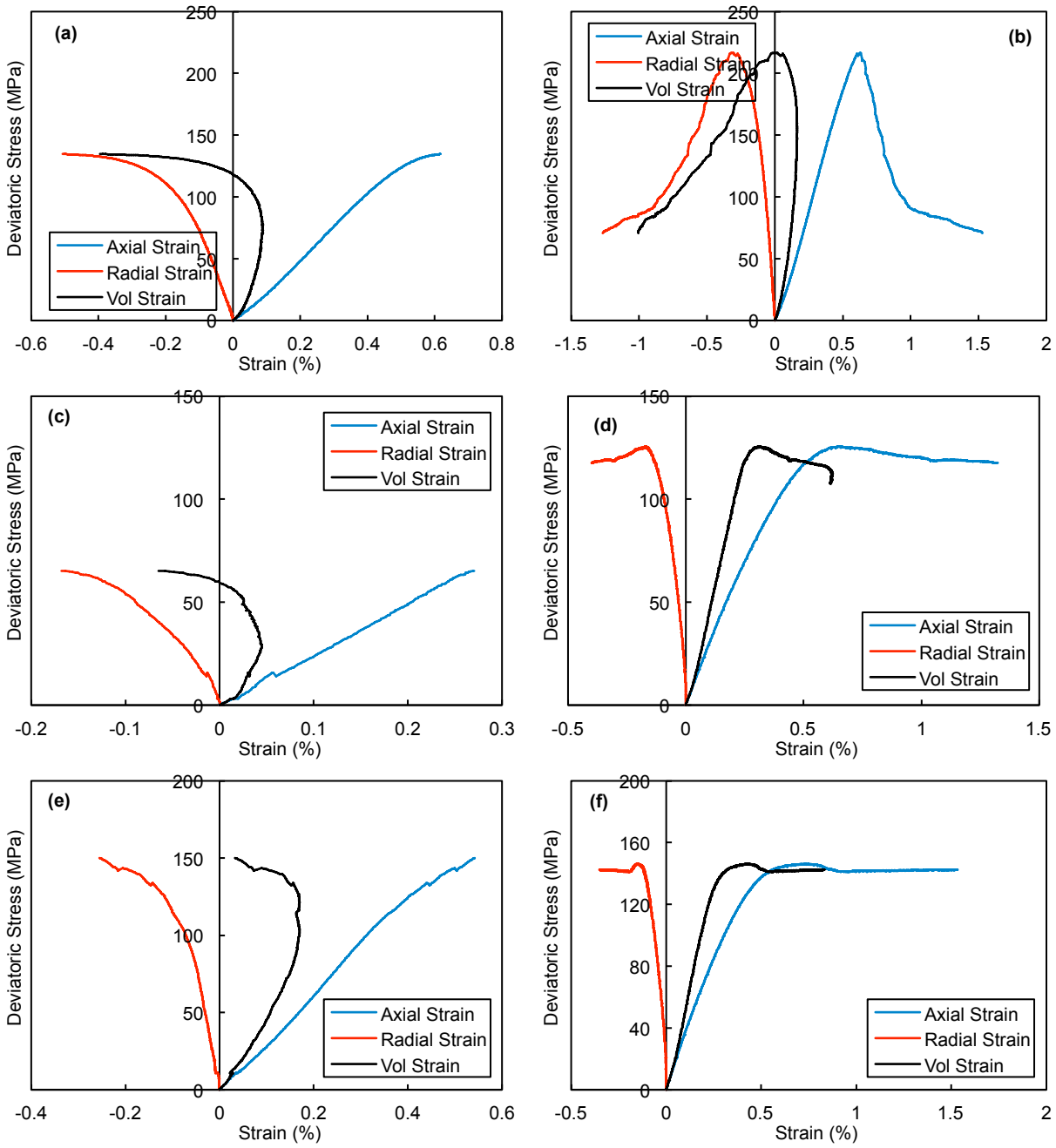

Figure 8. Deviatoric stress-strain results from triaxial compression tests (Stage 3) of (a) DH1b, (b) DH1c, (c) DH2b, (d) DH2c, (e) DH3b, and (f) DH3c.

Table 2. Summary of triaxial test results of RSU samples aged with brine and brine-CO_2

Sample ID	E (GPa)	υ	σ_{cd} (MPa)	$\Delta\sigma_{cd}$ (%)	ε_{cd} (%)	$\Delta\varepsilon_{cd}$ (%)	σ_{pk} (MPa)	$\Delta\sigma_{pk}$ (%)	ε_{pk} (%)	$\Delta\varepsilon_{pk}$ (%)	σ_r (MPa)	$\Delta\sigma_r$ (%)
SV1b	42.1	0.24	208.4	-19.4	0.58	-15.5	282.7	-17.9	0.83	-7.2	77.1	-45.9
SV1c	40.1	0.29	168.0		0.49		232.2		0.77		41.7	
SH1b	33.9	0.30	146.3	8.0	0.53	-3.8	302.6	-22.5	1.13	-27.4	46.1	74.8
SH1c	36.1	0.29	158		0.51		234.5		0.82		80.6	
DH1b	27.8	0.42	71.9	114.6	0.29	41.4	134.7	60.7	0.62	1.6	59.5	43.5
DH1c	41.0	0.31	154.3		0.41		216.5		0.63		85.4	
SV2b	31.4	0.29	320.9	21.3	1.03	-14.6	440.3	9.6	1.50	-14.0	#	#
SV2c	48.5	0.14	389.1		0.88		482.7		1.29		195.7	
SH2b	41.5	0.19	335.4	4.8	0.85	-3.5	426.7	9.4	1.25	5.6	174.2	#
SH2c	47.4	0.22	351.5		0.82		466.7		1.32		#	
DH2b[$]	24.6	0.42	29.3	NA	0.12	NA	65.2	92.6	0.27	129.6	#	NA
DH2c	24.5	0.26	NA		NA		125.6		0.62		NA	
SH3b[$]	37.8	0.20	174.6	163.6	0.50	118.0	214.9	152.0	0.65	135.4	34.0	551
SH3c	47	0.16	460.3		1.09		541.5		1.53		221.4	
DH3b	34.2	0.22	102.7	NA	0.32	NA	150.0	-2.5	0.54	35.2	#	NA
DH3c	29.7	0.25	NA		NA		146.2		0.73		NA	

E–Young's modulus; υ–Poisson's ratio; σ_{cd}–Crack damage strength; ε_{cd}–Crack damage strain; σ_{pk}–peak strength; ε_{pk}–Axial strain corresponding to peak strength; σ_r–Residual strength; Δ–Percent difference in strength or strain; #–No stable daviatoric stress was measured; [$]–Sample experienced abnormal P_c-ε_v response; and NA–Not applicable due to a ductile behavior.

For rocks under the nonlinear plastic regime (until reaching the failure strength), σ_{cd}, σ_{pk} and corresponding axial strains (ε_{cd} and ε_{pk}) were used to investigate the effect of CO_2 on the geomechanical behavior of rocks. To quantify the effect of CO_2 on the stress and strain data of rocks in the plastic regime, the change in deviatoric stress (or axial strain) is determined by

$$\Delta\sigma(\text{or }\Delta\varepsilon) = \frac{\sigma(\text{or }\varepsilon)_c - \sigma(\text{or }\varepsilon)_b}{\sigma(\text{or }\varepsilon)_b} \times 100\% \quad (1)$$

where $\sigma(\text{or }\varepsilon)_c$ is measured deviatoric stress (or axial strain) data of rocks aged with brine-CO_2, and $\sigma(\text{or }\varepsilon)_b$ is measured deviatoric stress (or axial strain) data of rocks aged with brine. Therefore, the positive value of $\Delta\sigma(\text{or }\Delta\varepsilon)$ indicates that the stress (or strain) increases as the result of CO_2. Calculated $\Delta\sigma_{cd}$, $\Delta\varepsilon_{cd}$, $\Delta\sigma_{pk}$, and $\Delta\varepsilon_{pk}$ in percentage are summarized Table 2. Comparing the results of SV1b and SV1c, all Δσ (or Δε) values are negative. However, the all-negative trend was not observed on other samples. For example, the comparison of SH2b and SH2c shows that only $\Delta\varepsilon_{cd}$ is negative. Considering different orientations and P_c states, no consistent relationship between stress (or strain) data and CO_2 in the nonlinear plastic regime was observed. The differences in induced crack propagation governed by physical properties (e.g. initial crack density and crack geometry) of samples are believed the main factor causing the inconsistent result outcomes. In other words, the CO_2 is not the dominant factor that affects the plastic properties of rocks. The post-failure behavior of rocks is quantified and investigated

based on the residual strength (σ_r). No consistent trend was again observed. For example, σ_r decreases from 77.1 MPa of SV1b to 41.7 MPa of SV1c while σ_r increases from 46.1 MPa of SH1b to 80.6 MPa of SH1c. For DH samples, the change in the mechanical properties in the plastic regime due to CO_2 is more significant than that of the sandstone samples (Table 2). However, no consistent trend was observed.

3.4 Mohr-Coulomb failure criterion

Linearized Mohr-Coulomb failure envelopes (red lines) along with Mohr's circles at two differential pressures for rock samples are plotted in Figure 9. For SV samples aged with brine, the inherent shear strength (c) and internal friction angle (ϕ) were estimated as 47.0 MPa and 47.8° (Figure 9(a)). For SV samples aged with brine-CO_2, c and ϕ were estimated as 26.7 MPa and 55.0° (Figure 9(b)). For SH samples aged with brine-CO_2, c and ϕ were estimated as 57.9 MPa and 43.8° (Figure 9(c)). For SH samples aged with brine-CO_2, c and ϕ were estimated as 28.8 MPa and 53.9° (Figure 9(d)). For DH samples aged with brine, c and ϕ were estimated as 57.7 MPa and 7.9°. For DH samples aged with brine-CO_2, c and ϕ were estimated as 30.6 MPa and 50.4°. Table 3 summarizes the Mohr-Coulomb failure coefficients of RSU samples.

Comparing the Mohr failure envelopes plotted in Figure 9(a) and Figure 9(b) for SV samples, the effect of CO_2 on mechanical properties includes the decrease in c from 47.0 MPa to 26.7 MPa and the increase in ϕ from 47.8° to 55.0°. Comparing the Mohr failure envelopes plotted in Figure 9(c) and Figure 9(d), the effect of CO_2 decreases the c from 57.9 MPa to 28.8 MPa and increases the ϕ from 43.8° to 53.9°. Comparing the Mohr failure envelopes plotted in Figure 9(e) and Figure 9(f) for DH samples, the effect of CO_2 decreases the c from 57.7 MPa to 30.6 MPa and increases the ϕ from 7.9° to 50.4°. The consistent trend of decreasing c and increasing ϕ was observed in all sandstone and dolomite samples.

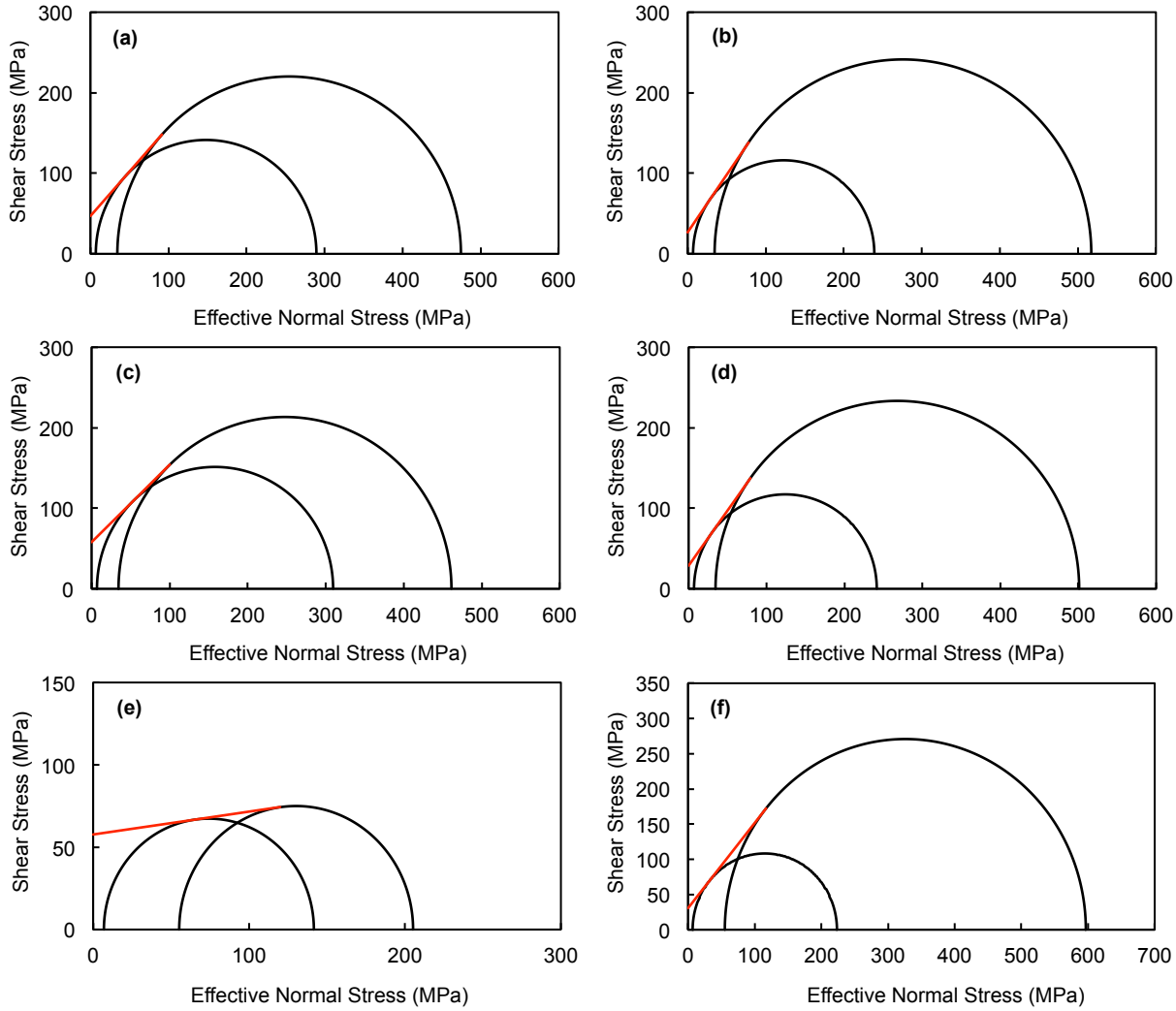

Figure 9. Linearized Mohr-Coulomb failure envelopes from triaxial compression tests of (a) SV samples aged with brine, (b) SV samples aged with brine-CO_2, (c) SH samples aged with brine, (d) SH samples aged with brine-CO_2, (e) DH samples aged with brine, and (f) DH samples aged with brine-CO_2.

Table 3. Summary of Mohr-Coulomb failure coefficients of RSU samples

Group	c (MPa)	ϕ (Deg.)
SV aged with brine	47	47.8
SV aged with brine and CO_2	26.7	55
SH aged with brine	57.9	43.8
SH aged with brine and CO_2	28.8	53.9
DH aged with brine	57.7	7.9
DH aged with brine and CO_2	30.6	50.4

4. Conclusions

To investigate the effect of CO_2 on geomechanical properties of reservoir rocks in RSU, Group 1 samples were aged with brine for 800 hours, and Group 2 samples were aged with brine-CO_2 for 800 hours. Triaxial compression tests were conducted to understand the stress-strain behaviors and quantify the geomechanical properties of Weber Sandstone and Madison Limestone. All geomechanical tests were conducted at reservoir conditions including temperature and P_p. Geomechanical properties were determined and investigated the effect of CO_2 on the linear elastic regime, plastic regime, and post-failure regime of rocks. The following conclusions are drawn from the experimental results:

1. Experimental results from the triaxial compression tests show that all sandstone samples exhibited nonlinear deviatoric stress-axial strain behavior in the beginning of applying the deviatoric load and followed by the linear elastic regime. After the linear stress-strain behavior, nonlinear plastic stress-strain behaviors were observed for all samples until reaching the peak (failure) strengths. Brittle failure (unstable stress drop) was observed on all sandstone samples. For the deviatoric stress-volumetric strain behavior, the volumetric strain increases in the beginning of increasing deviatoric stress and decreases after reaching the crack damage strength. For dolomite samples, DH2c and DH3c exhibit a brittle-ductile transition behavior.
2. For rocks with same orientation and geochemical preparation, except samples SV1b and SV2b, E increases and υ decreases with increasing P_c for rocks under linear elastic regime. For rocks under nonlinear plastic regime, σ_{cd}, ε_{cd}, σ_{pk}, and ε_{pk} increase with increasing P_c. However, no consistent trend was observed in the post-failure behavior of rocks in terms of σ_r as a result of increasing P_c.
3. For sandstone samples, considering the effect of CO_2 on the geomechanical properties of samples with same orientation and stress conditions, except the SV1b and SV1c, the estimated E values generally increase and the υ values generally decrease as the result of CO_2 under the linear elastic regime. Significant differences in E and υ were observed on SV2b and SV2c samples. Referring the unique stress-strain behavior of SV2b and estimated elastic constants, it is believed that the unique physical property of SV2b has a greater influence than the effect of CO_2 on geomechanical behavior of rocks. For dolomite samples, the change of elastic constants due to CO_2 is more significant than that of sandstone samples. However, no consistent trend was observed on the DH samples.
4. For sandstone samples, considering horizontal and vertical orientations and different P_c, no consistent relationship between stress (or strain) data and CO_2 in the nonlinear plastic regime was observed. The physical properties (e.g. initial crack density and crack geometry) rocks not the effect of CO_2 are believed the main factor causing the inconsistent result outcomes. No consistent trend was observed in the post-failure behavior of rocks in terms of σ_r. For limestone samples, no consistent relationship between stress (or strain) data and CO_2 in the nonlinear plastic regime was observed. No consistent trend was observed in the post-failure behavior of rocks in terms of σ_r.
5. Considering the effect of CO_2 on Mohr failure envelopes of rocks, the trend of decreasing cohesion and increasing friction angle was observed in both sandstone and dolomite samples.

5. References

ASTM D4543. 2008. Standard practices for preparing rock core as cylindrical test samples and verifying conformance to dimensional and shape tolerances. ASTM International, West Conshohocken, PA.

Bachu, S. 2002. Sequestration of CO_2 in geological media in response to climate change: road map for site selection using the transform of the geological space into CO_2 space. Energy Conversion Management, 43: 87–102.

Bachu, S. 2008. CO_2 storage in geological media: role, means, status and barriers to deployment. Progress in Energy and Combustion Sciences, 34: 254–273.

Busch, A., Kampman, N., Hangx, S.J., Snippe, J., Bickle, M., Bertier, P., ... Evans, J.P., 2014. The Green River Natural Analogue as A Field Laboratory To Study the Long-term Fate of CO_2 in the subsurface. Energy Procedia. 63, 2821–2830.

Cerasi, P., Kjøller, C., Sigalas, L., et al., 2016. Mechanical effect of CO_2 flooding of a sandstone sample. Energy Procedia 86, 361–370.

Erickson, K.P., Lempp, C., Pöllmann, H., 2015. Geochemical and geomechanical effects of $scCO_2$ and associated impurities on physical and petrophysical properties of Permotriassic sandstones (Germany): an experimental approach. Environ. Earth Sci.

Fabre, D., and Gustkiewicz, J. 1997. Poroelastic properties of limestones and sandstones under hydrostatic conditions. International Journal of Rock Mechanics and Mining Science, 34: 127–134.

Grana, D., S., Verma, J., Pafeng, X. Lang, H., Sharma, W. Wu, F. McLaughlin, E., Campbell, K., Ng, V. Alvarado, S., Mallick, and J. Kaszuba. 2017. A rock physics and seismic reservoir characterization study of the Rock Springs Uplift, a carbon dioxide sequestration site in Southwestern Wyoming. International Journal of Greenhouse Gas Control, 63: 296–309.

Hangx, S.J.T., Spiers, C.J., Peach, C.J., 2010. Mechanical behavior of anhydrite caprock and implications for CO_2 sealing capacity. J. Geophys. Res. 115, B07402.

Hangx, S., van der Linden, A., Marcelis, F., Bauer, A., 2013. The effect of CO_2 on the mechanical properties of the Captain sandstone: Geological storage of CO_2 at the Goldeneye field (UK). Int. J. Greenh. Gas Control 19, 609–619.

Hangx, S.J.T., Pluymakers, A., ten Hove, A., Spiers, C.J., 2014. Effects of lateral variations in rock composition and texture on anhydrite caprock integrity of CO_2 storage systems. Int. J. Rock Mech. Min. Sci. 69, 80–92.

Hangx, S., Bakker, E., Bertier, P., Nover, G., Busch, A., 2015. Chemical–mechanical coupling observed for depleted oil reservoirs subjected to long-term CO_2-exposure — a case study of the Werkendam natural CO_2 analogue field. Earth Planet. Sci. Lett. 428, 230–242.

Johnson, J.W., Nitao, J.J., Morris, J.P., 2004. Reactive transport modeling of cap rock integrity during natural and engineered CO_2 storage. In: Thomas, D.C., Benson, S.M. (Eds.), Carbon Dioxide Capture for Storage in Deep Geologic Formations. Elsevier, Oxford, UK, pp. 787–813.

Luquot, L., Gouze, P., 2009. Experimental determination of porosity and permeability changes induced by injection of CO_2 into carbonate rocks. Chem. Geol. 265,148–159. http://dx.doi.org/10.1016/j.chemgeo.2009.03.028.

Luquot, L., Rodriguez, O., Gouze, P., 2014. Experimental characterization of porosity structure and transport property changes in limestone undergoing different dissolution regimes. Transp. Porous Media 101, 507–532. http://dx.doi.org/10.1007/s11242-013-0257-4.

Mikhaltsevitch, V., Lebedev, M., Gurevich, B., 2014. Measurements of the elastic and anelastic properties of sandstone flooded with supercritical CO_2. Geophysical Prospecting 62 (6), 1266–1277.

Shafer, L.R. 2013. Assessing injection zone fracture permeability through the identification of critically stressed fractures at the Rock Springs Uplift CO_2 sequestration site, SW Wyoming. Master Thesis, Department of Geology and Geophysics, University of Wyoming, Laramie, WY.

Vialle, S., Vanorio, T., 2011. Laboratory measurements of elastic properties of carbonate rocks during injection of reactive CO_2-saturated water. Geophys. Res. Lett. 38, 1–5. http://dx.doi.org/10.1029/2010GL045606.

Vialle, S., Contraires, S., Zinzsner, B., Clavaud, J.B., Mahiouz, K., Zuddas, P., Zamora, M., 2014. Percolation of CO_2-rich fluids in a limestone sample: Evolution of hydraulic, electrical, chemical, and structural properties. J. Geophys. Res. Solid Earth 119, 2828–2847. http://dx.doi.org/10.1002/2013JB010656.

Zahm, C.K., and P.H., Hennings. 2009. Complex fracture development related to stratigraphic architecture: challenges for structural deformation prediction, Tensleep Sandstone at the Alcova anticline, Wyoming. AAPG Bulletin, 93(11): 1427–1446.

Appendix VII

Baseline Geomechanical Experiment Results

List of Acronyms

c	Inherent shear strength
D	Dry dolomite sample of Madison Limestone
DH	Horizontal dolomite sample of Madison Limestone
ε	Axial strain
ε_i	Axial strain data point
ε_f	Failure axial strain
ε_v	Total volumetric strain
ε_{cc}	Crack closure axial strain
ε_{cd}	Crack damage axial strain
ε_{ci}	Crack initiation axial strain
ε_{pk}	Axial strain coressponding to the peak deviatoric stress
ε_{vc}	Crack volumetric strain
ε_{ve}	Elastic volumetric strain
E	Young's modulus
E_{est}	Estimated Young's modulus
ESR	Effective stress ratio
G	Shear modulus
K_{dry}	Effective bulk modulus of a dry rock
K_{sat}	Bulk modulus of a saturated rock
LVDT	Linear variable differential transformers
n	User defined interval
P_c	Confining pressure
P_p	Pore pressure
R^2	Coefficient of determination
S	Dry sandstone sample
S_{Hmax}	Maximum horizontal stress
S_{Hmin}	Minimum horizontal stress
SH	Horizontal sandstone sample
SV	Vertical sandstone sample
UCS	Unconfined compressive strength
σ	Axial stress
σ_1	Major principal stress
σ_3	Minor principal stress
σ_{de}	Estimated deviatoric stress
σ_{dm}	Measured deviatoric stress
σ_{diff}	Difference in deviatoric stress
ϕ	Internal friction angle
υ	Poisson's ratio

Executive Summary

One of the challenges to successfully implementing geologic carbon sequestration is the lack of understanding and the inability to predict geomechanical behavior of storage reservoirs as a result of CO_2 injection. The Rock Springs Uplift (RSU) in Wyoming, a potential site for carbon sequestration, contains two suitable storage reservoirs, the Weber Sandstone and the Madison Limestone. In this Appendix, we present baseline geomechanical experiments that determine stress-strain behaviors and quantify geomechnical properties of samples of Weber Sandstone and Madison Limestone. These baseline experiments were performed on dry and brine-saturated samples of both formations. This dataset provides the foundational data for geomechanical experiments that evaluated CO_2-reacted samples (described in Appendix 6).

Weber Sandstone plugs were prepared at both horizontal and vertical orientations to the rock cores while dolomite plugs from Madison Limestone were prepared only at the horizontal orientation. Nine triaxial tests of brine-saturated samples were conducted at in-situ temperature and pressure conditions. The triaxial test procedure was designed and conducted in four stages to achieve these in-situ conditions while maintaining sample integrity. Additionally, three hydrostatic experiments were conducted on dry samples. Modified methods were proposed to better determine the Young's modulus, Poisson's ratio, and critical axial strains that define the regimes of crack development.

A substantial dataset of geomechanical properties was generated and is presented in this Appendix. These properties include Young's modulus, Poisson's ratio, dry and saturated bulk modulus, shear modulus, critical axial strains, inherent shear strength, and internal friction angle. Generally, the geomechanical properties of samples from Weber Sandstones are higher than those from Madison Limestone. The geomechnical properties are influenced by the applied differential pressures and existing microcracks of the samples. Geomechanical properties of dry samples determined by Shafer (2013) in a predecessor study are included for comparison. The Young's modulus, Poisson's ratio, shear modulus and internal friction angle of dry samples by Shafer (2013) are higher than those of brine-saturated rocks tested in this baseline experiment.

1. Introduction

This Appendix describes baseline triaxial experiments performed on rock samples obtained from the Rock Springs Uplift (RSU) #1 well and without exposure to CO_2. The objectives for this Appendix report are:

- Describe the design of the high temperature and pressure geomechanical experiments and the testing methods that were used
- Quantify the geomechanical properties of RSU rocks saturated with brine
- Determine the effect of brine saturation on geomechnical properties of RSU rocks

This dataset provides the baseline data for triaxial tests that evaluate the geomechanical sensitivity to CO_2-induced changes in geochemistry (Appendix VI).

2. Laboratory Experiments

2.1. RSU Sample Preparations

Original rock cores of the Weber Sandstone and the dolomite facies of the Madison Limestone from the RSU (Figure 1), were prepared using a rock core drilling machine (Figure 2) to 25.4 mm diameter and 50.8 mm of length in accordance with the ASTM D4543-08. Weber Sandstone plugs were prepared at both horizontal (i.e., drilled transversely across original cores and parallel to bedding) and vertical (i.e., drilled longitudinally through original cores and perpendicular to bedding) orientations. The Weber Sandstone plugs prepared at the horizontal and vertical orientations are denoted as SH and SV, respectively. Dolomite specimens from Madison Limestone were prepared only at the horizontal direction; these plugs are denoted as DH. Figure 3 shows the prepared RSU rock plugs. Twelve plugs were used in this study; nine were vacuum-saturated to 100% saturation with synthetic brine and three were left dry. Geological information, saturation conditions and corresponding geomechanical experiments of these twelve plugs are summarized in Table 1. Information about five rock plugs evaluated by Shafer (2013) is included in this table to facilitate data comparison and development of conclusions.

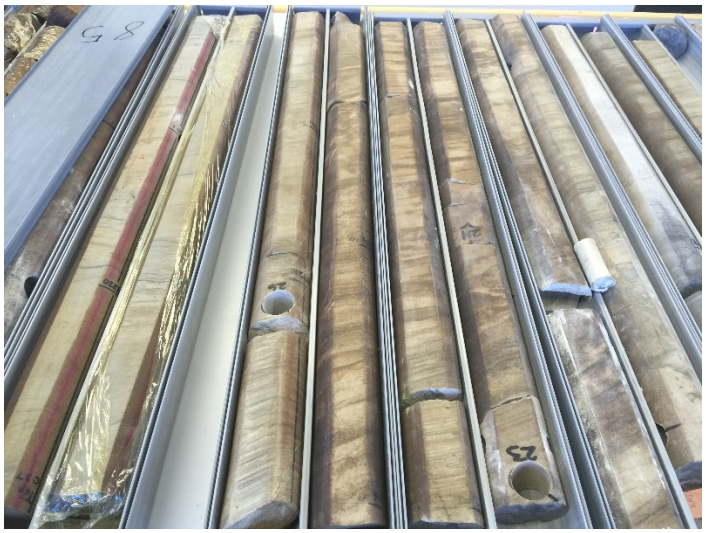

Figure 1. Weber Sandstone and Madison Limestone cores from RSU #1 well.

Figure 2. Rock core drilling machine for RSU specimen preparation.

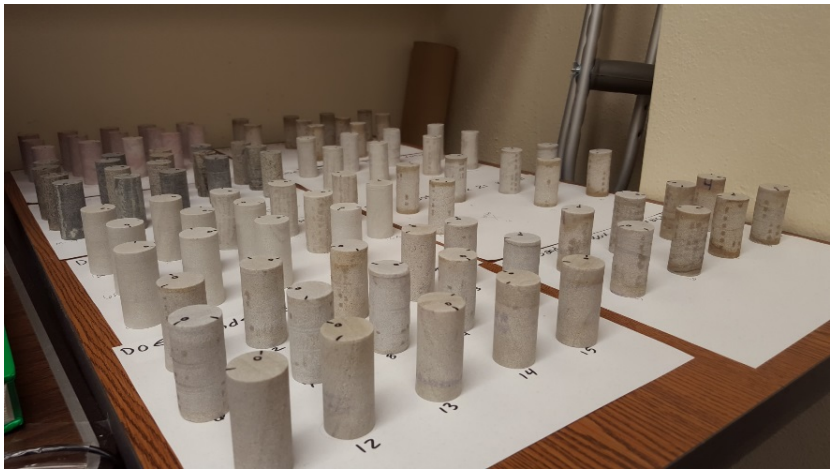

Figure 3. Prepared RSU rock plugs.

Table 1. Summary of geological information, saturation and geomechanical experiments

Research	Formation	Rock Plug ID	Depth (m)	Saturation	Geomechanical Experiment
Current Study	Weber	SV1	3527.21	100% Saturation	Triaxial
		SV2	3527.24	100% Saturation	Triaxial
		SV3	3527.08	100% Saturation	Triaxial
		SV4	3416.99	Dry	Hydrostatic
		SH1	3415.97	100% Saturation	Triaxial
		SH2	3416.83	100% Saturation	Triaxial
		SH3	3416.80	100% Saturation	Triaxial
		SH4	3417.08	Dry	Hydrostatic
	Madison	DH1	3784.66	100% Saturation	Triaxial
		DH2	3784.59	100% Saturation	Triaxial
		DH3	3784.62	100% Saturation	Triaxial
		DH4	3765.50	Dry	Hydrostatic
Shafer (2013)	Weber	S1	3516.33	Dry	Triaxial
		S2	3518.31	Dry	Triaxial
	Madison	D1	3813.66	Dry	Triaxial
		D2	3814.05	Dry	Triaxial
		D3	3815.97	Dry	Triaxial

2.2. Geomechanical Experiments

2.2.1 Test Equipment

A servo-controlled triaxial equipment RTR-1500 at the University of Wyoming, manufactured by GCTS (Figure 4), was used to conduct all geomechanical experiments. The equipment is capable of performing static and dynamic closed-loop strain- or stress-controlled loading as well as post-failure behavior tests on rock specimens. The stiff loading frame supports a maximum compressive load capacity of 1,500 kN and a tension load capacity of 820 kN. The testing system consists of a high-pressure triaxial cell with internal instrumentation allowing local axial and radial strain measurements using linear variable differential transformers (LVDTs) (Figure 5), ultrasonic velocity testing system allowing shear and compression wave velocities (with 200 kHz) measurements, and temperature control (up to 200 ℃). A 140-MPa servo-controlled pressure intensifier system is included to control and measure confining cell and pore pressures. Test data are automatically displayed on a monitor and digitally stored in a data acquisition system.

Figure 4. The GCTS RTR-1500 testing system at the University of Wyoming.

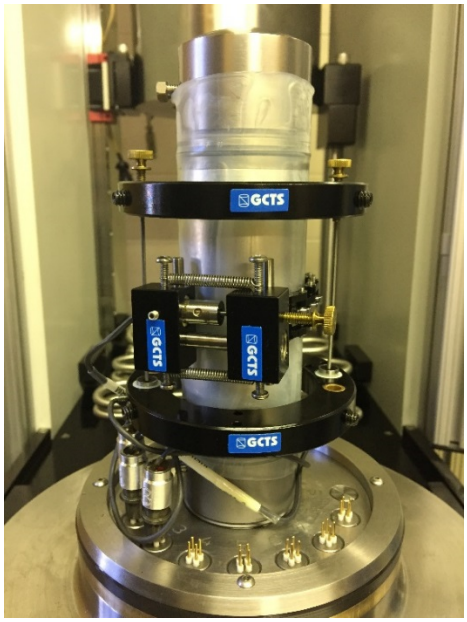

Figure 5. Axial and radial LVDTs in the GCTS testing system.

2.2.2 Test Criteria

Laboratory testing parameters (e.g., confining pressure, pore pressure, and temperature) were determined based on in-situ reservoir conditions measured at the RSU #1 well (Shafer, 2013). Reservoir temperatures estimated from the temperature profile for Weber Sandstone and Madison Limestone are 90℃ and 93℃, respectively. The in-situ pore pressure (P_p) was measured by isolating sections of the wellbore using inflatable packers set above and below the measurement interval. The pressure gradient associated with saline water was estimated at 10.52 MPa/km (Figure 6). Weber Sandstone cores were collected from 3.41 km to 3.52 km depth, and Madison Limestone cores were collected from 3.75 km to 3.81 km depth. Average P_p values for Weber Sandstone and Madison Limestone were determined to be 36.54 MPa and 39.30 MPa, respectively.

To understand the geomechanical behavior of reservoir rocks under different stress states, three confining pressures (P_c) were selected. Maximum P_c value was designed to cover the entire range of the magnitude of horizontal stresses based on the stress polygon for the most likely in-situ stress state of both the Weber Sandstone and Madison Limestone (Figure 7). Blue contours represent the tensile strength necessary to resist tensile failure, and red contour lines represent unconfined compressive strength (UCS) necessary for breakout formation for the given breakout width. The yellow polygon represents the ranges for UCS and minimum horizontal stress (S_{Hmin}) for the Weber Sandstone. The most likely in-situ stress state for the Weber Sandstone is located at the intersection of the yellow polygon and zero blue contour line. The interpreted in-situ stress state for the Madison Limestone is contained in the yellow polygon; this was calculated based on the effective stress ratio (ESR) from the most likely Weber Sandstone stress state (Shafer, 2013). The maximum horizontal stress (S_{Hmax}) for the Weber Sandstone was estimated between 84.11 MPa and 89.98 MPa at the specific depth of 3,516.3 m. For the Madison Limestone, S_{Hmax} was estimated between 86.18 MPa and 94.80 MPa at the specific depth of 3,816.7 m. Considering the different P_p values in these two formations (i.e., 36.54 MPa for Weber Sandstone and 39.30 MPa for Madison Limestone) and possibly wider S_{Hmax} ranges for larger depth intervals (summarized in Table 1) to yield a common maximum differential pressure ($P_c - P_p$) of 55.16 MPa, the maximum P_c values were designed as 91.70 MPa and 94.46 MPa for the Weber Sandstone and Madison Limestone, respectively. The minimum P_c value was selected to study the geomechanical behavior of reservoir rocks under a relatively low confining pressure. Since triaxial experiments had been conducted on dry specimens

(Shafer, 2013) for two formations at P_c of 6.89 MPa (i.e., same differential pressure of 6.89 MPa with zero P_p), the minimum P_c values were designed at 43.43 MPa and 46.19 MPa for Weber Sandstone and Madison Limestone, respectively to account for the respective P_p values and yield a minimum differential pressure of 6.89 MPa. To ensure a smooth transition between the maximum and minimum P_c values and reduce the stress gap, intermediate P_c values were designed as 71.02 MPa and 73.77 MPa for Weber Sandstone and Madison Limestone, respectively, to yield a common differential pressure of 34.47 MPa. The experimental conditions are summarized in Table 2.

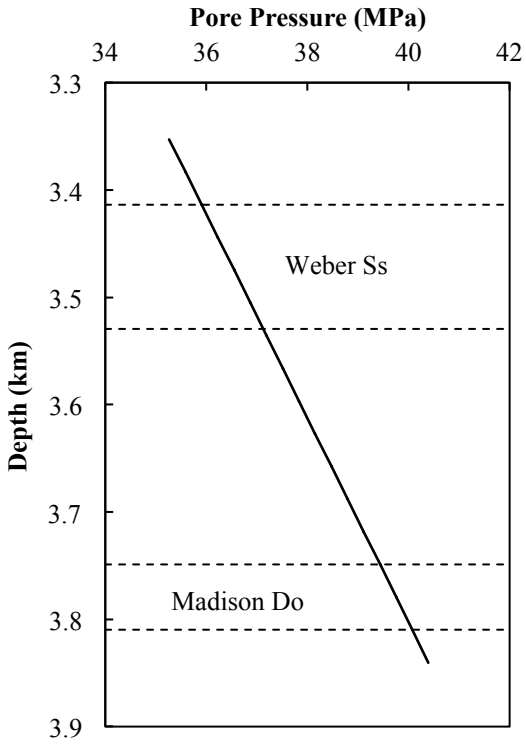

Figure 6. Pore pressure of saline water in the RSU #1 well (adapted after Shafer 2013).

Table 2. Summary of experimental test conditions

Geomechanical Parameter	Weber Sandstone (SH,SV)	Dolomite from Madison Limestone (DH)
Confining Pressure (MPa)	43.43; 71.01; 91.70	46.19; 73.77; 94.46
Pore Pressure (MPa)	36.54	39.30
Differential Pressure (MPa)	6.89; 34.47; 55.16	
Temperature (°C)	90	93

H−Horizontal orientation; and V−Vertical orientation.

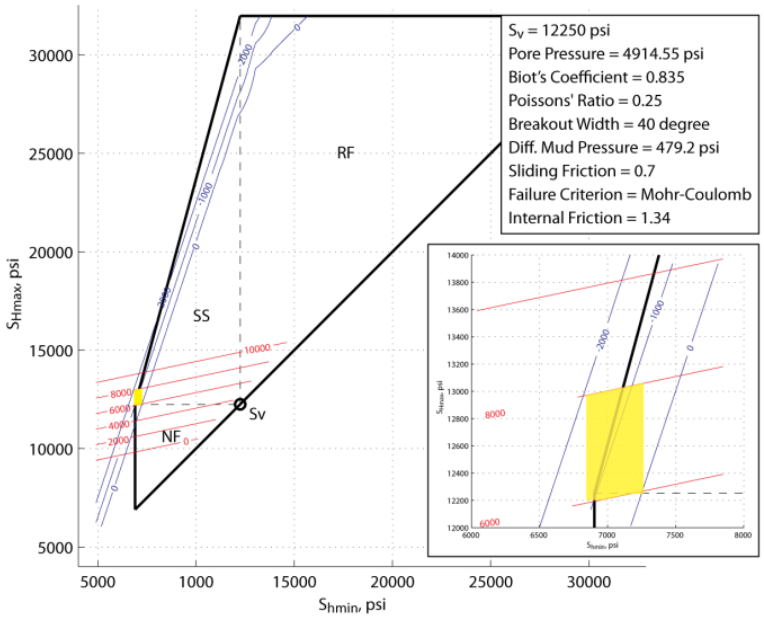

(a) Representative in-situ stress state in Weber Sandstone

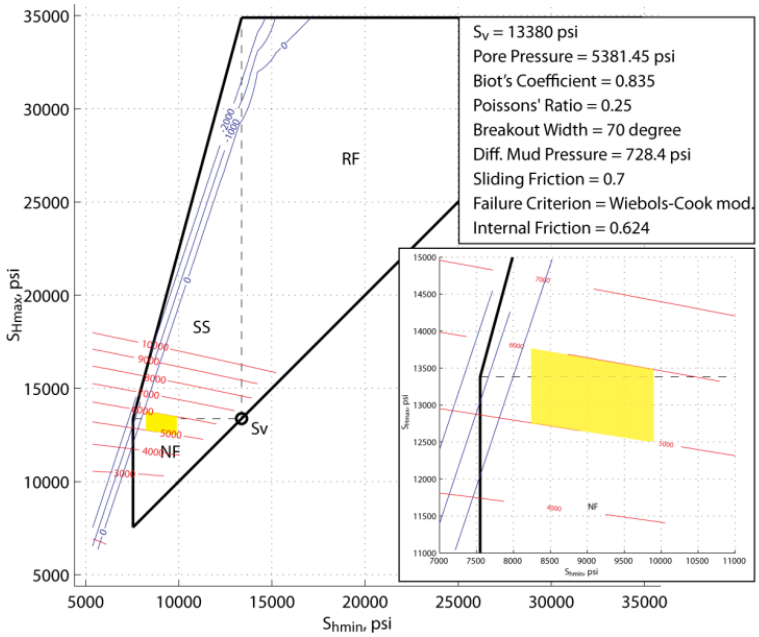

(b) Representative in-situ stress state in Madison Limestone

Figure 7. Stress polygon and associated stress contours for the most likely in-situ stress state in (a) Weber Sandstone and (b) Madison Limestone (after Shafer, 2013).

2.2.3 Hydrostatic Experiment

Axial and radial deformations of all specimens were measured in hydrostatic experiments. To determine the effective bulk modulus (K_{dry}) of dry rocks and characterize their plastic behavior under a high confining pressure, hydrostatic compression experiments using jacketed specimens were conducted under three loading and unloading cycles at a room temperature of approximately 24°C and zero pore pressure. A jacketed specimen is a rock specimen covered with a plastic membrane to prevent confining fluid from getting inside the rock. The loading and unloading cycle was used to quantify the permanent strain under

the range of in-situ maximum horizontal stress states described in Section 2.2.2. By repeating the loading and unloading cycles, the change of stiffness and permanent strain of rocks can be quantified. The hydrostatic compression test was conducted to a maximum confining pressure of 89.63 MPa prior to unloading. The P_c was applied at a stress rate of 5 MPa/min based on the recommendation of Fabre and Gustkiewicz (1997) on a similar lithology.

2.2.4 Triaxial Experiment

Triaxial compression experiments were conducted to determine shear strengths, friction angles, cohesions, and static moduli of samples. Each triaxial experiment was conducted in four stages.

Stage 1: After setting up a specimen (illustrated in Figure 5), temperature of the confining fluid was raised at a rate of 1.5°C/min until it attained the target reservoir temperature (

- Table 2). The temperature of the system was then allowed to reach equilibrium. The specimen was judged to be at thermal equilibrium when readings of two axial LVDTs and one radial LVDT were within 1% of each other; this procedure took approximately two hours.
- Stage 2: The P_c was increased at a rate of 5 MPa/min until it reached the target value while the P_p was kept constant at 0.34 MPa. This was done to keep the specimen in a saturated condition. The pressure of the system was then allowed to equilibrate for five minutes.
- Stage 3: The P_p was increased at a rate of 5 MPa/min until it reached the target value. The pressure and temperature were allowed to maintain equilibrium for 10 minutes.
- Stage 4: A shearing test was performed with strain control at a rate of 0.2%/min.

Figure 8 shows a generic path (Path 3) whereby both P_c and P_p were increased simultaneously (Zimmerman, 1991). Alternatively, two separate paths (Path 1 and Path 2) can be implemented to determine the compressibility of rock saturated with pore fluid. Considering the benefit of characterizing both the isotropic compressibility of the rock and the triaxial shear behavior of the rock in a single test, the two separate path approach was adopted. Hence, both P_c and P_p were separately increased to their respective target values in Stages 2 and 3 before conducting the triaxial shear test in Stage 4. The procedure used for each triaxial compression experiment in this study is illustrated in Figure 9.

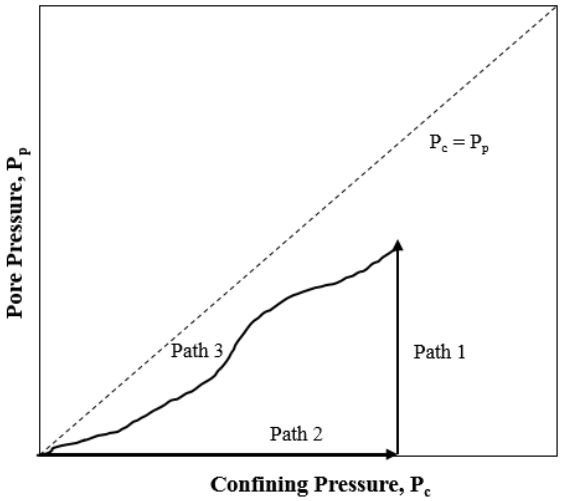

Figure 8. Stress paths in a P_c–P_p space (after Zimmerman, 1991).

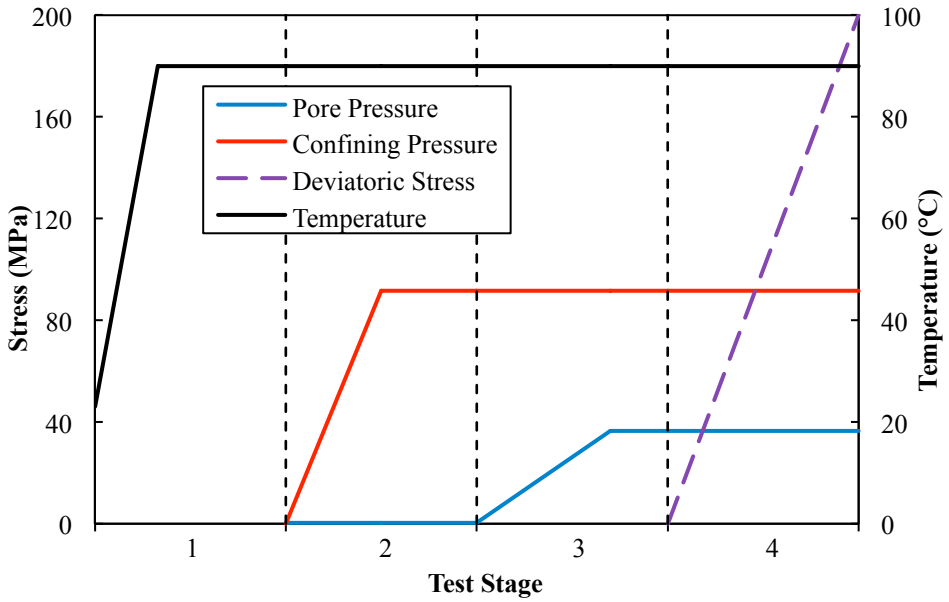

Figure 9. The procedure of a triaxial compression experiment.

3. Experimental Results and Discussions

3.1. Hydrostatic Results

Figure 10 shows the hydrostatic compression response of each sample under dry conditions. All samples indicate a classical behavior with a convex stress-strain curve due to the closure of existing microcracks at the beginning of loading followed by an almost constant stress-strain curve due to subsequent elastic deformation of minerals. The volumetric strain increased with increasing confining pressure. The increase in the volumetric strain is referred to as rock compression or decrease in rock volume. The mechanical behavior of samples in three loading-unloading cycles is influenced by the initial rock porosity.

Both vertical and horizontal sandstone samples (SV4 and SH4) with an average porosity of 8.2% share a similar stress-strain trend (Figure 10(a) and Figure 10(b)). Their plastic volumetric strains are less than 0.1%, and the stress-strain curves for three loading-unloading cycles are similar. In contrast, horizontal dolomite (DH4) with an average porosity of 20% experiences a higher plastic strain of 0.2% after the first loading-unloading cycle. The remaining two cycles (Cycles 2 and 3) share a similar stress-strain behavior, but which is different from Cycle 1. The larger plastic deformation of the dolomite could be attributed to the build-up of local deviatoric stresses on microstructures from the external confining stress (Fabre and Gustkiewicz, 1997). The high porosity exaggerates the effect of external hydrostatic pressure on the local plastic deformation and brittleness of microcracks that govern the plastic deformation of the rock. The similar behavior in Cycles 2 and 3 could be attributed to the reorganization of the mineral particles as the result of Cycle 1. The elastic mechanism due to the deformation of these mineral particles eventually dominates the behavior in Cycles 2 and 3.

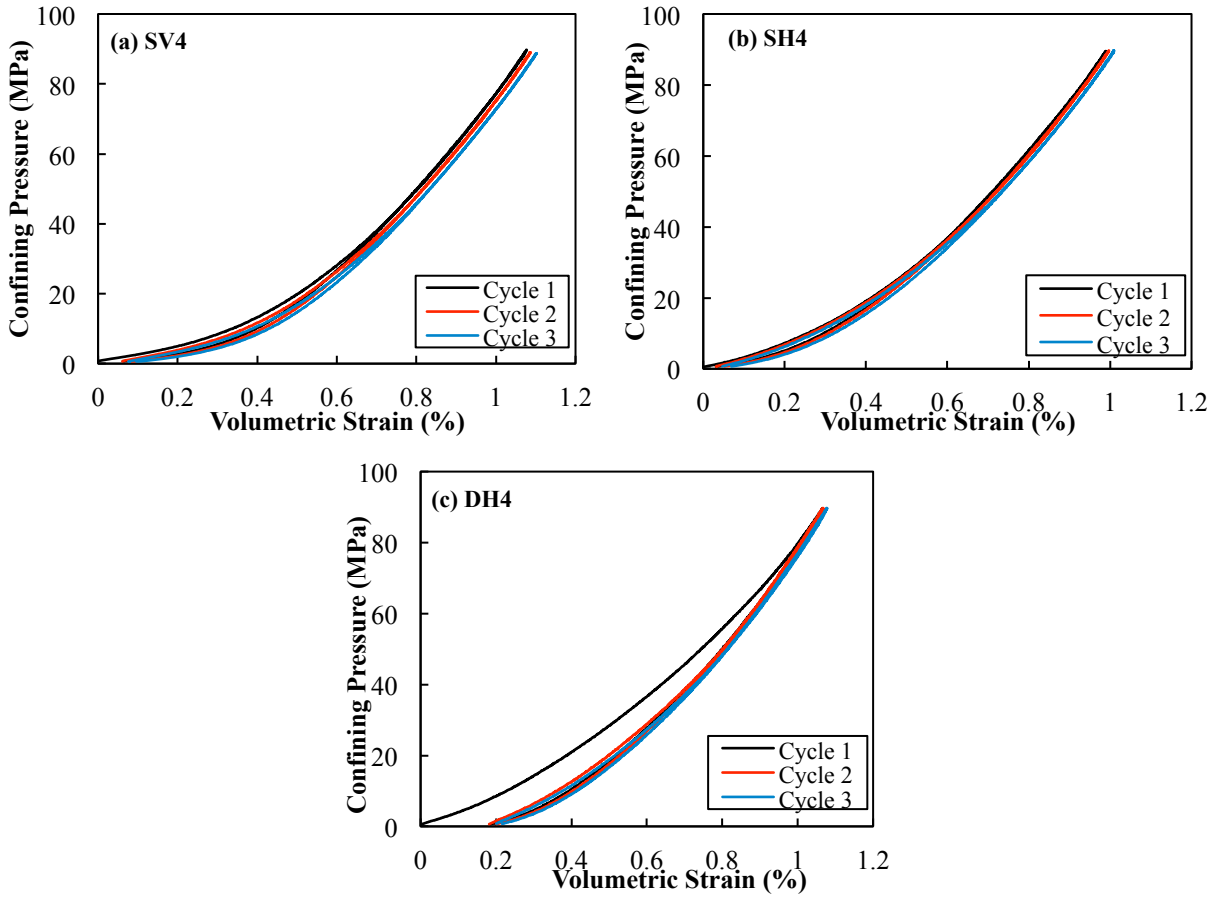

Figure 10. Hydrostatic test results of jacketed dry specimens for (a) vertical sandstone (SV4), (b) horizontal sandstone (SH4), and (c) horizontal dolomite (DH4).

The poroelastic behaviors of samples saturated with brine under different hydrostatic compression test conditions are shown in Figure 11. Solid and dashed lines indicate the increase in P_c and P_p with respect to volumetric strain, respectively. For each rock specimen, the P_c was increased to its maximum target value in Stage 2 followed by increasing the P_p to its target value in Stage 3.

Figure 11(a) shows the increase in the confining pressures up to three maximum values of 43.43 MPa, 71.01 MPa, and 91.70 MPa for the three vertical sandstone samples: SV1, SV2 and SV3, respectively. The confining pressure-volumetric strain curve began with an increasing gradient followed by an almost constant gradient. A similar confining stress-volumetric strain trend of these three vertical sandstones with a convex stress-strain relationship is observed. The volumetric strain increased with increasing confining stresses. The increase in the volumetric strain is referred to as rock compression or decrease in rock volume. In contrast, the decrease in the volumetric strain is referred to as rock expansion or increase in rock volume. For the pore pressure-volumetric strain results at three different maximum confining pressures, the volumetric strain decreased with increasing pore pressures. However, a smaller decrease in the volumetric strain is observed at a higher confining pressure. For example, the SV3 specimen at a maximum confining pressure of 91.70 MPa experienced the smallest decrease in the volumetric strain. This phenomenon could be attributed to the effect of applying a high confining pressure on the initial microcracks, which are difficult to reopen by the subsequent increase in the pore fluid pressure. At the high confining pressure, the minerals in the porous granular rock are also harder to be rearranged by the increasing pore pressure (i.e., the rock frame becomes stiffer under the high confining pressure).

In contrast, dolomite with a relatively high porosity of about 20% behaves differently (Figure 11(c)). When increasing the confining pressure in Stage 2, the volumetric strain increased as the result of decreasing pore fluid volume in microcracks to maintain the constant pore pressure of 0.34 MPa. Unlike the smooth curves of SVs (Figure 11(a)), the slightly jagged lines of DHs (Figure 11(c)) are likely the result of the relatively high porosity of horizontal dolomites. When the confining pressure reached the critical pressure and the volumetric strain decreased abruptly as experienced by DH2 and DH3. Some individual and isolated microcracks propagated, shifted and eventually connected. The pore fluid immediately filled these microcracks to maintain the constant pore pressure, causing the volumetric strain to decrease (i.e., the volume of the rock increases). After reaching the equilibrium at which the new microstructure stabilizes, the volumetric strain continued to increase with increasing confining pressures. However, this phenomenon has significantly decreased the final volumetric strain by the end of Stage 2. Similar pore pressure-volumetric strain relationships are observed. The volumetric strain decreased with increasing pore pressure in Stage 3. Sample DH1 at the lowest confining pressure of 43.43 MPa experienced the greatest decrease in the volumetric strain while DH3 at the highest confining pressure of 91.70 MPa experienced the smallest decrease in volumetric strain.

The confining pressure-volumetric strain relationship of the horizontal sandstones, except SH2 (Figure 11(b)), followed the typical trend observed for vertical sandstones. The sudden decrease in the volumetric strain experienced by SH2 is also observed in DH2 and DH3. The propagation and joining of isolated microcracks and subsequent pore fluid filling could explain this response. With the exception of SH3, similar pore pressure-volumetric strain relationships are observed. The volumetric strain for SH3 decreased with increasing pore pressure in Stage 3. The phenomenon causing the unique pore pressure-volumetric strain response of SH3 is currently unknown. Also, SH1 experienced a larger decrease in volumetric strain than SH2.

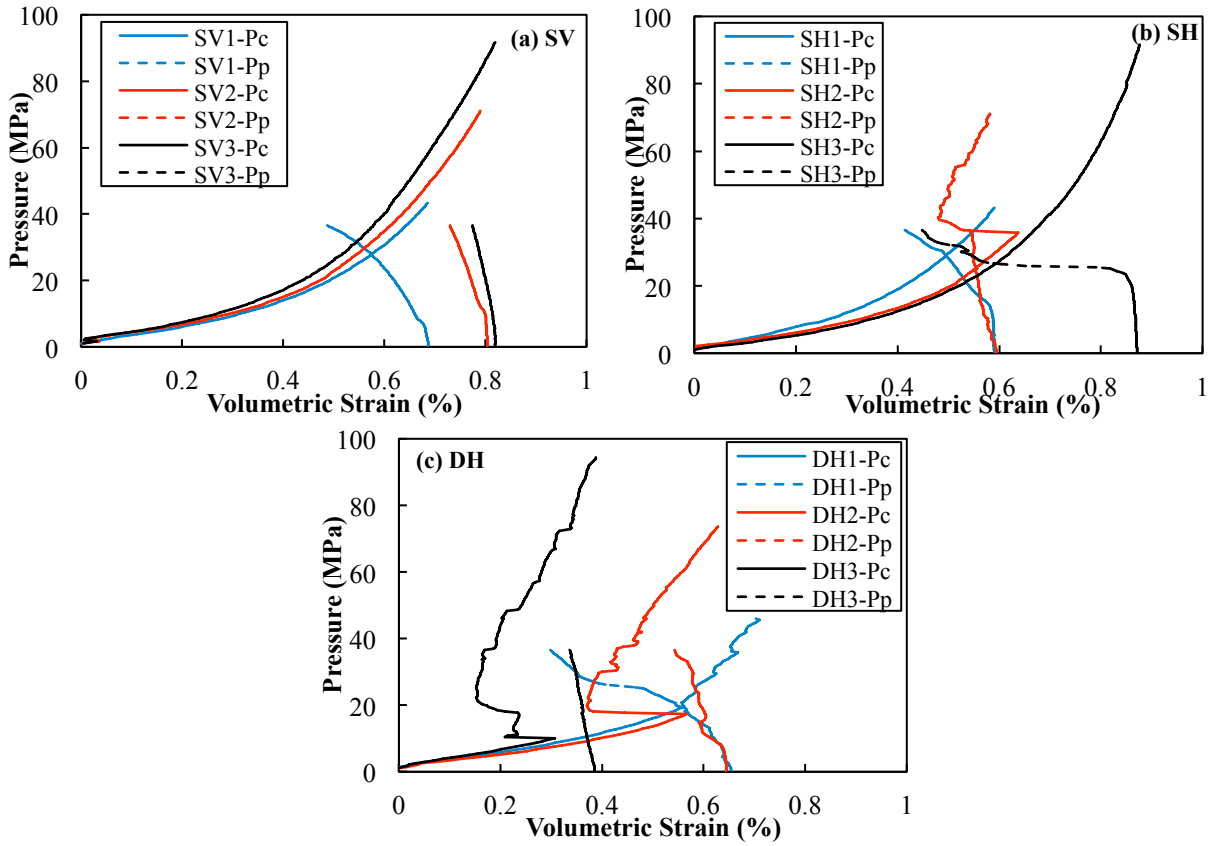

Figure 11. Hydrostatic test results of jacketed and saturated specimens for (a) vertical sandstone, (b) horizontal sandstone, and (c) horizontal dolomite.

Using the confining pressure and volumetric strain results for dry specimens (SV4, SH4 and DH4; Figure 10) and for saturated specimens (SV3, SH3 and DH3; Figure 11), the bulk moduli were determined using a linear least square fit method (Figure 12). The linear least square fit line (dashed line) was applied to the average slope of the almost straight (solid line) portion of the confining stress-volumetric strain curve. Two criteria were used to determine the linear portion of the curve: (1) to exclude the lower nonlinear response, and (2) to include as many data points as possible along the linear portion to achieve the highest coefficient of determination (R^2). To consider the equilibrium of the hydrostatic elasticity in rocks, the bulk modulus of the dry specimen (K_{dry}) was determined for each lithology based on its respective loading result of Cycle 3 (Figure 12(a)). The K_{dry} values were determined to be 14.72, 15.15, and 15.38 GPa for SV4, SH4, and DH4, respectively. The bulk moduli of the saturated specimens (K_{sat}) were determined using the confining pressure-volumetric strain responses of the saturated specimens (SV3, SH3 and DH3) tested at the highest differential pressure of 55.15 MPa. This highest differential pressure was chosen because the respective confining pressure-volumetric strain curves extend further into the almost straight portion. The K_{sat} values are 24.67, 35.79, and 30.39 GPa for SV3, SH3, and DH4, respectively. The K_{sat} of all samples are generally higher than the K_{dry}. The bulk moduli of SHs are larger than that of SVs (Table 3).

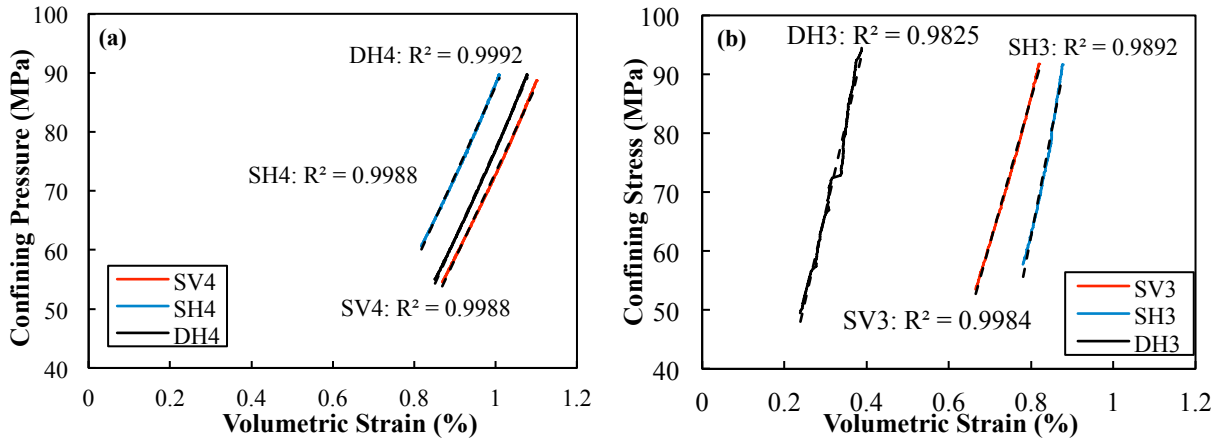

Figure 12. Dry and saturated bulk modulus of RSU specimens: (a) K_{dry} estimated on cycle 3, (b) K_{sat} estimated on differential pressure as 55.15 MPa.

3.2. Triaxial Test Results

The deviatoric stress-strain results of the saturated SVs performed at 90°C in Stage 4 are shown in Figure 13. The stress-strain responses are generally similar for SV1, SV2 and SV3 at three differential pressures ($P_c - P_p$) of 6.89 MPa, 34.47 MPa and 55.15 MPa, respectively. The positive axial strain indicates axial compression while the negative radial strain indicates radial expansion. The strains began with an initial non-linear behavior due to the closure of microcracks. The strains continued to increase along a linear relationship with the deviatoric stress before reaching the well-defined peak deviator stresses at 229.04, 381.96, and 496.4 MPa for SV1, SV2, and SV3, respectively. The peak stresses decreased abruptly to residual stresses of about 35.27, 113.72 and 227.88 MPa for SV1, SV2, and SV3, respectively. Higher peak and residual stresses were obtained at a higher confining pressure.

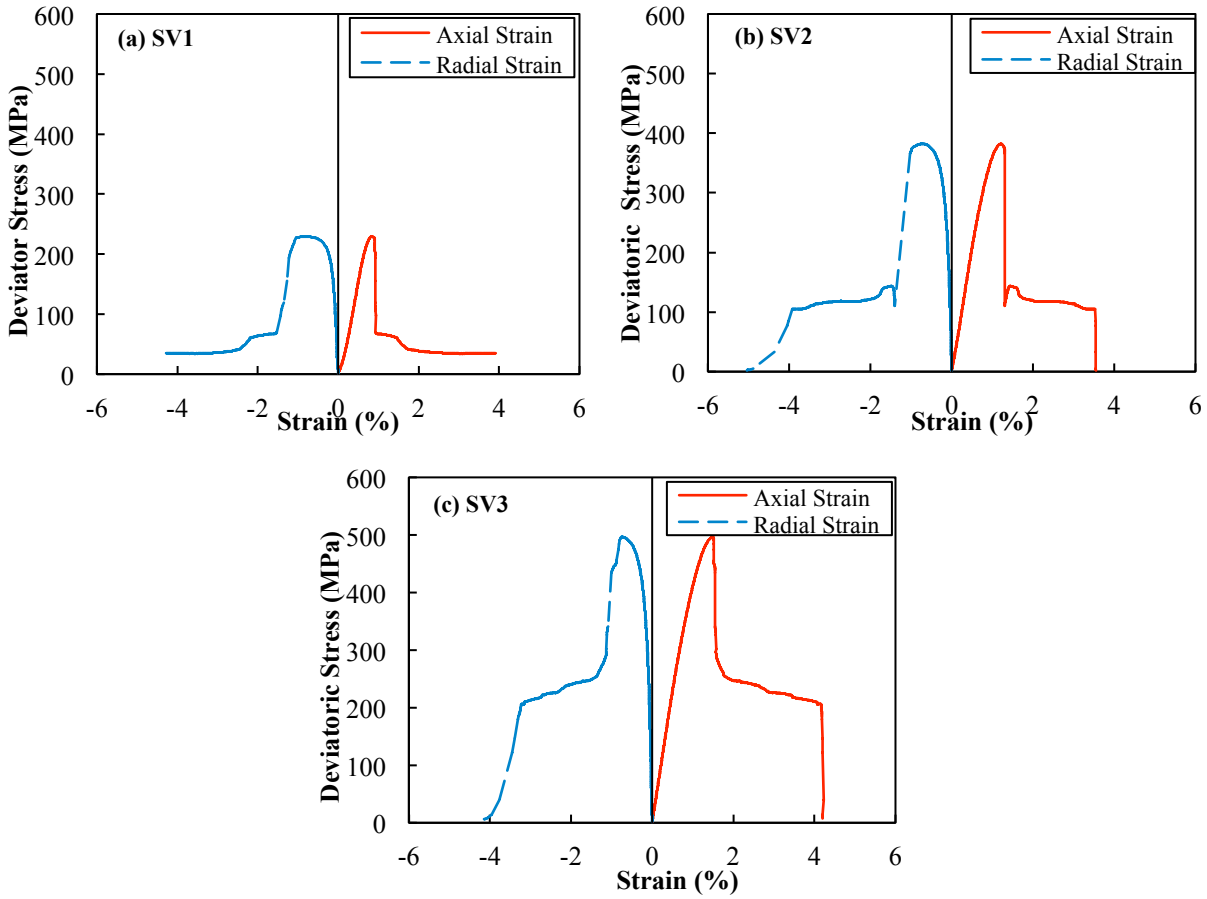

Figure 13. Triaxial test results of saturated SVs at three differential pressures: (a) $P_c - P_p = 6.89$ MPa, (b) $P_c - P_p = 34.47$ MPa, and (c) $P_c - P_p = 55.15$ MPa.

The deviatoric stress-strain results of the saturated SHs performed at 90°C in Stage 4 are shown in Figure 14. The stress-strain responses are generally similar in trend for SH1, SH2 and SH3 at three differential pressures (P_c–P_p) of 6.89 MPa, 34.47 MPa and 55.15 MPa, respectively. The strains began with an initial non-linear behavior due to the closure of microcracks. The strains continued to increase in a linear relationship with the deviatoric stress before reaching the well-defined peak deviator stresses at 282.68, 194.42, and 515.04 MPa for SH1, SH2, and SH3, respectively. The peak stresses decreased abruptly to residual stresses of about 24.5, 3.0 and 252 MPa for SH1, SH2, and SH3, respectively. Unlike the results of SVs, the peak and residual stresses of SHs did not increase with increasing confining pressures. In fact, the peak and residual stresses of SH2 were lower than that of SH1. This outcome could be attributed to the unique geomechanical response of SH2 observed during Stage 2 (Figure 11(b)). The propagation and joining of isolated microcracks and subsequent pore fluid filling in SH2 are believed to cause the sudden decrease in the volumetric strain and subsequent reduction in the peak and residual stresses.

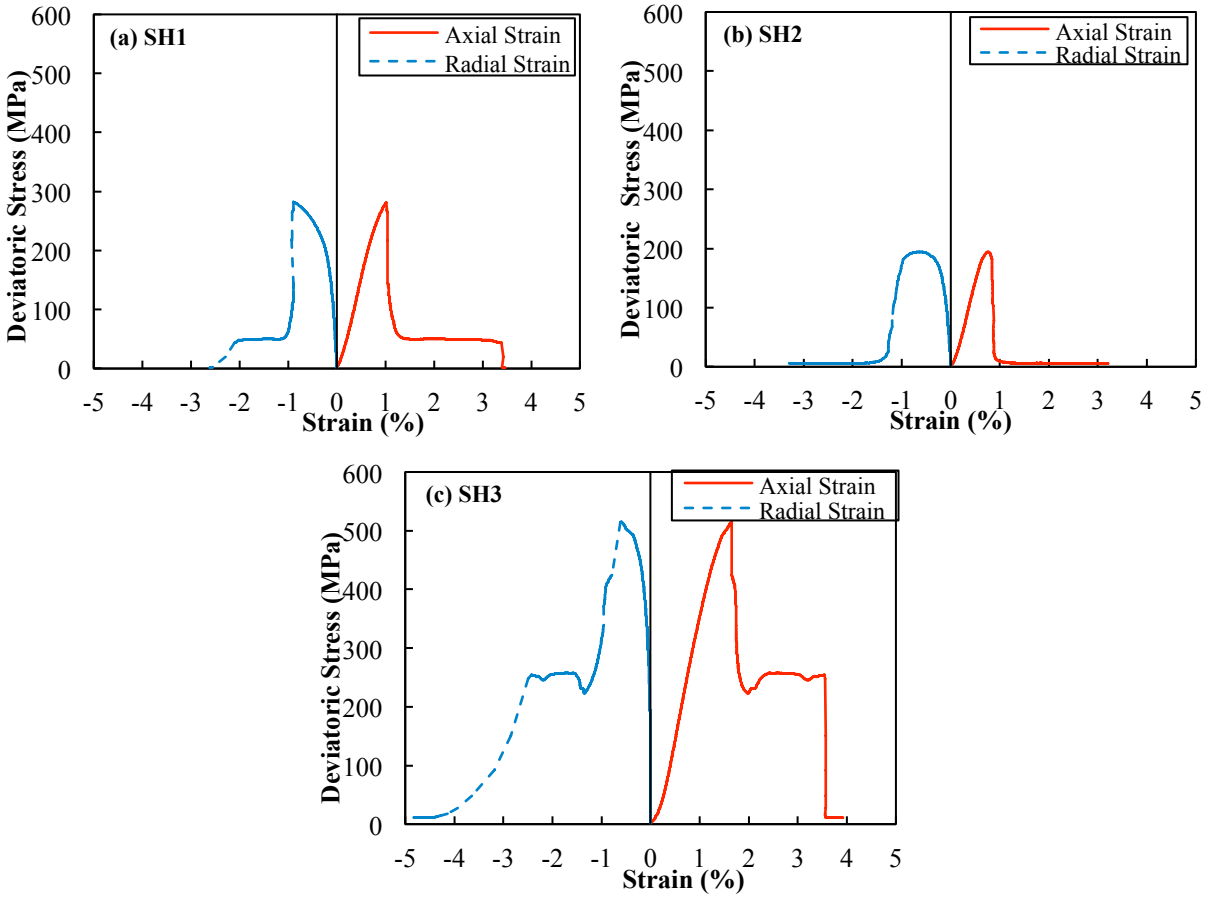

Figure 14. Triaxial test results of saturated SHs at three differential pressures: (a) $P_c - P_p = 6.89$ MPa, (b) $P_c - P_p = 34.47$ MPa, and (c) $P_c - P_p = 55.15$ MPa.

The deviatoric stress-strain results of the saturated DHs performed at 93°C in Stage 4 are shown in Figure 15. The stress-strain responses are generally similar in trend for DH1, DH2 and DH3 at three differential pressures (P_c–P_p) of 6.89 MPa, 34.47 MPa and 55.15 MPa, respectively. The strains began with an initial non-linear behavior due to the closure of microcracks. The strains continued to increase with a linear relationship with the deviatoric stress before reaching the well-defined peak shear stresses at 31.89, 40.97, and 21.67 MPa for DH1, DH2, and DH3, respectively. The peak stresses decreased abruptly to residual stresses of about 6.39 and 2.74 MPa for DH1 and DH3, respectively. The post peak stress behavior of DH2 was different from DH1 and DH3. DH2 experienced a post failure strain hardening before reaching the axial strain of 2.08%. Similar to the outcome of the horizontal sandstone samples, the peak and residual stresses of DHs did not follow an increasing trend with increasing confining pressures. The peak and residual stresses of DH3 were lower than that of DH1. This outcome was attributed to the geomechnical response of DH3 observed during the Stage 2 testing (Figure 11(c)). As similarly discussed, the propagation and joining of isolated microcracks and subsequent pore fluid filling in DH3 are believed to cause the sudden decrease in the volumetric strain and subsequent reduction in the peak and residual stresses. All peak and residual stresses are summarized in Table 3.

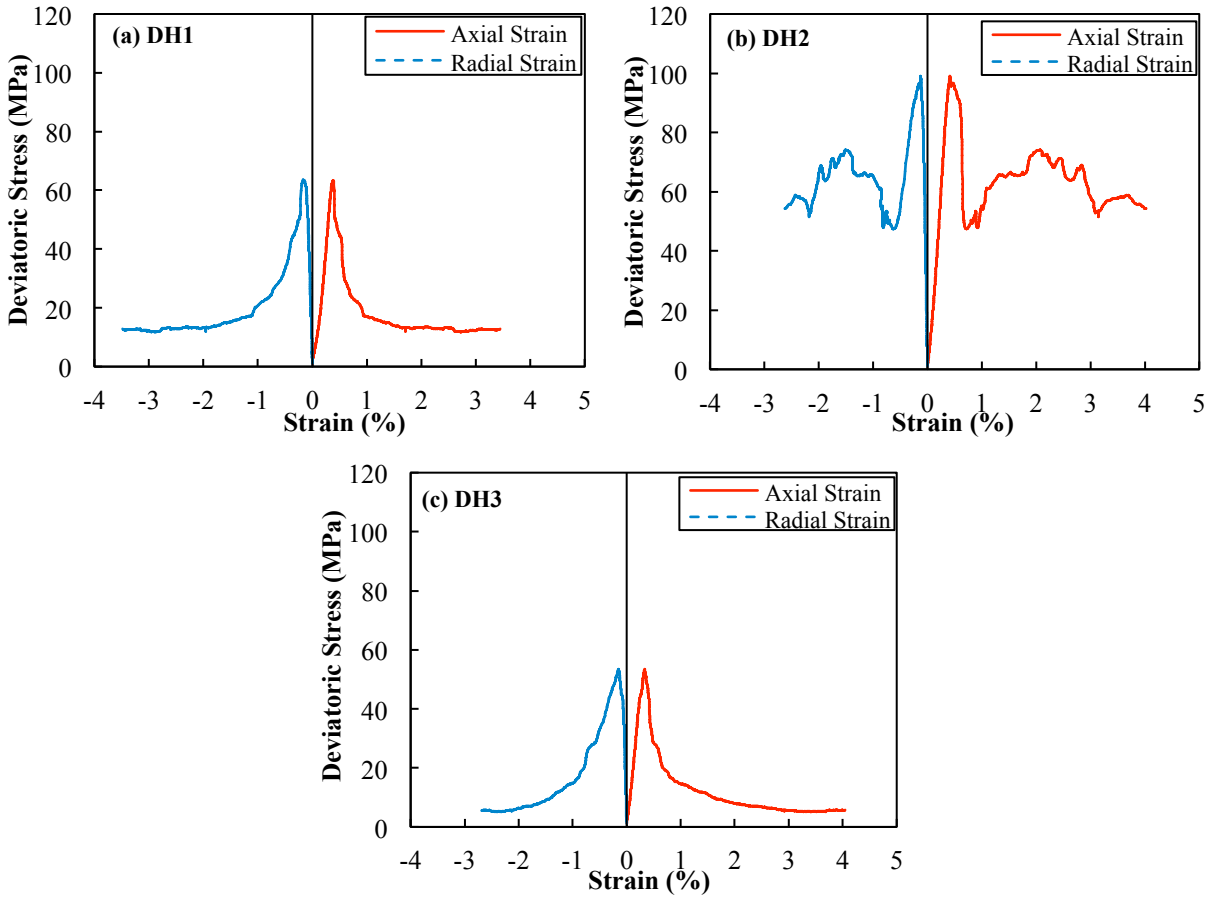

Figure 15. Triaxial test results of saturated DHs at three differential pressures: (a) $P_c - P_p = 6.89$ MPa, (b) $P_c - P_p = 34.47$ MPa, and (c) $P_c - P_p = 55.15$ MPa.

3.3. Elastic Properties

The deviatoric stress-axial strain results were used to determine the Young's modulus (E) and Poisson's ratio (υ) of the rocks. The most common methods described in ASTM D7012-14 include tangent modulus method, average slope of linear portion method, and secant method. However, none of these methods adequately considers the range of linear elastic behavior of the stress-strain curve. A potentially high degree of errors and subjectivity due to manually picking points describing the elastic range are embedded into these methods. To overcome this limitation, Eberhardt et al. (1998) proposed a moving point regression method to estimate E at each strain point. This method requires the plotting of this modulus as a function of axial strains. The representative E value can then be determined by averaging estimated E values over the linear elastic portion. This method does not account for the bias created by the variability of those estimated E values.

To accurately determine the E value while overcoming the aforementioned limitations, a modified method is proposed by estimating the Young's Modulus (E_{est}) at each axial strain data point (ε_i) over a user-defined interval (n) using

$$E_{est} = \frac{\sigma_{i+n} - \sigma_{i-n}}{\varepsilon_{i+n} - \varepsilon_{i-n}} \quad (1)$$

where, σ is the axial stress and ε is the axial strain. To demonstrate this modified method, triaxial test results of SV2 were used, and estimated elastic properties are presented in Figure 16. In this study, a n-value of 5 is recommended so that the axial stress and strain at the first data point i−5 and next data point i+5 are included to estimate E with respect to the strain at point i. Following this procedure over the entire data set, a relationship between E and axial strains is determined in Figure 16(a). The relatively level portion of the curve between the dashed lines at the corresponding axial strains of 0.2% and 0.35% indicates a relatively constant modulus at the stabilized elastic rock regime. By applying these corresponding axial strains on the axial stress-strain curve to define the elastic regime and preforming a linear regression analysis over this range, the representative E was determined to be 43.62 GPa for SV2 (Figure 16(b)). Likewise, the gradient of the regression line of the radial-axial strain curve over the corresponding axial strains of 0.2% and 0.35% (Figure 16(c)) defines the Poisson's ratio (υ) of 0.195 for SV2. The relatively high R^2 values suggest that the modified method provides a good estimation of the elastic properties.

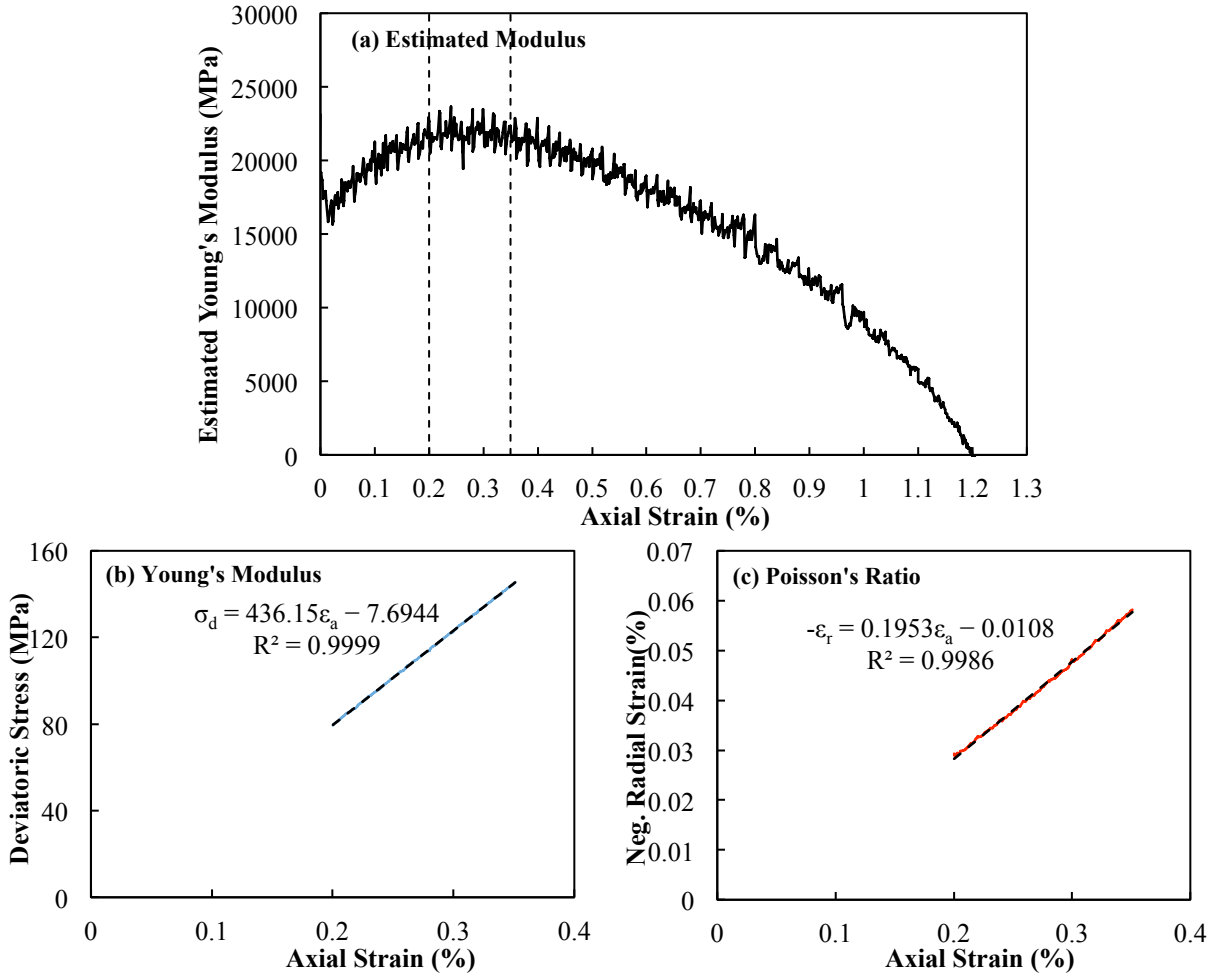

Figure 16. The proposed modified method for determining elastic properties for SV2.

Using this modified method, the Young's modulus and Poisson's ratio for each rock specimen were determined (Table 3). The Young's modulus of the sandstone is larger than that of the dolomite. For SV specimens, the Young's modulus increases and Poisson's ratio decreases at a higher differential pressure. Similar outcomes are observed for dry sandstones (S1 and S2) and dry dolomites (D1, D2 and D3). Due

to the effect of confining pressure in Stage 2 (Figure 11), a similar relationship between Young's modulus or Poisson's ratio and differential pressure is observed for SH and DH specimens. Additionally, Table 3 summarizes the peak shear, residual stresses, and shear modulus. The peak shear stress is defined to be half of the maximum deviatoric stress (i.e., radius of the Mohr's circle discussed in Section 4.5), and the residual stress is the constant deviatoric stress at the end of post failure. The shear modulus (G) is determined based on the estimated Young's modulus, and Poisson's ratio is determined using elastic theory. Comparing the results of sandstones at the same differential pressure of 55.16 MPa, the Young's modulus, shear modulus and Poisson's ratio of the dry sandstone S2 are larger by at least 30%, 23% and 70%, respectively, than those of the saturated sandstones SV3 and SH3. For the dolomites at the same differential pressure of 34.47 MPa, the Young's modulus, shear modulus and Poisson's ratio of DH2 are marginally larger than that of D2. In contrast, the Young's modulus, shear modulus and Poisson's ratio of DH3 are smaller than that of D3. Inconsistent outcomes observed for dolomites could be attributed to the unusual responses of DH2 and DH3 experienced in Stage 2 (Figure 11). Furthermore, the dry bulk moduli (K_{dry}) of past rock specimens estimated by the elastic theory using the measured Young's modulus and Poisson's ratio by assuming an intact condition with no discontinuities are generally larger than those measured for SV4, SH4 and DH4.

Table 3. Summary of geomechanical parameters determined from hydrostatic and triaxial compression experiments.

Sample ID	Differential Pressure (MPa)	K_{dry} (GPa)	K_{sat} (GPa)	Peak Shear Stress (MPa)	Residual Stress (MPa)	ε_{Pk} (%)	E (GPa)	G (GPa)	υ
SV1	6.89	N/A	N/A	114.52	35.27	0.85	37.90	13.71	0.36
SV2	34.47	N/A	N/A	190.98	113.72	1.21	43.62	18.24	0.20
SV3	55.16	N/A	24.67	248.20	227.88	1.49	46.21	18.30	0.14
SV4	0	14.72	N/A	N/A	N/A	N/A	N/A	N/A	N/A
SH1	6.89	N/A	N/A	141.33	24.50	1.03	36.57	12.83	0.35
SH2*	34.47	N/A	N/A	97.21	3.00	0.75	34.97	12.53	0.38
SH3	55.16	N/A	35.79	257.52	252.00	1.57	44.46	19.88	0.08
SH4	0	15.15	N/A	N/A	N/A	N/A	N/A	N/A	N/A
DH1	6.89	N/A	N/A	31.89	6.39	0.43	23.38	7.95	0.47
DH2*	34.47	N/A	N/A	40.97	-	0.47	30.10	11.89	0.27
DH3*	55.16	N/A	30.39	21.67	2.74	0.33	20.16	7.69	0.31
DH4	0	15.38	N/A	N/A	N/A	N/A	N/A	N/A	N/A
S1	20.68	31.65[#]	N/A	N/A	N/A	N/A	48.81	19.65	0.24
S2	55.16	39.71[#]	N/A	N/A	N/A	N/A	60.88	24.48	0.24
D1	17.17	14.20[#]	N/A	N/A	N/A	N/A	18.06	7.03	0.29
D2	34.47	16.13[#]	N/A	N/A	N/A	N/A	27.17	11.17	0.22
D3	55.16	30.61[#]	N/A	N/A	N/A	N/A	49.23	19.99	0.23

K_{dry}−Bulk modulus of a dry specimen; K_{sat}−bulk modulus of a saturated bulk modulus; ε_{pk}−axial strain coressponding to the peak deviatoric stress; E−Young's modulus; G−Shear modulus; υ−Poisson's ratio; N/A−Not applicable; *−Rock specimens experience an abrupt decrease in volumetric strain during the Stage 2 (see Figure 11); and [#]−Bulk modulus estimated by elastic theory using Young's modulus and Poisson's ratio.

3.4. Stress-strain Behavior through Progressive Fracture Theory

Progressive fracture theory was utilized to better understand the stress-strain behaviors of our test samples. Bieniawski (1967) suggested that the stress-strain curve of a brittle rock can be divided into five regimes. Regime 1 describes the non-linear elastic behavior due to the closure of initial microcracks. Regime 2 describes the linear elastic behavior as a result of the completed closure of the initial microcracks. Regime 3 describes the non-linear elastic behavior due to the tensile stable crack propagation. Regime 4 describes the plastic behavior due to the propagation of unstable cracks. Regime 5 describes the post-peak deformation.

Figure 17 shows the five regimes of crack development on the triaxial test results of SV2. The crack closure axial strain (ε_{cc}) defines the transition from Regime 1 to Regime 2. Before reaching the ε_{cc}, the non-linear stress-strain curve in Regime 1 represents the closure of existing microcracks in the rock. Once these existing microcracks are closed, stress-strain deformation of the rock becomes linear and elastic in Regime 2. The crack initiation axial strain (ε_{ci}) defines the transition from Regime 2 to Regime 3. The non-linear stress-strain behavior in Regime 3 represents the onset of dilation due to the introduced cracks parallel to the direction of the maximum applied load (Martin and Chandler 1994). The crack damage axial strain (ε_{cd}) defines the transition from Regime 3 to Regime 4 where unstable cracks propagation occurs. Bieniawski (1967) defined the ε_{cd} at the point of reversal in the volumetric strain-axial strain curve as illustrated in Figure 18. The failure axial strain (ε_f) corresponds to the peak stress of the stress-strain curve and the beginning of Regime 5.

Martin and Chandler (1994) proposed the use of a crack volumetric strain-axial strain curve to determine the ε_{cc} and ε_{ci} strains. The crack volumetric strain (ε_{vc}) can be determined by subtracting an elastic volumetric strain (ε_{ve}) from a total volumetric strain (ε_v). The total volumetric strain is determined by Eq. (2), and the elastic volumetric strain is determined by Eq. (3) using elastic properties determined from the linear potion of stress-strain curves in Regime 2

$$\varepsilon_v = \varepsilon_{vc} + \varepsilon_{ve} \tag{2}$$

$$\varepsilon_{ve} = \frac{1-2\upsilon}{E}(\sigma_1 - \sigma_3) \tag{3}$$

where E is the Young's modulus, υ is the Poisson's ratio, and σ_1 and σ_3 are major and minor principal stresses, respectively. Martin and Chandler (1994) suggested manually identifying the two boundaries of the relatively flat portion of the crack volumetric-axial strain line as the ε_{cc} and ε_{ci} strains. This approach is applicable to dry rock specimens which were originally tested by them for the determination of ε_{cc} and ε_{ci} strains. However, our triaxial experiments were performed on saturated rock specimens considering the P_p measurement. It is challenging to visually identifying this flat portion in Figure 18, which shows the plot of calculated crack volumetric strain versus the measured axial strain for SV2. To overcome this limitation, a method is proposed to determine more accurate ε_{cc} and ε_{ci} strains. Using the linear regression function of the deviatoric stress-axial strain determined in Figure 16(b), the difference between the measured deviatoric stress (σ_{dm}) from the triaxial test and estimated deviatoric stresses (σ_{de}) using the linear regression function is determined using

$$\sigma_{diff} = \sigma_{dm} - \sigma_{de} \tag{4}.$$

Figure 19 shows the difference in deviatoric stresses as a function of the axial strain for SV2. Regime 2 is identified when the σ_{diff} values are approximately zero. The ε_{cc} and ε_{ci} strains are determined at the first and last σ_{diff} values closest to zero before departing from the linearity in Figure 19.

Figure 20 shows the stress-strain curves of SV1, SV2 and SV3 under three different differential pressures considering the regimes of crack developments. All curves are plotted up to the peak stress (i.e., from Regime 1 to Regime 4). Using the proposed method, the ε_{cc}, ε_{ci} and ε_{cd} that define the four regimes were determined as indicated by dashed lines in Figure 20 and summarized in Table 4. Figure 21 shows the stress-strain curves of SH1, SH2 and SH3 under three different differential pressures while Figure 22 shows the stress-strain curves of DH1, DH2 and DH3. The results show that ε_{cc} and ε_{ci} values generally decrease with increasing differential pressures except for sample SH3. No clear relationship between ε_{cd} and differential pressure is observed. All ε_{ci} values are larger than the ε_{cc} values. For rock specimens SV1, SH1, SH2, DH1 and DH3, the ε_{cd} values are either equal or smaller than the ε_{ci} values. These results suggest that the initiation of tensile stable crack defined in Regime 3 occurred instantaneously and transformed immediately into unstable cracks in Regime 4. Another possible reason could be attributed to the overestimation of the linear Regime 2 by the proposed method, leading to larger ε_{ci} values.

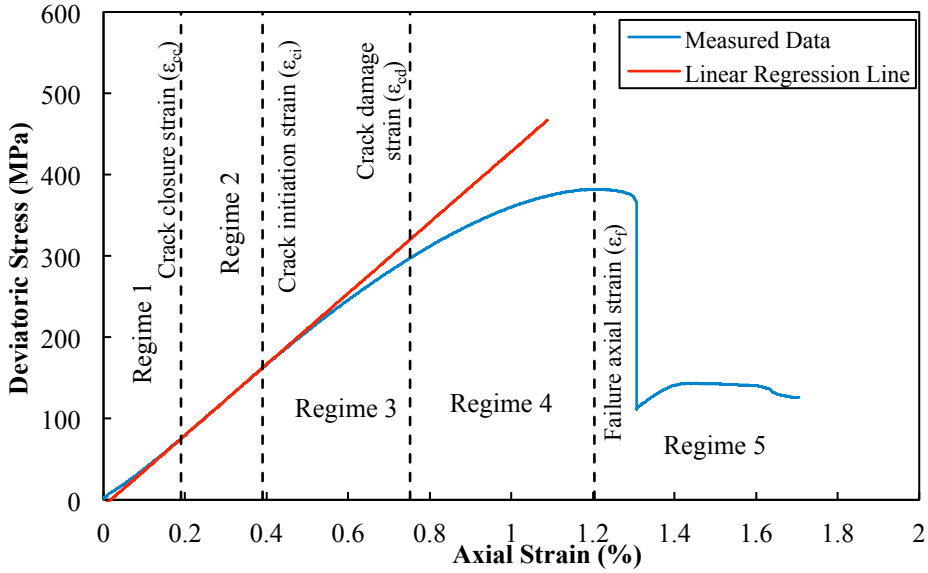

Figure 17. Stress-strain results for Weber Sandstone (SV2) showing the five regimes.

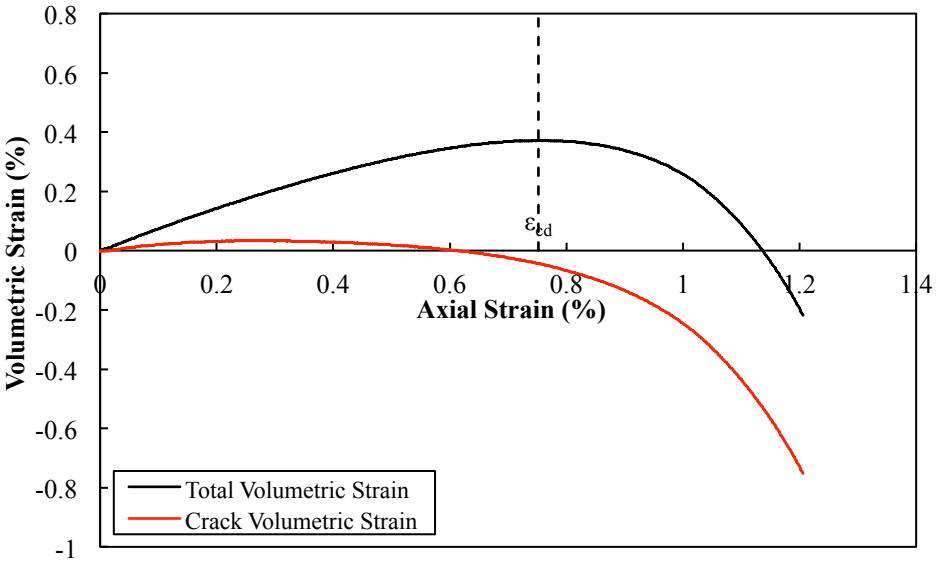

Figure 18. Total and crack volumetric strains versus axial strain for Weber sandstone (SV2).

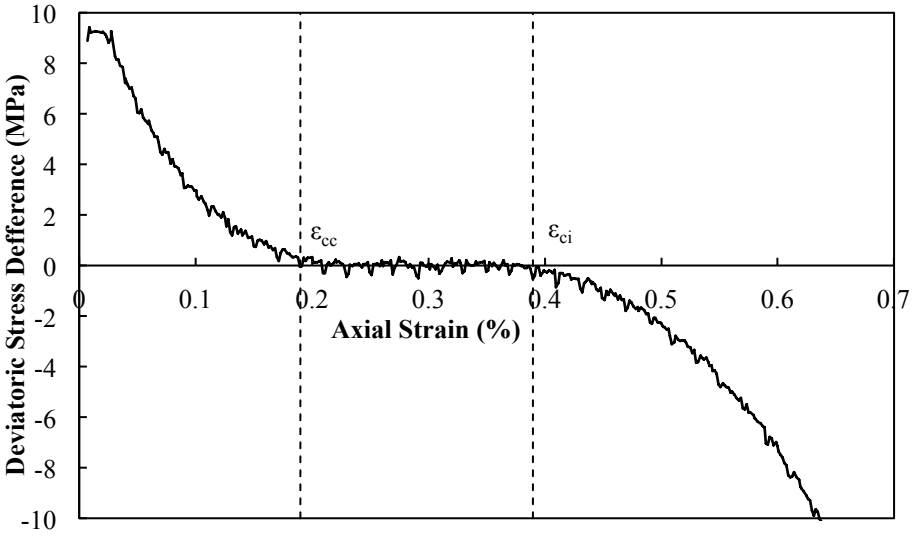

Figure 19. Deviatoric stress difference versus axial strain for Weber sandstone (SV2).

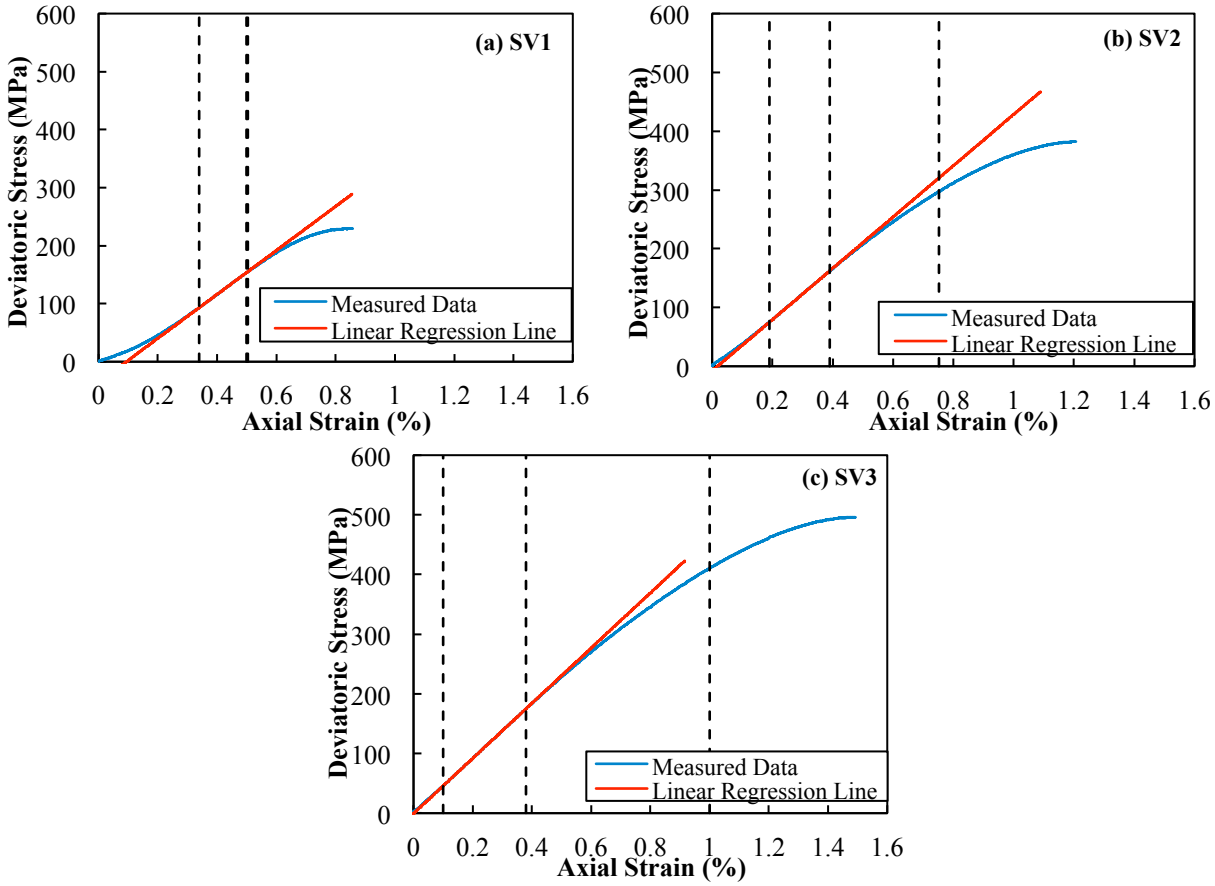

Figure 20. Stress-strain results and the linear regression lines showing the regimes of crack development for (a) SV1, (b) SV2, and (c) SV3.

Table 4. Estimated strain parameters.

Specimen ID	ε_{cc} (%)	ε_{ci} (%)	ε_{cd} (%)	c (MPa)	ϕ (°)
SV1	0.34	0.50	0.50		
SV2	0.19	0.39	0.75	39.5	47.2
SV3	0.10	0.38	1.00		
SH1	0.33	0.50	0.49		
SH2	0.26	0.41	0.39	51.72	45.0
SH3	0.46	0.66	1.21		
DH1	0.23	0.31	0.29		
DH2	0.19	0.28	0.39	15.73	27.6
DH3	0.11	0.23	0.22		
S1; S2	N/A	N/A	N/A	N/A	53.27
D1; D2; D3	N/A	N/A	N/A	N/A	31.96

ε_{cc}–crack closure strain; ε_{ci}–crack initiation strain; ε_{cd}–crack damage strain; c–Inherent shear strength; and ϕ–Internal friction angle.

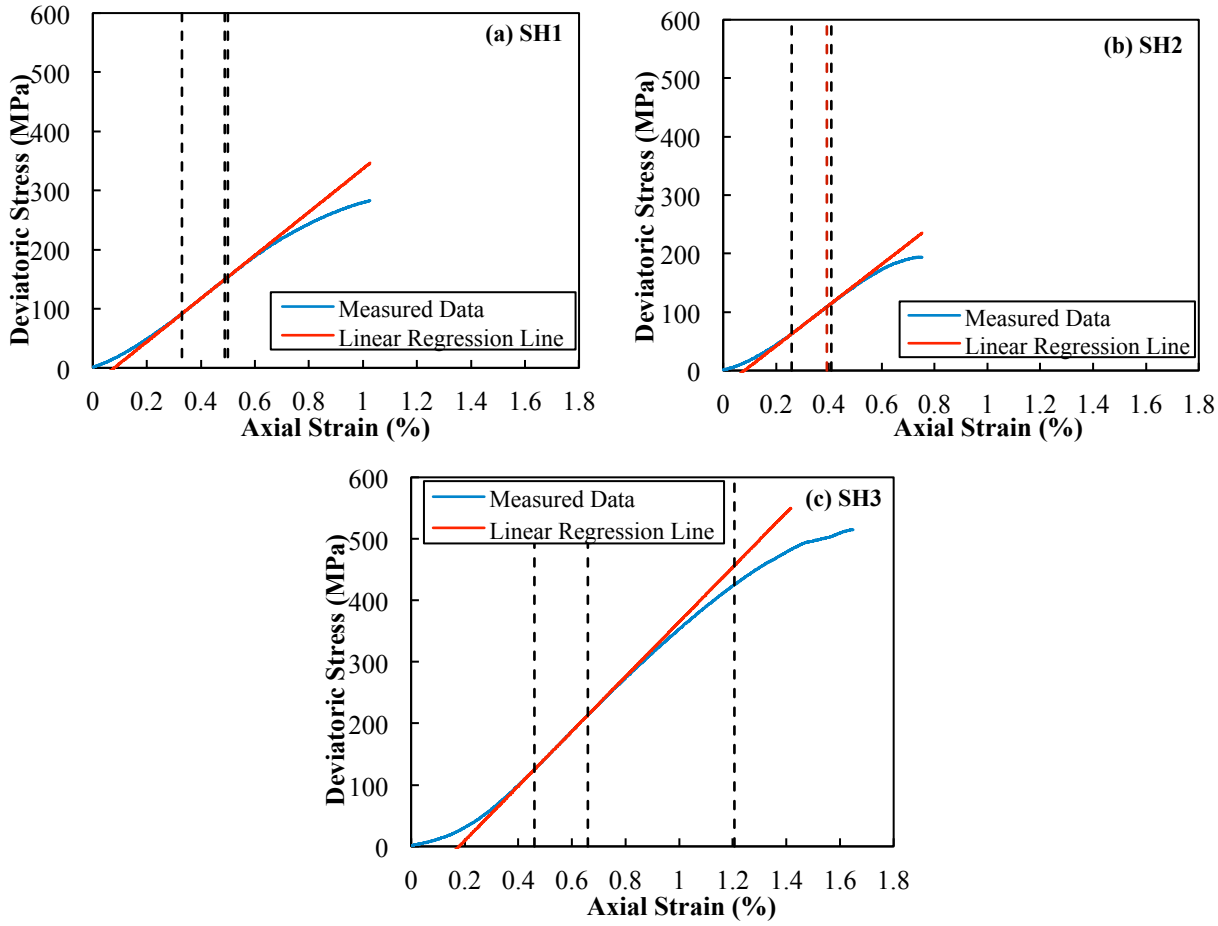

Figure 21. Stress-strain results and the linear regression lines showing the regimes of crack development for (a) SH1, (b) SH2, and (c) SH3.

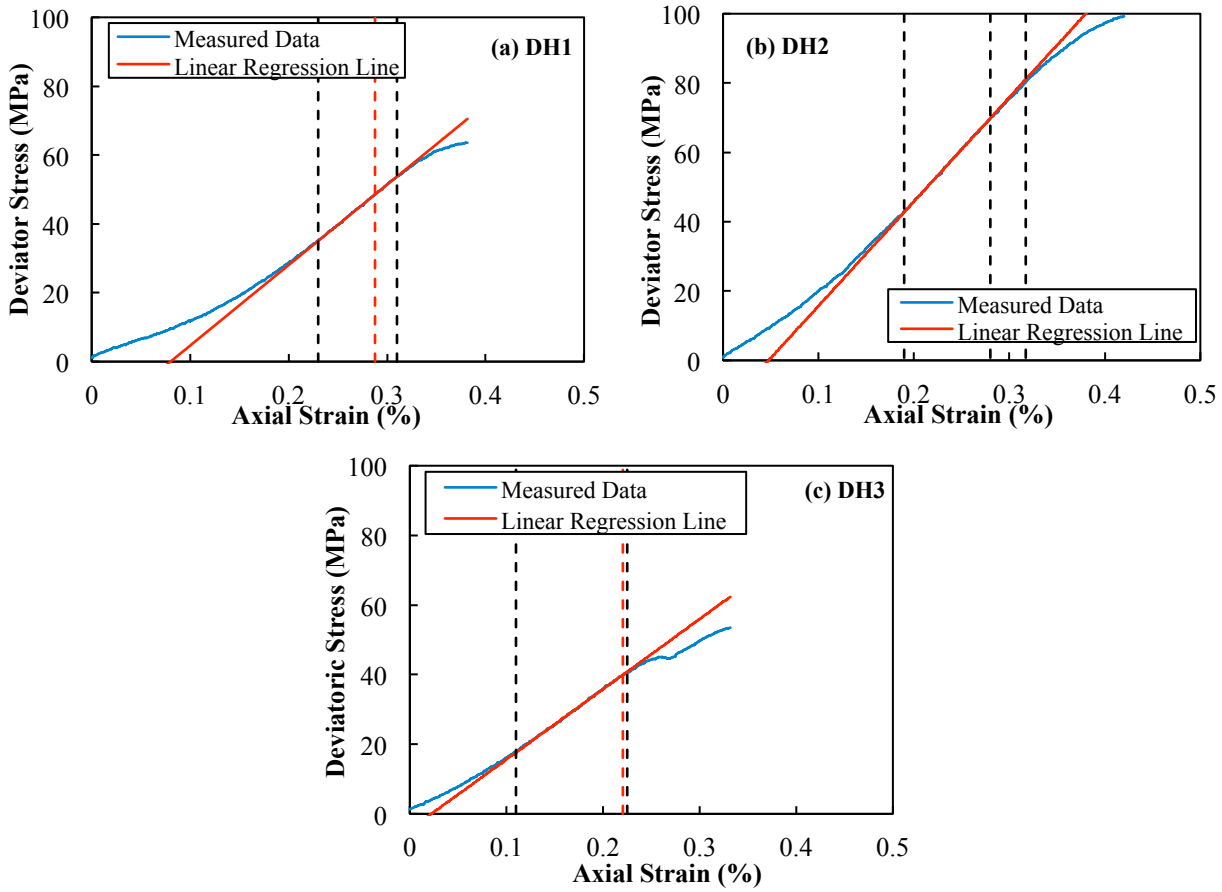

Figure 22. Stress-strain results and the linear regression lines showing the regimes of crack development for (a) DH1, (b) DH2, and (c) DH3.

3.5. Linearized Mohr-Coulomb Failure Theory

Linearized Mohr-Coulomb failure envelopes (dashed lines) determined based on Mohr's circles at three differential pressures for three RSU rocks are plotted in Figure 23. The inherent shear strength (c) and internal friction angle (ϕ) of the vertical sandstones (SVs) were estimated as 39.50 MPa and 47.2° (Figure 23(a)). Comparing the Mohr circles of SV2 and SH2, the maximum shear stress of SH2 (97.21 MPa) is significantly less than 190.98 MPa of SV2. Furthermore, the Mohr's circle of SH2 does not following the increasing trend of the Mohr's circles of SH1 and SH3 in Figure 23(b). This could be attributed to the unusual triaxial test results of SH2 (Figure 11 and Figure 14). Therefore, the c and ϕ values of 51.72 MPa and 45.0°, respectively, were determined based on SH1 and SH3. For the horizontal dolomites (Figure 23(c)), the maximum shear stress of 21.67 MPa for DH3 is less than 31.89 MPa and 40.97 MPa of DH1 and DH3, respectively. The Mohr's circle of DH3 does not touch the linearized Mohr-Coulomb failure envelope. Therefore, the c and ϕ values of 15.73 MPa and 27.6° were determined based on DH1 and DH2 in Figure 23(c). Generally, the strength parameters of sandstones are larger than those of dolomites. The ϕ value of dry sandstones (53.27°) is at least 12% higher than that of saturated sandstones (Table 4). Likewise, the ϕ value of dry dolomites (31.96°) is 16% higher than 27.6° of saturated dolomites.

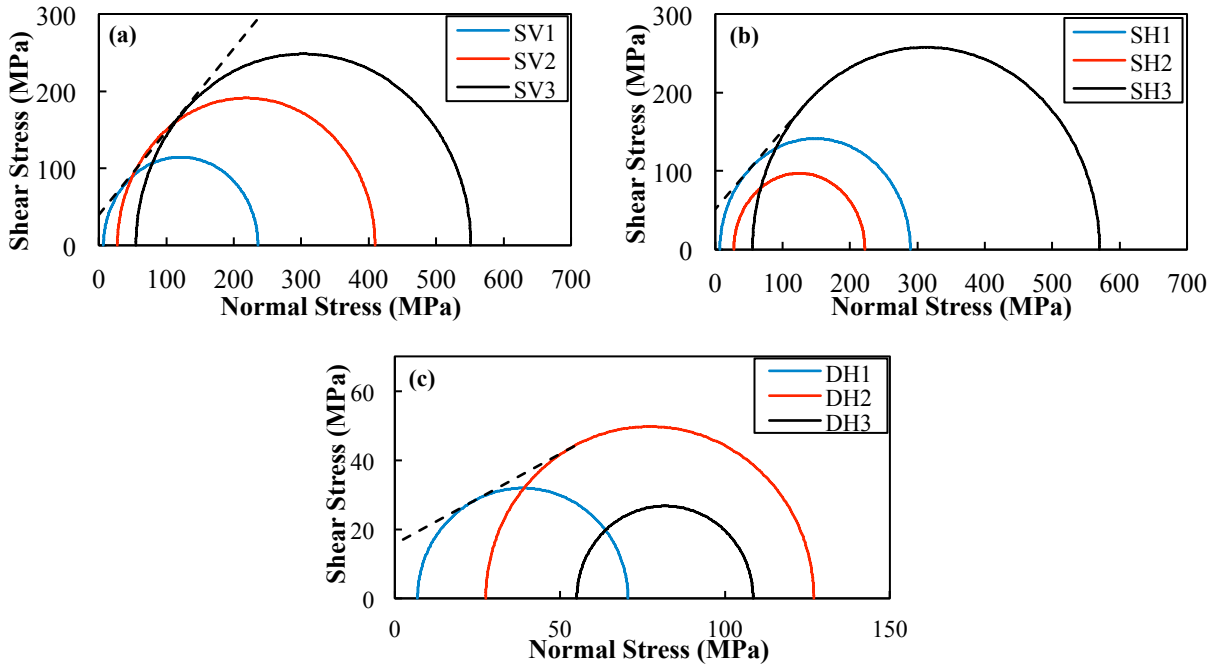

Figure 23. Mohr's circles and linearized Mohr-Coulomb failure envelopes for (a) vertical sandstones, (b) horizontal sandstones, and (c) horizontal dolomites.

4. Summary and Conclusions

Baseline geomechanical experiments were completed to understand the stress-strain behaviors and quantify the geomechnical properties of Madison Limestone and Weber Sandstone plugs saturated with brine. Nine triaxial tests at in-situ reservoir temperature and pressure conditions were conducted. Additionally, three hydrostatic experiments were conducted. Modified methods are proposed to better determine the Young's modulus, Poisson's ratio, and critical axial strains that define the regimes of crack development. The following conclusions are drawn from the experimental results:

1) Results from the hydrostatic tests show that all dry samples experienced an increase in volumetric strain with increasing confining pressure. Dolomite of the Madison Limestone with a porosity of approximately 20% experienced plastic deformation of 0.2%. Weber Sandstone with a porosity of approximately 8.2% experienced less than 0.1% plastic deformation. The results of subsequent loading-unloading cycles are governed by the elastic mechanism of the samples.
2) For saturated vertical sandstones, the volumetric strain increased with increasing confining pressure in Stage 2. The volumetric strain decreased with increasing pore pressure while maintaining the confining pressure during Stage 3. However, a smaller decrease in the volumetric strain is observed at a higher confining pressure. Similar results are observed for horizontal sandstones and dolomites in the Stage 2 except in SH2, DH2 and DH3. The abrupt decrease in volumetric strains in these three specimens is believed to be the result of propagation, shifting, and joining of existing microcracks that are eventually filled with pore fluid.
3) The bulk moduli of saturated specimens (K_{sat}) are larger than those of dry specimens (K_{dry}), and the bulk moduli of SHs are larger than those of SVs. The K_{dry} values estimated by Shafer (2013) using an elastic theory by assuming an ideally intact condition with no discontinuities are generally larger than those measured from hydrostatic experiments that account for the natural condition of the test samples with existing microcracks.

4) The triaxial test results of all specimens show that the axial strains continued to increase in a linear relationship with the deviatoric stress before reaching the well-defined peak deviatoric stresses. The peak stresses decreased abruptly to residual stresses with increasing axial strain. Higher peak and residual stresses were obtained at a higher confining pressure.
5) Using the proposed modified method, geomechanical elastic properties were determined with a significantly higher accuracy. The Young's modulus of the Weber Sandstone is larger than that of dolomite from the Madison Limestone. The Young's moduli of sandstones range from 34.97 GPa to 46.21 GPa while the Young's moduli of dolomites range from 20.16 GPa to 30.10 GPa. The Poisson's ratios of sandstones range from 0.08 to 0.36 while the Poisson's ratios of dolomites range from 0.27 to 0.47. Generally, the Young's modulus increases and Poisson's ratio decreases at a higher differential pressure. The Young's modulus and Poisson's ratio of dry sandstones are larger than those of saturated sandstones. However, inconsistent outcomes are observed for dolomites due to the unusual responses of DH2 and DH3 experienced during Stage 2.
6) A modified method is proposed to systematically determine the critical axial strains that define the five regimes of crack development in a rock specimen. The results show that the crack closure strain (ε_{cc}) and crack initiation strain (ε_{ci}) values generally decrease with increasing differential pressures except SH3. No clear relationship between crack damage strain (ε_{cd}) and differential pressure is observed. All ε_{ci} values are larger than the ε_{cc} values. For rock specimens SV1, SH1, SH2, DH1 and DH3, the ε_{cd} values are either equal or smaller than the ε_{ci} values. These results suggest that the initiation of tensile stable cracks defined in Regime 3 occurred instantaneously and transformed immediately into unstable cracks in Regime 4. Another possible reason could be attributed to the overestimation of the linear Regime 2 by the proposed method, leading to larger ε_{ci} values.
7) The shear strength parameters, inherent shear strength and internal friction angle, of sandstones are larger than that of dolomites. The internal friction angles of dry sandstones and dolomites are higher than that of saturated sandstones and dolomites, respectively.

5. References

ASTM D4543. (2008). "Standard Practices for Preparing Rock Core as Cylindrical Test Specimens and Verifying Conformance to Dimensional and Shape tolerances." ASTM International, West Conshohocken, PA.

Bieniawski Z. T. (1967). "Mechanism of Brittle Fracture of Rock: Part I−Theory of the Fracture Process." International Journal of Rock Mechanics and Mining Sciences & Geomechanics Abstracts, 4(4), pp. 395-404.

Eberhardt, E., Stead, D., Stimpson, B., and Read, R.S. (1998). "Identifying Crack Initiation and Propagation Thresholds in Brittle Rock." Canadian Geotechnical Journal, 35 (2), pp. 222-233.

Fabre, D. and Gustkiewicz, J. (1997). "Poroelastic Properties of Limestones and Sandstones under Hydrostatic Conditions." International Journal of Rock Mechanics and Mining Sciences, 34, pp. 127-134.

Martin, C.D., and Chandler, N.A. (1994). "The Progressive Fracture of Lac Du Bonnet Granite." International Journal of Rock Mechanics and Mining Sciences & Geomechanics Abstracts, 31(6), pp. 643–659.

Shafer, L.R. (2013). "Assessing Injection Zone Fracture Permeability through the Identification of Critically Stressed Fractures at the Rock Springs Uplift CO2 Sequestration Site, SW Wyoming." Master Thesis, Department of Geology and Geophysics, University of Wyoming, Laramie, WY.

Zimmerman R.W. (1991). Compressibility of Sandstones. Volume 29, 1st Edition, Elsevier Science Publishers B.V., Amsterdam, Netherlands, 172 p.

Appendix VIII

Initial Fluid Flow Simulation

For the initial fluid flow simulation, a compositional model corresponding to a section of the Teapot Dome Tensleep Sandstone (the Tensleep and Weber Sandstones are the same formation, the different names are used in different parts of Wyoming and adjoining states) was developed. This model, containing roughly 6,000 gridcells, was uploaded in CMG-GEM version 2015.106 (Computer Modelling Group compositional simulator most recent update). The model was set up as an aquifer containing two up-dip vertical injection wells and one down-dip horizontal brine producer for pressure management. The simulation included the traditional hydrostatic geomechanical consideration of pore compressibility, but no effect on absolute permeability. Compressibility values in this simulation corresponded to the Teapot Dome Tensleep Sandstone. Data for the Madison Limestone and Weber Sandstone were collected and incorporated into the final fluid flow models (Appendix 9).

The initial fluid flow simulation were run on a Dell Optiplex 7010 (64-bit, 3rd Gen Intel Core i&-3770 processor (Quad Core, 3.40 GHz), 16 GB of RAM) using multithreading (parallel) tokens to enable use of the four onboard cores. The simulation ran for storage scenarios of 250 years, with previously tested numerical controls, including 50 years of carbon dioxide injection at roughly 2% pore volumes injected per year and 200 years with shut-in wells, needing an elapsed time of 20 minutes.

Appendix IX

Final Fluid Flow Simulations

Executive Summary

This appendix summarizes analyses and results of Conducting Fluid Flow Simulations. These simulations consisted of multiphase flow fluid evaluations of CO_2 storage scenarios in the Weber Sandstone and the Madison Limestone at the Rock Springs Uplift. The CMG-GEM software was used to build composition models with different degrees of process coupling (Appendix 8). Considerations of property upscaling (petrophysics, rock physics, and multiphase flow) were evaluated in an integrated fashion along with the need to optimize both the geomechanical and fluid flow grids.

This appendix is comprised of two parts. The first part summarizes the results of *Time-independent and Two-way Coupling Simulations* and the sec- ond part summarizes the results of *Time-dependent Model Update*. The first part also includes results and discussion of experiments that were conducted on the Weber Sandstone and the Madison Limestone. Experiments were needed because coreflooding data (pressure and fluid volumes as functions of time) were necessary for the history-matching exercise to draw relative permeability and capillary pressure curves. These experiments are presented in this report because they were outside the scope of the relevant experimental program for this project (Appendix 5).

The key findings are:

1) When time-independent properties are considered (i.e. porosity, permeability), geomechanical properties can be neglected, but use of relative permeability curves before and after rock exposure to carbonic acid leads to a measurable in terms of rates and residual phases saturation. This indicates that when these more simplified simulations are considered, relative permeability dependence on reactive should be considered.

2) Given the low permeability of the Weber Sandstone, injectivity values lead to quite modest injection rates that ultimately results is small volumes of carbon dioxide stored.
3) Perhaps more importantly, when more realistic simulations that consider coupling of geomechanics, geochemistry and fluid flow, the estimates for the Madison Limestone cannot disregard the time-dependent considerations (i.e. Young's modules, Poisson ratio) of these couplings. However, this is not an important consideration of the Weber Sandstone.
4) The results in this report directly indicate that the workflow for the Weber Sandstone formation can be simplified, except for the multiphase flow dependence on reactivity. On the other hand, a more complex workflow for the Madison Limestone should incorporate time-dependencies (i.e. Young's modules, Poisson ratio) of the multiple couplings.

Part 1
Time-Dependent Supercritical CO_2 Relative Permeability and its Impact on Large-Scale CO_2 Storage in Carbonate Reservoirs

Abstract

In geologic CO_2 storage, supercritical (sc) CO_2-brine relative permeability may be influenced by $scCO_2$-brine-rock reactions. This alteration of relative permeability can significantly impact multi-phase flow properties of $scCO_2$ displacing brine in large-scale injection of CO_2 into deep saline aquifers. We present unsteady-state core-scale CO_2 drainage experiment designed to collect water production and pressure responses. We also measured endpoint CO_2 relative permeability properties at in-situ reservoir brine composition, pressure and temperature conditions before and after 400 hrs aging with $scCO_2$ saturated water. Residual water saturation and $scCO_2$ permeability after CO_2 aging were changed from 0.62/0.03 mD to 0.68/0.04 mD, respectively. This change indicates that CO_2 is more movable and more of it is left trapped after geochemical reactions. $scCO_2$-brine relative permeability curves were obtained from history matching experimental results. To better understand and quantify estimates of the effect of relative permeability changes on large-scale CO_2 storage, simulations of CO_2 injection were performed in a Madison Limestone reservoir model. Simulation results show that CO_2 injectivity will be reduced and pressure-limited reservoirs will have reduced disposal capacity, though area-limited reservoirs may have increased capacity. Future reservoir-scale modeling efforts should incorporate the observed sensitivity in relative permeability on CO_2 injection. Assuming applicability of the experimental results to other lithologies, accounting for the fact and that the majority of reservoirs are pressure limited, geologic carbon sequestration would require approximately twice the number of wells for the same injectivity.

1 Introduction

The burning of fossil fuel has increased the concentration of CO_2 in the atmosphere, leading to climate change. The reduction of CO_2 emission nowa-

days might be possible through available sequestration technologies. The geologic storage of CO_2 in the subsurface, such as oil reservoirs for CO_2-EOR [1, 2, 3, 4, 5], depleted oil/gas reservoirs [6, 7, 8, 9], unminable coal beds [10, 11, 12, 13, 14], and deep saline aquifers [15, 16, 17, 18, 19], have been reported in recent years. Four dominant trapping mechanisms contribute to the long-term storage of CO_2 in deep saline aquifers, including structural stratigraphic trapping, capillary residual trapping, solubility trapping, and mineral trapping [14, 20]. As CO_2 is injected into aquifer formations, CO_2 flows through the porous media and the non-wetting CO_2 displaces the water-wetting brine in a drainage-like process. In addition, the buoyant CO_2 migrates laterally and upwardly, and the capillary effects such as snap-off lead to disconnection of the continuous gas phase into immobile blobs and ganglia, which is referred to as capillary or residual trapping. The Rock Springs Uplift (RSU) in Southwestern Wyoming (Figure 1) has been atrgeted as a large-scale deep saline aquifers for storage [21, 22, 23]. In this document, CO_2 storage saline aquifers in this paper is the Madison limestone (130 m thick) at the RSU #1 well site on the eastern flank of the RSU is one of the targets. This carbonate reservoir consists of massive limestone and dolomite with gray cherty limestone and dolomite, deposited in a shallow marine environment [24].

Relative permeability is critical when one has to accurately predict the spatial distribution of CO_2 saturation and dynamic migration of the CO_2 plume in the subsurface. The impact of the relative permeability parameters (i.e. curvature, endpoint residual saturations and the corresponding relative permeability) on CO_2 trapping, long-term plume migration behavior and the injection parameters (i.e. injection pressure or rate) have been studied through simulation [25, 26, 27, 28]. Doughty and Pruess,Kopp et al., Burton et al. [25, 27, 28] studied the differences in plume behavior by applying different sets of relative permeability characteristic curves, showing that the small residual liquid saturation and a large residual gas saturation slow the plume migration during the injection period and keep the gas as immobile shortly after injection ends. McMillan et al. [26] show that different rel-

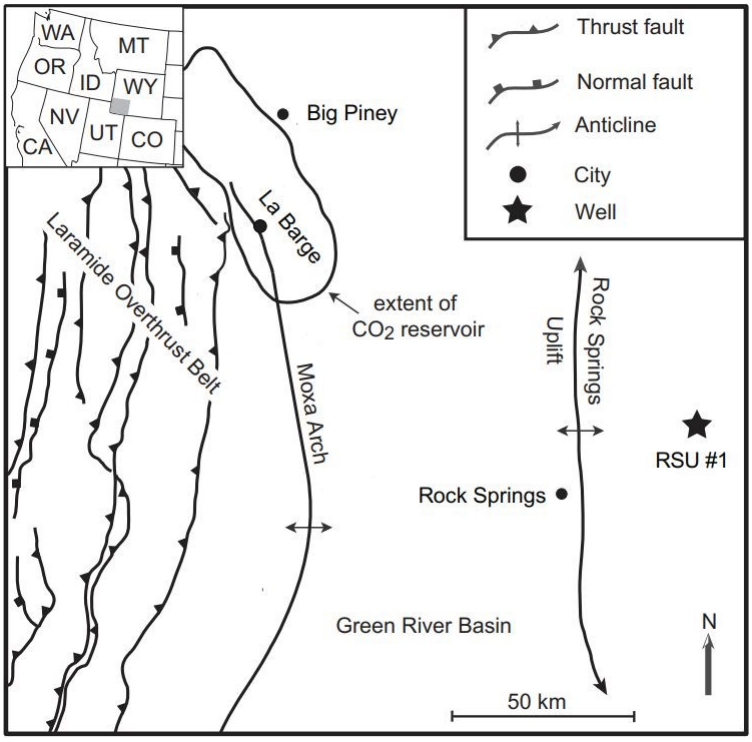

Figure 1: Geologic map of Rock Springs Uplift, southwestern Wyoming, USA and the location of well RSU #1 where studied core was sampled.

ative permeability curves affect the mobility of the Buckley-Leverett region, thus affect injectivity. Relative permeability varies with pore size characteristics, rock wettability and heterogeneity, as well as fluid properties (interfacial tension and viscosity) under reservoir pressure and temperature conditions [29]. Bachu and Bennion [29] conducted relative permeability measurements in carbonate samples exhibiting various pore-size distributions, and observed that the very low relative permeability to CO_2 at irreducible water saturation for carbonate sample, which contains large vugular porosity, contributed to channeling or bypassing effects. While no relationship was found between the pore-size distribution and the irreducible water saturation. With respect to wettability, the wetting phase relative permeability tends to decrease rapidly with decreasing wetting phase saturation [30]. Hu et al. [31] studied the impact of wettability on capillary trapping using water-wet and intermediate-wet glass micromodels. They found a high displacement front velocity and higher $scCO_2$ volume, which means that residual saturation and relative permeability are different under different wettability conditions. The impact of interfacial tension and viscosity under different pressure and temperature conditions on relative permeability are complex. Bachu and Bennion[29] concluded that IFT and viscosity contribute to the changes in relative permeability characteristics, while Pini and Benson [32] stated that the influence of fluid properties on the relative permeability curves depended on the capillary number and their effect can be ignored when capillary number is less than 10^{-6}. However, capillary pressure is affected by IFT, which increases with temperature and salinity, and it decreases when pressure is increased [33, 29].

Numerous studies have been published regarding the change of pore networks (i.e. pore shape, pore-size distribution, and mineral reactive surface area), thus changing porosity, permeability and wettability due to geochemical reactions, i.e. mineral dissolution and precipitation, especially for carbonate reservoirs when CO_2 is injected in saline reservoirs. As the formation brine becomes enriched with CO_2 along the edge of the plume, the pH of the formation brine can decreases by 1-2

units inducing a state of geochemical disequilibrium [17]. Wang et al. [34] studied the reactivity of dolomite with water-saturated $scCO_2$ at reservoir conditions and the brine composition and pore structure after reactions indicate that dolomite dissolves and carbonate minerals precipitate. The results of our previous experiment by reacting core plugs with water saturated brine under reservoir conditions after 400 hours showed that small mineral particles were dissolved, but it was hard to identify the changes on the surface and corners of big dolomite crystals. In addition, permeability is changed even though porosity does not exhibit changes, and the pore-size distribution broadens so slightly as shown from T_2 and diffusion coefficient distributions. Many wettability measurements in CO_2-brine-rock systems have been conducted for a subset of mineral surfaces, i.e. quartz, calcite or mica. The contact angle changes with increasing pressure and temperature when rock is exposed to $scCO_2$ [35, 36, 37].On the other hand, Espinoza and Santamarina[38] found that the contact angle is independent of pressure. The cleaning procedures, equilibrium states of the phases, brine composition (ionic strength), measuring conditions and surface roughness might be responsible for contradictory conclusions. Even through wettability has been studied when minerals are exposed to dense CO_2, the literature rarely considers the wettability alteration due to mineral dissolution and precipitation, which affect surface roughness, brine composition and pore size distribution as mentioned already. Moreover, wettability heterogeneity such as intermediate water-wet due to chemical heterogeneity of pore surfaces cannot be characterized by contact angle measurements. In summary, mineral dissolution and precipitation can change pore networks and wettability, and thereby affect relative permeability.

In this work, our objectives are to study the impact of geochemical reaction on relative permeability curves and to investigate the change of relative permeability characteristics contributing to dynamic plume evolution and stabilization. We conducted CO_2 unsteady-state $scCO_2$ flooding on a limestone rock sample before and after aging with CO_2-saturated brine under same reservoir conditions. CMG-

GEM was employed to match the water production of unsteady-state corefloods to obtain the relative permeability curves. To investigate the influence of the relative permeability curves on larger-scale CO_2 storage process, numerical simulations of CO_2 injection in Madison Limestone formation at Rock Springs Uplift were performed. A realistic 3D model of Madison Limestone formation, as well as relative permeability curves obtained from history matching were used.

2 RSU Static Model Buildup

Permeability can be derived from laboratory analysis of core samples. However, for thick reservoir sections or poorly cored wells, it becomes impractical. Instead, permeability is commonly estimated in uncored sections or poorly cored wells from the following permeability-versus-porosity relationship:

$$log(K) = a\phi + b \tag{1}$$

where K and ϕ are permeability and porosity, and a and b are fitting parameters. Calibrated well-logs using a few lan measurements are used to generate permeability fields from porosity distributions.

Prediction of permeability in carbonate rocks is more difficult than in sandstone, because carbonate pore geometry can be very complex. The porosity-permeability relationship varies considerably in different facies of the Madison Limestone. The flow zone index (FZI) and Winland's R_{35} methods were used to classify different rock types in Madison Limestone, and used at different locations for different rock types. For the Weber Sandstone reservoir, permeability was estimated from the permeability-porosity relationship in equation (1) and fitting parameters are 0.443 and -3.263.

Figures 2 to 5 show the histograms and distribution of the Weber Sandstone formation and the Madison Limestone formation in RSU built using Petrel (Schlumberger). The average porosity and permeability in the Weber Sandstone formation

and the Madison Limestone formation are: 4.8%/11.2% and 0.04/9.32 mD, respectively.

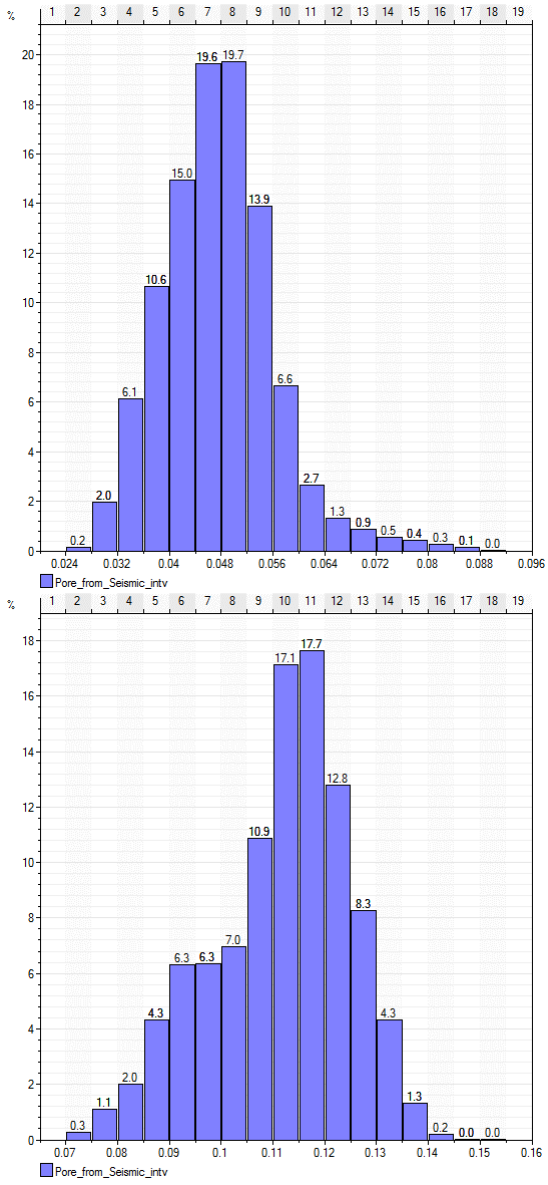

Figure 2: Histograms of the porosity of (left) the Weber Sandstone and (right) the Madison Limestone, Rock Springs Uplift

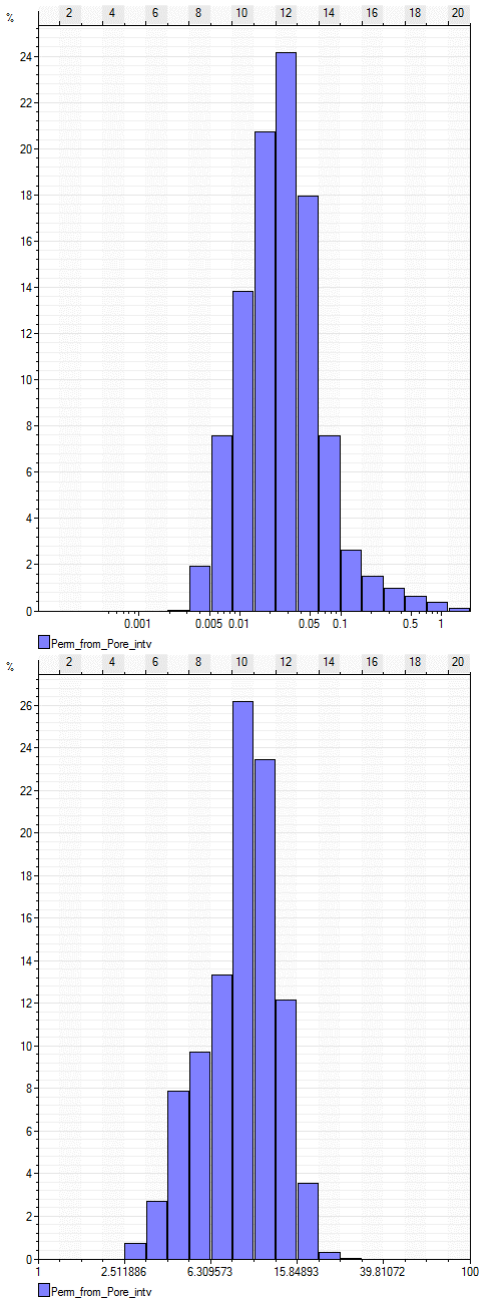

Figure 3: Histograms of the permeability of (left) the Weber Sandstone and (right) the Madison Limestone, Rock Springs Uplift

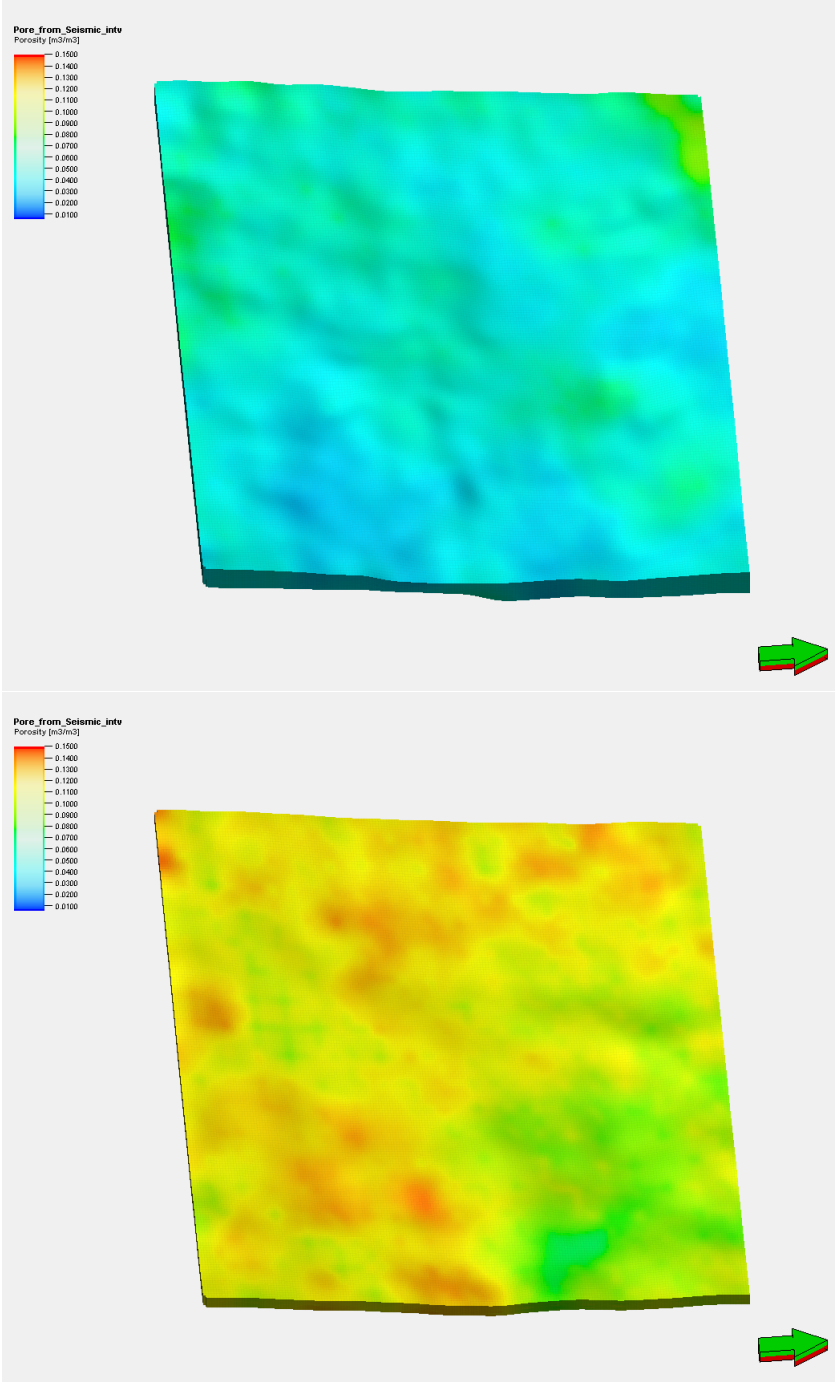

Figure 4: Porosity distribution of (up) the Weber Sandstone and (low) the Madison Limestone, Rock Springs Uplift

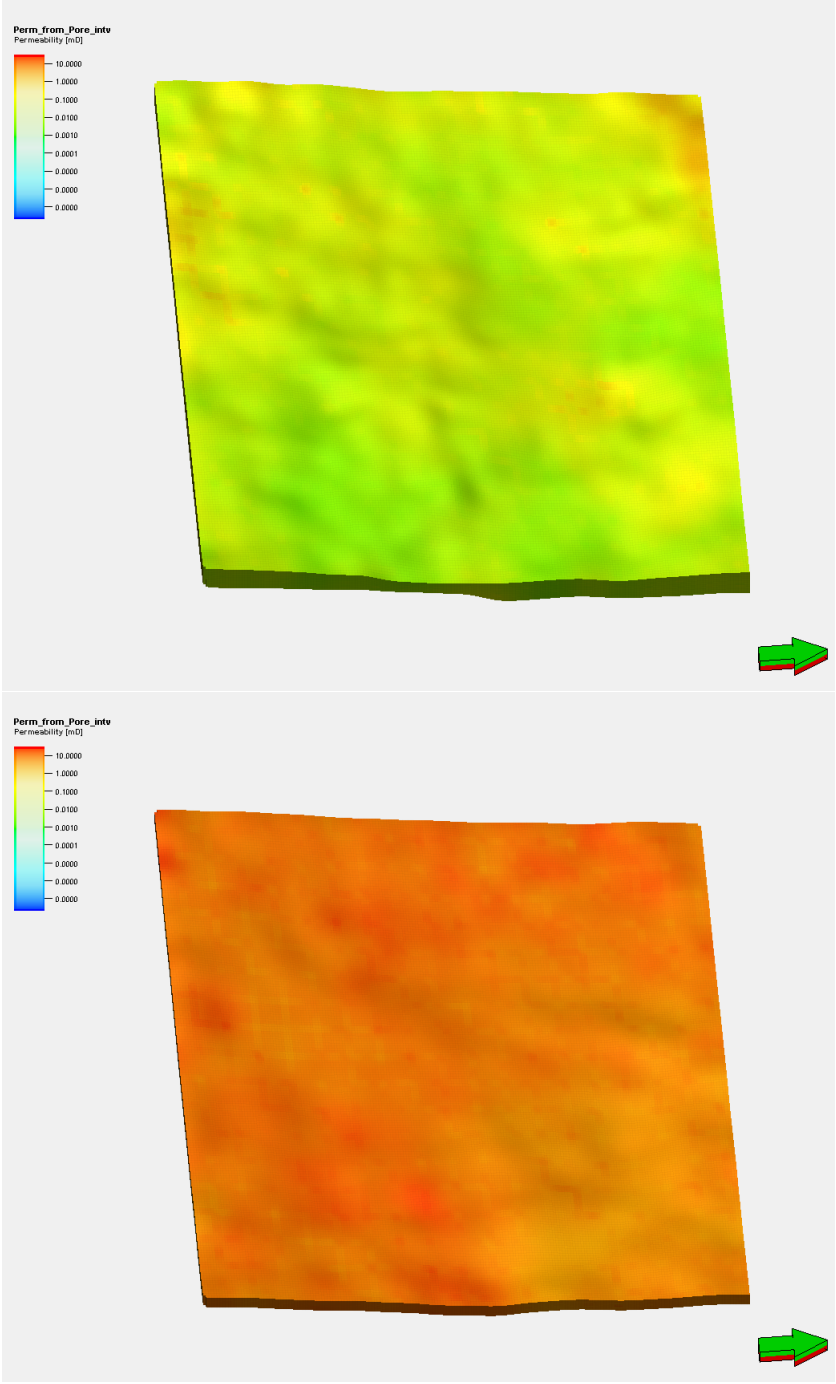

Figure 5: Permeability distribution of (up) the Weber Sandstone and (low) the Madison Limestone, Rock Springs Uplift

3 Materials and Methods

Multi-phase flow properties included unsteady-state CO_2 floodings (drainage) in a limestone core before and after aging with scCO_2-saturated brine and the aging process. The unsteady-state CO_2 floodings were designed to study changes of relative permeability curve due to mineral dissolution and precipitation after the aging process.

3.1 Materials

Core samples used were drilled from the Weber Sandstone and Madison Limestone formations. Table 1 lists dimensions and petrophysical properties of the core sample and the conditions of CO_2 flooding. Gas (N_2) porosity and permeability were measured, while for outcrop core 1 (OC1), porosity was measured volumetrically. Brine absolute permeability was measured for all samples before and after aging. Because the pore volume for all core samples from the subsurface is too small (less than dead volume of the system: 4.7 cm^3), they are mostly useful to obtain a qualitative interpretation of coreflooding results, so an outcrop limestone core was selected to obtain quantitative results. History matching and reservoir simulation were conducted based on the relative permeability of OC1. To synthesize the formation brine, research-grade salts and standards were mixed with deionized water. The initial brine composition was calculated to be in equilibrium, or as close as possible at equilibrium with the rock minerals used in the experiments at reservoir conditions to minimize reaction between the minerals and brine. Table 2 lists the chemical concentrations of synthesized formation brine prepared for CO_2 flooding.

3.2 Experimental Setup and Procedure

The experimental equipment used in this study is a custom-designed high-pressure/high-temperature (HPHT) core-flooding syste. Figure 6 shows a schematic diagram of it. Two high precision syringe pumps (Teledyne ISCO 260D) were used to control

Table 1: Core properties

Sample	Formation	Diameter, cm	Length, cm	ϕ, %	K_{abs}, mD	Pore volume, cm^3
WS1	Weber	2.54	3.81	9.44	5.52	2.50
ML1	Madison	2.54	5.23	24.80	47.90	3.28
ML2	Madison	2.53	5.28	23.47	23.82	3.13
ML3	Madison	2.53	5.22	19.46	10.67	2.57
ML4	Madison	2.52	5.16	17.43	25.13	2.12
OC1	Outcrop	3.81	14.61	12.5	230.44	20.7

Table 2: Chemical Concentrations of synthesized formation Brine

Major Species/Complexes	Concentration, mol/kg
SO4	0.105
Cl	1.619
Na	1.476
K	0.060
Mg	0.003
Ca	0.004

pore pressure, confining pressures, and to inject fluids. Two floating piston accumulators connecting to the syringe pump were used for transferring $scCO_2$ and brine at reservoir conditions. The reactant fluid (CO_2-saturated brine) was generated through equilibrium between the brine and $scCO_2$ phases for 24 hours in another floating piston accumulator. Pore pressure and differential pressure between the inlet and outlet of the coreholder were monitored by two pressure transducers. A Schlumberger Back Pressure Regulator (Schlumberger Canada Limited, Edmonton, Alberta) connecting an ISCO pump regulates the outlet pressure. A two-phase separator was used to separate gas and water phase and the produced brine volume was collected. All the wetted parts of the apparatus are made with Hastelloy C-276 to avoid corrosion by acid. The core flooding system is equipped with a forced convection oven (Memmert), providing temperature uniformity within the air bath. In addition, high-pressure steel tubing, fittings, and valves (HIP) were used for plumbing the HPHT core-flooding system. Finally, pressure and cumulative fluid production was collected by computer software.

The following explains a brief experimental procedure to perform the unsteady-state corefloodings and aging process in three steps. In the first step, the core sample was wrapped with heat shrinkage tubing and then inside asleeve to prevent CO_2 from migrating out of the core, and then mounted inside the coreholder before being saturated with 'dead' brine (gas-free). The core was brought to target pressure and temperature (pressure: 34.5 MPa and temperature: 90 $^{\circ}$C) for 400 hrs. Before CO_2 injection, different injection rates were applied and the corresponding differential pressure across the core were collected. Water permeability was calculated by Darcy's law. A fixed CO_2 injection rate (0.25 cm^2/min) was employed, together with collecting inlet pressure, differential pressure and produced brine volume. As no brine is produced, CO_2 relative permeability was measured by injection a series of CO_2 rates. In the second step, pore pressure was decreased to ambient pressure and the core was vacuumed for 12 hrs and saturated with $scCO_2$-saturated brine again. The core sample was displaced with $scCO_2$-saturated brine until a constant

gas production was reached. Then the outlet valve was closed and let CO_2-brine-rock react for another 400 hrs which is longer enough compared with literature. In the final step, The vacuum and re-saturation processes were repeated, and water permeability, CO_2 flooding and CO_2 relative permeability were performed as showed in the first step.

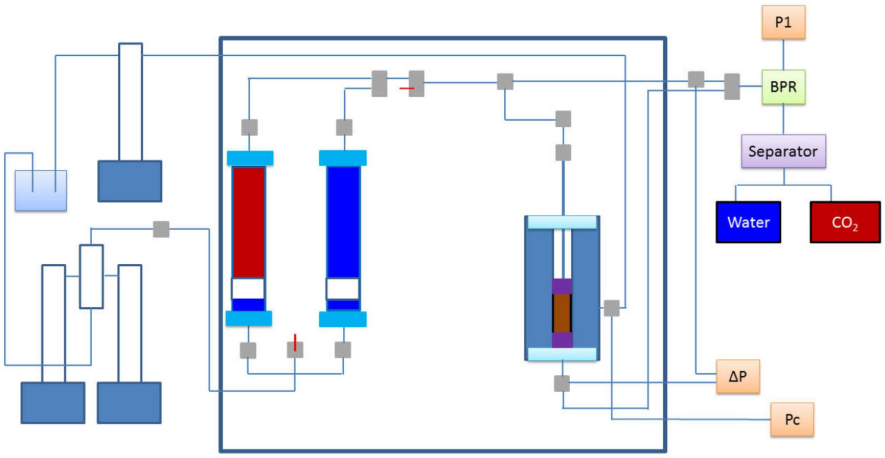

Figure 6: Schematic diagram of the experimental setup used in this work.

3.3 Numerical Simulation

A compositional model was build to obtain relative permeability curves. Since the capillary pressure curve is not available in this study, a history-matching procedure is applied to unsteady-state coreflooding experiments to obtain the relative permeability curves. In this history-matching process, the drainage relative permeability curves were determined by the following equations:

$$K_{r,w}(S_w) = K_{r,w}(S_{nw,r}) \left(\frac{S_w - S_{wc}}{1 - S_{wc} - S_{nw,r}} \right)^{n_w} \tag{2}$$

$$K_{r,nw}(S_{nw}) = K_{r,nw}(S_{wc}) \left(\frac{1 - S_w - S_{nw,r}}{1 - S_{wc} - S_{nw,r}} \right)^{n_{nw}} \tag{3}$$

where $K_{r,w}$ and $K_{r,nw}$is the water relative permeability and non-wetting relative per-

meability (CO_2) at S_w and S_{nw}, respectively. S_{wc} and $S_{nw}$is the residual water and non-wetting phase (CO_2) saturation, and $K_{r,w}(S_{nw,r})$ and $K_{r,nw}(S_{wc})$ are the corresponding relative permeability endpoints. n_w and n_{nw} are the fitting components, which were determined by history matching a homogeneous core to the measured experimental results. The pressure difference between the wetting and non-wetting phases is the capillary pressure: $p_c = p_{nw} - p_w$, which is a function of S_w and is also determined by history matching.

4 Results and Discussion

4.1 Porosity, Permeability and Compressibility

Previous studies of the Weber and Madison formations at the RSU #1 well have defined the architecture of the primary pore systems. Eolian and massive sandstone lithofacies of the Weber Sandstone have different pore character due to differences in their grain distribution.[21, 39] The bimodality of grain distribution in the eolian lithofacies generally produces a similar (bimodal) porosity distribution. The massive sandstone lithofacies typically have more evenly distributed porosity, with regards to size and distribution, reflecting the distribution of the grains.[21, 39] However, digenetic process such as cementation, pressure solution, cementation, mineral dissolution and authigenic mineral nucleation can greatly influence the heterogeneity of the pore architecture. Porosity systems in the Madison Limestone are intergranular and/or vug dominated.[21, 39] The intergranular porosity is generally located near the top of the reservoir interval, and has a relatively uniform pore character and distribution. Vuggy, sometimes moldic, porosity formed by dissolution of the carbonate. The dissolution has produced zones with massive pores and the highest overall porosity values, though they have a highly heterogenic distribution.

The petrophysical properties of the studied core samples are shown in Table 3. Different injection rates were applied and the corresponding differential pressure across the core were collected. The relationship between injection rate and dif-

Table 3: Core petrophysical properties before aging

Sample	ϕ, %	K_{N_2}, mD	K_C, mD	K_W, mD	C_P, 10^{-6} psi^{-1}
WS1	9.440	6.663	5.520	2.984	11.1
ML1	24.824	61.369	47.861	44.239	8.49
ML2	24.468	29.684	23.816	20.483	6.55
ML3	19.463	14.212	10.666	12.370	6.72
ML4	16.337	30.761	16.432	17.801	15.5
OC1	12.200	NA	NA	230.44	NA

ferential pressure is showed in Figure 7. Water absolute permeability (K) was calculated by Darcy's law:

$$q = c\frac{KA\Delta P}{\mu L} \tag{4}$$

where q is flowing rate, A is cross-sectional area, L is core length, μ is brine viscosity, ΔP is differential pressure across the core, and c is a constant value from unit conversion and equals 245.

4.2 Geomechanical Experimental Results before Aging

Geomechanical experiments were conducted by Dr. Kam Ng. Table 4 shows experimental results for Madison Limestone and Weber Sandstone samples before aging with carbonic acid, and results show that Young's modulus and Poisson's ratio of both Madison Limestone and Weber Sandstone samples vary with confining pressure and sample even though experimental conditions (i.e. pressure, temperature and pore pressure) were same for both lithologies.

4.3 CO_2 Flooding Results

In this study, coreflood tests were carried out in the Madison Limestone and Weber Sandstone samples with different absolute permeability and porosity value to study CO_2 relative permeability at reservoir conditions. Total water production curves

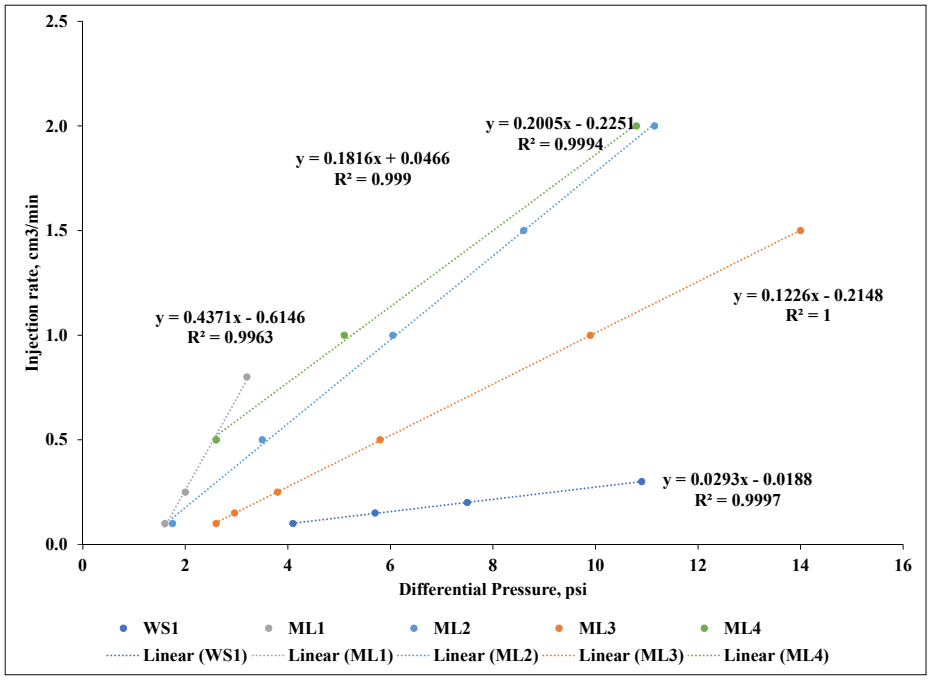

Figure 7: Relationship between differential pressure and injection rate for water permeability measurement.

Table 4: Geomechanical experiment results for the Madison Limestone and Weber Limestone samples before aging. Experimental temperature for Madison Limestone and Weber Sandstone are 93 and 90 °C, respectively.

Sample ID	Category	Pc(MPa)[1]	E (GPa)[2]	υ [3]	c (MPa) [4]	ϕ (Deg.) [5]	Pp (MPa) [6]
DH1	Madison Limestone	46.2	23.5	0.47	15.7	27.6	39.3
DH2	Madison Limestone	73.8	30.0	0.27	15.7	27.6	39.3
DH3	Madison Limestone	94.5	19.4	0.31	15.7	27.6	39.3
SH1	Weber Sandstone	43.4	36.8	0.35	51.7	45.0	35.4
SH2	Weber Sandstone	71.0	35.0	0.38	51.7	45.0	35.4
SH3	Weber Sandstone	91.7	44.4	0.08	51.7	45.0	35.4

[1] confining pressure, [2] Yong's modulus, [3]Poisson's ratio, [4] cohesion for Mohr-Coulomb

[5] internal friction angle for Mohr-Coulomb, [6] in-situ pore pressure

are shown in Figure 8. The residual water saturation for WS1 is 0.72, which is larger than Madison Limestone samples (around 0.28). In general, the higher the permeability is, the lower the residual water saturation.

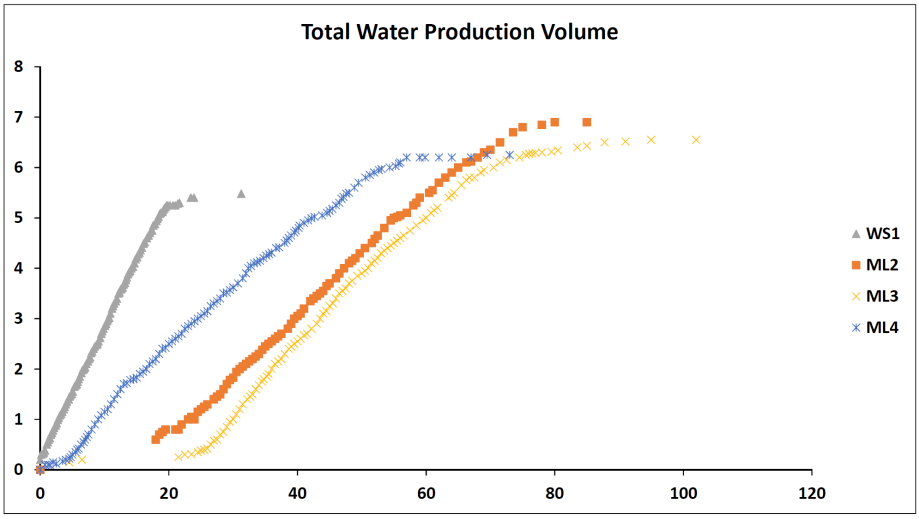

Figure 8: Total water production versus time. The dead volume of the coreflooding system is 4.7 cm^3The residual water saturation are 0.72, 0.30, 0.28 and 0.27 respectively.

The residual water saturation does not have a good relationship with permeability. It might due to the lower pore volume compared with the dead volume of the coreflooding system (4.7 cm^3), while the maximum pore volume of all core samples is 3.3 cm^3. However, it is not possible to drill a longer core sample. In addition, petrophysical properties, i.e. porosity and permeability, and petrographysical properties observed from SEM indicate that no apparent changes. Therefore, an outcrop limestone sample was selected to draw a quantitive effect of relative permeability curve changes due to CO_2-brine-rock reactions.

The total water production curves of the outcrop limestone sample (OC1) before and after aging are shown in Figure 9. It is worth noticing that compared with total water production curve before CO_2 aging, water production rate is smaller and

less water was produced. The relative permeability and capillary pressure curves might be changed because of the alteration of the pore structure and wettability, induced by CO_2-brine-rock reactions. Relative permeability parameters, like curvature, endpoint values and $scCO_2$ relative permeability, and capillary pressure might be responsible for the decrease of total water productio. However, it is hard to determine which parameter plays a more important role in this study.

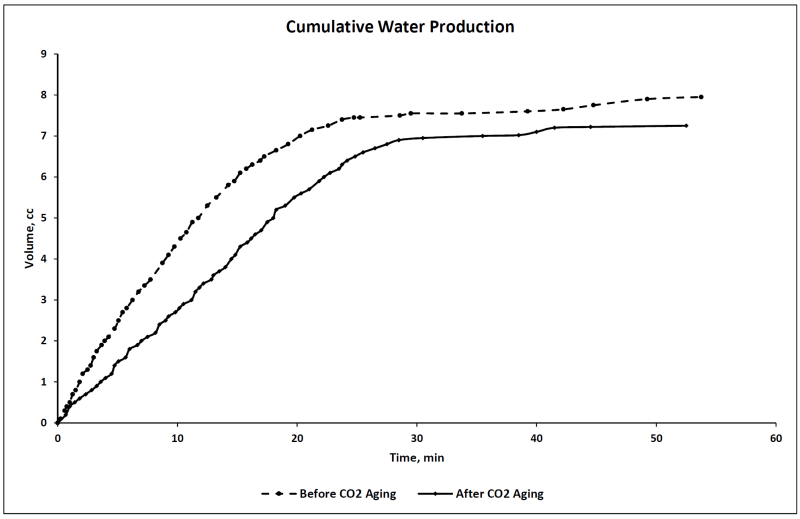

Figure 9: Total water production versus time. The dead volume of the coreflooding system is 2 cm^3. The residual water saturation before and after aging are 0.62 and 0.65 respectively.

4.4 History Match Results of Unsteady-state Coreflooding Experiments

In order to study the change of relative permeability and capillary pressure, core-scale numerical simulation was set up and history matching cases were conducted to obtain the relative permeability and capillary pressure curves before and after aging.

A 1-D model, shown in Figure 10, was built using CMG GEM (compositional simulator) to simulate the unsteady-state coreflooding process before and after ag-

ing. The initial water saturation for all gridblocks is 100% and pressure and temperature are reservoir conditions. All input parameters used in the simulation model are:

- Dimension: 100*1*1 (I*J*K)
- DI=DJ=0.0337m
- Porosity (before and after): 12.2/12.4%
- Permeability (before and after): 230/237 mD
- Length:0.00146m*100=0.146m
- Temperature: 90C
- Water viscosity: 0.39 cP
- CO_2 Injection Rate: 3.6E-4 m3/day
- Producer Constrain: Constant BHP
- Swir (before and after):0.618/0.650
- Initial water saturation: 100%

The relative permeability curves and capillary pressure curve obtained from the history process are shown in Figure 11. The history matching results before and after aging are shown in Figure 12. History matching results show that after carbonic acid aging, gas relative permeability increases and water relative permeability decreases. In addition, capillary pressure decreases. This might be due to wettability alteration. After aging, wettability turns less water wet, which results from CO_2-brine-rock reactions. The small particles on the pore surfaces dissolved during aging process and wettability response is determined by the wettability of the dolomite crystals. Furthermore, the dissolution of small particles also increases the smoothness of the pore surface, which is also responsible for the wettabiity alteration. As the rocks becomes less water wet, capillary pressure ($Pc = 2\gamma cos\theta / r$)

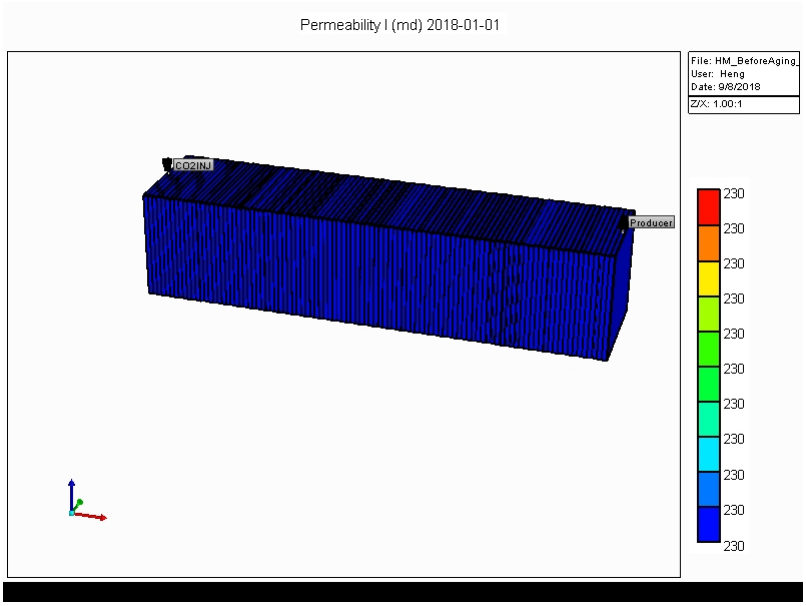

Figure 10: Simulation model used for history coreflooding result matching. Here shows permeability of the core

decreases since the change of pore size could be neglected in our previous study. On the other hand, cross point shifts to the left in the relative permeability curve when wettability altered are shown in Figure 11.

4.5 Time-independent and Two-way Coupling Simulations in RSU

In this section, time-independent and two-way coupling simulations are performed in RSU model to study the effect of pore pressure, hydrostatic pressure and geo-chemistry reactions on permeability, porosity and fluid flow. The following steps will be included:

- Simulation will be conducted incorporating effects of pore pressure on porosity, and permeability will be changed as a function of porosity;
- Simulations will be carried out considering that permeability will be changed as a function of hydrostatic pressure;

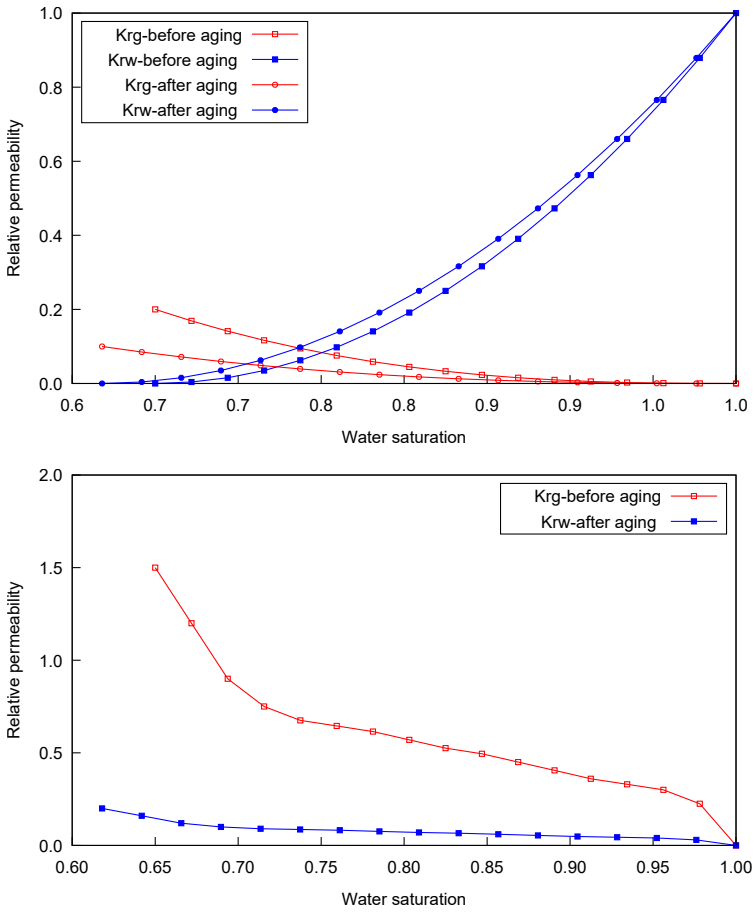

Figure 11: Relative permeability and capillary pressure curves used for history matching

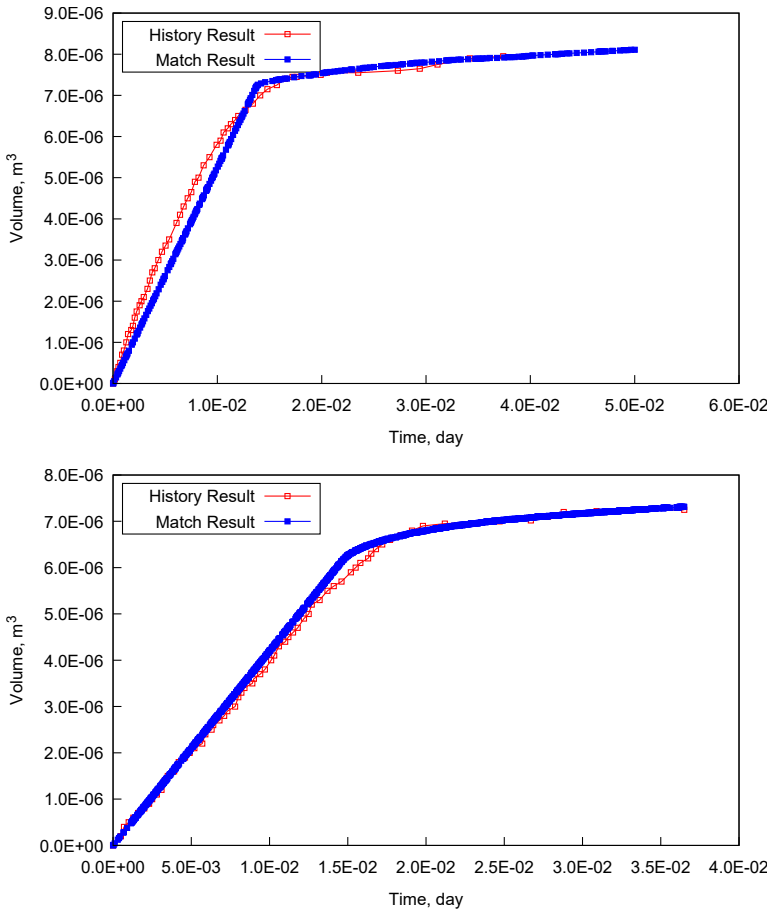

Figure 12: History matching results of cumulative water production-left: before aging; right: after aging

- Simulation model will incorporate the two-way coupling between geomechanics and fluid flow.

Since no obvious changes of geochemical properties were observed in Weber Sandstone samples, geomechanical properties were only studied for Madison Limestone formation. The designed injection rate for the Weber Sandstone and Madison Limestone formations is injected 500,000 ton/year (45000 m^3/day). Because pressure will build up rapidly if water is not produced, one producer well is drilled to hinder reservoir pressure increasing too high.

4.5.1 Weber Sandstone Formation

Relative permeability curve used for the Weber Sandstone formation were obtained from the Carbon Management Institute (CMI) at the University of Wyoming, shown in Figure 13. The injection rate of the injector is 500,000 ton/year (45000 m^3/day), and the maximum bottom hole pressure is limited to 65 MPa. As for the producer, bottom hole pressure is set as a constant, 30 MPa. Simulation was conducted for 30 years.

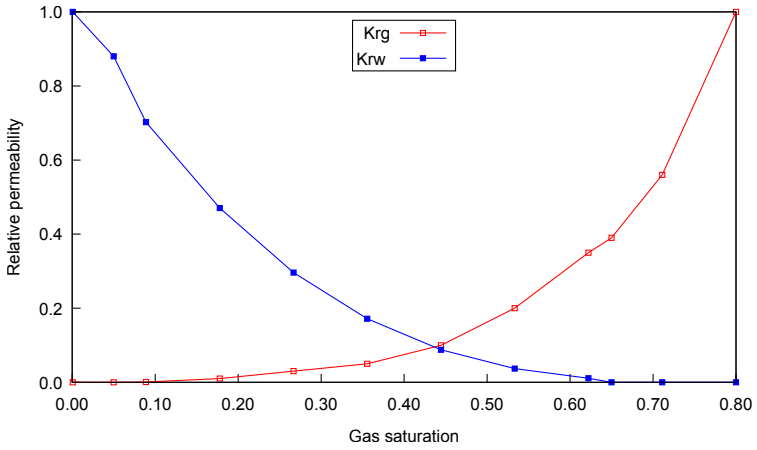

Figure 13: Relative permeability curve for the Weber Sandstone formation

Figure 15 shows gas injection rate, cumulative gas injection, water production rate and cumulative water production with time for four cases. The following is the

description of four case:

- Weber_inj_pro or Case A: base case without considering properties changes with CO_2 injection;
- Weber Pore Pressure or Case B: incorporating effects of pore pressure on porosity, and permeability will be changed as a function of porosity;
- Weber Confining Pressure or Case C: considering that permeability will be changed as a function of hydrostatic pressure;
- Weber Both or Case D: incorporate the two-way coupling between geomechanics and fluid flow. Given that geomechanical properties varied with experimental conditions (confining pressure and samples), results for a specific Weber Sandstone sample, SH1, were used in this study as representative of the formation. The effect of the initial variability of geomechanical properties was not evaluated in this study, and consequently only one rock type in terms of geomechanics was considered. The input of geomechanical properties for CMG is shown in Figure 14 (a)

From CO_2 injection curves for all cases in Figure 15, gas injection rate decreases at the beginning, increases again and stabilizes to reach a plateau value. In addition, the injection rate at the beginning is smaller than designed injection rate (45000 m^3/day). The decrease of injection rate is due to the limited injectivity, which is because of low permeability (average permeability is 0.045 md). Pressure difference between injector BHP and reservoir pressure decreases, leading to a decreasing injection rate at the beginning. With water being produced, reservoir pressure decreases, then injection rate increases again. Finally, pressure difference between injector BHP and reservoir pressure stabilized, and similarly for the injection rate. As for water production, it decreases immediately at the beginning as pressure difference between producer BHP and reservoir pressure decreases. In addition, pressure buildup from injector is too slow to recharge the reservoir pressure of gridblocks nearby the producer. As reservoir pressure is built up due to gas

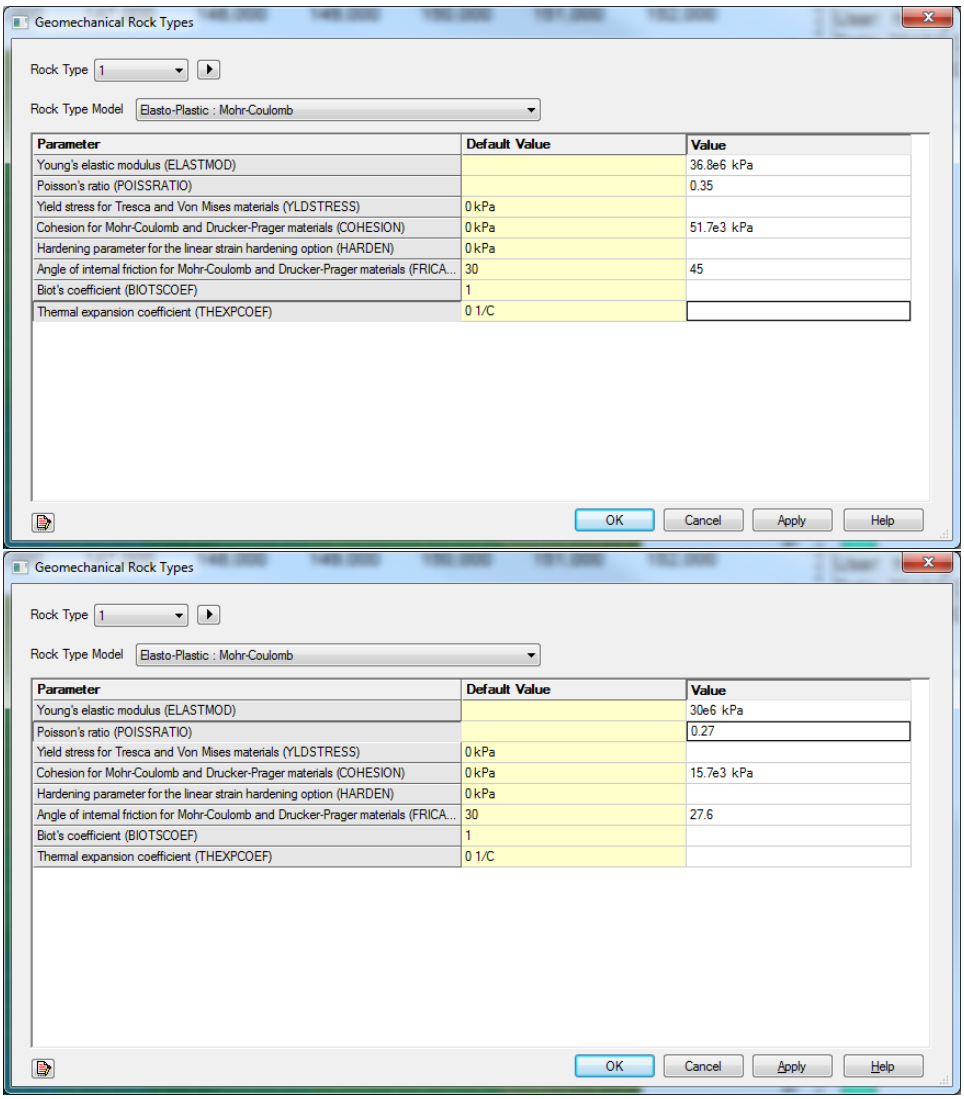

Figure 14: The input of geomechanical results in CMG. Only one geomechanical rock type is considered in fluid simulation. Geochanical experimental results of sample SH1 and DH3 were used for Weber Sandstone and Madison Limestone, respectively

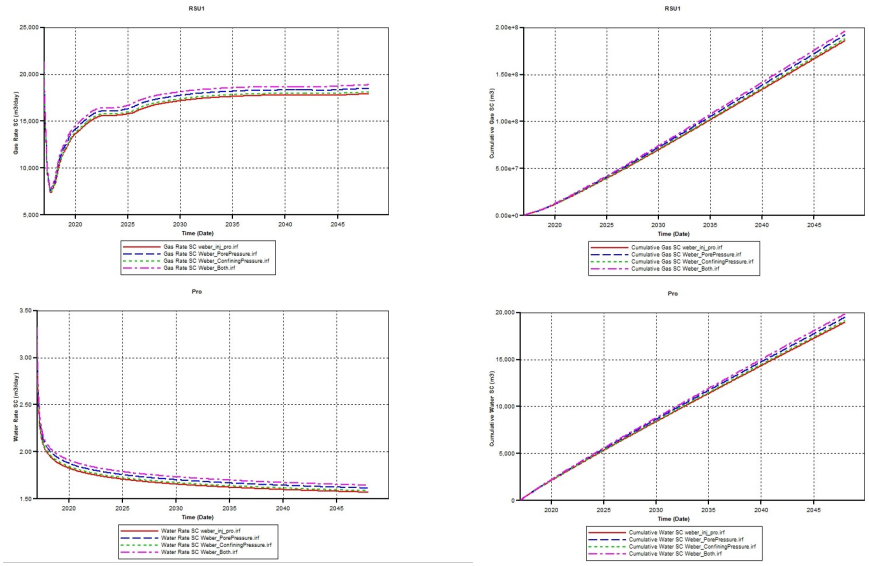

Figure 15: Comparison of CO_2 injection rate, cumulative injection, water production rate and cumulative water production of different cases with basic case: top row is gas injection and bottom row is water production

injection, water production decreases in a slow rate after 10 years and stabilizes finally.

As for the case considering porosity and permeability changes due to pore pressure buildup, at the beginning gas injection rate is the same as the base case. On the other hand, as the injection rate increases, the injection rate increases as well. Finally, reservoir pressure stabilizes, and the same happens for the injection rate. For the case considering permeability changes as a function of hydrostatic pressure, the injection rate is the same as that of the base case, and finally it is almost the same as the base case. The latter can be explained by noticing that as the pore pressure increases, the pressure difference between confining pressure and pore pressure gets smaller and reaches a constant value. Permeability changes can be ignored as pressure difference changes. Therefore the effect of pressure difference changes is small. However, when both effects of pore pressure increasing and confining pressure decreasing, the injection rate increase cannot be ignored. CO_2 saturation

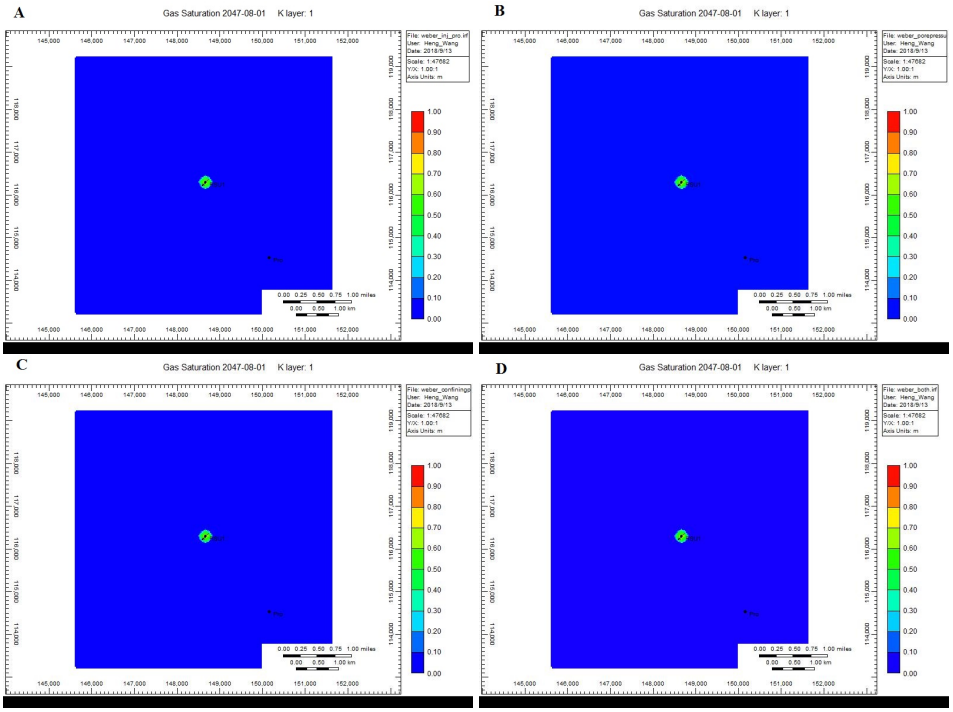

Figure 16: Comparison of CO_2 distribution of different cases with basic case

distributions are shown in Figure 16, and CO_2 plume is very small.

4.5.2 Madison Limestone Formation

From CO_2 injection curve for all cases in Figure 17, designed CO_2 injection rate can be reached because permeability of Madison Limestone formation (9.32 mD) is larger than that of Weber Sandstone formation (0.045 mD). For water production, it decrease immediately at the beginning as pressure difference between producer BHP and reservoir pressure decreases. From Figure 18, CO_2 plume size is larger than that of Weber Sandstone formation. No CO_2 viscous fingering showed between injector and producer. Two reasons might be in responsible for the circular plume. One reason is that producer locates in the downhill direction. CO_2 prefers to flow upward direction because of gravity segregation. Another reason is that permeability between injector and producer is not too heterogeneity. CO_2 flows in a piston-like displacement.

From Figure 17 and 18, effects of porosity and permeability change due to changes of pore pressure and confining pressure can be ignored. As permeability of Madison Limestone formation is relative large, changes of pore pressure and confining pressure is relative small because of water production.

5 Conclusions

CO_2 floodings were conducted for Madison Limestone and Weber Sandstone samples from Rock Springs Uplift. Cumulative water production and water recovery are different for different formation samples and different rock types also. However, as pore volume of all formation samples is relative smaller than that of dead volume of the coreflooding system, the CO_2 flooding results is not accurate. In addition, changes of petrophysical and geomechanical properties can be ignored before and after CO_2 aging, a large size limestone sample was selected to study the relative permeability curve change. CO_2 flooding results after CO_2 aging shows

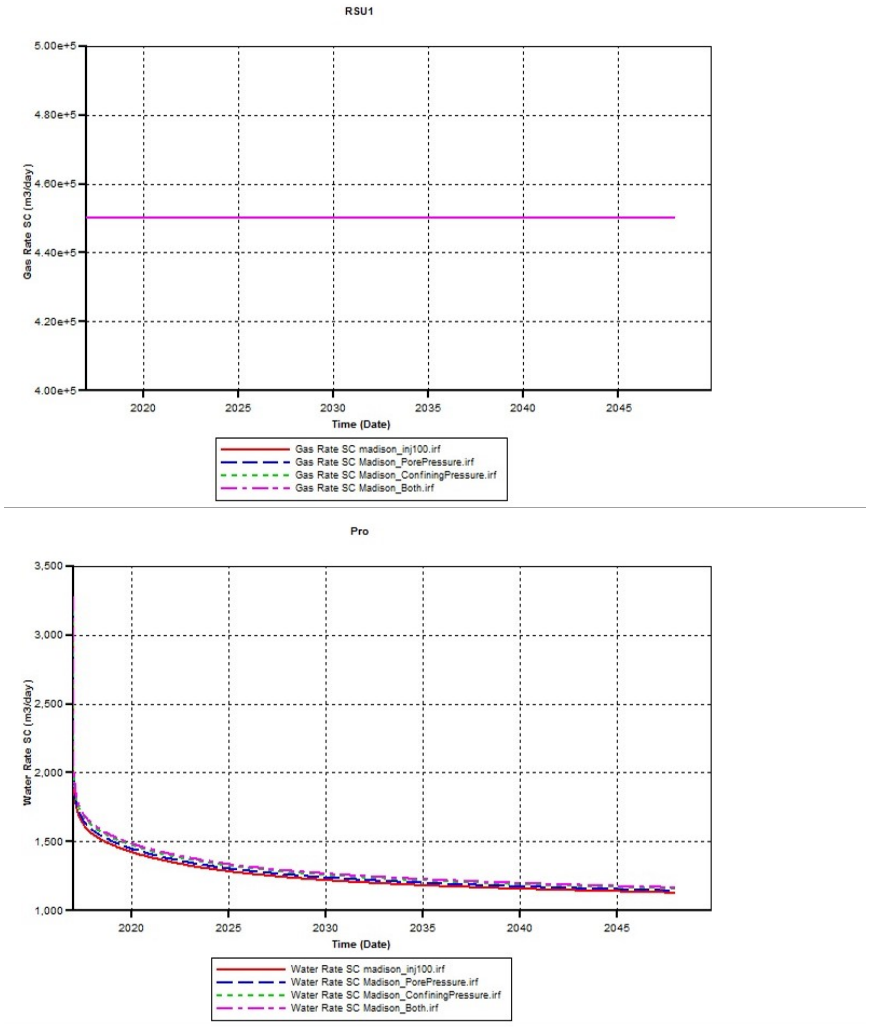

Figure 17: Comparison of CO_2 injection rate, cumulative injection, water production rate and cumulative water production of different cases with basic case: top row is gas injection and bottom row is water production

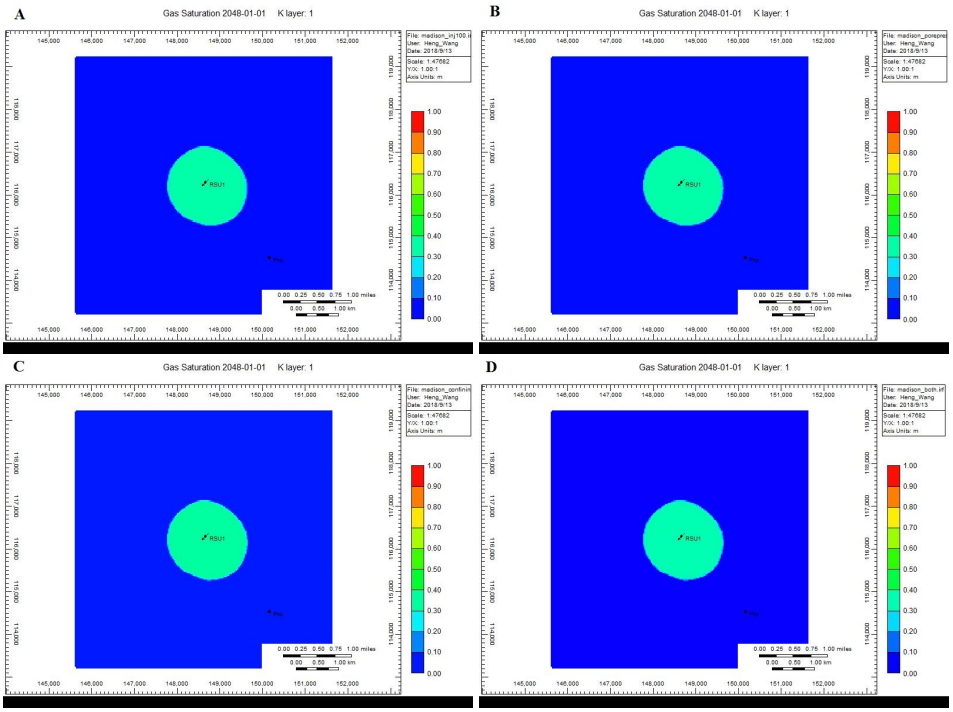

Figure 18: Comparison of CO_2 distribution of different cases with basic case

that water production rate and cumulative water production are different with that of before aging, meaning CO_2 flowability and trapped volume are different because of changes of relative permeability curve. Relative permeability curves were obtained by matching water production and results show that CO_2 relative permeability and irreducible water saturation are changed.

Reservoir simulation was performed to study the porosity and permeability changes due to changes of pore pressure and confining pressure during CO_2 injection process. Simulation results shows that for Weber Sandstone formation, injectivity is too small due to low permeability. The effect of confining pressure change on injection rate can be ignored, while the effect of pore pressure change can not. On the other hand, the effect of confining pressure and pore pressure change on CO_2 plume size of Madison Limestone formation is negligible because of higher permeability.

Part 2
CO_2 Storage Simulation Studies Considering Time-Dependent Geomechanical and Petrophysical Properties

1 Introduction

Many researcher in recent times have studied geomechanical properties, such as Yong's modulus and Possion ratio[40], as well as petrophysical properties, e.g. pore structure, porosity, permeability and wettability [41, 35, 38] as influenced by geochemical reactions (CO_2-brine-rock). The alteration of geomechanical and petrophysical properties are time-dependent, and these two group of properties will affect each other also. For example, the change of Yong's modulus and Possion ratio will cause the change of porosity and permeability, and vice versa. Furthermore, as petrophysical properties change, relative permeability and capillary pressure change also. Therefore, fluid flow will be affected by the change of geomechanical and petrophysical properties. In this study, we integrated the time-dependent geomechanical and petrophysical properties into the fluid flow model and compared their effects on CO_2 plume migration, plume size and total storage. Since no obvious changes of geochemical and petrophysical properties were observed in Weber Sandstone samples, we focused on the Madison Limestone formation.

In this study, all work elements required to update the reservoir model, from evolving geomechanical and petrophysical properties were considered. Geomechanical and petrophysical properties were assumed time-dependent. The basic static model used is described in Part 1 of this appendix. Experimental results used include coreflooding experiment, geochemical tests and geomechanical assays. Hence, the details can be found in the corresponding report and will not be repeated here. To realize the evaluation, the restart option of the simulator was used. Geomechanics-fluid flow models was run for a period of time. Then geomechanical properties will be remapped according to experimental results. The update/restart process were con- tinued until the end of the simulation. For comparison purposes, the studied case considers the properties change, while the base case does not.

2 Results and Discussion

2.1 Geomechanical Experimental Results

Changes in subsurface geochemical environment may also alter geomechanical properties of reservoir rock and seal rock through dissolution and precipitation of mineral phases and cements that can either mechanically weaken or strengthen or rock[42]. Rathnaweera et al.[43] conducted chemico-mineralogical experiment to obtain a comprehensive understanding of the effect of long-term CO_2 exposure on the chemico-mineralogical structure and corresponding strength characteristics of saline aquifer rock formations using silicate cement (SS) and carbonate cement (CS) sandstone samples and found that CS formations are subject to much greater strength property changes upon exposure to CO_2 than SS formations. Yasuhara et al.[44] studied the evolution of mechanical and hydraulic properties in sandstone inducted by mineral dissolution and precipitation and found that permeability after CO_2 injection is affected by changes of surface area and porosity. As for Weber Sandstone, no obvious porosity and permeability change, and mineral dissolution and precipitation were found, we suppose geomechanical properties were not changed too much to be considered in reservoir simulation study. Zhang et al.[45] studied petrophysical and petrographysical properties change after acid injection and observed that a significant permeability increase due to significant dissolution of the rock. The experimental results agree with our observations for Madison Limestone. Therefore, CO_2 injection process considering geomechanical properties change was simulation only for Madison Limestone. Geomechanical experimental results of the Madison Limestone samples after CO_2 aging shown in Figure 5 were obtained by Dr. Kam Ng's group. Same as results before CO_2 aging, geomechanical properties vary with experimental condition (confining pressure) and samples used. Time-dependent geomechanical properties (e.g. Young's modulus, Poisson's ratio) were considered. To simplify the simulation, only one restart was used, which served to provide a qualitative sense of the impact of ge-

omechanical properties alteration induced by CO_2 injection. Geomechanical results for sample DH3c were used in our simulation.

Table 5: Geomechanical experiment results for the Madison Limestone samples after CO_2 aging.

Sample ID	Category	Pc(MPa)[1]	E (GPa)[2]	υ [3]	c (MPa) [4]	ϕ (Deg.) [5]	Pp (MPa) [6]
DH1c	Brine+CO_2[a]	46.2	41.0	0.31	30.6	50.4	39.3
DH2c	Brine+CO_2	73.8	24.5	0.26	30.6	50.4	39.3
DH3c	Brine+CO_2	94.5	29.7	0.25	30.6	50.4	39.3

[a] aging with brine and CO_2

[1] confining pressure, [2] Yong's modulus, [3]Poisson's ratio, [4] cohesion for Mohr-Coulomb

[5] internal friction angle for Mohr-Coulomb, [6] in-situ pore pressure

2.2 Time-dependent Model Update

The geomechanics module in CMG solves for the force equilibrium of the formation and calculates the volumetric dilatation/compression as a result of both elastic and plastic straining. The pore volume changes may be caused by a combination of compression/tension or shear stresses. These changes in pore volume and the associated changes in transmissibilities are used in the reservoir model for calculating mass and energy balances in the reservoir. However, porosity and permeability changes due to induced CO_2-rock-brine reactions are not considered for the geomechanics module only. Therefore, geochemical reactions should be considered with CO_2 injection (time-scale).

Time-dependent geomechanical and petrophysical properties induced by CO_2-brine-rock reactions and CO_2 injection after CO_2 was injected into deep saline aquifer have an impact on fluid flow through porous media, like injectivity, porosity distribution, pressure distribution and gas saturation, etc. Figure 19 shows gas injection rate and water production rate for the base case and case considering geomechanical and geochemical properties change. Gas injection rate is not affected by the changes, because the injection pressure does not reach the set maximum

injection pressure. However, from Figure 20, the bottom hole pressure (BHP) at the beginning is larger for the studied case than the base case, which shows that gas injectivity is affected. After three years of injection, the BHP for the injector is smaller than that of the base case.

Water production decreased for the studied cases when properties changes were considered. As CO_2 was injected, pore pressure increased, leading to an increase of porosity around the injector, which slowed pressure migration. Therefore, the increasing of reservoir pressure around producer is smaller, which reduced pressure difference between reservoir pressure and BHP of producer. Hence, water production rate decreases faster.

After 30 year's injection, the changes of CO_2 plume and pressure distribution are not visible from Figure 21 and 22. It is because the total injected CO_2 volume is relative smaller compared to the pore volume of the reservoir. In addition, injection time is relative short to show the changes of pressure and gas saturation distribution. However, since grid properties around injector are affected both by geomechemical and geochemical properties change over time, porosity around injector increased after CO_2 injection, shown in Figure 23. While for porosity around producer, porosity is only affected by geomechemical properties change due to water production, it decreased compared with base case, shown in Figure 23.

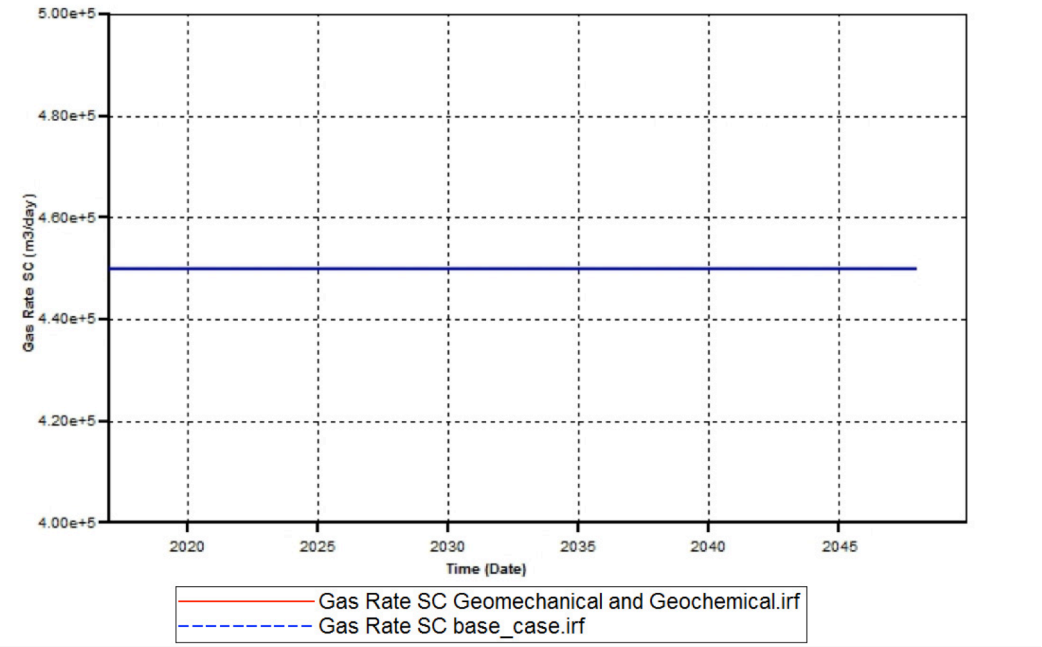

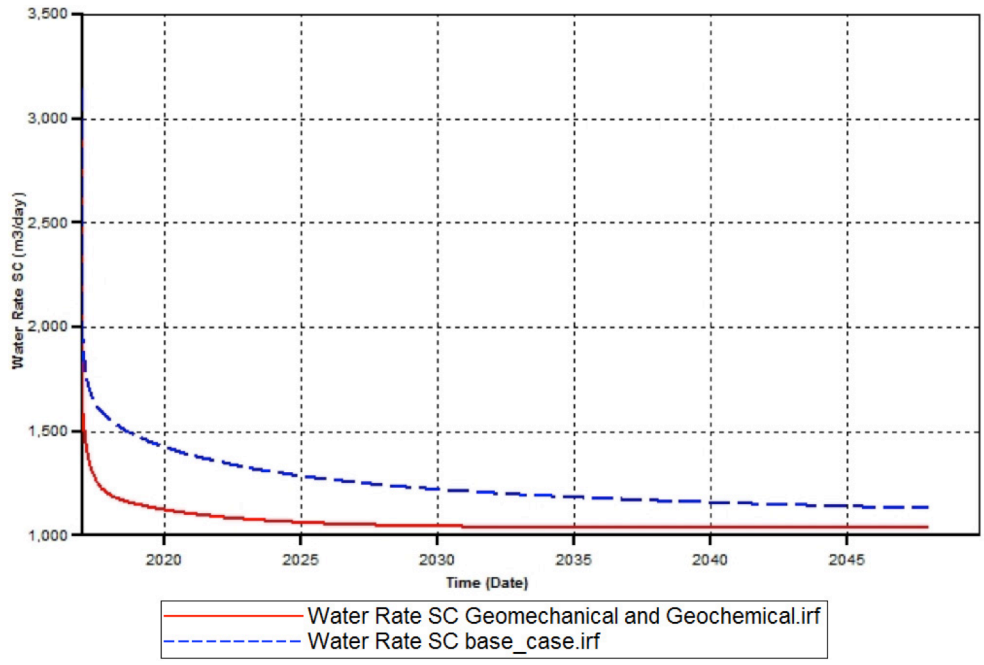

Figure 19. Comparison of CO_2 injection rate (top chart) and water production rate (bottom chart) for base case (blue dashed line) and case considering effects of CO_2–water rock interactions on geomechanical and geochemical properties (solid red line) of Madison Limestone. In the top chart, note that lines for the two cases overlie each other.

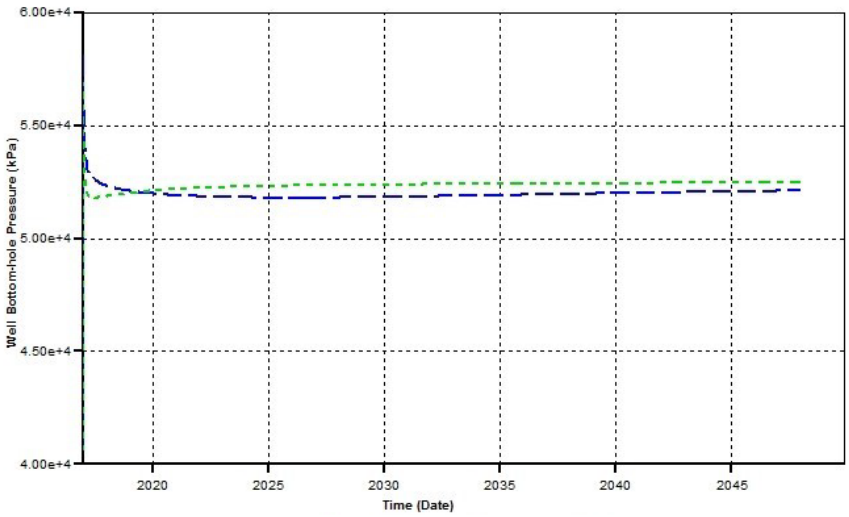

Figure 20: Comparison of bottom hole pressure in CO_2 injection well for base case (green dashed line) and case considering effects of CO_2–water rock interactions on geomechanical and geochemical properties (blue dashed line) of Madison Limestone.

3 Conclusions

In this study, all work elements required to update the reservoir model from evolving geomechanical and petrophysical properties were considered. Geomechanical and petrophysical properties were time-dependent. Simulation results considering time-dependent geomechanical and petrophysical properties induced by CO_2-brine-rock reactions and CO_2 injection after CO_2 was injected into deep saline aquifer were compared with base case, showing fluid flow through porous media, like injectivity, porosity distribution, pressure distribution and gas saturation was affected. Therefore, the effect of geomechanical and protrophysical properties changes as CO_2 is injected into deep saline aquifer is not negligible.

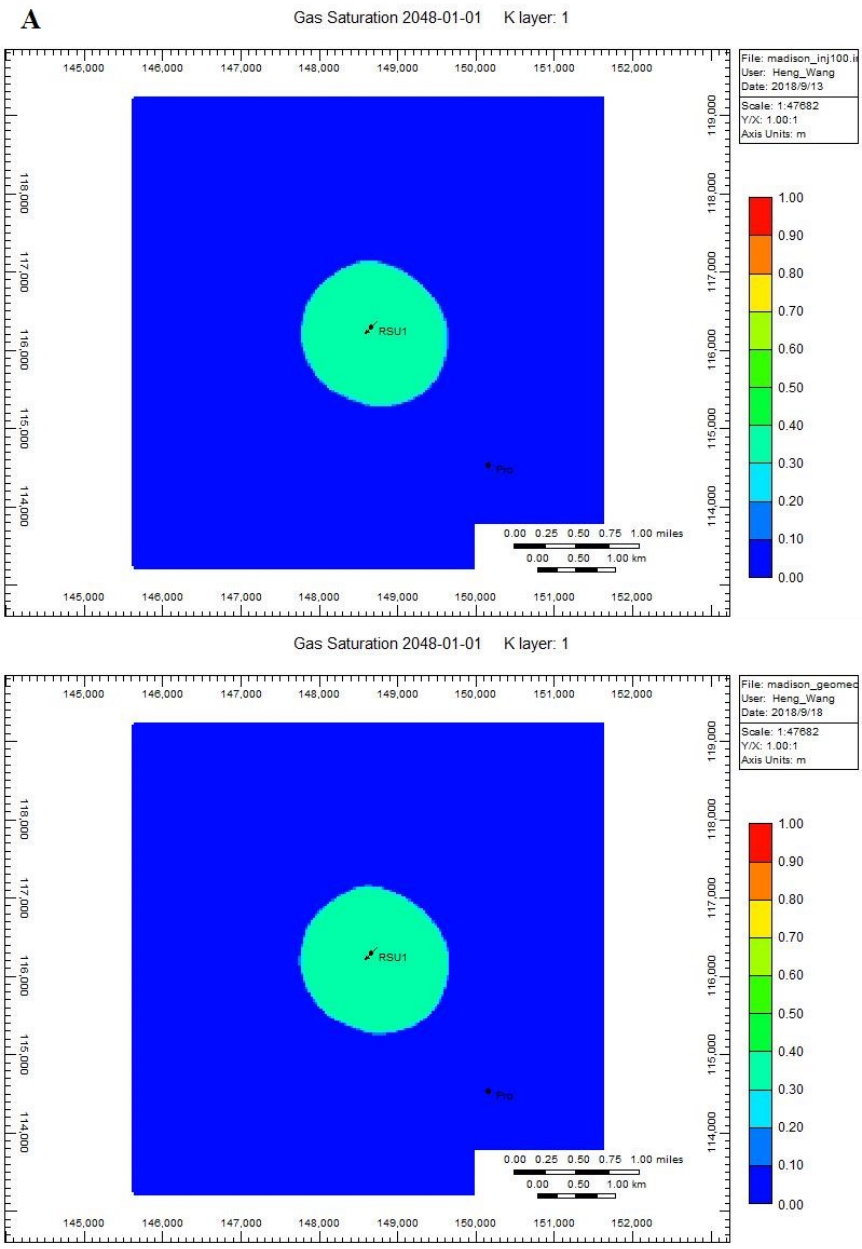

Figure 21: Comparison of gas saturation distribution for base case (up) and case considering geomechanical and geomechanical properties change (below)

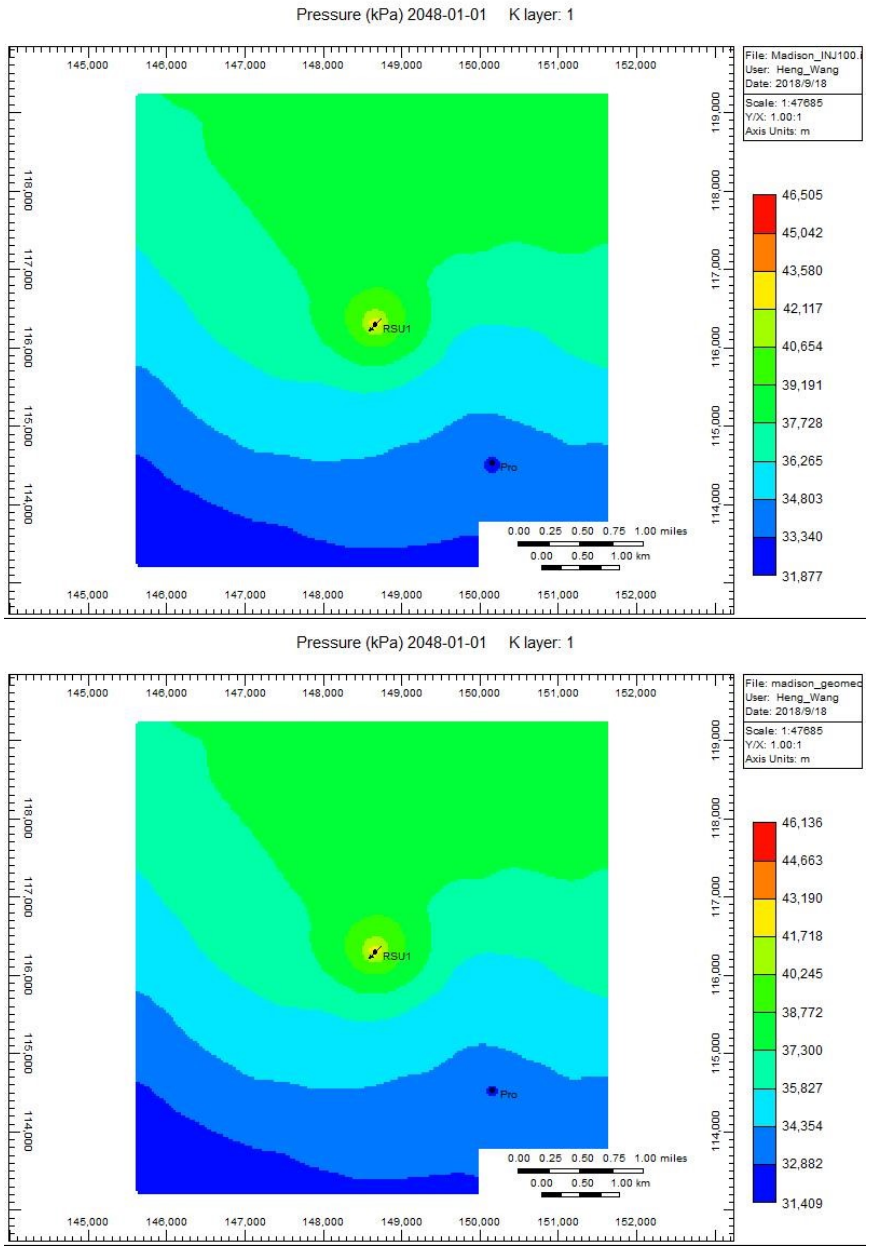

Figure 22: Comparison of pressure distribution for base case (up) and case considering geomechanical and geomechanical properties change (below)

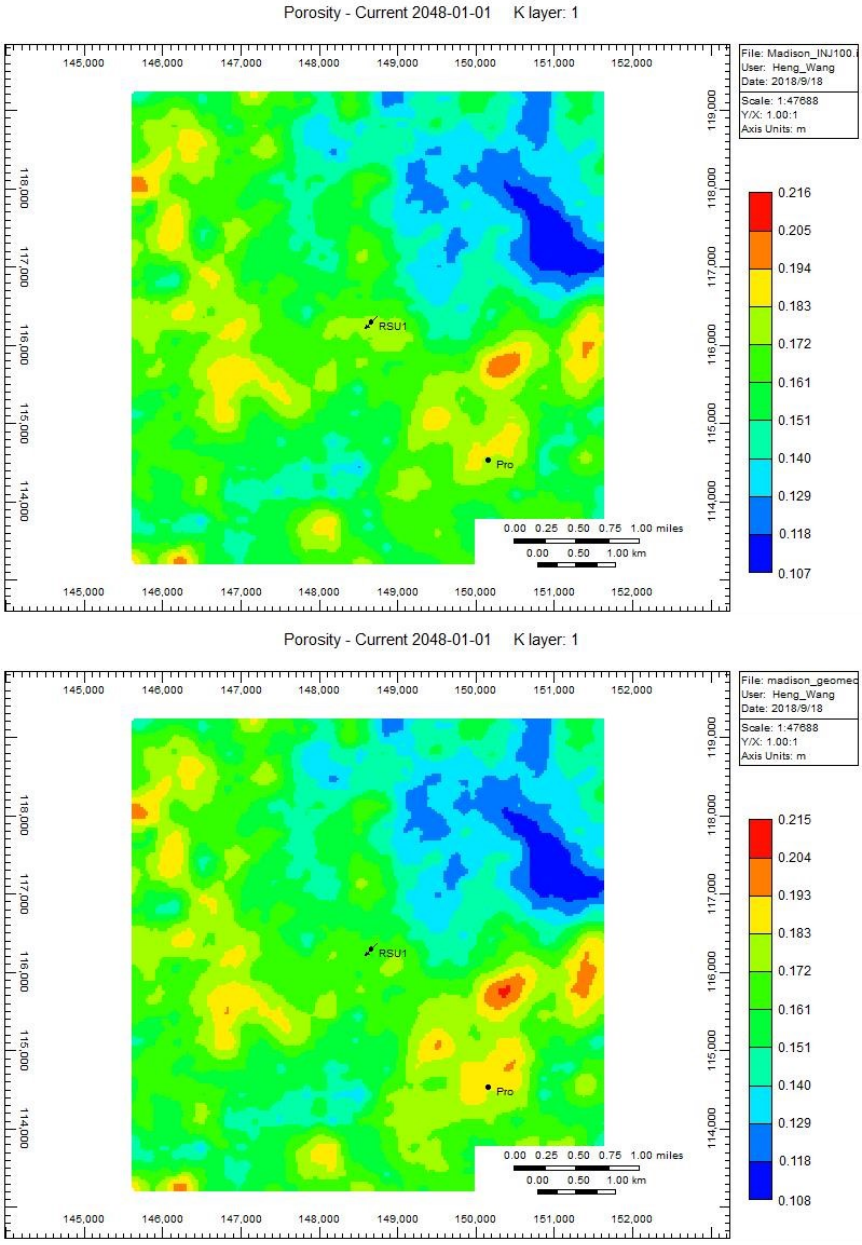

Figure 23: Comparison of porosity distribution for base case (up) and case considering geomechanical and geomechanical properties change (below)

References

[1] Y. Gong and Y. Gu, "Miscible CO_2 simultaneous water-and-gas (CO_2-swag) injection in the Bakken Formation," *Energy & Fuels*, vol. 29, no. 9, pp. 5655–5665, 2015.

[2] J. Shaw and S. Bachu, "Screening, evaluation, and ranking of oil reservoirs suitable for CO_2-flood EOR and carbon dioxide sequestration," *Journal of Canadian Petroleum Technology*, vol. 41, no. 09, 2002.

[3] Z. Dai, R. Middleton, H. Viswanathan, J. Fessenden-Rahn, J. Bauman, R. Pawar, S.-Y. Lee, and B. McPherson, "An integrated framework for optimizing CO_2 sequestration and enhanced oil recovery," *Environmental Science & Technology Letters*, vol. 1, no. 1, pp. 49–54, 2013.

[4] Z. Tao and A. Clarens, "Estimating the carbon sequestration capacity of shale formations using methane production rates," *Environmental science & technology*, vol. 47, no. 19, pp. 11 318–11 325, 2013.

[5] H. Wang, X. Liao, X. Dou, B. Shang, H. Ye, D. Zhao, C. Liao, and X. Chen, "Potential evaluation of CO_2 sequestration and enhanced oil recovery of low permeability reservoir in the junggar basin, china," *Energy & Fuels*, vol. 28, no. 5, pp. 3281–3291, 2014.

[6] D. Sun, J. Ripmeester, and P. Englezos, "Phase equilibria for the $CO_2/CH_4/N_2/H_2O$ system in the hydrate region under conditions relevant to storage of CO_2 in depleted natural gas reservoirs," *Journal of Chemical & Engineering Data*, vol. 61, no. 12, pp. 4061–4067, 2016.

[7] W. Ampomah, R. S. Balch, R. B. Grigg, Z. Dai, and F. Pan, "Compositional simulation of CO_2 storage capacity in depleted oil reservoirs," in *Carbon Management Technology Conference*. Carbon Management Technology Conference, 2015.

[8] A. Kovscek and Y. Wang, “Geologic storage of carbon dioxide and enhanced oil recovery. I. Uncertainty quantification employing a streamline based proxy for reservoir flow simulation,” *Energy Conversion and Management*, vol. 46, no. 11, pp. 1920–1940, 2005.

[9] A. Kovscek and M. Cakici, “Geologic storage of carbon dioxide and enhanced oil recovery. II. Co-optimization of storage and recovery,” *Energy Con- version and Management*, vol. 46, no. 11, pp. 1941–1956, 2005.

[10] J. Gale and P. Freund, “Coal-bed methane enhancement with CO_2 sequestration worldwide potential,” *Environmental Geosciences*, vol. 8, no. 3, pp. 210–217, 2001.

[11] S. Harpalani, B. K. Prusty, and P. Dutta, “Methane/CO_2 sorption modeling for coalbed methane production and CO_2 sequestration,” *Energy & Fuels*, vol. 20, no. 4, pp. 1591–1599, 2006.

[12] E. Ozdemir, “Modeling of coal bed methane (CBM) production and CO_2 sequestration in coal seams,” *International Journal of Coal Geology*, vol. 77, no. 1, pp. 145–152, 2009.

[13] C. M. White, D. H. Smith, K. L. Jones, A. L. Goodman, S. A. Jikich, R. B. LaCount, S. B. DuBose, E. Ozdemir, B. I. Morsi, and K. T. Schroeder, “Sequestration of carbon dioxide in coal with enhanced coalbed methane recovery a review,” *Energy & Fuels*, vol. 19, no. 3, pp. 659–724, 2005.

[14] S. Bachu, “Sequestration of CO_2 in geological media: Criteria and approach for site selection in response to climate change,” *Energy Conversion and Management*, vol. 41, no. 9, pp. 953–970, 2000.

[15] ——, “Screening and ranking of sedimentary basins for sequestration of CO_2 in geological media in response to climate change,” *Environmental Geology*, vol. 44, no. 3, pp. 277–289, 2003.

[16] S. Bachu and J. Adams, "Sequestration of CO_2 in geological media in response to climate change: Capacity of deep saline aquifers to sequester CO_2 in solution," *Energy Conversion and management*, vol. 44, no. 20, pp. 3151–3175, 2003.

[17] J. P. Kaszuba, D. R. Janecky, and M. G. Snow, "Carbon dioxide reaction processes in a model brine aquifer at 200°C and 200 bars: Implications for geologic sequestration of carbon," *Applied Geochemistry*, vol. 18, no. 7, pp. 1065–1080, 2003.

[18] L. Trevisan, R. Pini, A. Cihan, J. T. Birkholzer, Q. Zhou, A. González-Nicolás, and T. H. Illangasekare, "Imaging and quantification of spreading and trapping of carbon dioxide in saline aquifers using meter-scale laboratory experiments," *Water Resources Research*, vol. 53, no. 1, pp. 485–502, 2017.

[19] N. I. Gershenzon, R. W. Ritzi, D. F. Dominic, M. Soltanian, E. Mehnert, and R. T. Okwen, "Influence of small-scale fluvial architecture on CO_2 trapping processes in deep brine reservoirs," *Water Resources Research*, vol. 51, no. 10, pp. 8240–8256, 2015.

[20] X. Wang, V. Alvarado, N. Swoboda-Colberg, and J. P. Kaszuba, "Reactivity of dolomite in water-saturated supercritical carbon dioxide: Significance for carbon capture and storage and for enhanced oil and gas recovery," *Energy Conversion and Management*, vol. 65, pp. 564 – 573, 2013. [Online]. Available: http://www.sciencedirect.com/science/article/pii/S019689041200310X

[21] J. F. McLaughlin, S. Quillinan, and R. Surdam, "Characterizing diagenesis and its opposing impacts on porosity in the Weber and Madison Formations in southwest Wyoming: Applying geochemical, petrographic, and isotopic analysis to describe reservoir heterogeneity in potential CO_2 storage sites," in *2012 GSA Annual Meeting in Charlotte*, 2012.

[22] D. Grana, S. Verma, J. Pafeng, X. Lang, H. Sharma, W. Wu, F. McLaughlin, E. Campbell, K. Ng, V. Alvarado *et al.*, "A rock physics and seismic reservoir characterization study of the Rock Springs Uplift, a carbon dioxide sequestration site in southwestern Wyoming," *International Journal of Greenhouse Gas Control*, vol. 63, pp. 296–309, 2017.

[23] H. Wang, V. Alvarado, J. F. McLaughlin, D. A. Bagdonas, J. P. Kaszuba, E. Campbell, and D. Grana, "Low-field nuclear magnetic resonance characterization of carbonate and sandstone reservoirs from Rock Spring Uplift of Wyoming," *Journal of Geophysical Research: Solid Earth*.

[24] R. C. Surdam, *Geological CO_2 storage characterization: The key to deploying clean fossil energy technology*. Springer Science & Business Media, 2013.

[25] C. Doughty and K. Pruess, "Modeling supercritical carbon dioxide injection in heterogeneous porous media," *Vadose Zone Journal*, vol. 3, no. 3, pp. 837–847, 2004.

[26] B. McMillan, N. Kumar, and S. L. Bryant, "Time-dependent injectivity during CO_2 storage in aquifers," in *SPE Symposium on Improved Oil Recovery*. Society of Petroleum Engineers, 2008.

[27] A. Kopp, H. Class, and R. Helmig, "Investigations on CO_2 storage capacity in saline aquifers: Part 1. Dimensional analysis of flow processes and reservoir characteristics," *International Journal of Greenhouse Gas Control*, vol. 3, no. 3, pp. 263–276, 2009.

[28] M. Burton, N. Kumar, and S. L. Bryant, "CO_2 injectivity into brine aquifers: Why relative permeability matters as much as absolute permeability," *Energy Procedia*, vol. 1, no. 1, pp. 3091–3098, 2009.

[29] S. Bachu and B. Bennion, “Effects of in-situ conditions on relative permeability characteristics of CO_2-brine systems,” *Environmental Geology*, vol. 54, no. 8, pp. 1707–1722, 2008.

[30] J. W. Amyx, D. M. Bass, R. L. Whiting, “Petroleum reservoir engineering: Physical properties,” McGraw-Hill Book Company, Inc. , 610 pages, 1960.

[31] R. Hu, J. Wan, Y. Kim, and T. K. Tokunaga, “Wettability impact on supercritical CO_2 capillary trapping: Pore-scale visualization and quantification,” *Water Resources Research*, vol. 53, pp. 6377–6394, 2017.

[32] R. Pini and S. M. Benson, “Simultaneous determination of capillary pressure and relative permeability curves from core-flooding experiments with various fluid pairs,” *Water Resources Research*, vol. 49, no. 6, pp. 3516–3530, 2013.

[33] C. Chalbaud, M. Robin, J. Lombard, F. Martin, P. Egermann, and H. Bertin, “Interfacial tension measurements and wettability evaluation for geological CO_2 storage,” *Advances in Water Resources*, vol. 32, pp. 98–109, 2009.

[34] X. Wang, V. Alvarado, N. Swoboda-Colberg, and J. P. Kaszuba, “Reactivity of dolomite in water-saturated supercritical carbon dioxide: Significance for carbon capture and storage and for enhanced oil and gas recovery,” *Energy Conversion and Management*, vol. 65, pp. 564–573, 2013.

[35] P. Chiquet, D. Broseta, and S. Thibeau, “Wettability alteration of caprock minerals by carbon dioxide,” *Geofluids*, vol. 7, no. 2, pp. 112–122, 2007.

[36] P. K. Bikkina, “Contact angle measurements of CO_2-water–quartz/calcite systems in the perspective of carbon sequestration,” *International Journal of Greenhouse Gas Control*, vol. 5, no. 5, pp. 1259–1271, 2011.

[37] S. Wang, I. M. Edwards, and A. F. Clarens, "Wettability phenomena at the CO_2-brine-mineral interface: implications for geologic carbon sequestration," *Environmental Science & Technology*, vol. 47, pp. 234–241, 2012.

[38] D. N. Espinoza and J. C. Santamarina, "Water-CO_2-mineral systems: Interfacial tension, contact angle, and diffusion—Implications to CO_2 geological storage," *Water Resources Research*, vol. 46, no. 7, 2010.

[39] J. F. McLaughlin, R. D. Bentley, and S. A. Quillinan, "Regional geologic history, CO_2 source inventory, and groundwater risk assessment of a potential CO_2 sequestration site on the Rock Springs Uplift in southwest Wyoming," in *Geological CO2 Storage Characterization*. Springer, 2013, pp. 33–54.

[40] M. Wigand, J. Carey, H. Schütt, E. Spangenberg, and J. Erzinger, "Geochemical effects of CO_2 sequestration in sandstones under simulated in situ conditions of deep saline aquifers," *Applied Geochemistry*, vol. 23, no. 9, pp. 2735–2745, 2008.

[41] B. M. Tutolo, A. J. Luhmann, X.-Z. Kong, M. O. Saar, and W. E. Seyfried Jr, "Experimental observation of permeability changes in dolomite at CO_2 sequestration conditions," *Environmental Science & Technology*, vol. 48, no. 4, pp. 2445–2452, 2014.

[42] J. R. Major, P. Eichhubl, T. A. Dewers, and J. E. Olson, "Effect of CO_2–brine–rock interaction on fracture mechanical properties of CO_2 reservoirs and seals," *Earth and Planetary Science Letters*, vol. 499, pp. 37–47, 2018.

[43] T. Rathnaweera, P. Ranjith, M. Perera, A. Ranathunga, W. Wanniarachchi, S. Yang, A. Lashin, and N. Al Arifi, “An experimental investigation of coupled chemico-mineralogical and mechanical changes in varyingly-cemented sandstones upon CO_2 injection in deep saline aquifer environments,” *Energy*, vol. 133, pp. 404–414, 2017.

[44] H. Yasuhara, N. Kinoshita, D. S. Lee, J. Choi, and K. Kishida, “Evolution of mechanical and hydraulic properties in sandstone induced by simulated mineral trapping of CO_2 geo-sequestration,” *International Journal of Greenhouse Gas Control*, vol. 56, pp. 155–164, 2017.

[45] Y. Zhang, M. Sarmadivaleh, M. Lebedev, A. Barifcani, R. Rezaee, N. Testamantia, S. Iglauer *et al.*, “Geo-mechanical weakening of limestone due to supercritical CO_2 injection,” in *Offshore Technology Conference Asia*. Offshore Technology Conference, 2016.

Appendix X

Development and Analyses of the Initial Static Model

Introduction

From a geophysical point of view, the injection of CO_2 will cause changes in pressure and saturation in the target formations, which can be monitored using time-lapse seismic surveys (Grude et al., 2013; 2014). Before planning such time-lapse surveys, it is important to first test the 4D feasibility of monitoring CO_2. The goal of this research is to investigate if seismic data could be used to monitor CO_2 at the Rock Springs Uplift (RSU) during time-lapse studies, which would be important to address any possible safety issues (leakage, contamination of overlying aquifers, …) caused by the CO_2 injection.

In the following, we first investigate the joint effects of pressure and saturation on elastic attributes (V_P, V_s and ρ). The pressure effect on dry moduli is applied using MacBeth's equations and the fluid effect is modeled using Gassmann's equations (Mavko et al., 2009). The different synthetic elastic attributes are then used to compute synthetic seismograms using the convolutional model.

Pressure-saturation-velocity model

A quantitative assessment of variations in reservoir state during time-lapse surveys requires a numerical modeling of the effects of pressure and saturation changes due to injection on elastic properties. Many relationships linking velocities and effective pressure have been developed (Eberhart-Phillips et al., 1989; Dvorkin et al., 1996) and show a general increase in elastic velocities with effective pressure. P_e represents the effective pressure, equal to the difference between the overburden pressure (P_o) and the pore pressure (P_p):

$$P_e = P_o - \alpha P_p \qquad (1)$$

where α is the effective stress coefficient, also called Biot's poroelastic coefficient. It is a function of the compressibility of the rock framework, the grain compressibility and the applied pressures or stresses (Nur and Byerlee, 1971). We assume it to be equal to 1.

These relations can be regression, exponential or complex equations and are usually calibrated using laboratory data or pressure measurements at the well location. A physical law that encapsulates the dependence of dry-rock bulk and shear moduli on pressure was derived by MacBeth (2004). Fluid effects are commonly modelled using Gassmann's equations. In the RSU target formations, we applied MacBeth's equations (MacBeth, 2004) given by the following expressions:

$$K_{dry}(P_e) = \frac{K^{\infty}}{1+A_k exp\left(-\frac{P_e}{P_k}\right)} \quad (2)$$

$$\mu_{dry}(P_e) = \frac{\mu^{\infty}}{1+A_\mu exp\left(-\frac{P_e}{P_\mu}\right)} \quad (3)$$

where K_{dry} and μ_{dry} are respectively the dry-rock bulk modulus and shear modulus; K^{∞} and μ^{∞} are the asymptotic values of the moduli at high pressures; P_k and P_μ are the characteristic pressure constants in the rocks; the parameters A_k and A_μ are related to the rock compliance. These parameters are empirical and are obtained by calibration of equations 2 and 3 with formation pressure measurements or laboratory measurements.

Figure 1 shows the dry-rock bulk and shear moduli equations calibrated to compiled laboratory data in the Weber (left plots) and the Madison (right plots). Because MacBeth's equations were calibrated using measurements from one core sample only, the absolute values of the predictions are valid only for the specific core sample, i.e., for a rock with the same porosity. We assume that the shape of the curve is the same for other porosity values and we impose the same relation by increasing or decreasing the value according to the bulk moduli at different porosities at reservoir pressure conditions.

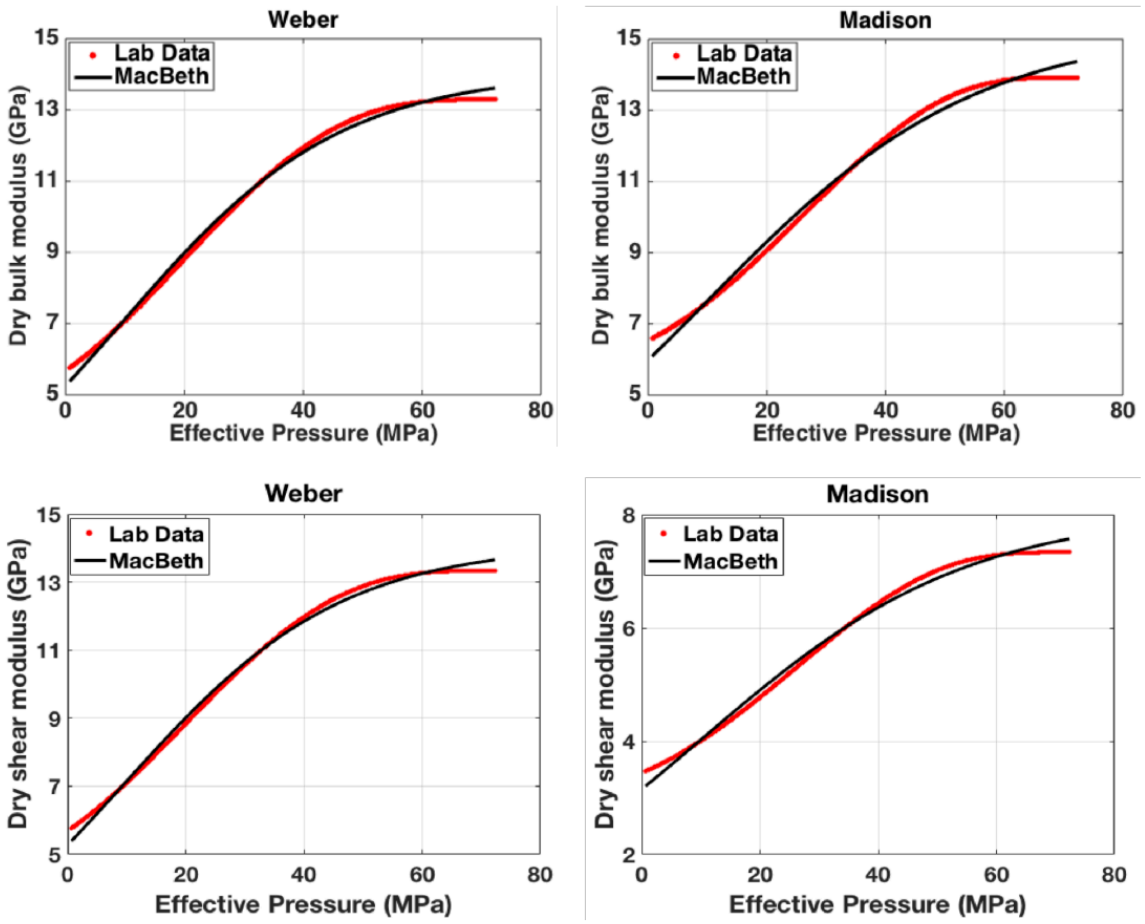

Figure 1: Calibration of MacBeth's equations with compiled laboratory data. Top: Dry-rock bulk modulus in the Weber (left) and Madison (right). Bottom: Dry-rock shear modulus in the Weber (left) and Madison (right).

Saturation and pressure effects on elastic properties at the well location

Upon CO_2 injection, pore pressure is expected to increase at the injection well. We assume a decrease of effective pressure and we simulate multiple saturation scenarios. For simplicity, we assume only one fluid saturation type in the entire reservoir for each scenario. The following pressure and fluid scenarios were applied and synthetic velocities and seismograms were modeled:

1. The effective pressure is the in situ effective pressure;P_e= 52.38 MPa in the Weber and P_e= 57.52 MPa in the Madison. The reservoir is fluid saturated with the in situ fluid

which is dominantly brine with some residual oil (base case).

2. The effective pressure is decreased to P_e= 40 MPa and the reservoir is saturated with the initial fluid.
3. The effective pressure is decreased to P_e= 40 MPa and the reservoir is fully saturated with brine.
4. The effective pressure is decreased to P_e= 40 MPa and the reservoir is saturated with a partial homogeneous mixture of brine and gas. We will test two different fluid proportions: 95% of brine and 5% of gas, 80% of brine and 20% of gas. A mixture of brine and gas could be a realistic scenario because CO_2 displaces brine as it moves through the pore space.

The elastic velocities and densities for the five scenarios above are plotted in Figure 2 for the Weber and Figure 3 for the Madison. The corresponding synthetic seismograms are displayed in Figures 4 and 5. For all the plots, effective pressure is equal to 40 MPa. When the effective pressure decreases with no change in fluid, the elastic moduli decrease and hence the P- and S-wave velocities decrease (Figures 2 and 3). When we do a fluid substitution with gas (third and fourth plots of Figures 2 and 3), the low bulk modulus of gas causes V_P to decrease further, and this shows that both pressure and saturation effects produce a decrease V_P in gas-saturated rocks. The pressure effect dominates V_P over the saturation effect. Both pressure and saturation effects tend to decrease shear waves in brine-saturated rocks (Figures 2 and 3). Similarly, to compressional waves, the pressure effect also dominates shear waves over the saturation effect. For all scenarios mentioned above, the changes observed in velocities are rather small. On the other hand, and irrespective of the target formation, a change of density would be observed due to the difference in gas saturation. An absolute change in density of about 1.2% was observed for a 20% gas saturation, and about 5% change was observed for 80% gas saturation.

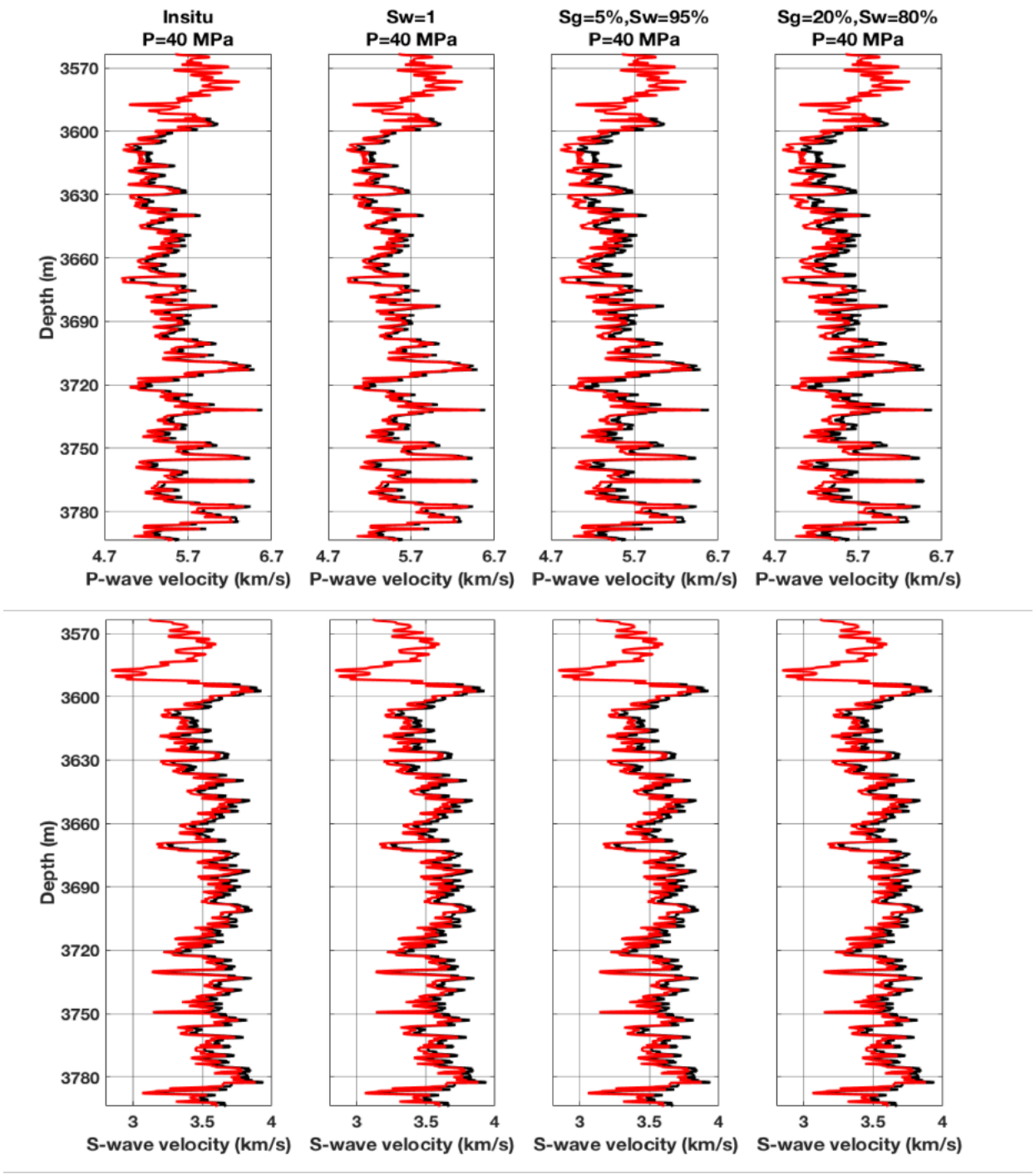

Figure 2: P-wave velocity, S-wave velocity and density for different saturation and pressure scenarios in the Weber Sandstone. Effective pressure in the Weber Sandstone is 52.38 MPa. For all scenarios, effective pressure is decreased to 40 MPa. From top to bottom: P-wave velocity, S-wave velocity and density. In situ well logs (black), modeled scenarios (red).

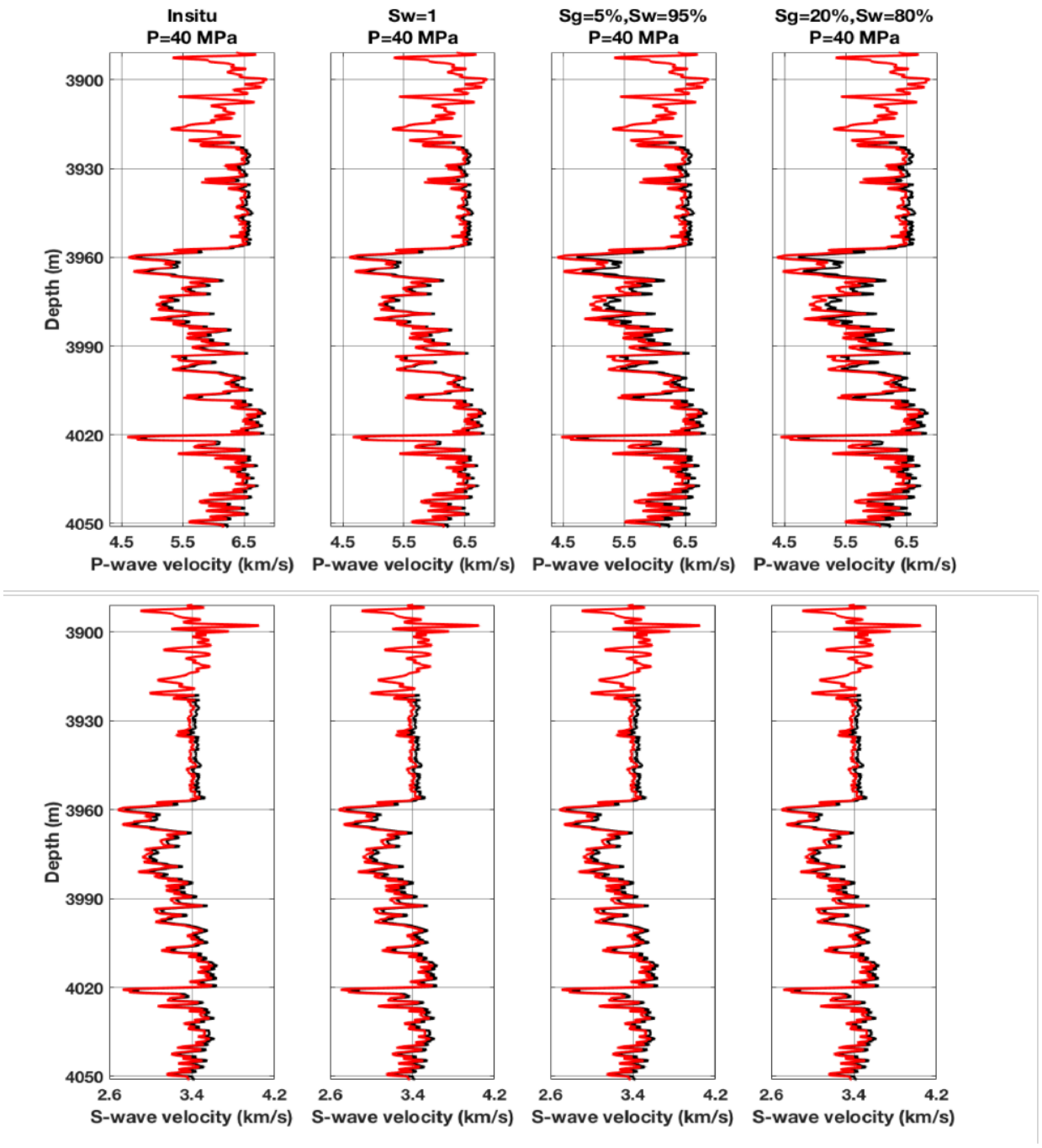

Figure 3: P-wave velocity, S-wave velocity and density for different saturation and pressure scenarios in the Madison. Effective pressure in the Madison is 57.52 MPa. For all scenarios, effective pressure is decreased to 40 MPa. From top to bottom: P-wave velocity, S-wave velocity and density. In situ well logs (black), modeled scenarios (red).

The synthetic seismic traces were computed at the well location using the convolutional model which is based on the Aki-Richards linear approximation method and for the angle range from 0^o to 34^o. The decrease in pressure followed by fluid substitution caused the velocities to decrease, which should lead to longer travel times. Seismic amplitudes of those synthetic seismograms are plotted in Figures 4 and 5 for the Weber Sandstone and Madison Limestone respectively. In both formations, we could observe small time shifts and changes in amplitudes in the different scenarios.

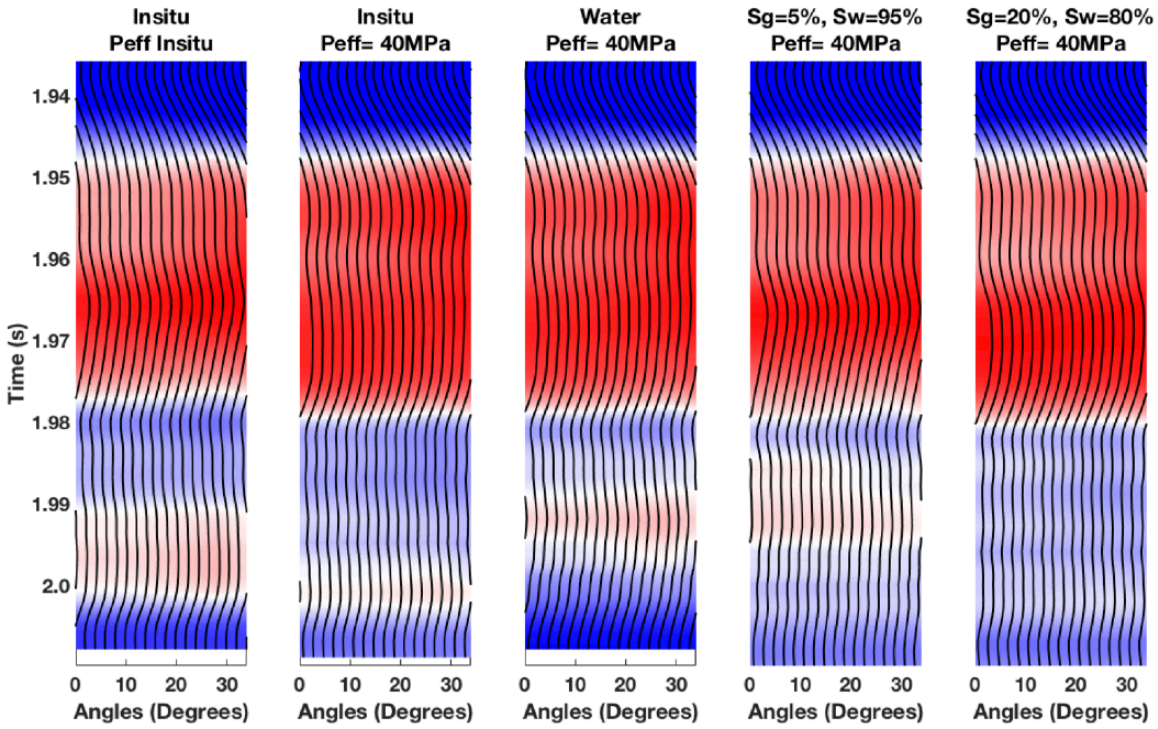

Figure 4: Synthetic seismograms computed for the Earth models of the different scenarios plotted in Figure 2 in the Weber Sandstone. Synthetics seismograms are displayed for the range of angles (0^o – 34^o). Seismic amplitude normalized, from -1 to 1.

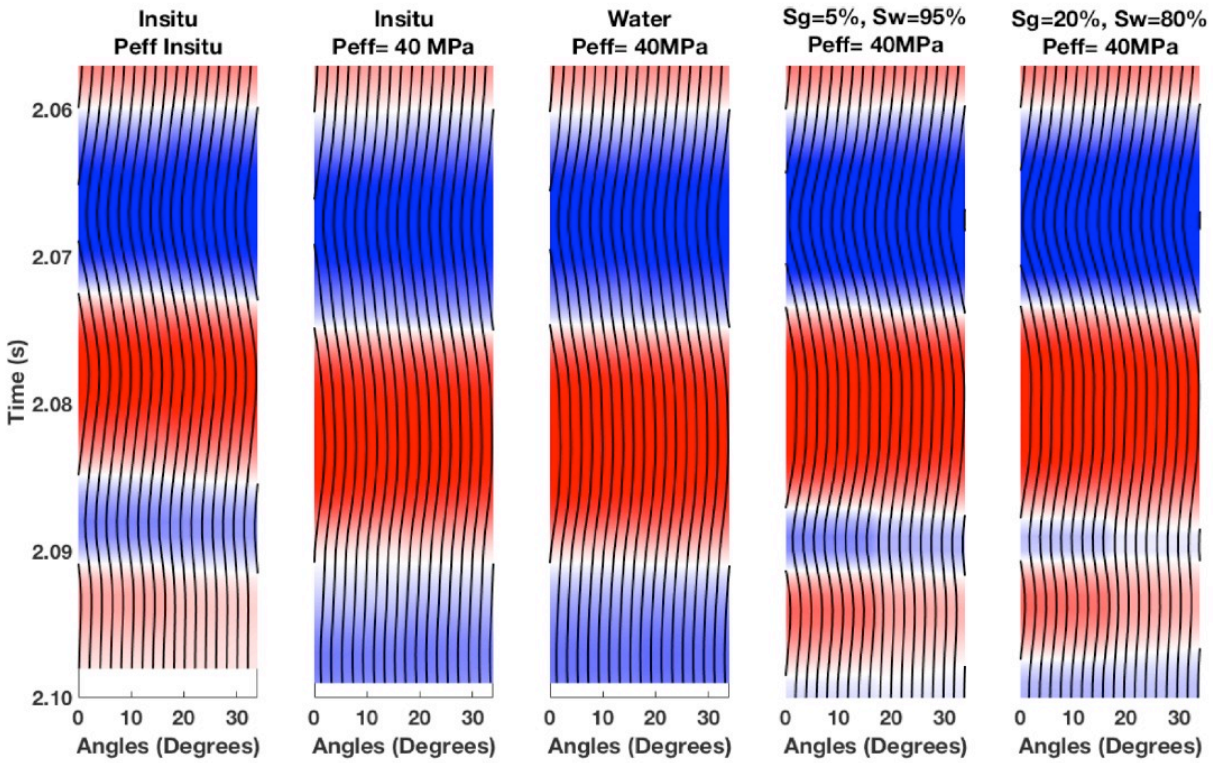

Figure 5: Synthetic seismograms computed for the Earth models of the different scenarios plotted in Figure 3 in the Madison. Synthetic seismograms are displayed for the range of angles (0^o – 34^o). Seismic amplitude normalized, from -1 to 1.

Conclusions

To assess the feasibility of monitoring CO_2 displacement during injection and to mitigate leakage-risks situations, we simulated different pressure and saturation scenarios and modeled their effects on elastic velocities and synthetic seismograms. MacBeth's and Gassmann's equations were used to account for the pressure and saturation effects. Our tests showed that the pressure and saturation effects on velocities are small. The small variations are due to the low porosity of the sandstone and the high stiffness of the dolomite. These small changes on elastic velocities and density might be challenging to capture because of the presence of noise in recorded data. Therefore, we believe that time-lapse seismic data are insufficient for efficient CO_2 monitoring at the RSU area.

References

Dvorkin, J., N. Amos, and C. Chaika, 1996, Stress sensitivity of sandstones: Geophysics, 61, 444–455.

Eberhart-Phillips, D., D.-H. Han, and M. D. Zoback, 1989, Empirical relationships among seismic velocity, effective pressure, porosity, and clay content in sandstone: Geophysics, 54, 82–89.

Grude, S., M. Landrø, and B. Osdal, 2013, Time-lapse pressure-saturation discrimination for CO_2 storage at the Snøhvit field: International Journal of Greenhouse Gas Control, 19, 369-378.

Grude, S., M. Landrø, and J. Dvorkin, 2014, Pressure effects caused by CO_2 injection in the Tubåen Fm., the Snøhvit field: International Journal of Greenhouse Gas Control, 27, 178–187.

MacBeth, C., 2004. A classification for the pressure-sensitivity properties of a sandstone rock frame: Geophysics, 69, 497–510.

Mavko, G., T. Mukerji, and J. Dvorkin, 2009, The rock physics handbook: Tools for seismic analysis of porous media: Cambridge University Press.

Nur, A., and J. D. Byerlee, 1971, An exact effective stress law for elastic deformation of rocks with fluids: Journal of Geophysical Research, 76, 6414–6419.